



UNICA

UNIVERSITÀ
DEGLI STUDI
DI CAGLIARI

**Ph.D. DEGREE IN
Chemical Sciences and Technologies**

Cycle XXXVIII

TITLE OF THE Ph.D. THESIS

Hydrogen permeation in uncoated and W-coated X60steel...

Scientific Disciplinary Sector(s)

CHEM-01, Chimica Analitica

Ph.D. Student:	Raouaa Hannachi
Supervisor	Professor Antonella Rossi
Co-Supervisor	Professor Marzia Fantauzzi

Final exam. Academic Year 2024/2025
Thesis defence session: May 2026

This Thesis is dedicated to my parents
Your love, support and strength have guided me throughout this journey

“Guided by the Arabic saying **من جد وجد** (*Man jadda wajada*), which translates as ‘who strives, succeeds,’ This work is the result of perseverance, learning, and the experiences gained along the way.”

Abstract

The sustainable storage and transport of hydrogen are critical challenges in the transition toward renewable energy systems, necessitating a detailed understanding of hydrogen–material interactions in pipeline steels and the development of effective strategies to mitigate hydrogen uptake. In this PhD work, hydrogen diffusion and permeation in API 5L X60 pipeline steel were investigated, with the primary objective of developing, optimizing, and validating experimental and analytical methodologies for the determination of hydrogen in RF-Magnetron sputtering tungsten coating that act as hydrogen permeation barrier (HPB).

The central innovation of this work lies in the comprehensive analytical optimization of tungsten as a HPB by examining hydrogen uptake, transport, and barrier effectiveness in tungsten-coated X60 steel as well as X60 steel, this research provides new insights into the application of tungsten for mitigating hydrogen ingress and the development of an analytical approach by combining electrochemical and surface analytical techniques for characterizing X60 steel and tungsten that act as hydrogen permeation barrier.

Hydrogen permeation experiments on **X60 steel** enabled accurate determination of the effective hydrogen diffusion coefficient (D_{eff}) and subsurface hydrogen concentration (C_0). D_{eff} values, calculated using both the time-lag (t_{lag}) and breakthrough time (t_b) methods, the results ranged from $2.0 (0.4) \times 10^{-10}$ to $2.9 (0.5) \times 10^{-10} \text{ m}^2 \text{ s}^{-1}$ and were in agreement with literature data. Subsurface hydrogen concentrations were found to be $0.66 (0.02) \text{ ppm}$ for solvent-cleaned X60 steel and $0.8 (0.1) \text{ ppm}$ for mechanically polished samples.

Three series of **W coatings** were prepared using RF magnetron sputtering: Series 1 (tungsten coating thickness $d = 3 \text{ }\mu\text{m}$, substrate roughness $R_a = 0.4 \text{ }\mu\text{m}$), Series 2 ($d = 3 \text{ }\mu\text{m}$, $R_a = 0.2 \text{ }\mu\text{m}$), and Series 3 ($d = 1.5 \text{ }\mu\text{m}$, $R_a = 0.2 \text{ }\mu\text{m}$). Electrochemical hydrogen permeation measurements revealed that Series 1 exhibited a permeation reduction factor (PRF) of 4 and an effective hydrogen diffusion coefficient (D_{eff}) of $3.5 (0.5) \times 10^{-10} \text{ m}^2 \text{ s}^{-1}$. Series 2 demonstrated a significantly higher PRF of 35–40 and a lower D_{eff} of $4.9 (0.2) \times 10^{-11} \text{ m}^2 \text{ s}^{-1}$, while Series 3 showed a PRF of 25–30 with D_{eff} of $9.1 (0.2) \times 10^{-11} \text{ m}^2 \text{ s}^{-1}$.

Another innovation of this work is the development of a rapid, non-destructive XPS-based analytical approach to quantify through-thickness porosity in tungsten coatings, using the Fe 2p/W 4f area ratio from survey spectra. Using this method, a porosity of $3.5 (0.8)\%$ was measured for $3 \text{ }\mu\text{m}$ thick tungsten coatings on rough substrates ($R_a \approx 0.4 \text{ }\mu\text{m}$). In contrast, no detectable porosity was observed for the same thickness on smoother substrates ($R_a \approx 0.2 \text{ }\mu\text{m}$). For $1.5 \text{ }\mu\text{m}$ thick coatings on smooth substrates, porosity values below 0.5% were measured in selected samples. These results were statistically validated across multiple areas and independent samples.

Electrochemical permeation tests established a strong correlation between coating porosity and hydrogen barrier effectiveness. Dense tungsten coatings on smoother substrates reduced hydrogen permeation by a permeation reduction factor (PRF) of up to 40, whereas coatings with higher porosity exhibited much lower reduction (PRF = 4–5). These findings highlight that

coating uniformity, defect density, and interfacial quality are the primary determinants of HPB performance, while coating thickness plays a secondary role.

Depth-resolved RBS/ERDA analyses revealed an oxygen-enriched region near the surface of tungsten coatings, extending 30–40 nm deep. Additional AR-XPS and HAXPES measurements demonstrated depth-dependent tungsten oxidation, suggesting that chemically modified near-surface layers contribute to the hydrogen barrier function in addition to structural factors.

Table of contents

1.	General Introduction	1
1.1.	Challenges and background.....	1
1.2.	Objectives of this research:.....	2
1.3.	Structure of the thesis	2
	References	4
2.	Literature review	6
1.4.	The danger of hydrogen embrittlement in steels	6
2.1.1	Formation of hydrogen atoms	6
2.1.2	Hydrogen embrittlement of steels	6
2.1.3	Critical influencing factors	7
2.2.	Hydrogen permeation barriers (HPBs)	8
2.2.1	Materials for HPB	8
2.2.2	Performance of HPB	10
2.2.3	Technologies to produce HPB coatings	17
2.3.1	Properties of tungsten	19
2.3.2	Tungsten coatings as hydrogen permeation barrier	23
2.3.3	Critical influencing factors on hydrogen permeation barrier efficiency	24
	References	25
3.	Experimental	32
3.1.	Materials	33
3.1.1	The substrate: X60 steel.....	33
3.1.2	Roughness test	33
3.1.3	Coating materials and deposition: RF magnetron sputtering.....	33
3.2	Sample preparation	34
3.2.1	Sample preparation for hydrogen permeation test (Devanathan and Stachurski cell)	34
3.2.2	Sample preparation for analysis via inert gas fusion LECO ONH836	35
3.3.	Electrochemical hydrogen permeation test (HPT)	36
3.3.1	Electrochemical hydrogen permeation cell and potentiostats (at the University of Cagliari (UniCa), Italy)	36
3.3.2	Modified electrochemical hydrogen permeation cells and potentiostats (at Laboratory of joining technologies and corrosion EMPA Dübendorf (CH))	37
3.4.	Local hydrogen measurements: Microcapillary cell technique	40
3.5.	Hydrogen Analysis by inert gas Fusion (LECO ONH836)	42

3.6. Surface analytical techniques	42
3.6.1. X-ray photoelectron spectroscopy (XPS)	43
3.6.3. X ray photoelectron spectroscopy /Hard X ray photoelectron spectroscopy (XPS/HAXPS)	44
3.7 Other techniques	45
3.7.1. Portable X-ray fluorescence (p-XRF).....	45
3.7.3. X ray diffraction (XRD).....	45
3.7.4. Rutherford Backscattering Spectrometry / Elastic Recoil Detection (RBS/ERDA)	46
3.7.5. Scanning Electron Microscopy/Energy Dispersive X-ray Spectroscopy (SEM /EDS) and metallographic characterization	47
References	47
4. Results	50
4.1. Diffusion of hydrogen in X60 steel	51
4.1.1. Sample characterization before hydrogen permeation test	51
4.1.1.1. X-ray fluorescence (XRF).....	51
4.1.1.2. Scanning electron microscopy-Energy dispersive X ray spectroscopy (SEM- EDS).....	51
4.1.1.3 X-ray diffraction (XRD).....	52
4.1.1.4. X-ray photoelectron spectroscopy (XPS).....	53
4.1.1.5 Rutherford Backscattering spectrometry/Elastic recoil detection (RBS/ERDA)	57
4.1.2 Electrochemical hydrogen permeation results (HPT).....	58
4.1.3 Sample characterization after the hydrogen permeation test	62
4.1.3.1. Local Hydrogen Measurements: Microcapillary cell technique	62
4.1.3.2. Hydrogen Analysis by Inert Gas Fusion.	63
4.1.3.3 Rutherford Backscattering spectrometry/Elastic recoil detection (RBS/ERDA)	63
4.2. Tungsten coatings as a hydrogen permeation barrier	65
4.2.1 Characterization of the coated samples.....	65
4.2.1.1 X-ray fluorescence (XRF) results	65
4.2.1.2 Scanning electron microscopy (SEM) results	66
4.2.1.3 X-ray diffraction (XRD).....	67
4.2.1.4 Porosity measurements on the W-coated X60 steel: Development of a Survey XPS-Based Analytical approach	72
References	80
5. Discussion	81

5.1. Hydrogen diffusion in X60 steel	81
5.1.1. Surface composition and homogeneity	81
5.1.2. Hydrogen content in X60 steel before Hydrogen charging	82
5.1.3. Hydrogen uptake after hydrogen charging	82
5.2. Tungsten as a hydrogen permeation barrier	87
5.2. 1. Influence of surface roughness	87
5.2.2. Influence of coating thickness	90
5.2.3. Correlation of the substrate roughness and coating thickness with hydrogen permeation behavior	91
References	95
6. Conclusions and outlook.....	99
7. Appendix	101
7.1. Techniques overview.....	101
7.1.1.. Electrochemical hydrogen permeation test: Devanathan and Stachurski cell	101
7.1.2. The Electrochemical Microcapillary cell technique.....	108
7.1. 3.. X-ray photoelectron spectroscopy	110
7.1.4. Combined X-ray photoelectron spectroscopy /Hard X-ray photoelectron spectroscopy (XPS/HAXPES)	114
7.1. 4.. Rutherford Backscattering Spectrometry (RBS) and Elastic Recoil Detection Analysis (RBS/ERDA).....	115
7.1.5. . Inert Gas Fusion (LECO ONH836).....	117
7.1. 6.. X-ray diffraction.....	117
7.2. Supplementary data on X-ray Photoelectron Spectroscopy (XPS) Results	119
7.3. Published papers.....	126

1. General Introduction

This chapter introduces the challenges associated with the dangers of hydrogen embrittlement and provides a brief overview of the importance of studying steel materials and developing coatings that act as hydrogen permeation barriers to mitigate or reduce hydrogen uptake into steel.

1.1. Challenges and background

One of the major challenges in sustainable energy production is the mismatch between electricity generation and consumption [1]. For instance, solar energy systems often generate excess electricity during the summer months, while energy demand typically peaks in the winter. As large-scale battery storage remains insufficient for seasonal energy storage, alternative solutions are required to bridge this gap. Among the most promising approaches is the use of electrolysis to convert surplus electricity into “green hydrogen”; hydrogen produced by renewable sources which can then be stored and later reconverted to electricity during periods of high demand. However, efficient storage and transport of hydrogen remain significant hurdles. Conventional storage methods, such as liquefaction at cryogenic temperatures or compression in high-pressure tanks, are expensive. To address these limitations, various chemical storage methods have been proposed, including the steam-iron process [1] and the emerging “power to aluminum” concept [2] where excess electricity is used to reduce aluminum hydroxide to elemental aluminum, which can later be oxidized to release hydrogen and heat. For hydrogen transport over long distances, steel pipelines are preferred due to their cost-effectiveness, high efficiency, and safety [3],[4]. Nonetheless, steel’s susceptibility to hydrogen absorption and diffusion can significantly degrade its mechanical properties, a phenomenon known as hydrogen embrittlement (HE) [5],[6]. Laboratory studies have shown that hydrogen accelerates fatigue and crack growth in pipeline steel and its welds; the reported crack growth acceleration factors is high [7]. The stress corrosion cracking (SCC) susceptibility of X60 steel was studied with slow strain rate tests in a solution simulating groundwater: it was found that the failure process was controlled by hydrogen embrittlement and anodic dissolution [8]. When considering the repurposing of existing gas pipelines for hydrogen transport, it is crucial to evaluate the hydrogen embrittlement sensitivity of the pipeline steels. In fact, X60 steel has been observed to exhibit increased embrittlement severity and secondary crack formation under pure hydrogen [9], and tensile tests have revealed an 83% reduction in ductility in hydrogen-charged environments [10]. Hydrogen embrittlement impairs the integrity of steel pipelines, increasing the risk of hydrogen leakage and subsequent combustion or explosion due to hydrogen’s wide flammability range [11], [12]. Beyond pipelines, HE poses reliability and safety issues for metal structures in aerospace, automotive, construction, and particularly in critical energy infrastructure such as power and nuclear plants [13], [14]. To prevent or at least significantly reduce hydrogen uptake in steel, hydrogen permeation barriers (HPBs) offer a promising solution. HPBs are specialized coatings designed to block or limit hydrogen ingress into the underlying steel substrate. Achieving optimal performance with these barriers,

however, remains a formidable challenge. It requires not only reproducible and carefully tailored substrate surface preparation, but also precisely controlled coating procedures and rigorously regulated deposition parameters. The complexity of these requirements highlights the innovative and demanding nature of developing effective HPBs for advanced energy infrastructure applications. Moreover, it is essential to recognize that the effectiveness of HPBs cannot be fully assessed without also considering the properties and behavior of the base material itself. As the steel substrate forms an integral part of the system for hydrogen transport, its microstructure, hydrogen diffusion characteristics, must be studied alongside the coatings. This is crucial for developing a strong solution for safe and reliable hydrogen transportation in advanced energy infrastructure.

1.2. Objectives of this research:

- **Development of an analytical approach by combining electrochemical** such as (Devanathan–Stachurski cell) for in situ investigation of hydrogen diffusion behavior in materials **and surface analytical techniques for characterizing materials that act as HPBs.**
- **To study hydrogen permeation and diffusion in X60 steel**, using a combination of analytical techniques and electrochemical cells
- **To investigate the hydrogen trapping in X60 steel**, determining both the effective diffusion coefficient and subsurface hydrogen concentration.
- **The optimization of a hydrogen permeation barrier (HPB) based on RF-magnetron sputtered tungsten coatings on steel substrates.** This includes varying the substrate roughness and coating thickness to evaluate their influence on barrier performance and hydrogen uptake.
- **To establish an innovative analytical approach for determining through - thickness porosity**, integrating XPS analysis with electrochemical permeation data to directly correlate microstructural features with functional performance.

1.3. Structure of the thesis

This work is organized into six chapters, followed by an appendix:

- **Chapter 1** provides a brief introduction to the challenges and background of this research, giving the importance of characterizing steel and developing effective hydrogen permeation barriers (HPBs).
- **Chapter 2** presents a comprehensive literature review on the danger of hydrogen embrittlement, as well as proposed solutions involving HPBs. A wide range of examples of HPBs from the literature are discussed, and tungsten is introduced as a candidate material, with an overview of its relevant properties.

- **Chapter 3** describes the experimental procedures in detail, including sample preparation and the characterization techniques employed in this study.
- **Chapter 4** presents the results obtained from experimental investigations.
- **Chapter 5** is dedicated to the discussion and interpretation of the results, linking them to the research objectives and existing literature.
- **Chapter 6** provides the main conclusions of the work and discusses perspectives for future research.

Following the main chapters, the appendix is divided into three parts. **Appendix 7.1** contains the physical principles underlying the techniques used in this study, while **Appendix 7.2** contains supplementary data related to the X-ray photoelectron spectroscopy (XPS) analyses, including tables reporting the curve-fitting parameters and representative XPS spectra. **Appendix 7.3** contains all the published papers related to this PhD thesis.

References

- [1] S. P. Heiniger, Z. Fan, U. B. Lustenberger, and W. J. Stark, “Safe seasonal energy and hydrogen storage in a 1: 10 single-household-sized pilot reactor based on the steam-iron process,” *Sustainable Energy & Fuels*, vol. 8, no. 1, pp. 125–132, 2024.
- [2] M. Y. Haller, D. Carbonell, M. Dudita, D. Zenhäusern, and A. Häberle, “Seasonal energy storage in aluminium for 100 percent solar heat and electricity supply,” *Energy Conversion and Management: X*, vol. 5, p. 100017, 2020.
- [3] D. Mahajan, K. Tan, T. Venkatesh, P. Kileti, and C. R. Clayton, “Hydrogen blending in gas pipeline networks—a review,” *Energies*, vol. 15, no. 10, p. 3582, 2022.
- [4] E. Ohaeri, U. Eduok, and J. Szpunar, “Hydrogen related degradation in pipeline steel: A review,” *International Journal of Hydrogen Energy*, vol. 43, no. 31, pp. 14584–14617, 2018.
- [5] A. Negi, M. Elkhodbia, I. Barsoum, and A. AlFantazi, “Coupled analysis of hydrogen diffusion, deformation, and fracture: a review,” *International Journal of Hydrogen Energy*, vol. 82, pp. 281–310, 2024.
- [6] Y. He, Y. Su, H. Yu, and C. Chen, “First-principles study of hydrogen trapping and diffusion at grain boundaries in γ -Fe,” *International Journal of Hydrogen Energy*, vol. 46, no. 10, pp. 7589–7600, 2021.
- [7] L. E. Faucon, T. Boot, T. Riemsdag, S. P. Scott, P. Liu, and V. Popovich, “Hydrogen-accelerated fatigue of API X60 pipeline steel and its weld,” *Metals*, vol. 13, no. 3, p. 563, 2023.
- [8] A. Contreras, S. L. Hernández, R. Galvan-Martinez, and O. Vega-Becerra, “Tension Tests Behavior of API 5L X60 Pipeline Steel in a Simulated Soil Solution to Evaluate SCC Susceptibility,” *MRS Online Proceedings Library (OPL)*, vol. 1481, pp. 71–80, 2012.
- [9] R. Walallawita *et al.*, “Evaluating the effect of blended and pure hydrogen in X60 pipeline steel for low-pressure transmission using hollow-specimen slow-strain-rate tensile testing,” *Metals*, vol. 14, no. 10, p. 1132, 2024.
- [10] M. A. Mohtadi-Bonab, M. Eskandari, K. M. M. Rahman, R. Ouellet, and J. A. Szpunar, “An extensive study of hydrogen-induced cracking susceptibility in an API X60 sour service pipeline steel,” *International Journal of Hydrogen Energy*, vol. 41, no. 7, pp. 4185–4197, 2016.
- [11] B. Sun *et al.*, “Current challenges in the utilization of hydrogen energy—a focused review on the issue of hydrogen-induced damage and embrittlement,” *Advances in Applied Energy*, vol. 14, p. 100168, 2024.
- [12] J. Hoschke, M. F. W. Chowdhury, J. Venezuela, and A. Atrens, “A review of hydrogen embrittlement in gas transmission pipeline steels,” *Corrosion Reviews*, vol. 41, no. 3, pp. 277–317, 2023.
- [13] Y.-S. Chen *et al.*, “Hydrogen trapping and embrittlement in metals—a review,” *International Journal of Hydrogen Energy*, vol. 136, pp. 789–821, 2025.

[14] G. A. Young Jr, E. Richey, and D. S. Morton, “Hydrogen embrittlement in nuclear power systems,” in *Gaseous hydrogen embrittlement of materials in energy technologies*, Elsevier, 2012, pp. 149–176.

2. Literature review

This chapter reviews the challenges associated with hydrogen embrittlement, discusses the development and effectiveness of hydrogen permeation barriers (HPBs), and introduces tungsten as a promising HPB material.

1.4. The danger of hydrogen embrittlement in steels

Hydrogen embrittlement (HE) is a phenomenon in which metals become brittle and prone to cracking due to the absorption and diffusion of hydrogen atoms within their structure. This process has been studied for a long time[1],[2]

2.1.1 Formation of hydrogen atoms

Hydrogen atoms can be produced, in principle, from hydrogen molecules (H_2 gas) through dissociation and adsorption [3]. Once they enter the steel microstructure, hydrogen atoms are distributed between voids in the lattice (referred to as lattice-mobile hydrogen) or trapped in microstructural inhomogeneities such as grain boundaries, dislocations, and voids (Figure 2.1) In the environment containing gaseous hydrogen, the H_2 molecules are chemically adsorbed on the metal surface, dissociate (in small amount) into H atoms that then permeate into the material (Figure 2.1) In aqueous environments atomic hydrogen can be produced by electrochemical process, e.g. cathodic protection, corrosion, or electroplating. In these circumstances where the source of hydrogen is not from gaseous phase, the term is Internal hydrogen embrittlement (IHE).

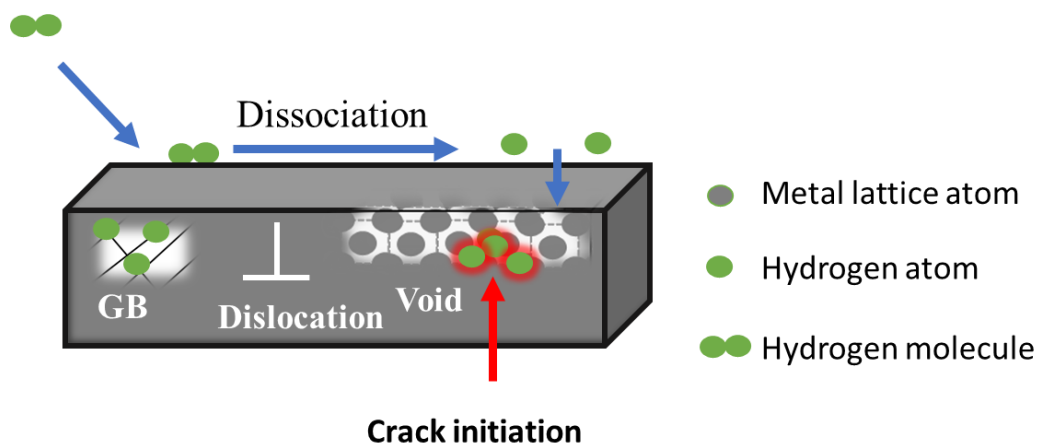


Figure 2.1. Hydrogen atom formation and hydrogen uptake in steel

2.1.2 Hydrogen embrittlement of steels

Hydrogen embrittlement in steels is closely linked to the material's ability to permit hydrogen ingress and diffusion throughout its structure. The permeability of hydrogen in steels is a critical parameter, as it directly influences the ability to which hydrogen can penetrate and accumulate at microstructural defects, subsequently leading to embrittlement phenomena [4], [5].

Compared to other bulk materials, such as pure metals (e.g., palladium, nickel) and certain ceramics, steels generally exhibit moderate hydrogen permeability, with the actual value depending strongly on alloy composition, microstructure, and temperature

Pure metals like Vanadium, Niobium, Titanium, Iron Nickel and Molybdenum have the higher hydrogen permeability, while the permeability of tungsten is extremely low in order of 10^{-15} mol H₂/(m s Pa^{0.5}), In contrast, steels (Ferritic steels and Austenitic steels) exhibit hydrogen permeability on the order of 10^{-11} mol H₂/(m s Pa^{0.5}) as indicated in Table 2.1 [6] The permeability in steels are sufficiently elevated under numerous service conditions to permit considerable hydrogen absorption, thereby presenting an ongoing risk of hydrogen embrittlement. This highlights the critical importance of comprehending and regulating hydrogen transport within steels.

Table 2.1. Hydrogen permeability of metals, steels, and ceramics [6].

Material class	Material	Permeability (mol H ₂ /(m s Pa ^{0.5}))
Metals	Vanadium	2.9×10^{-8}
	Niobium	7.5×10^{-9}
	Titanium	7.5×10^{-9}
	Iron	1.8×10^{-10}
	Nickel	1.2×10^{-10}
	Molybdenum	1.2×10^{-11}
	Tungsten	4.3×10^{-15}
Steels	Ferritic steels	3.0×10^{-11}
	Austenitic steels	1.0×10^{-11}
Ceramics	Titanium carbide (TiC)	8.0×10^{-15}
	TiC/TiN layered	7.0×10^{-16}
	Aluminium oxide (Al ₂ O ₃)	9.0×10^{-17}
	β-SiC	1.0×10^{-20}

2.1.3 Critical influencing factors

Hydrogen permeability and uptake are critical considerations in the performance and reliability of steels, especially in applications subjected to hydrogen-rich or corrosive environments. High-strength steels for example; characterized by their refined microstructures and increased levels of alloying elements, generally exhibit high susceptibility to hydrogen embrittlement [6]. The permeability of hydrogen in these steels is often moderated by microstructural features [7].

Several other key factors in addition to **microstructure** influence the susceptibility of steels to hydrogen embrittlement such as:

Hydrogen Concentration: The amount of hydrogen absorbed by the steel, for example during fabrication or service as hydrogen may enter the steel during processing steps such as welding,

pickling, or electroplating, or during service in corrosive or hydrogen-rich environments. [8] directly affects the material's susceptibility to hydrogen embrittlement.

Residual Stress : residual stress promotes crack initiation and propagation in the presence of hydrogen.[9]

2.2. Hydrogen permeation barriers (HPBs)

Hydrogen permeation barriers (HPB) are an effective means to block or at least greatly reduce the permeation of hydrogen atoms into the base metal, mostly carbon steel,[10] [11] Research has been performed in the past in the fields of nuclear plants (avoid ingress of radioactive tritium), in the space industry (hydrogen is used as fuel for rockets) and in energy research, too. Several reviews have been published, and the promising hydrogen permeation barriers have been identified These can be metals, oxides, carbides or nitrides[12],[13],[14] Irrespective of the type of barrier the main challenge is to produce an as much defect free barrier (coating) on the substrate. In the following paragraphs candidates for hydrogen permeation barriers are presented, discussed, and compared respect their efficiency; the main results shall be summarized in a comprehensive Table 2.2.

The factor that help the researcher classify the effectiveness of the HPBs is known as the permeation reduction factor (PRF). PRF is determined as the ratio of the steady-state hydrogen flux through the uncoated substrate to the coated sample ($PRF = \frac{J_{uncoated}}{J_{coated}}$).[15]

2.2.1 Materials for HPB

Hydrogen Permeation Barrier requires a little defect such as pores, cracks and should have a compact microstructure, low hydrogen diffusion, hydrogen diffusion coefficient, hydrogen permeability and high Permeation Reduction Factor .

Permeation Reduction factor is defined as the ratio of the permeation through the uncoated membrane $J_{uncoated}$ versus the permeation ratio through the coated membrane J_{coated} .

The information presented here focuses on the last recent promising hydrogen barriers, including metals, ceramics such as oxides, nitrides, carbon, and carbide and polymers.

- **Metals**

The microstructure and microstructure defect of metals plays significant function for metallic hydrogen permeation barrier (MHPBs). As instance MHPBs requires a compact microstructure. For ferritic (BCC) and austenitic steels (FCC) as example, there is a considerable difference between diffusivity values: 10^{-9} m²/s for the (BCC) ferritic steels and 10^{-16} m²/s for the (FCC) austenitic steels at room temperature [16] .

Metal alloy has a considerable effect on the diffusivity of hydrogen. Marques e al [16] highlight in their work The effect of Cr_{eq}/Ni_{eq} on some steels in addition to their work on the 2Cr-30Ni non equiatomic high entropy alloy and 20Cr-20Ni high entropy alloy. They concluded that the Cr and Ni concentration define the type of crystal structural and the formation of biphasic (austenite and ferrite) they well also showed that the hydrogen diffusivity decreased with the

increase of Cr concentration. Nemanic et al [17] have measured the hydrogen permeability of pure bulk chromium and it was $P_0 = 3.23 \times 10^{-7} \text{ mol H}_2/\text{s/m/Pa}^{0.5}$ and diffusivity $D_0 = 9.0 \times 10^{-5} \text{ m}^2/\text{s}$.

However, the elements constitute the HPBs should have also low hydrogen permeability, hydrogen solubility and high permeation reduction factor (PRF). Lakdher et al [11] have studied the effect of W concentration on the hydrogen permeability. The addition of W on Al-Ti coating deposited on 100C6 steel improved the hydrogen permeation resistance. Houben et al [18] have also deposited pure tungsten on Eurofer 97 steel by DC-magnetron sputtering and the permeability was reduced by 8 (PRF).

A comparative study have been done by Zhang et al [19] on AlCrTaTiZr, AlCrTaTiZrN and AlCrTaTiZrO coatings deposited on CLF steel. They concluded that AlCrTaTiZr coating had the higher hydrogen permeability.

- **Oxides and carbides**[20]

Oxides are the dominant hydrogen permeation barriers presented in the literature due to their ability to form over uneven geometrical forms simply by exposing the metal to air at elevated temperatures. Several oxides, such as aluminum oxide (Al_2O_3), zirconium oxide (ZrO_2), erbium oxide (Er_2O_3), chromium oxide, titanium oxide, and silicon oxide, have been reported as effective hydrogen permeation barriers. These coatings can significantly reduce hydrogen permeation, with some achieving permeation reduction factors up to 1000 when applied to steel substrates.

Carbides, including titanium carbide (TiC), silicon carbide (SiC), and vanadium carbide (VC), have been widely studied as hydrogen permeation barriers. TiC coatings on stainless steel have shown permeation reduction factors (PRFs) of around 10, while TiN-TiC bilayers on martensitic steels can achieve PRFs up to 100, which is ten times higher than TiC alone. Silicon carbide (SiC) coatings, known for their high melting point and excellent corrosion resistance, have also demonstrated PRFs of 10 at elevated temperatures when deposited on steel substrates.

- **Nitrides**

Nitrides are categorized as hard ceramic materials. They are primarily used as wear-resistant coatings and serve more often as hydrogen permeation barriers than carbides. The literature features numerous studies on this topic.

Metal nitride have been significantly used as barriers because of their high mechanical properties. WN, CrWN, CrN, Cr₂N, AlCrN and ZrN were used as hydrogen permeation barriers on Eurofer97 steel and they were investigated by Matějčíček et al [13] and the PRF were 38, 100, 117, 263, 300 and 4600 respectively. The deposition technique used was physical vapor deposition. All coatings showed a good property; they were crack free, dense and adherent. Based on the PRF value ZrN showed the best performance, and it was concluded that ZrN contained an amount of hydrogen that was outgassing during the permeation measurement. Titanium nitrides TiN is one of the most famous members of refractory group, its properties such as high thermal and chemical stability and corrosion resistance make it a good barrier. TiN deposited on steel and stainless steels show a good performance with PRF 100-1100 [21] [22].

However, a study by LuLu Hu et al [23] showed that nanonitride multilayer coatings have higher hydrogen permeation resistance than monolayer coatings for instance the permeability of CrN-AlTiN multilayer is 10 times lower than CrN and AlTiN monolayer coated on 304 stainless steel.

- **Polymers**

Recent research has increasingly focused on the development and application of polymeric coatings as effective hydrogen permeation barriers. Polymers such as polyvinyl alcohol (PVA), and polyethyleneimine (PEI), polyvinylidene fluoride (PVDF), polyester, polyamide (PA), and ethylene vinyl alcohol (EVOH) have garnered significant attention due to their inherently low hydrogen permeability. Due to the presence of hydroxyl groups, materials such as poly(vinyl alcohol) (PVA), which is abundant in hydroxyl groups, exhibit excellent resistance to hydrogen. This is because the hydrogen bonds formed between the polymer chains of poly(vinyl alcohol) create a highly compact structure with minimal channels for hydrogen passing. [24]. Simmons K.L et al. have studied the hydrogen compatibility of various elastomers commonly used in infrastructure including butyl rubber (IIR), silicone rubber and they found that most of the tested materials showed a good compatibility with hydrogen gas ambient [25].

2.2.2. Performance of HPB

The performance of HPBs is evaluated by comparing the permeation reduction factors for hydrogen diffusion through coated and uncoated materials. Over the years, a wide variety of materials such as metals, oxides, carbides, and nitrides, as discussed in the previous section, have been extensively studied. The data presented in Table 2.2 lists examples of hydrogen barriers, including metals, oxides, nitrides and carbides presents in the literature. The permeation reduction factor, permeabilities of both coating and substrate ($P_{\text{substrate}}$ and P_{film}), and test methods are reported. The thickness of the substrate used in these articles ranged between 0.5 mm and 2 mm.

Table 2.2. list of hydrogen permeation barriers (data points for [16], [21], [33], [40], [41] were extracted from [23])

Material	L (μm)	Substrate	Area (cm ²)	Gas P (Pa)	Gas T (°C)	Test method	PRF	P _s	P _f	Ref
Al ₂ O ₃	1	316L Stainless Steel	15.02	10 ⁻⁶	300	Gas phase technique	1000	1.3	25.9	[26]
Cr ₂ O ₃	10	Chromium containing alloys	6.9	>10 ⁵	950		1000	0.017	0.72	[27]
Cr ₂ O ₃ /Al ₂ O ₃	1	316L Stainless steel	3.8	10 ⁻⁶ -10 ⁻⁷		Membrane gas permeation	3500	1.3	7.41	[28]
Er ₂ O ₃	1	Eurofer 97	3.14	10 ⁻⁷ and 10 ⁻⁶		Membrane gas permeation	1000	1.3	25.9	[29]
Er ₂ O ₃	1.3	RAFM steel					1000	1.3	33.7	[30]
SiO ₂	0.2	Stainless steel	3.14	2x10 ⁵	212-382	Gas phase permeation	1	0.13	1711	[31]
BN	1.5	316L Stainless steel	5.5	10 ⁻⁶	500	differential pressure methods	100	0.13	193	[21]
TiN	1.5	316L Stainless steel	5.5	10 ⁻⁶	500	differential pressure methods	100	0.13	193	[21]
TiN	1.78	AISI 316l Stainless steel	5.65	2x10 ⁵	550		1100	0.13	5.7	[22]

TiN	1.7	AISI 316L Stainless steel	5.65	2×10^5			1000	0.13	21.8	[22]
SiN	0.5	Eurofer	6.28	1.2×10^5	>400		2000	1.3	6.5	[32]
WN	2.3	Eurofer 97	6.28	1.2×10^5	>400		38	1.3	1570	[13]
CrWN	4.4	Eurofer 97	6.28	1.2×10^5	>400		100	1.3	1140	[13]
CrN	2.6	Eurofer 97 steel	6.28	1.2×10^5	>400		117	1.3	576	[13]
Cr₂N	2.2	Eurofer 97 steel	6.28	1.2×10^5	>400		236	1.3	241	[13]
AlCrN	4.5	Eurofer 97 steel	6.28	1.2×10^5	>400		350	1.3	333	[13]
ZrN	1.4	Eurofer 97 steel	6.28	1.2×10^5	>400		4600	1.3	7.9	[13]
TiC	1	316L Stainless steel	15.07	5×10^2 5×10^4	500	Gas Phase technique	10	0.27	2750	[33]
TiN+TiC	1+0.25	Martensitic stainless steel	5.65	2×10^5	197 to 297	The membrane technique	100	1.3	234	[34]
Al₂O₃	0.2	316L Stainless Steel	7.85	10^3 - 5×10^4	242-469	Gas phase technique	42			[35]
Al₂O₃	0.8	316L Stainless steel	7.85	10^3 - 5×10^4	242-469	Gas phase technique	60			[35]

Al₂O₃	1.6	316L Stainless steel	7.85	10 ³ - 5x10 ⁴	242- 469	Gas phase technique	80			[35]
Al-Ti-W	4	100C6 steel	31.4			Electrochemical permeation test				[11]
AlCrTaTiZr	4	CLF-1 Steel	4.55			Electrochemical hydrogen permeation test				[19]
AlCrTaTiZr(N)	4	CLF-1 Steel	4.55			electrochemical hydrogen permeation test				[19]
AlCrTaTiZr(O)	4	CLF-1 Steel	4.55			electrochemical hydrogen permeation test				[19]
AlCrTaTiZr	4	CLF-1 Steel	1.88	7x10 ⁴	550 to 700	gas-driven deuterium permeation tests				[19]
AlCrTaTiZr(N)	4	CLF-1 Steel	1.88	7x10 ⁴	550 to 700	gas-driven deuterium permeation test				[19]
AlCrTaTiZr(O)	4	CLF-1 Steel	1.88	7x10 ⁴	550 to 770	gas-driven deuterium permeation test				[19]
CrN/AlTiN multilayer	7x10 ⁻³	Stainless steel	3.14	4x10 ⁴	673	gas-deuterium permeation test	5000	0.1	3x10 ²	[23]
CrN/AlTiN multilayer	18x10 ⁻³	304 Stainless Steel	3.14	4x10 ⁴	673	Gas-deuterium permeation test	1300	0.1	8 x10 ²	[23]

CrN/AlTiN multilayer	32x10 ⁻³	304 Stainless steel	3.14	4x10 ⁴	673	Gas-deuterium permeation test	1300	0.1	8 x10 ²	[23]
CrN/AlTiN multi layer	70x10 ⁻³	304 Stainless steel	3.14	4x10 ⁴	673	gas-deuterium permeation test	1000	0.1	3x10 ³	[23]
CrN/AlTiN multilayer	110x10 ⁻³	304 Stainless steel	3.14	4x10 ⁴	673	gas-deuterium permeation test	500	0.1	9x10 ³	[23]
Al₂O₃		Ferritic steel Fe-Cr-Al-Air	3.14	High vacuum	400	gas deuterium permeation test		1.64x10 ⁻⁴	0.2	[36]
Al₂ O₃		Ferritic steel Fe-Cr-Al- Ar 7700 ppm O ₂	3.14	High vacuum	400	gas deuterium permeation test		1.64x10 ⁻⁴	0.2	[36]
Al₂ O₃		Ferritic steel Fe-Cr-Al- -Ar 1700 ppm O ₂	3.14	High vacuum	400	gas-deuterium permeation test		1.64x10 ⁻⁴	0.003	[36]
W	2	Eurofer97 steel	4.9	25x10 ² 8x10 ⁴	300- 550	deuterium-gas-driven permeation	8			[18]
WN	2	Eurofer97 steel	4.9	25x10 ² 8x10 ⁴	300- 550	deuterium gas-driven permeation	31			[18]
WN+W	2	Eurofer97 steel	4.9	25x10 ² 8x10 ⁴	300- 550	deuterium gas-driven permeation	1000			[18]
Ti₂AlN	2.7	430 ferritic stainless-steel		UHV	30–400	deuterium gas permeation test	45			[37]
TiAlN	1.7	316L Stainless steel	10.97	2x10 ⁵	550		6800	0.13	0.92	[22]

TiAlN	5	316L Stainless steel	10.17	2×10^5	550		20000	0.13	6.5	[22]
ZrO₂	0.18	Ferritic steel	12.56	10^5	300-550	electrochemical permeation test	1000			[38]
ZrO₂	0.1	Ferritic steel	3.14	10^5	400	electrochemical permeation test	100			[39]
SiC		martensitic steel JLF-1	3.14	3×10^4	500	deuterium permeation test	160			[40]
SiC		martensitic steel JLF-1	3.14	9×10^4	500	deuterium permeation test	35			[40]
SiC	1.5	austenitic SS316	6.25	8×10^4	500			0.1	4.1×10^4	[41]
SiC	1.5	ferritic/martensitic (RAFM) steel F82H	6.25	8×10^4	500			1	9.2×10^4	[41]
Ti-Al-Ni	5	Eurofer97	12.56	10^{-7} - 10^{-6}	400		20.000			[42]
AlN	0.4	316l Stainless steel	4.9		600	Gas permeation test	36			[43]
AlN	0.4	316l stainless steel	4.9		400	Gas permeation test	53			[43]
AlN	0.4	316l Stainless steel	4.9		250	Gas permeation test	144			[43]
FeAl/Al₂O₃	4	316l stainless steel	3.14			Electrochemical permeation test				[44]
Er₂O₃	0.2	316l stainless steel	4.9	12×10^4		Deutrium permeation test				[45]

Ni	23	QP980 steel				Electrochemical permeation test				[46]
Ni-Graphene	20	QP980 steel				Electrochemical permeation test				[46]
Graphene multilayer		X70 pipe steel	15	-	-	Electrochemical hydrogen permeation test	48			[47]
MXene-4mg/ml		X70 pipe steel	15	-	-	Electrochemical hydrogen permeation test		9.43×10^{12}	2.85×10^{13}	[48]
Mxene-2mg/ml		X70 pipe steel		-	-	Electrochemical permeation test		1.36×10^{13}	2.85×10^{13}	[48]
Mxene-1mg/ml		X70 pipe steel		-	-	Electrochemical permeation test		1.34×10^{13}	2.85×10^{13}	[48]
Mxene-0.5mg/ml		X 70 pipe steel		-	-	Electrochemical permeation test		2.38×10^{13}	2.85×10^{13}	[48]
GO-Al₂O₃	0.8	RAFM steel	4.52.	10^5	500	Gas Deuterium permeation test	178		4.49×10^5	[49]
GO-AlPO₄ /Cr₂O₃		AISI 316 L stainless steel	4.55	10^5	550	Gas Deuterium Permeation test	100	0.02	2×10^7	[50]

2.2.3 Technologies to produce HPB coatings

The advancement of effective hydrogen permeation barriers is fundamentally reliant on the selection of appropriate coating technologies. Hydrogen barrier coatings must exhibit low hydrogen permeability, high permeation reduction factor, and high adhesion. Over recent decades, an extensive study of coating technologies has been investigated to mitigate hydrogen ingress in metals employed in pipelines, pressure vessels, nuclear reactors, fuel cells, and hydrogen separation membranes [51],[24].

The literature consistently demonstrates that the choice of coating techniques influences the resultant coating performance, which directly impacts hydrogen transport behavior [14].

This section provides a comprehensive review of the principal coating technologies utilized for hydrogen permeation barriers such as metallic coating technologies, ceramic and oxides coating technologies and polymers coating technologies.

- **Metallic coating technologies**

The following subsection will discuss the Physical vapor deposition (PVD) and electroplating and electroless deposition techniques for metallic deposition:

Physical vapor deposition(PVD) methods, including magnetron sputtering and electron-beam evaporation, are widely used for the fabrication of thin metallic. PVD enables precise control over coating composition, thickness, and microstructure. Commonly used PVD barrier materials include palladium, nickel, chromium, titanium, aluminum, and multilayer metallic stacks. Extensive research demonstrates that PVD coatings deposited under optimized conditions can achieve low hydrogen permeability[52]. The primary limitations of PVD deposition is it is high costs, which currently restrict large-scale industrial deployment.

Electroplating and electroless deposition represent some of the earliest methods implemented for the fabrication of metallic hydrogen permeation barriers. Metals such as nickel, copper, chromium, and their alloys have been extensively studied due to their lower hydrogen diffusivity relative to steels. In particular, electroless nickel–phosphorus (Ni–P) coatings have garnered considerable attention [53]. Studies have reported that dense electroplated coatings are capable of reducing hydrogen permeation [54]; however, the major issue related the introduction of hydrogen into the substrate during electroplating process that might prone to hydrogen embrittlement [55].

- **Ceramic and oxide-based coating technologies**

Thermal oxidation and chemical conversion processes form oxide layers directly on metallic substrates. Oxides such as α -Al₂O₃/Cr₂O₃ oxide layers [56] has demonstrated efficacy as hydrogen barriers due to their inherently low hydrogen solubility and diffusivity. In addition

other studies have studied the oxide films grown on iron nickel base stainless steel by thermal oxidation at high temperatures which showed a good barrier properties that exhibit different composition such as chromia or spinel oxides, FeCr_2O_2 [57].

These studies indicate that naturally grown or thermally formed oxides can significantly reduce hydrogen permeation; however, their effectiveness is highly dependent on factors such as oxide thickness, and adhesion.

Chemical vapor deposition (CVD) facilitates the formation of dense, conformal ceramic coatings, including alumina coatings [58]. Multiple studies have demonstrated that CVD-grown ceramic layers can substantially reduce hydrogen permeation, especially when coating thickness exceeds the critical defect-percolation threshold.[59],[60] However, Researcher on modeling CVD processes demonstrate that conventional CVD typically requires requires temperatures between 600-1000°C, which are high enough to cause significant and often change in microstructure and mechanical properties of steel substrates [61].

- **Polymer coatings technologies**

Polymer-based coatings, are widely used on steel substrate to reduce the hydrogen permeation , particularly in low temperature applications, several deposition techniques such as Dip coating and spray coating were applied by several literature in the field, offering compatibility to complex geometries, however limitation can be attributed to the non-uniform thickness or solvent evaporation issues geometries [62]-

- **Comparison of Deposition Techniques for Hydrogen Barrier Coatings: Advantages and disadvantages**

As discussed in the previous section, deposition techniques such as PVD, CVD, electroplating, electroless and dip/spin coating were used in the literature to produce the coating that act as a barriers again hydrogen uptake , which offers distinct advantages and disadvantages. Table 2.3 provides a comparatives overview of these deposition techniques. These comparative studies highlight how the coating method choice must balance factors such as coating uniformity and adhesion.

Table 2.3. Coating techniques; advantages and disadvantages.

Coating technology	Advantages	Disadvantages
Physical vapor deposition (PVD)	Corrosion, resistance Durability and Microstructure control	Expensive
Chemical vapor deposition (CVD)	Dense and uniform coating	Require high temperature
Electroless deposition	No need for external power supply	Slower deposition rate and high cost of chemicals
Electroplating	Strong adhesion on substrate	Environmental and chemical safety and possible residual stress

Thermal oxidation	Simple and high temperature resistance	Limited control over coating (composition and thickness)
Dip and spin coating	Simple and compatible with simple geometries	Non uniform coating thickness and solvent evaporation issues

2.3 Tungsten as hydrogen permeation barrier

The body of literature on tungsten-based coatings as hydrogen permeation barriers for structural steels is still relatively limited. Most existing studies focus on bulk tungsten or tungsten alloys under conditions relevant to fusion reactors, while experimental investigations of thin tungsten coatings deposited on steel substrates are comparatively scarce. In particular, there is a notable lack of systematic research addressing the hydrogen permeation characteristics, trapping mechanisms, and long-term stability of tungsten coatings applied to carbon or low-alloy steels. This gap is especially significant for pipeline and energy infrastructure materials, where exposure to hydrogen is expected to increase with the growing adoption of hydrogen-based energy systems. In this section, the properties of tungsten, hydrogen permeability and diffusion in bulk tungsten, as well as a few example of studies on tungsten as HPB, together with the critical factors influencing barrier performance, will be reviewed.

2.3.1. Properties of tungsten

Tungsten is a refractory metal characterized by one of the highest melting points (3410 °C) and excellent mechanical stability. Thermodynamically, tungsten exhibits a strong affinity for oxygen, and the formation of tungsten oxides (notably WO_3) is highly favorable, as reflected by the substantial negative Gibbs free energy of oxide formation. Kinetically, however, oxidation proceeds slowly at room temperature, resulting in the development of a thin native oxide layer. Although a comprehensive thermodynamic and kinetic analysis of tungsten oxidation is beyond the scope of this thesis, a thorough investigation of its exceptional oxidation properties is essential for understanding the subsequent analysis of barrier performance.

- **Thermodynamic affinity of tungsten with oxygen**

The thermodynamic affinity of tungsten for oxygen is a factor that affects the oxidation behavior. Tungsten exhibits a particularly strong tendency to oxidize, as evidenced by the highly negative standard Gibbs free energy of formation ($\Delta_f G^\circ$) for its oxides, such as WO_3 and WO_2 . [38]. tungsten trioxide (WO_3), reported as -764.056 kJ/mol at 298 K, while tungsten dioxide (WO_2) also possess a high negative $\Delta_f G^\circ$ at 298 K according to the NIST Standard Reference Database 13 [63].

The Ellingham diagram [64], which consists of the Gibbs free energy of oxide formation as a function of temperature for various metals, gives a good comparison of the oxidation behavior.

The Ellingham diagram (Figure 2.2) further illustrates the high affinity of tungsten for oxygen, as the formation line for WO_3 lies significantly below those of many other metals. An example

of an Ellingham diagram constructed using data from the NIST database is presented in Figure 2.2.

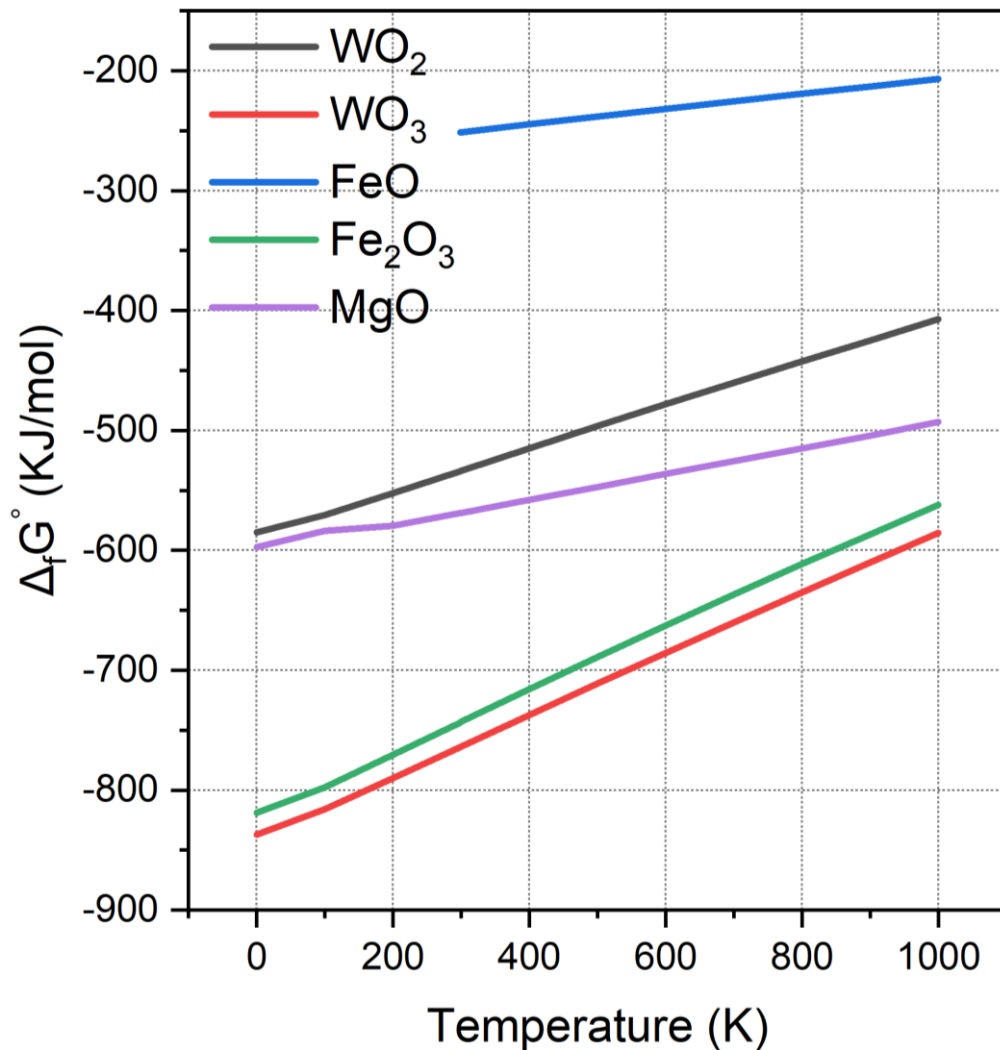


Figure 2.2. Ellingham diagram constructed using the data reported in [63]

- **Phase stability and the W-O phase Diagram**

While tungsten trioxide (WO₃) is thermodynamically the most stable oxide of tungsten, its stability is highly dependent on both temperature and the chemical potential of oxygen. Consequently, the phase behavior of the tungsten–oxygen system is most effectively described using the W–O phase diagram (Figure 3 from [65]), which delineates the stability regions of metallic tungsten, its various oxides, and the transitions between them under varying conditions.

Phase stability in the tungsten-oxygen (W-O) system is dependent by both temperature and oxygen content (see phase diagram in Figure 2.3) at low oxygen concentrations, tungsten remains in its metallic α -W phase. When oxygen content increases, oxidation initially forms tungsten dioxide (WO₂), further increase in oxygen leads to the formation and stabilization tungsten trioxide (WO₃), The diagram presents indeed, a series of intermediate oxides phase

such as $W_{18}O_{49}$, $W_{24}O_{68}$ and members of the W_nO_{3n-2} series. In addition, WO_3 exhibits structural polymorphism and phase transitions occur at different temperature during heating or cooling (γ , δ , β , and α) and The most commonly found room temperature stable phase is the monoclinic I (γ - WO_3) from 17 to 330°C. When heated above 330°C (γ - WO_3) is converted to orthorhombic (β - WO_3) and is stable up to 740°C, for $T > 740^\circ\text{C}$, tetragonal α - WO_3 is found. However, these two phases are only stable at high temperatures and upon cooling, they are converted back to γ - WO_3 .

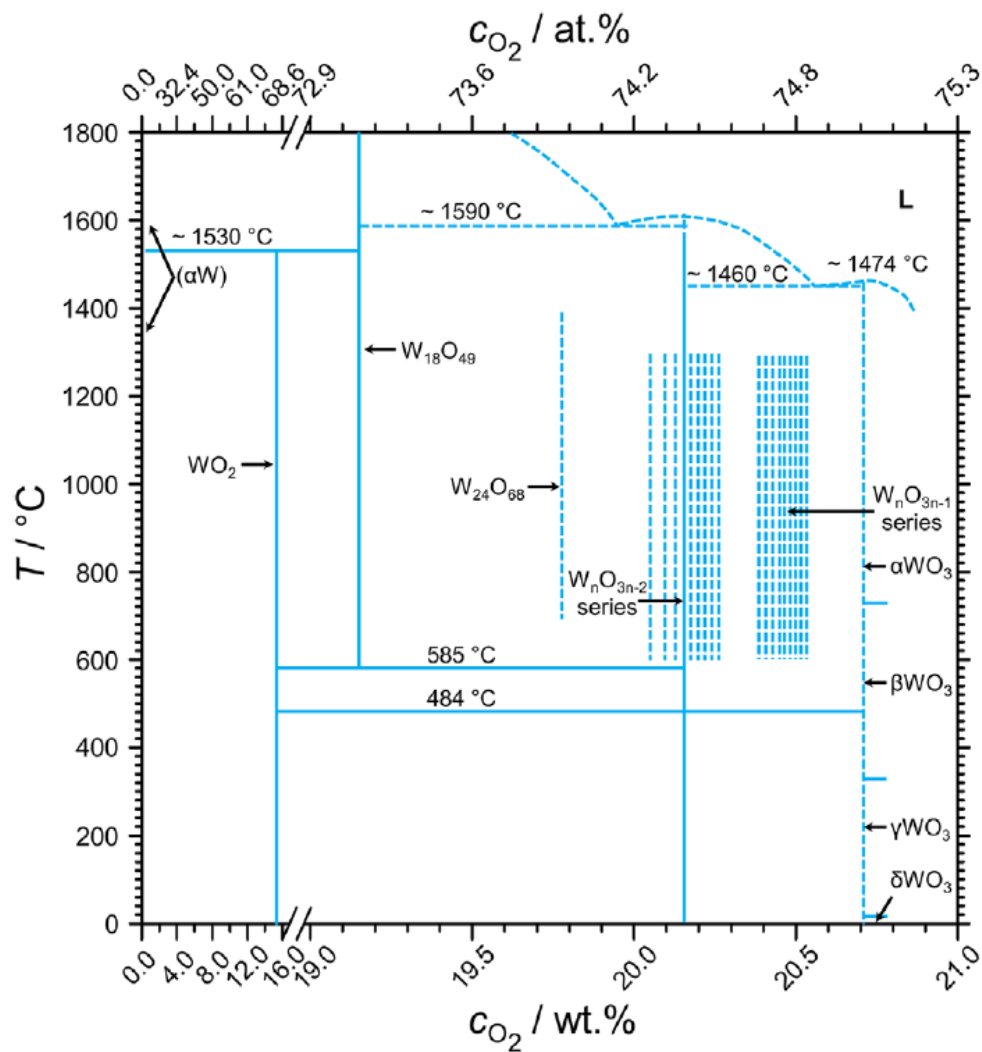


Figure 2.3. Phase diagram of the tungsten oxygen system (W-O) [66]

- Oxidation mechanisms and kinetic behavior of tungsten [66]

Adsorption of oxygen on tungsten surfaces

Upon exposure to oxygen, clean tungsten surfaces adsorb oxygen in a variety of atomic and molecular states. At low temperatures (below 0 °C), oxygen adsorption is primarily molecular, while at room temperature, molecular adsorption acts as a precursor to atomic adsorption. This process leads to the formation of ordered oxygen superstructures on the tungsten surface and, as temperature increases, more extensive coverage and the formation of oxide-like surface layers, often described as adsorbed oxide, are observed. These surface phenomena have been investigated extensively, revealing that the initial stages of oxidation are dominated by surface adsorption processes.

Diffusion and permeation of Oxygen

Following adsorption, oxygen can diffuse into the tungsten crystal lattice structure, the diffusion coefficients for oxygen in polycrystalline tungsten at 1700°C are reported as $D = 1 \times 10^{-7}$ to 5×10^{-8} cm²/s . t

Oxidation Kinetics and oxide layer growth

The oxidation of tungsten depends on the temperature and oxygen partial pressure. Even at room temperature a thin native oxide layer, typically WO₃ can form, the thickness increases slowly with temperature up to around 200°C, but beyond this the growth rate accelerates. Humidity further increases the oxidation rate. Between 327–400 °C, a thin oxide film primarily forms and acts as a protective layer and growing according to a parabolic rate law due to diffusion-limited processes. At higher temperatures (above 500 °C), the oxide layer cracks, and above 600 °C, WO₃ forms on the top of the first thin layer. WO₃ is permeable to oxygen, and its growth is initially mixed parabolic and linear but becomes strictly linear once the inner layer reaches maximum thickness. Sublimation of WO₃ becomes significant above 750 °C and matches the oxidation rate above 1300 °C, leaving the surface free of oxide at even higher temperatures.

At very high temperatures (> 2100 K) and low oxygen partial pressures, volatile WO₂ forms more rapidly than WO₃, and above 2500 K, metal volatilization becomes significant.

- **Permeability and diffusion of pure tungsten**

Tungsten exhibits exceptionally low intrinsic hydrogen permeability relative to other metals and alloys, primarily due to its low hydrogen solubility and moderate diffusion rates. In pure tungsten, hydrogen atoms preferentially occupy interstitial sites, particularly tetrahedral positions, migrating between them via thermally activated jumps with activation energies ranging from 0.20 to 0.38 eV, depending on the migration pathway and computational model employed. Density functional theory (DFT) studies corroborate that tetrahedral interstitial sites are the most energetically favorable for hydrogen, and that the migration energy barriers between these sites govern the overall diffusion behavior. Diffusion coefficients and permeability values derived from first-principles calculations are in good agreement with experimental observations. Notably, hydrogen diffuses more rapidly than its heavier isotopes,

such as deuterium and tritium, owing to its lower atomic mass and reduced migration energy barriers.[67]

Hydrogen permeability in thin tungsten films and bulk specimens has been experimentally determined through extended permeation tests. For instance, studies on magnetron-deposited tungsten films at 400 °C under constant hydrogen pressure have reported permeation coefficients ranging from approximately 3.2×10^{-14} to 1.1×10^{-15} mol m⁻¹ s⁻¹ Pa^{-0.5}. These results further demonstrate the inherently low hydrogen permeation characteristics of tungsten when compared to more permeable metals.[15] These values align with previous experimental diffusion studies, which demonstrate that hydrogen within the bulk tungsten lattice at elevated temperatures exhibits Arrhenius-type behavior, with diffusivity and solubility parameters indicative of an interstitial diffusion mechanism.[68] Thermodynamic models that account for grain boundary effects in polycrystalline tungsten indicate that grain size significantly impacts effective hydrogen solubility, diffusivity, and thus permeability, up to temperatures of at least 1000 K. By incorporating hydrogen binding energies at grain boundaries and adjusted diffusion barriers, these models can accurately predict macroscopic hydrogen transport, showing good agreement with experimental observations in polycrystalline tungsten.[69] Experiments with hydrogen isotopes have further clarified the isotope dependence of diffusion and permeability in tungsten. Tritium permeation studies conducted on polycrystalline tungsten over temperatures from approximately 573 to 873 K demonstrated Arrhenius-type behavior, characterized by a specific pre-exponential factor and a temperature-dependent activation energy. These findings are particularly valuable for fusion safety analyses, highlighting the practical importance of accurate hydrogen transport data in the design of reactor systems.[70]

2.3.2. Tungsten coatings as hydrogen permeation barrier

Although bulk tungsten exhibits intrinsically low hydrogen permeability, its practical use as a hydrogen permeation barrier (HPB) in engineering applications typically involves its deposition as a thin coating on structural substrates. Magnetron-sputtered tungsten coatings applied to reduced-activation ferritic–martensitic (RAFM) steels, such as F82H, have been extensively investigated as model hydrogen permeation barriers (HPBs). Systematic permeation experiments conducted at low temperatures (30 °C–70 °C) revealed that high-purity tungsten films with nominal thicknesses of 100 nm and 300 nm significantly reduced hydrogen permeability compared to uncoated steel, with permeation reduction factors (PRFs) ranging from approximately 3 up to 4000. Thicker coatings generally achieved greater reductions in hydrogen flux. The wide variation in PRF values was largely attributed to differences in coating quality, particularly the occurrence of microcracks, pinholes, and other imperfections that serve as preferential pathways for hydrogen penetration. Among the factors studied, coating thickness had a more substantial effect on PRF than the substrate’s surface preparation before deposition. [71]

One limitation of using tungsten coatings as hydrogen permeation barriers is the mismatch in thermal expansion coefficients between the tungsten coating and common structural substrates. For example, substrates like Eurofer97 or F82H experience changes in microstructure when exposed to high temperatures during thermal annealing or repeated thermal cycling in service. This mismatch generates internal stress that often cause cracks to

form in the pure tungsten coating. Such cracks can act as pathways for hydrogen diffusion, reducing the effectiveness of the barrier.[72]

SEM cross-sectional microscopy studies have shown that pure tungsten coatings frequently develop these defects after annealing, resulting in actual barrier performance that is significantly lower than predicted by the intrinsic diffusivity of bulk tungsten. [72]

2.3.3. Critical influencing factors on hydrogen permeation barrier efficiency

Although hydrogen permeation barriers can provide an effective solution for preventing hydrogen ingress, several factors may compromise their performance and should be carefully considered. Further literature research is needed to fully understand these influences. Key factors include microstructural defects, coating thickness, operational temperature and thermal cycling, interface adhesion, substrate compatibility, deposition technique, microstructural control, and coating composition.

- **Defects and microstructure**

Defects and the microstructure of HPB coatings can strongly affect their performance. These defects, such as microcracks, columnar grains, and voids, may act as pathways for hydrogen transport and diffusion, reducing the effectiveness of the barrier. [71]

- **Coating thickness**

Increasing the thickness of a coating can improve its effectiveness as a hydrogen permeation barrier; however, this improvement depends on the presence of microstructural defects. For example, under identical deposition conditions, 300 nm tungsten coatings have demonstrated higher permeation reduction factors (PRFs) compared to 100 nm films. [71]

- **Temperature and Thermal Cycling**

Temperature has a big impact on how well hydrogen permeation barriers work. When the temperature goes up, hydrogen moves and diffuses more easily in materials [73] Although tungsten and tungsten-based coatings are good barriers, they can develop problems when heated and cooled repeatedly. This is because tungsten and steel expand at different rates, causing stress that leads to cracks in the coating, especially in pure tungsten. These cracks make the barrier less effective. However, experiments show that tungsten nitride (WN) coatings without cracks can still block hydrogen well, even at high temperatures like 400 °C, while pure tungsten coatings are more likely to crack and lose their protective ability [72].

- **Substrate coating adhesions**

The adhesion between the coating barrier and the substrate is another critical factor that can limit the effectiveness of hydrogen permeation barriers (HPBs). Weak adhesion can affect the hydrogen permeation barrier performance [24] ; low adhesion is due to the presence of voids, which can form as a result of substrate roughness[74] negatively impacting the bond between the coating and the substrate. Additionally, the development of interdiffusion zones at the interface can create weak spots or localized pathways that facilitate easier hydrogen penetration.[75] Ensuring strong and uniform adhesion is therefore essential for optimal HPB performance

References

- [1] J. Hoschke, M. F. W. Chowdhury, J. Venezuela, and A. Atrens, "A review of hydrogen embrittlement in gas transmission pipeline steels," *Corrosion Reviews*, vol. 41, no. 3, pp. 277–317, 2023.
- [2] S. Lynch, "Hydrogen embrittlement phenomena and mechanisms," *Corrosion reviews*, vol. 30, no. 3–4, pp. 105–123, 2012.
- [3] Y. Sun and Y. F. Cheng, Thermodynamics of spontaneous dissociation and dissociative adsorption of hydrogen molecules and hydrogen atom adsorption and absorption on steel under pipelining conditions," *International Journal of Hydrogen Energy*, vol. 46, no. 69, pp. 34469–34486, 2021.
- [4] R. A. Oriani, The diffusion and trapping of hydrogen in steel," *Acta Metallurgica*, vol. 18, no. 1, pp. 147–157, Jan. 1970, doi: 10.1016/0001-6160(70)90078-7.
- [5] Lynch, Stan P. "Hydrogen embrittlement (HE) phenomena and mechanisms." *Stress corrosion cracking*. Woodhead Publishing, 2011. 90-130..
- [6] Rudomilova, D., Prošek, T., Salvetr, P., Knaislová, A., Novák, P., Kodým, R., ... & Luckeneder, G. (2020). The effect of microstructure on hydrogen permeability of high strength steels. *Materials and corrosion*, 71(6), 909-917.
- [7] M. Nagumo, Hydrogen related failure of steels – a new aspect," *Materials Science and Technology*, vol. 20, no. 8, pp. 940–950, Aug. 2004, doi: 10.1179/026708304225019687.
- [8] M. Smialowski, *Hydrogen in Steel: Effect of Hydrogen on Iron and Steel During Production, Fabrication, and Use*. Elsevier, 2014.
- [9] J. Toribio and V. Kharin, "Effect of residual stress-strain profiles on hydrogen-induced fracture of prestressing steel wires," *Mater Sci*, vol. 42, no. 2, pp. 263–271, Mar. 2006, doi: 10.1007/s11003-006-0079-4.
- [10] H. Yang, Z. Shao, W. Wang, X. Ji, and C. Li, "A composite coating of GO-Al₂O₃ for tritium permeation barrier," *Fusion Engineering and Design*, vol. 156, p. 111689, Jul. 2020, doi: 10.1016/j.fusengdes.2020.111689.
- [11] I. Lakdhar, A. Alhussein, J. Capelle, and J. Creus, "Al-Ti-W alloys deposited by magnetron sputtering: Effective barrier to prevent steel hydrogen embrittlement," *Applied Surface Science*, vol. 567, p. 150786, Nov. 2021, doi: 10.1016/j.apsusc.2021.150786.
- [12] D. Levchuk, S. Levchuk, H. Maier, H. Bolt, and A. Suzuki, "Erbium oxide as a new promising tritium permeation barrier," *Journal of Nuclear Materials*, vol. 367, pp. 1033–1037, 2007.
- [13] Matějčíček, J., Veverka, J., Nemanič, V., Cvrček, L., Lukáč, F., Havránek, V., & Illková, K. (2019). Characterization of less common nitrides as potential permeation barriers. *Fusion Engineering and Design*, 139, 74-80..

- [14] Xiao, S., Meng, X., Shi, K., Liu, L., Wu, H., Lian, W., ... & Chu, P. K. (2022). Hydrogen permeation barriers and preparation techniques: A review. *Journal of Vacuum Science & Technology A*, 40(6)..
- [15] V. Nemanič, J. Kovač, C. Lungu, C. Porosnicu, and B. Zajec, "Characterization of tungsten films and their hydrogen permeability," *Journal of Vacuum Science & Technology A: Vacuum, Surfaces, and Films*, vol. 32, no. 6, p. 061511, 2014, doi: 10.1116/1.4898061.
- [16] S. C. Marques, A. V. Castilho, and D. S. dos Santos, "Effect of alloying elements on the hydrogen diffusion and trapping in high entropy alloys," *Scripta Materialia*, vol. 201, p. 113957, Aug. 2021, doi: 10.1016/j.scriptamat.2021.113957.
- [17] V. Nemanič, J. Kovač, M. Žumer, and J. Zavašnik, "Impact of surface oxide on hydrogen permeability of chromium membranes," *International Journal of Hydrogen Energy*, vol. 48, no. 26, pp. 9723–9733, Mar. 2023, doi: 10.1016/j.ijhydene.2022.11.267.
- [18] A. Houben, M. Rasiński, L. Gao, and Ch. Linsmeier, "Tungsten nitride as tritium permeation barrier," *Nuclear Materials and Energy*, vol. 24, p. 100752, Aug. 2020, doi: 10.1016/j.nme.2020.100752.
- [19] Zhang, W., Wang, L., Luo, X., Gong, B., Wang, X., Yang, J., & Feng, Y. (2021). Deuterium permeability of a novel AlCrTaTiZr high entropy alloy coating. *Materials Research Express*, 8(5), 056401.
- [20] V. Nemanič, "Hydrogen permeation barriers: Basic requirements, materials selection, deposition methods, and quality evaluation," *Nuclear Materials and Energy*, vol. 19, pp. 451–457, 2019.
- [21] M. Tamura, M. Noma, and M. Yamashita, "Characteristic change of hydrogen permeation in stainless steel plate by BN coating," *Surface and Coatings Technology*, vol. 260, pp. 148–154, Dec. 2014, doi: 10.1016/j.surfcoat.2014.09.041.
- [22] B. Y. Man, L. Guzman, A. Miotello, and M. Adami, "Microstructure, oxidation and H₂-permeation resistance of TiAlN films deposited by DC magnetron sputtering technique," *Surface and Coatings Technology*, vol. 180–181, pp. 9–14, Mar. 2004, doi: 10.1016/j.surfcoat.2003.10.021.
- [23] Hu, L., Wei, G., Yin, R., Hong, M., Cheng, T., Zhang, D., ... & Ren, F. (2020). Significant hydrogen isotopes permeation resistance via nitride nano-multilayer coating. *International Journal of Hydrogen Energy*, 45(38), 19583-19589.
- [24] Li, Y., Barzagli, F., Liu, P., Zhang, X., Yang, Z., Xiao, M., ... & Zhang, R. (2023). Mechanism and evaluation of hydrogen permeation barriers: a critical review. *Industrial & Engineering Chemistry Research*, 62(39), 15752-15773.
- [25] Simmons, K. L., Kuang, W., Burton, S. D., Arey, B. W., Shin, Y., Menon, N. C., & Smith, D. B. (2021). H-Mat hydrogen compatibility of polymers and elastomers. *International Journal of Hydrogen Energy*, 46(23), 12300-12310.

- [26] E. Serra, A. Calza Bini, G. Cosoli, and L. Pilloni, "Hydrogen Permeation Measurements on Alumina," *Journal of the American Ceramic Society*, vol. 88, no. 1, pp. 15–18, 2005, doi: 10.1111/j.1551-2916.2004.00003.x.
- [27] D. Stöver, H. P. Buchkremer, and R. Hecker, "Hydrogen and deuterium permeation through metallic and surface-oxidized chromium," *Surface and Coatings Technology*, vol. 28, no. 3, pp. 281–290, Jul. 1986, doi: 10.1016/0257-8972(86)90085-X.
- [28] Oya, Y., Kobayashi, M., Osuo, J., Suzuki, M., Hamada, A., Matsuoka, K., ... & Okuno, K. (2012). Effect of surface oxide layer on deuterium permeation behaviors through a type 316 stainless steel. *Fusion Engineering and Design*, 87(5-6), 580-583.
- [29] D. Levchuk, S. Levchuk, H. Maier, H. Bolt, and A. Suzuki, "Erbium oxide as a new promising tritium permeation barrier," *Journal of Nuclear Materials*, vol. 367–370, pp. 1033–1037, Aug. 2007, doi: 10.1016/j.jnucmat.2007.03.183.
- [30] T. Chikada, A. Suzuki, F. Koch, H. Maier, T. Terai, and T. Muroga, "Fabrication and deuterium permeation properties of erbia-metal multilayer coatings," *Journal of Nuclear Materials*, vol. 442, no. 1, Supplement 1, pp. S592–S596, Nov. 2013, doi: 10.1016/j.jnucmat.2013.03.084.
- [31] R. Checchetto, L. M. Gratton, A. Miotello, and C. Tosello, "Deuterium permeation through SiO₂ thin film deposited on stainless steel substrate," *Journal of Non-Crystalline Solids*, vol. 216, pp. 65–70, Aug. 1997, doi: 10.1016/S0022-3093(97)00173-7.
- [32] V. Nemanič, P. J. McGuinness, N. Daneu, B. Zajec, Z. Siketić, and W. Waldhauser, "Hydrogen permeation through silicon nitride films," *Journal of Alloys and Compounds*, vol. 539, pp. 184–189, Oct. 2012, doi: 10.1016/j.jallcom.2012.05.110.
- [33] K. S. Forcey, A. Perujo, F. Reiter, and P. L. Lolli-Ceroni, "The formation of tritium permeation barriers by CVD," *Journal of Nuclear Materials*, vol. 200, no. 3, pp. 417–420, May 1993, doi: 10.1016/0022-3115(93)90319-T.
- [34] Checchetto, R., Bonelli, M., Gratton, L. M., Miotello, A., Sabbioni, A., Guzman, L., ... & Benamati, G. (1996). Analysis of the hydrogen permeation properties of TiN-TiC bilayers deposited on martensitic stainless steel. *Surface and Coatings Technology*, 83(1-3), 40-44.
- [35] Q. Li, J. Wang, Q.-Y. Xiang, K. Yan, W.-Q. Yao, and J.-L. Cao, "Study on influence factors of permeation reduction factor of Al₂O₃-hydrogen isotopes permeation barriers," *International Journal of Hydrogen Energy*, vol. 41, no. 7, pp. 4326–4331, Feb. 2016, doi: 10.1016/j.ijhydene.2016.01.018.
- [36] Lyu, Y. M., Xu, Y. P., Pan, X. D., Liu, H. D., Li, X. C., Zhou, H. S., ... & Luo, G. N. (2020). Efficient deuterium permeation reduction coating formed by oxidizing the Fe–Cr–Al ferritic steel in reduced oxygen atmosphere at 973 K. *Journal of Nuclear Materials*, 530, 151962.

- [37] Gröner, L., Mengis, L., Galetz, M., Kirste, L., Daum, P., Wirth, M., ... & Burmeister, F. (2020). Investigations of the deuterium permeability of as-deposited and oxidized Ti₂AlN coatings. *Materials*, 13(9), 2085.
- [38] Y. Hatano, K. Zhang, and K. Hashizume, "Fabrication of ZrO₂ coatings on ferritic steel by wet-chemical methods as a tritium permeation barrier," *Phys. Scr.*, vol. 2011, no. T145, p. 014044, Dec. 2011, doi: 10.1088/0031-8949/2011/T145/014044.
- [39] K. Zhang and Y. Hatano, "Sealing of pores in sol-gel-derived tritium permeation barrier coating by electrochemical technique," *Journal of Nuclear Materials*, vol. 417, no. 1, pp. 1229–1232, Oct. 2011, doi: 10.1016/j.jnucmat.2010.12.276.
- [40] Z. Yao, A. Suzuki, D. Levchuk, and T. Terai, "SiC Coating by RF Sputtering as Tritium Permeation Barrier for Fusion Blanket," *Fusion Science and Technology*, vol. 52, no. 4, pp. 865–869, Nov. 2007, doi: 10.13182/FST07-A1601.
- [41] T. Chikada, A. Suzuki, and T. Terai, "Deuterium permeation and thermal behaviors of amorphous silicon carbide coatings on steels," *Fusion Engineering and Design*, vol. 86, no. 9, pp. 2192–2195, Oct. 2011, doi: 10.1016/j.fusengdes.2011.01.036.
- [42] P. J. McGuinness, M. Čekada, V. Nemanič, B. Zajec, and A. Rečnik, "Hydrogen permeation through TiAlN-coated Eurofer '97 steel," *Surface and Coatings Technology*, vol. 205, no. 8, pp. 2709–2713, Jan. 2011, doi: 10.1016/j.surfcoat.2010.08.133.
- [43] J. Wang, Q. Li, Q.-Y. Xiang, and J.-L. Cao, "Performances of AlN coatings as hydrogen isotopes permeation barriers," *Fusion Engineering and Design*, vol. 102, pp. 94–98, Jan. 2016, doi: 10.1016/j.fusengdes.2015.11.043.
- [44] J. Huang, H. Xie, L. Luo, X. Zan, D. Liu, and Y. Wu, "Preparation and properties of FeAl/Al₂O₃ composite tritium permeation barrier coating on surface of 316L stainless steel," *Surface and Coatings Technology*, vol. 383, p. 125282, Feb. 2020, doi: 10.1016/j.surfcoat.2019.125282.
- [45] Q. Li, J. Wang, Q.-Y. Xiang, T. Tang, Y.-C. Rao, and J.-L. Cao, "Thickness impacts on permeation reduction factor of Er₂O₃ hydrogen isotopes permeation barriers prepared by magnetron sputtering," *International Journal of Hydrogen Energy*, vol. 41, no. 4, pp. 3299–3306, Jan. 2016, doi: 10.1016/j.ijhydene.2015.11.046.
- [46] P. Zhou, Z. Yan, Y. Wu, W. Li, and X. Jin, "Communication—The Mechanism of Hydrogen Permeation Resistance of Ni Coating Enhanced by the Incorporation of Graphene," *ECS J. Solid State Sci. Technol.*, vol. 9, no. 9, p. 093004, Jun. 2020, doi: 10.1149/2162-8777/ab96ae.
- [47] Shi, K., Xiao, S., Ruan, Q., Wu, H., Chen, G., Zhou, C., ... & Chu, P. K. (2022). Hydrogen permeation behavior and mechanism of multi-layered graphene coatings and mitigation of hydrogen embrittlement of pipe steel. *Applied Surface Science*, 573, 151529.

- [48] Shi, K., Meng, X., Xiao, S., Chen, G., Wu, H., Zhou, C., ... & Chu, P. K. (2021). MXene coatings: novel hydrogen permeation barriers for pipe steels. *Nanomaterials*, *11*(10), 2737.
- [49] H. Yang, Z. Shao, W. Wang, X. Ji, and C. Li, "A composite coating of GO-Al₂O₃ for tritium permeation barrier," *Fusion Engineering and Design*, vol. 156, p. 111689, 2020.
- [50] Liu, W., Xue, L., Di, J., Zhou, Q., Zhang, H., Li, H., & Yan, Y. (2021). An efficient graphene oxide reinforced aluminum phosphate/Cr₂O₃ double coating as an enhanced tritium permeation barrier. *Surface and Coatings Technology*, *405*, 126699.
- [51] S. A. Khwaja and S. Paul, "Inspection of Coated Hydrogen Transportation Pipelines," *Applied Sciences*, vol. 12, no. 19, p. 9503, Jan. 2022, doi: 10.3390/app12199503.
- [52] Duminica, F. D., Vanden Eynde, X., Mandy, M., Nabi, B., Georges, C., Sturel, T., ... & Grigorieva, R. (2020). Investigation of PVD thin films as hydrogen barriers in aluminized press hardened steels (PHS). *Surface and Coatings Technology*, *397*, 125940.
- [53] Biggio, D., Elsener, B., & Rossi, A. (2025). Ni-P Coatings as Hydrogen Permeation Barriers—A Review. *Coatings*, *15*(4), 365.
- [54] Zheng, L., Li, H., Zhou, J., Tian, X., Zheng, Z., Wang, L., ... & Yan, Y. (2022). Layer-structured Cr/Cr x N coating via electroplating-based nitridation achieving high deuterium resistance as the hydrogen permeation barrier. *Journal of Advanced Ceramics*, *11*(12), 1944-1955.
- [55] K. Sadananda, J. H. Yang, N. Iyyer, N. Phan, and A. Rahman, "Sacrificial Zn–Ni coatings by electroplating and hydrogen embrittlement of high-strength steels," *Corrosion Reviews*, vol. 39, no. 6, pp. 487–517, Dec. 2021, doi: 10.1515/correv-2021-0038.
- [56] He, Y., Guo, E., Zhong, F., Fu, B., Cai, G., Zhang, D., ... & Ren, F. (2024). A novel method for preparing α -Al₂O₃ (Cr₂O₃)/Fe–Al composite coating with high hydrogen isotopes permeation resistance. *Ceramics International*, *50*(11), 20367-20375.
- [57] C. Zeng, Y. Bai, Y. Ling, Z. Xin, H. Liang, and X. Deng, "Hydrogen interaction characteristic of nanoscale oxide films grown on iron–nickel based stainless steel by selective thermal oxidation," *International Journal of Hydrogen Energy*, vol. 42, no. 32, pp. 20910–20921, Aug. 2017, doi: 10.1016/j.ijhydene.2017.02.206.
- [58] Li, S., He, D., Liu, X. P., Zhang, C., Wang, S. M., Yu, Q. H., ... & Jiang, L. J. (2013). Hydrogen permeation properties of alumina coating on 316L stainless steel. *J. Inorg. Mater*, *28*(7), 775-79..
- [59] K. T. Young, C. Smith, T. M. Krentz, D. A. Hitchcock, and E. M. Vogel, "Graphene synthesized by chemical vapor deposition as a hydrogen isotope permeation barrier," *Carbon*, vol. 176, pp. 106–117, May 2021, doi: 10.1016/j.carbon.2021.01.127.
- [60] M. Amanipour, E. Ganji Babakhani, A. Safekordi, A. Zamaniyan, and M. Heidari, "Effect of CVD parameters on hydrogen permeation properties in a nano-composite SiO₂–

Al₂O₃ membrane,” *Journal of Membrane Science*, vol. 423–424, pp. 530–535, Dec. 2012, doi: 10.1016/j.memsci.2012.09.007.

[61] Ł. Łach and D. Svyetlichnyy, “Recent Progress in Heat and Mass Transfer Modeling for Chemical Vapor Deposition Processes,” *Energies*, vol. 17, no. 13, p. 3267, Jan. 2024, doi: 10.3390/en17133267.

[62] Fotovvati, B., Namdari, N., & Dehghanghadikolaei, A. (2019). On coating techniques for surface protection: A review. *Journal of Manufacturing and Materials processing*, 3(1), 28.

[63] Thomas C. Allison, “NIST-JANAF Thermochemical Tables - SRD 13.” National Institute of Standards and Technology, Jan. 01, 2013. doi: 10.18434/T42S31.

[64] H. J. T. Ellingham, *Reducibility of oxides and sulphides in metallurgical processes*. Society of Chemical Industry, 1944.

[65] C. Mardare and A. W. Hassel, “Review on the Versatility of Tungsten Oxide Coatings,” *physica status solidi (a)*, vol. 216, Apr. 2019, doi: 10.1002/pssa.201900047.

[66] E. Lassner and W.-D. Schubert, *Tungsten: properties, chemistry, technology of the element, alloys, and chemical compounds*. New York London: Kluwer Academic, 1999.

[67] A. Boda, M. A. Sk, K. T. Shenoy, and S. Mohan, “Diffusion, permeation and solubility of hydrogen, deuterium and tritium in crystalline tungsten: First principles DFT simulations,” *International Journal of Hydrogen Energy*, vol. 45, no. 53, pp. 29095–29109, Oct. 2020, doi: 10.1016/j.ijhydene.2020.07.275.

[68] T. Ikeda, T. Otsuka, and T. Tanabe, “Determination of hydrogen diffusivity and permeability in W near room temperature applying a tritium tracer technique,” *Journal of Nuclear Materials*, vol. 415, no. 1, Supplement, pp. S684–S687, Aug. 2011, doi: 10.1016/j.jnucmat.2010.12.007.

[69] T. Oda, “Thermodynamic model for grain boundary effects on hydrogen solubility, diffusivity and permeability in poly-crystalline tungsten,” *Fusion Engineering and Design*, vol. 112, pp. 102–116, Nov. 2016, doi: 10.1016/j.fusengdes.2016.08.001.

[70] M. Shimada and R. J. Pawelko, “Tritium permeability in polycrystalline tungsten,” *Fusion Engineering and Design*, vol. 146, pp. 1988–1992, Sep. 2019, doi: 10.1016/j.fusengdes.2019.03.083.

[71] D. R. Chalfoun, T. M. Brizuela, C. Hurtado Noreña, F. Alvarez, A. Zavala, and P. Bruzzoni, “Evaluation of tungsten as a hydrogen permeation barrier in reduced activation steel F82H for nuclear fusion applications,” *International Journal of Hydrogen Energy*, vol. 136, pp. 833–842, Jun. 2025, doi: 10.1016/j.ijhydene.2024.03.358.

[72] A. Houben, M. Rasiński, L. Gao, and Ch. Linsmeier, “Tungsten nitride as tritium permeation barrier,” *Nuclear Materials and Energy*, vol. 24, p. 100752, Aug. 2020, doi: 10.1016/j.nme.2020.100752.

[73] Y. Fukai and H. Sugimoto, "Diffusion of hydrogen in metals," *Advances in Physics*, vol. 34, no. 2, pp. 263–326, Jan. 1985, doi: 10.1080/00018738500101751.

[74] S. G. Croll, "Surface roughness profile and its effect on coating adhesion and corrosion protection: A review," *Progress in Organic Coatings*, vol. 148, p. 105847, Nov. 2020, doi: 10.1016/j.porgcoat.2020.105847.

[75] Ratwani, C. R., Novoselov, K. S., & Abdelkader, A. M. (2025). Applications and mechanistic insights into intrinsically self-healing polymers with multifunctional 2D materials. *SusMat*, 5(4), e70028.

3. Experimental

This chapter presents the experimental procedures and methodologies employed to investigate the X60 steel and of tungsten-coated X60 steel. Three series of W-coated samples (Series 1, Series 2, and Series 3) were deposited using radio frequency magnetron sputtering. The chapter provides detailed descriptions of the experimental approach, including materials, sample preparation, and the various characterization and testing methods utilized.

The electrochemical hydrogen permeation test served as a primary technique to evaluate hydrogen transport behavior in the samples. In selected samples local hydrogen measurements were conducted using the microcapillary cell technique.

and also the total hydrogen content was determined by inert gas fusion analysis using the oxygen, nitrogen, hydrogen analyzer LECO ONH836. The surface analytical techniques included X-ray photoelectron spectroscopy (XPS) and, in some cases, combined conventional XPS and Hard X-ray photoelectron spectroscopy (HAXPES) were used for surface characterization.

Furthermore, complementary methods such as X-ray diffraction, portable X-ray fluorescence (p-XRF), surface roughness testing, Rutherford Backscattering Spectrometry/Elastic Recoil Detection Analysis (RBS/ERDA), scanning electron microscopy with energy dispersive spectroscopy (SEM-EDS), and metallography were employed. RBS/ERDA analysis and data elaboration were also performed.

This chapter is based on my personal work under the supervision of Prof. Antonella Rossi, Prof. Marzia Fantauzzi, Prof. Bernhard Elsener, Dr. Nicoletta Zacchetti, Dr. Claudia Cancellieri, Dr. Lars P.H. Jeurgens and Dr. Deborah Biggio.

Three series of coatings were deposited within the Coating and NDT Group at RINA Consulting – CSM S.p.A.. Series 1 was prepared and deposited by Mr. Francesco Sciarrabba, while Series 2 and Series 3 were prepared by me and deposited by Eng. Francesco Sciarrabba in my presence during an internship at RINA Consulting. SEM/EDS measurements were performed at the Advanced Metallography Laboratory at RINA Consulting – CSM S.p.A., Castel Romano, Rome. The X-ray diffraction (XRD) analyses were performed by Dr. Claudia Cancellieri at EMPA's Center for X-ray Analytics, Dübendorf, Switzerland, in my presence. RBS/ERDA measurements were performed by Dr. Arnold Müller at the Laboratory of Ion Beam Physics, ETH Zurich. Inert gas fusion analysis using a LECO ONH836 analyzer was performed by Ms. Emma Trivellin at the Analytical Center Laboratory, EMPA Dübendorf, Switzerland.

Unless explicitly stated otherwise, all other experiments were performed by me.

Part of the experimental work and data analysis described in this chapter has been published in three scientific papers [1],[2],[3].

The published papers are included in the appendix of this thesis for reference. (Appendix 7.3)

3.1. Materials

3.1.1. The substrate: X60 steel

The substrate used in this study is API 5L X60QS steel. According to the American Petroleum Institute, API 5L is the standard specification for pipelines, and X60 is the minimum yield strength (415 MPa). The steel is quenched and tempered (Q), which provides a combination of high strength and toughness due to controlled heat treatment. S indicates that the material is intended for sour service applications. The chemical composition of X60 steel, as specified by the API, is presented in Table 3.1.

Table 3.1: Chemical composition in weight percentage (wt.%) of X60 steel according to the analysis of API datasheet [4]

wt %	Fe	Mn	Cr	Mo	Ni	Cu	C	P	S
	Balance	≤ 1.4	≤ 0.50	≤ 0.15	≤ 0.50	≤ 0.50	≤ 0.28	≤ 0.03	≤ 0.03

Metallographic characterization was performed on the steel substrate after etching with 2% Nital solution for 5 seconds and were conducted at the Advanced Metallography Laboratory at RINA Consulting CSM S.p.A, Castel Romano, Rome and were characterized using the Scanning electron microscopy (SEM). The instrument details are presented in section 3.7.5.

3.1.2. Roughness test

The average surface roughness (R_a) of the samples is measured by a Mitutoyo SV-3200 H4 surface roughness tester in RINA Consulting CSM S.p.A laboratories.

3.1.3. Coating materials and deposition: RF magnetron sputtering

Prior to deposition, samples were degreased and ultrasonically (US) cleaned in ethanol acetone and isopropanol for 10 minutes and blown dry with nitrogen for 3 minutes. The tungsten coatings were deposited by radiofrequency (RF) magnetron sputtering in an Ar^+ plasma sputtering chamber in the laboratories of RINA Consulting CSM S.p.A, the partner of this project. Before coating, the steel had a 6 minutes glow, an 11 minutes ramp-up, and a 5 minutes cleaning time. Sputtering targets of pure tungsten (purity > 99.95 %) were used. RF magnetron sputtering (RF) with a power of 800 W was applied. The deposition temperature was 350 °C, and the total pressure in the chamber was 10^{-2} bar. The steel (substrate) was mounted on a substrate holder and installed 75 mm from the target surface.

Three series of tungsten coatings were produced and named: Series 1 (S1), Series 2 (S2), and Series 3 (S3), each differing in substrate roughness and coating thickness (Table 3.2). The roughness of the steel surface was found not to be suitable for the post-deposition characteristics of the samples as hydrogen permeation barriers. The coating deposition time was 4 hours for the 3 μm thick coating and 2 hours for the 1.5 μm one.

Table 3.2: Roughness and nominal coating thickness of the samples prepared by RF magnetron sputtering.

Series	S1	S2	S3
Coating	Tungsten	Tungsten	Tungsten
Substrate Roughness (R_a)	0.4 μm	0.2 μm	0.2 μm
Nominal Coating Thickness	3 μm	3 μm	1.5 μm

3.2 Sample preparation

3.2.1. Sample preparation for hydrogen permeation test (Devanathan and Stachurski cell)

In this study, X60 steel samples with varying geometries (rectangular and disc-shaped) were employed to fit the requirements of the various experimental setups. Disc-shaped samples (5 cm in diameter and 2 mm in thickness) were cut from X60 steel pipelines and were specifically used for the ISO standard electrochemical cell (section 3.3.1). Rectangular samples 2cm x 2cm x 2mm were cut from disk samples and were employed for the measurements in the modified electrochemical hydrogen permeation test (section 3.3.2.).

Preparation of X60 steel samples

Two distinct procedures were employed to clean the surface of the samples on both sides:

Five-Solvents Cleaning (C X60 steel)

Samples were sequentially ultrasonically (US) cleaned at 40 °C using five different solvents for 5 minutes each:

- Butan-2-one, purity > 99.5% (CAS No. 78-93-3, Chem-lab, Zedelgem, Belgium),
- Acetone, purity \geq 95.5% (CAS No. 67-64-1),
- Ethanol absolute, purity \geq 99.8% (CAS No. 64-17-5, Honeywell, Offenbach, Germany),
- Petroleum ether (CAS No. 650-001-01, Carlo Erba Reagents S.r.l., Cornaredo, MI, Italy),
- Double-distilled water (specific conductivity $1.5 \pm 0.1 \mu\text{S/cm}$ at 20° C).

Organic solvents were employed to minimize carbon contamination on the sample surface, whereas the polar solvent (double-distilled water) was used to remove any inorganic salt that might be present at the surface. After cleaning with each solvent, survey XPS spectra were recorded in three different areas of the samples. This protocol was developed to ensure reproducible electrochemical measurements and to eliminate potential interferences from surface adsorbates.

Five-Solvent Cleaning combined with Mechanical Polishing (MP X60 steel)

Samples were first cleaned using the five-solvent procedure described above and then mechanically polished (MP) with 4000-mesh SiC paper (Struers, Ballerup, Denmark) using ethanol as a lubricant for 3 minutes and 30 seconds. After polishing, samples were subjected to ultrasonic cleaning at 40 °C in ethanol for 5 minutes, followed by immersion in double-distilled water for 10 minutes at ambient temperature (25.0 °C ± 0.1 °C).

Preparation of square X60 steel

The samples were cleaned with isopropanol, acetone, and ethanol and mechanically polished using 4000-mesh SiC paper and distilled water as a lubricant for three minutes and thirty seconds. After mechanical polishing, the samples were sonicated at 40 °C in ethanol for 5 minutes and in double-distilled water for 10 minutes. Following the cleaning and/or the mechanical polishing the samples were blown dry with nitrogen.

Preparation of W-coated X60 steel (Series 1, Series 2 and Series 3)

The W-coated samples were mechanically polished (MP) using a DP Plus cloth and diamond sprays with particle sizes of 9 µm, 6 µm, and 3 µm (Struers, Ballerup, DK). Each polishing step was carried out for 3 minutes and 30 seconds. After each polishing step, the samples were ultrasonically cleaned in ethanol at 40 °C for 5 minutes. A final ultrasonic cleaning step was performed in double-distilled water under the same conditions (see Table 3.3).

Table 3.3. Mechanical polishing and ultrasonic cleaning procedure for W-coated samples

Step	Procedure /Materials	Duration
1	Mechanical polishing using DP Plus cloth and 9 µm diamond spray	3 min and 30 seconds
2	US-cleaning in Ethanol	5 minutes at 40 °C.
3	Mechanical polishing using DP Plus cloth And 6 µm diamond spray	3 min and 30 seconds
4	US-cleaning in Ethanol	5 minutes at 40 °C.
5	Mechanical polishing using DP Plus cloth paper and 3 µm diamond spray	3 min and 30 seconds
6	US-cleaning in Ethanol	5 minutes at 40 °C.
7	US-cleaning in double distilled water	5 minutes at 40 °C.

Before the hydrogen permeation test, all samples were heated at 80 °C for 15 hours to remove any hydrogen that might be trapped in the steel after cutting.

3.2.2. Sample preparation for analysis via inert gas fusion LECO ONH836

For hydrogen analysis via inert gas fusion using the Oxygen/Nitrogen/Hydrogen Elemental Analyzer ONH836 manufactured by LECO (US) samples with mass of 1.000g ± 0.003g were cut from X60 steel sample 2cm x 2cm x 2mm using a precision sectionizing machine as shown in Figure 3.1.a. This machine is used for accurately cutting small samples of materials without damaging their structure. It uses a diamond blade to cut the sample, which is fixed in a holder. The machine operates on three axes: X, Y, and Z, as shown in Figure 3.1.b. The samples were cut along the Y axis. During the cutting process, tap water was used to cool the sample.

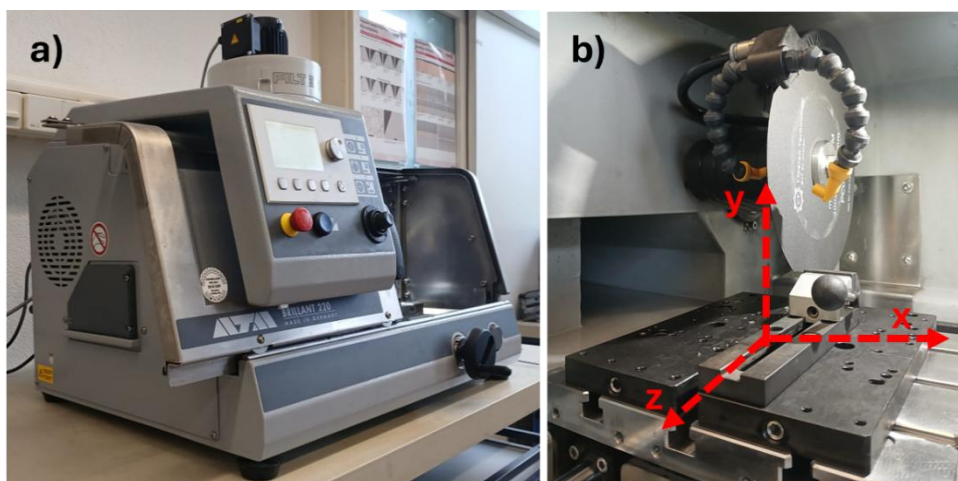


Figure 3.1. a: Precision cut off machine, b: holder sample, cutting axis, and diamond blade (at Laboratory of joining technologies and corrosion EMPA Dübendorf - CH).

After cutting, the samples were degassed in an oven for one hour and thirty minutes at 200 °C. Then they were polished with abrasive paper of 4000 grit, subsequently rinsed with ethanol, and cleaned with diethyl ether; then, the samples were charged in an electrochemical cell for one hour and thirty minutes in contact with 0.1 M HCl solution. The applied current density was -20 mA/cm^2 . After hydrogen charging, the samples were mechanically polished with abrasive paper until the corroded region was removed (this step is essential because the LECO instrument is highly surface sensitive), then rinsed with ethanol and cleaned in a beaker with diethyl ether. These steps took around 7 to 10 minutes before the measurement.

3.3. Electrochemical hydrogen permeation test (HPT)

The electrochemical hydrogen permeation test is used to investigate hydrogen diffusion in steel, and it was conducted using a Devanathan and Stachurski [5] hydrogen permeation cell. It consists of two compartments: the charging (or cathodic) cell, where hydrogen is produced, and the detection (or anodic) cell, where hydrogen is detected.

3.3.1. Electrochemical hydrogen permeation cell and potentiostats (at the University of Cagliari (UniCa), Italy)

The surface of the sample exposed to the anodic and cathodic cells is 6.95 cm^2 (the diameter of the sample is 5 cm). Both cells are equipped with three electrodes: an Ag/AgCl (KCl-saturated) reference electrode (RE), a platinum counter electrode (CE), and the sample under analysis as the working electrode (WE) (Figure 3.2.b). The three electrodes in the anodic and cathodic cells are connected to two VersaSTAT3F Potentiostats, manufactured by Ametek (USA), which are operated in floating mode; this procedure is carried out according to an optimized procedure described in ISO 17081.

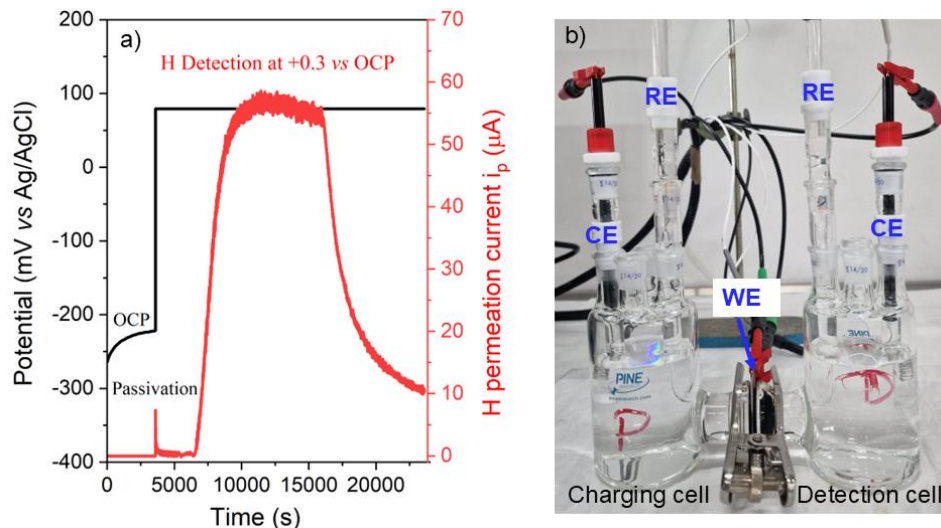


Figure 3.2. (a) Representative of the hydrogen permeation curve and timing (b) scheme of the hydrogen permeation cell (Devanathan and Stachurski cell).

3.3.2. Modified electrochemical hydrogen permeation cells and potentiostats (at Laboratory of joining technologies and corrosion EMPA Dübendorf (CH))

The cell used for another experiments is still an electrochemical hydrogen permeation apparatus and differs from the previous one for the geometry and for the potentiostats. The sample surface exposed to the anodic and cathodic cells has a diameter corresponding to an area of 3 cm². The detection cell is equipped with three electrodes: an Ag/AgCl (saturated with KCl) electrode as the reference electrode (RE), a platinum electrode as the counter electrode (CE), and the sample under analysis as the working electrode (WE). These electrodes are connected to an Ivium potentiostat. The production cell is equipped with two electrodes: a platinum counter electrode (CE) and the sample under analysis as working electrode (WE). These two electrodes are connected to a high precision current and voltage source (DIGISTANT 4462, Burster, Gernsbach, Germany).

The hydrogen permeation experiments with both the instrumental setups followed a precise timing, which is summarized in the following. First, the H detection cell is filled with a 0.1 M NaOH solution, and the open-circuit potential (OCP) of the mechanically polished and heated in oven at 80°C for 24 hours sample is recorded for 3600 seconds (Figure 3.2.a). Then an anodic potential of + 0.3 V vs OCP is applied in the detection cell. The passivation current decreases upon time, reaching values lower than 0.1 $\mu\text{A}/\text{cm}^2$ (Figure 3.2.a). Then, the charging cell is filled with 0.1 M HCl and 0.2 g/L As₂O₃.

A galvanostatic cathodic polarization was applied using a current density of -0.86 mA/ cm².

3.3.3 Data processing: determination of the diffusion coefficient

The hydrogen permeation experiment gives a current versus time curve that typically consists of three main regions [6]:

- **Transient (Build-Up):** Immediately after the start of hydrogen charging, the permeation current increases as hydrogen atoms diffuse through the sample, reaching a steady state.

- **Steady state:** Steady state is reached when the permeation current stays nearly constant. This means the amount of hydrogen entering the detection side is equal to the amount being supplied at the charging side.
- **Decay:** After hydrogen charging is stopped, the permeation current decreases as the hydrogen content begins to de-trap and to be oxidized to H⁺.

The time lag method (t_{lag}) and the breakthrough (t_b) method [7] are used to determine the effective hydrogen diffusion coefficient (D_{eff} (m²/s)) from the transient region in the permeation curve. In the t_{lag} method, D_{eff} is calculated using Equation 3.1 and in the t_b method the D_{eff} is calculated using Equation 3.2.

$$D_{eff} = \frac{L^2}{6t_{lag}} \quad (\text{Equation 3.3})$$

$$D_{eff} = \frac{L^2}{15.3t_b} \quad (\text{Equation 3.4})$$

Where L is the thickness in (m) of the sample, t_{lag} is the time in (s) required to reach 63 % of steady state current density (i_{ss}), and t_b is the breakthrough time in seconds that corresponds to the intersection of the tangent line at the inflection point and the x-axis in the permeation curve.

Alternatively, the transient build-up and decay regions can be directly fitted to Fick's diffusion-based permeation equations [6]. Equation 3.5 and Equation 3.6 respectively.

$$\frac{I_p - I_p^0}{I_p^\infty - I_p^0} = \frac{2L}{\sqrt{\pi D_{eff} t}} \sum_{n=0}^{\infty} \exp\left(-\frac{L^2(2n+1)^2}{4D_{eff} t}\right) \quad (\text{Equation 3.7})$$

$$\frac{I_p - I_p^\infty}{I_p^0 - I_p^\infty} = 1 - \frac{2L}{\sqrt{\pi D_{eff} t}} \sum_{n=0}^{\infty} \exp\left(-\frac{L^2(2n+1)^2}{4D_{eff} t}\right) \quad (\text{Equation 3.8})$$

where I_p is the permeation current at time t , I_p^0 the initial steady-state current, and I_p^∞ is the new steady-state current after the hydrogen production stops.

In addition, the subsurface hydrogen concentration of mobile hydrogen, C_0 , can be determined by Equation 3.9 [8]

$$C_0 = \frac{i_{ss} L}{F D_{eff} \rho_{Fe}} 10^6 \text{ (ppm)} \quad (\text{Equation 3.10})$$

Where i_{ss} is the steady state permeation current density (A/m²), L is the thickness of the sample (m), D_{eff} is the effective diffusion coefficient (m²/s), F is the Faraday constant (96,485 C/mol), M_H is the molar mass of hydrogen (1g/mol), and ρ_{Fe} is the iron density (7.87 x 10⁶ g/m³).

Data processing: determination of the diffusion coefficient for a coated sample

The effective diffusion coefficient D_{eff} is calculated with eq. (1) or (2) both for uncoated and coated samples and it includes the contribution of both the substrate and the coating. To determine the diffusion coefficient D_f of the coating (the hydrogen permeation barrier), a model proposed by [9] has to be used that takes into account the bi-layer structure of the sample (Equation 3.11)

$$D_f = \frac{D_s D_{eff}(PRF+2)}{D_{eff}(2-3PRF)\left(\frac{L_s}{L_f}\right)^2 + D_s PRF\left(1+\frac{L_s}{L_f}\right)^2} \quad (\text{Equation 3.12})$$

where: D_f is the diffusion coefficient of the film (m^2/s), D_s is the diffusion coefficient of the substrate (m^2/s), D_{eff} is the effective diffusion coefficient of the two-layer membrane obtained from time-lag analysis (m^2/s) $D_{eff} = \frac{L_s + L_f}{6t_{lag2}}$, L_s is the substrate thickness (m) and L_f is the film thickness (m).

PRF is the permeation reduction factor determined as the ratio of the steady-state hydrogen flux through the uncoated substrate to the coated sample ($PRF = \frac{J_{uncoated}}{J_{coated}}$).

Data processing: determination of the trapped hydrogen concentration

The amount of trapped hydrogen in the X60 steel samples was determined using the Zakroczymski approach[6], which consists of analyzing the decay/desorption region of the transient hydrogen permeation. The method consists of two main steps:

1) Determination of the diffusion coefficient of mobile hydrogen

The diffusion coefficient of mobile hydrogen (also termed lattice diffusion coefficient), D_L , is obtained from permeation transients measured in the electrochemical permeation cell described in Section 3.3.2. The charging conditions are identical except for the cathodic current density, which is used as the only variable.

The sample is first charged at cathodic charging current density - 0.5 mA/cm^2 until the anodic current reaches the steady state. Immediately afterwards, the cathodic charging current is increased to -1 mA/cm^2 to generate a second transient. The decay region of the second transient (corresponding to the cathodic current density -1 mA/cm^2) is fitted using the build-up equation (Equation 3.3) to determine D_L . This provides the diffusion coefficient of the mobile hydrogen.

2) Analysis of the decay/desorption region to quantify trapped and diffusible hydrogen.

Once D_L is known, the decay/desorption region of the transient permeation can be determined to distinguish between trapped hydrogen and mobile hydrogen. Basically, the anodic current of the desorption curve $I_H(t)$ corresponds to the sum of the current of the trapped hydrogen $I_{tH}(t)$ and the current of the mobile hydrogen $I_{mH}(t)$ (Equation 3.7).

$$I_H(t) = I_{mH}(t) + I_{tH}(t) \quad (\text{Equation 3.13})$$

Where, $I_{mH}(t)$ is the desorption current of mobile hydrogen and $I_{tH}(t)$ is the desorption current of reversible trapped hydrogen.

Knowing D_L and assuming that the steady-state current I_p^∞ (equivalent to the initial desorption current I_H^0) corresponds to the desorption current of diffusible hydrogen, the desorption current of mobile hydrogen, $I_{mH}(t)$, was reconstructed using decay equation (Equation 3.4). Subtracting $I_{mH}(t)$ from the total desorption current $I_H(t)$ gives the trapped hydrogen desorption current:

$$I(t) = I_H(t) - I_{mH}(t) \quad (\text{Equation 3.14})$$

The total hydrogen per unit area is given by the area under the measured curve:

$$q_H = \int I_H(t) dt \quad (\text{Equation 3.15})$$

Similarly:

$$q_{mH} = \int I(t) dt \quad (\text{Equation 3.16})$$

$$q_{tH} = \int I(t) dt \quad (\text{Equation 3.17})$$

Where q_{mH} is the amount of mobile hydrogen and q_{tH} is the amount of trapped hydrogen.

3.4. Local hydrogen measurements: Microcapillary cell technique

The glass microcapillary was prepared by softening a borosilicate glass microcapillary with a heated filament and then stretching it by gravity to form a fine-tipped micropipette (Figure 3.3.a). Following pulling, the tip of the microcapillary is mechanically polished (MP) using a microforge. The microcapillary is placed on the microforge stage, and the tip is gently brought into contact with a heated glass bead to smooth and refine the opening (Figure 3.3.b). ensured a clean, reproducible geometry and removed any irregularities or sharp edges from the tip, which is critical for consistent and localized hydrogen measurements.

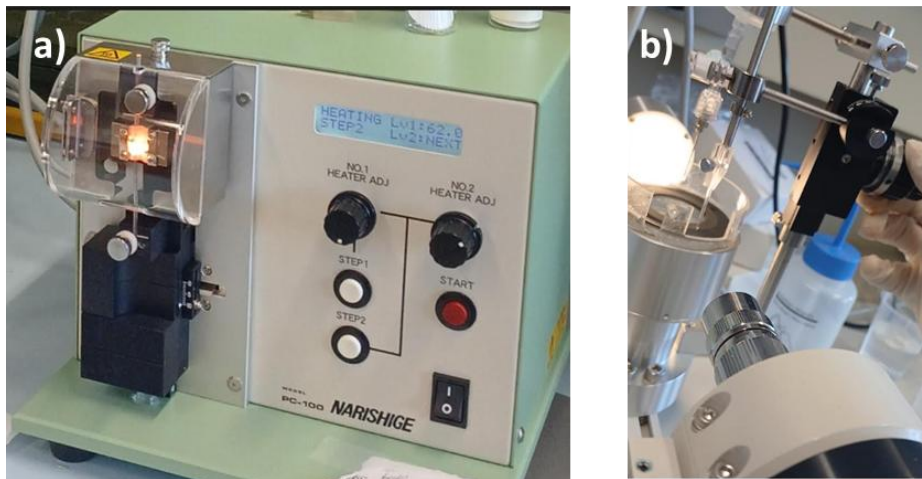


Figure 3.3: Steps in glass microcapillary preparation: (a) thermal softening of a borosilicate glass capillary followed by gravity-assisted pulling to generate a fine tip; (b) mechanical polishing of the microcapillary tip for final shaping (Laboratory of joining technologies and corrosion EMPA Dübendorf (CH)).

The experimental procedure comprises two main–steps: hydrogen charging and hydrogen discharging.

1) Hydrogen charging:

The steel samples were charged with hydrogen using an electrochemical cell using 0.1 M HCl and 0.2 g/L As_2O_3 while applying a current of - 4mA for two hours using a two-electrode configuration, with a sample as WE and platinum as RE. the applied current was controlled using a These two electrodes are connected to a the DIGISTANT 4462, Burster.

2) Hydrogen discharging and local measurements (microcapillary cell technique):

Hydrogen discharging is performed by the microcapillary cell. The microcell setup (Figure 3.4) consists of a glass microcapillary, a counter electrode featuring a 0.5 mm

thick gold wire, and a stainless-steel quasi-reference electrode.(SSQRE) ;Quasi-reference electrode (QRE) is defined as “ *Electrode that maintains a constant, but not generally well defined, potential in an electrochemical cell*”[10] During microelectrochemical hydrogen measurements, the steel samples are exposed to a 0.2 M NaOH solution and anodically polarized at a potential within the passive range (+ 520 mV vs SSQRE).

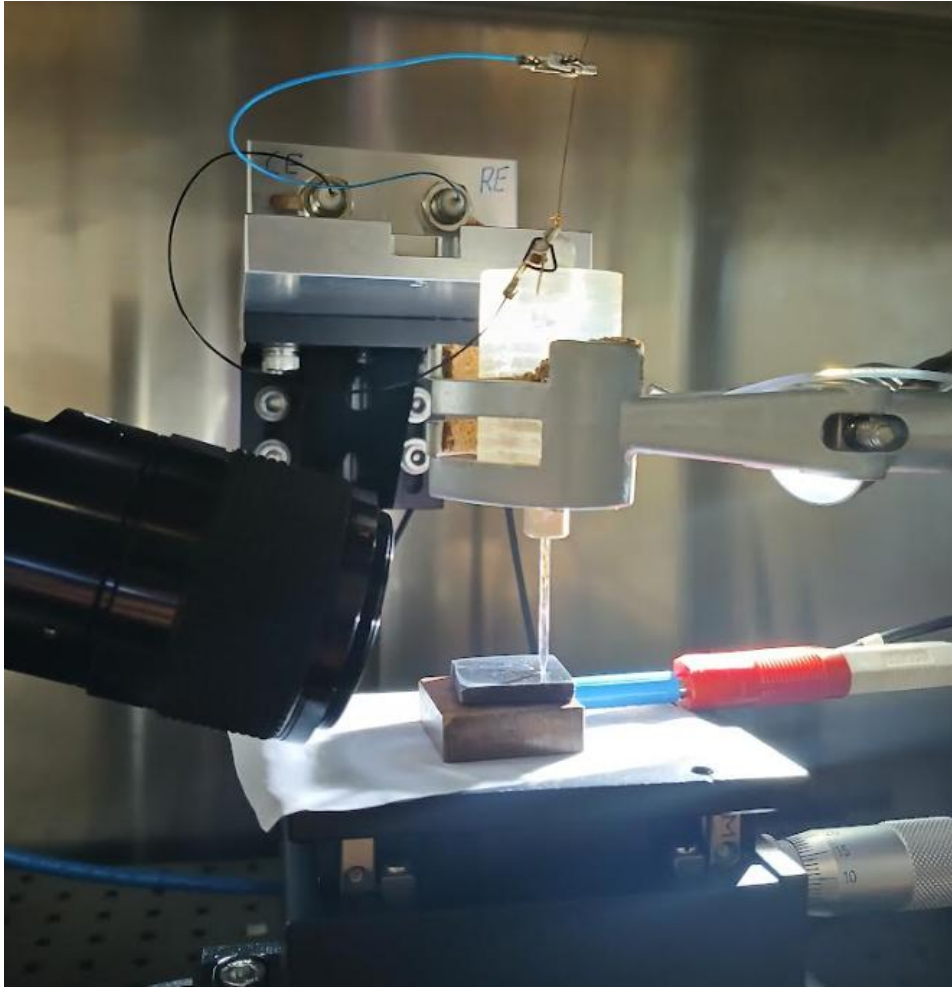


Figure 3.4. Microcapillary cell setup (at Laboratory of joining technologies and corrosion EMPA Dübendorf (CH)).

The experimental procedure involved the following steps:

3) *Baseline measurements (uncharged X60 steel):*

The passivation behavior of the uncharged X60 steel is initially characterized by recording its polarization curve using the microcapillary cell technique. This experiment passivates the surface of the steel in the absence of hydrogen charging. This is essential for distinguishing subsequent hydrogen-related electrochemical phenomena from the passivation behavior of the materials. This passivation current will then be subtracted from the measured data.

4) *Hydrogen charged sample measurements:*

After the baseline is established the same microcapillary cell is applied to the hydrogen charged X60 steel samples. During the process, atomic hydrogen (H^0) that diffuses through the sample,

is oxidized to H^+ ions at the steel surface and then reacts with OH^- ions from the 0.2 M NaOH electrolyte and form water. The current associated with the hydrogen oxidation reaction is measured and recorded.

Data processing

The hydrogen concentration is determined from the microcapillary cell measurements using the approach based on the Faraday second law as described in [10]. Faraday's second law states "that the amount of a given species (here, hydrogen) deposited at an electrode is directly proportional to the electric charge (here, the integral value between the oxidation current of the reference and charged sample)". The total electric charge (Q) passed during the oxidation of hydrogen is obtained by integrating the current $i(t)$ over the measurement interval, ($t = 0s$ to $1800s$). For each sample, the charge measured for the hydrogen-charged X60 steel (Q_H) is compared with the reference uncharged sample (Q_{ref}). The difference between these values represents the charge associated with oxidized hydrogen and the hydrogen concentration is then determined using Equation 3.12:

$$c_H = \frac{Q_H - Q_{Ref}}{n * F * V} \quad (\text{Equation 3.18})$$

where: c_H is the hydrogen concentration in ppm, Q_H is the electric charge in Coulomb, C, of the charged sample; Q_{ref} is the electric charge in Coulomb of the uncharged sample; n is the number of electrons participating in the oxidation reaction (i.e. $H \rightarrow H^+ + e^-$), F is the Faraday's constant and V is the effective diffusion volume, which can be calculated using the Equation 3.13 assuming the volume is a half-ellipsoid.

$$V = \frac{4}{3} \cdot (a + L_D)^2 L_D \quad (\text{Equation 3.13})$$

Where a : is the radius of the microcapillary, L_D is the diffusion distance of the hydrogen during the measurement.

3.5. Hydrogen Analysis by inert gas Fusion (LECO ONH836)

This technique allows for accurate determination of the total hydrogen content, including both mobile and trapped hydrogen, in metallic samples.

The hydrogen content of selected samples was determined by inert gas fusion analysis using a LECO ONH836 analyser at the Analytical Center Laboratory, EMPA Dübendorf, Switzerland. The measurements were performed by the laboratory's technical staff responsible for the instrument. In this method, each sample was placed in a graphite crucible and heated in a stream of inert gas to $1000^\circ C$ to release the hydrogen present in the material. The liberated hydrogen was then carried by the inert gas to a thermal conductivity detector, where its concentration was measured. Calibration was performed by the instrument technician using certified reference samples (stainless steel) with a known hydrogen concentration.

3.6. Surface analytical techniques

Surface chemical composition and chemical state of the elements present in the surface are determined using X-ray photoelectron spectroscopy (XPS). Two spectrometers were employed in this work: a Theta Probe XPS, manufactured by Thermo Scientific, East Grinstead (UK) and

a combined XPS/hard X-ray photoelectron spectroscopy (HAXPS) instrument, PHI Quantes™ fabricated by ULVAC-PHI developed and fabricated by a joint venture between USA (Chanhassen, MN) and Japan (Chigasaki, Kanagawa). The Theta Probe XPS provides surface-sensitive measurements, and it is used in two different modes: standard lens mode and angular-resolved mode; some experiments are carried out in combination with argon ion etching, using an Al K α source alternating acquisition and ion aetching. The PHI Quantes enables variable information depth analysis through the combined use of Al K α and Cr K α excitation sources. More details on the principle of the techniques are given in Appendix 1 of this thesis.

3.6.1. X-ray photoelectron spectroscopy (XPS)

The Theta Probe spectrometer operates with a monochromated Alka source ($h\nu = 1486.6$ eV). Measurements were performed using a nominal spot size of 400 μm , with a current of 6.7 mA and applying a voltage of 15kV. The analyzed area is calculated to be: 0.13 mm^2 . Survey and high-resolution spectra were acquired (Table 3.4, Table 3.5, Table 3.6, Table 3.7). The pass energy was set to 200 eV for the survey and 100 eV for the high-resolution (HR) spectra in standard lens mode. Under these conditions the full width at the half-maximum height (FWHM) of the Ag 3d $_{5/2}$ peak was found to be equal to 0.96 ± 0.05 eV. The angle between the source and the lens axis is 67.38°, while the emission angle is 53°. Linearity response of the binding energy scale was periodically checked according to ISO 15472:2010 [11] and an accuracy on the BE measurements of ± 0.1 eV was found. More detailed information about the instrument can be found in Hannachi et al. [1].

Table 3.4. X-ray photoelectron spectroscopy (XPS) acquisition parameters for the high-resolution spectra and survey spectra collected using XPS (at University of Cagliari) of X60 steel samples

Regions	Binding energy range (eV)		Number of scans	Pass energy (eV)	Step size (eV)
	from	to			
Survey	-10	1350	9	200	1
C 1s	279	298	9	100	0.05
O 1s	525	545	9	100	0.05
Fe 2p	700	740	9	100	0.05
Valence	-5	40	3	100	0.1

Table 3.5. X-ray photoelectron spectroscopy (XPS) acquisition parameters for the high resolution spectra and survey spectra collected at UniCa of W-coated X60 steel samples Series 1, series 2 and series 3

Regions	Binding energy range (eV)		Number of scans	Pass energy (eV)	Step size (eV)
	from	to			
Survey	-10	1350	9	200	1
C 1s	279	298	27	100	0.05
O 1s	525	545	9	100	0.05
W 4f	25	50	9	100	0.05
Fe 2p	700	740	9	100	0.05
Valence	-5	40	3	100	0.1

Table 3.6. X-ray photoelectron spectroscopy (XPS) Acquisition parameters for the high resolution spectra and survey spectra collected using XPS at UniCa for ion sputtered pure tungsten

Regions	Binding energy range (eV)		Number of scans	Pass energy (eV)	Step size (eV)
	from	to			
Survey	-10	1350	9	200	1
C 1s	279	298	27	100	0.05
O 1s	525	545	9	100	0.05
W 4f	25	50	9	100	0.05
W 4d	230	270	9	100	0.1
W NNN	1280	1340	27	100	0.1
O KLL	950	1030	27	100	0.1

Table 3.7. X-ray photoelectron spectroscopy (XPS) Acquisition parameters for the high resolution spectra and survey spectra collected using XPS at Unica for standard reference tungsten oxides WO₂ and WO₃

Regions	Binding energy range (eV)		Number of scans	Pass energy (eV)	Step size (eV)
	from	to			
Survey	-10	1350	9	200	1
C 1s	279	298	27	100	0.05
O 1s	525	545	9	100	0.05
W 4f	25	50	9	100	0.05
W 4d	230	270	9	100	0.1
W NNN	1280	1340	27	100	0.1
O KLL	950	1030	27	100	0.1

Data processing

Spectra are processed using CasaXPS software (v2.3.26PR1.0) [12]. The iterative Shirley background subtraction routine was applied before the curve fitting. The contamination layer, l_c , and the thickness of the native oxide layer, t , are determined using a three-layer model [13].

The curve fitting of the Fe 2p high-resolution spectra was performed according to parameters reported in the literature[14] and based on standard reference compounds, while the fitting of the W 4f high-resolution spectra was carried out by fixing the parameters based on measurements of the pure tungsten after ion sputtering and tungsten oxides WO₂ and WO₃ as references.

3.6.3. X ray photoelectron spectroscopy /Hard X ray photoelectron spectroscopy (XPS/HAXPS)

XPS/HAXPES spectra were collected using a PHI QuantesTM spectrometer (ULVAC-PHI) equipped with a dual monochromatic X-ray source, soft AlK α (1486.6 eV) spot size 200 mm at 48 W and a hard Cr K α (5414.7 eV) spot size 300 mm at 53W, which corresponds to an analysis area of 0.03 mm² and of 0.07 mm², respectively. The AlK α and CrK α X-ray beams are separated by an angle of 22 ° and are directed to the sample at effective angles 45° and 49°, respectively, relative to the analyzer [15]In this instrument, the emission angle can be varied by tilting the sample stage. In this work, the stage was tilted to 90° and corresponded to an emission angle of 0° (normal emission angle). The emission angle according to ISO 18115-1:2023[16]

is defined as “angle between the trajectory of a particle or photon as it leaves a surface, and the local or average surface normal”. The survey spectra were measured with both the soft AlK α source and the hard X-ray CrK α source and were measured at a pass energy of 224 eV, while the HR spectra were performed at 69 eV pass energy using a step size of 0.1 eV for HR spectra, and step size of 0.8 eV for survey spectra. The acquired regions for W coated X60 steel samples are presented in Table 3.8. The spectrometer was calibrated by the instrument technician according to ISO 15472 [17] by referencing the Au 4f_{7/2} and Cu 2p_{3/2} main peaks (as measured in situ for corresponding sputtered cleaned, high-purity metal references using the soft X-ray) to the recommended binding energy (BE) positions of 83.96 and 932.62 eV, respectively.

Table 3.8. X-ray photoelectron spectroscopy (XPS) and hard X-ray photoelectron spectroscopy (HAXPES) Acquisition parameters for the high resolution spectra and survey spectra collected using a PHI Quantes™ spectrometer (ULVAC-PHI) at Laboratory of joining technologies and corrosion EMPA Dübendorf (CH)) for W-coated X60 steel Series 1, Series 2 and Series 3

XPS and HAXPES	Elements	Binding energy range (eV)		Number of scans	Pass energy	Step size
		from	to			
XPS Alka source (1486.6 eV)	Survey	0	1200	9	224	1
	C 1s	282	292	9	69	0.1
	O 1s	523	540	9	69	0.1
	W 4f	25	50	9	69	0.1
	W 4d	232	272	9	69	0.1
	Fe 2p	700	740	9	69	0.1
HAXPES CrKa source (5414.7 eV)	Survey	0	5200	9	224	0.8
	C 1s	279	291	9	69	0.1
	O 1s	526	537	9	69	0.1
	W 4f	26	50	9	69	0.1
	W 4d	231	271	9	69	0.1

3.7 Other techniques

3.7.1. Portable X-ray fluorescence (p-XRF)

X-ray fluorescence spectroscopy (XRF) is used to determine the bulk composition of both the X60 QS substrate and the W-coated X60, employing a hand-held, standardless XRF spectrometer (SPECTRO xSORT, Spectro Analytical Instruments GmbH, Kleve, Germany). The spectrometer calibration is automatically performed by the instrument itself, using the ICAL algorithm. More details on the instrument calibration and set up are reported in [14]

3.7.3. X ray diffraction (XRD)

Phase identification and microstructural characterization of the X60QS steel substrate and the W-coated X60QS steel are carried out using a Bruker D8 Discover X-ray diffractometer in at EMPA’s Center for X-ray Analytics, Dübendorf (CH), operating in Bragg–Brentano geometry. Diffraction patterns are collected over a 2 θ range of 10–90°, and 20–90°, with a step size of 0.02°. The instrument is equipped with a Cu K α radiation source ($\lambda = 1.5406 \text{ \AA}$).

To simultaneously determine the average crystallite size and the microstrain (ϵ), the Williamson–Hall method (WH) was employed using the Equation 3.13:[18]

$$\beta\cos\theta = K\lambda/D + 4\epsilon\sin\theta \quad (\text{Equation 3.13})$$

$\beta\cos\theta$ was plotted versus $4\sin\theta$, and the crystallite size was obtained from the intercept, while the strain was extracted from the slope.

Stress analysis has been performed on W-coated X60 steel samples of thicknesses range between 1.5 mm and 3 mm using the same diffractometer.

The $\sin^2\psi$ method was used for determining residual stresses in W coated X60 steel. It is based on measuring the variation in the spacing of specific crystallographic planes (d_{hkl}) as the sample is tilted at different angles (ψ) 0° , 5° , 10° , 15° , 30° , 45° and 60° relative to the incident X-ray beam on the (211) plane.

When a material is stressed, the interplanar spacing changes depending on the direction of measurement. By collecting diffraction data at multiple ψ tilt angles, the change in lattice spacing can be plotted as d_{hkl} versus $\sin^2\psi$.

From the slope of this plot, the residual stress (σ (GPa)) is calculated using the general relationship:[19]

$$\sigma = \frac{E}{1+\nu}m \quad (\text{Equation 3.14})$$

where:

E is the Young's modulus, ν is the Poisson's ratio, and m is the slope of the d_{hkl} vs $\sin^2\psi$ curve. A positive slope indicates tensile stress, whereas a negative slope indicates compressive stress.

3.7.4. Rutherford Backscattering Spectrometry / Elastic Recoil Detection (RBS/ERDA)

Beam analysis (BA) was carried out by the technician at the Laboratory of Ion Beam Physics, ETH Zurich, using Rutherford Backscattering Spectrometry (RBS) and heavy-ion Elastic Recoil Detection Analysis (HI-ERDA) to determine the elemental composition of samples in particular to determine the depth profile of light elements such as hydrogen, oxygen and carbon. For the RBS measurements, a 2 MeV ^4He ion beam was employed, and the backscattered particles were detected with a Si PIN diode positioned at a scattering angle of 167.5° . For the ERDA measurements, a 13 MeV ^{127}I ion beam was used, with recoil ions detected at a scattering angle of 36° . The ERDA spectra were analyzed using the Potku software [20], and elemental depth profiles were obtained.

Depth profiles of ERDA have been established for H, C, N, O, and W in the case of W-coated X60 steel across three series: S1, S2, and S3. However, the process of analyzing heavy elements such as tungsten presents challenges, making precise quantitative analysis difficult. The data provided should therefore be regarded as semi-quantitative. In the case of the X60 steel samples, depth profiles have been obtained for H, C, O, and Fe.

3.7.5. Scanning Electron Microscopy/Energy Dispersive X-ray Spectroscopy (SEM /EDS) and metallographic characterization

Scanning Electron Microscopy (SEM) combined with Energy Dispersive X-ray Spectroscopy (EDS) was employed to investigate the microstructure and composition of the samples. SEM micrographs provided detailed images of the coating's surface morphology as well as cross-sectional views, enabling direct measurement of the coating thickness. Scanning electron microscopy investigations were carried out on three sample series and the X60 steel: Series 1 (R_a 0.4 μm), Series 2 (R_a 0.2 μm), and Series 3 (R_a 0.2 μm). The SEM analysis of Series 1 was performed using a ESEM: FEI Quanta 200 at CeSAR, CeSAR (Centro Servizi d'Ateneo per la Ricerca) of the University of Cagliari using a 30 kV electron beam voltage in the secondary electron mode. The SEM measurements of Serie 2 and Serie 3, SEM cross section analysis of S1, S2 and S3 and the metallographic examinations of X60 steel were performed in the cross-section of X60 steel after etching with 2% Nital solution for 5 seconds were conducted at the advanced metallography laboratory at RINA Consulting CSM S.p.A. , Castel Romano, Rome by SEM Zeiss EVO M 15 using a 15 - 20 kV electron beam voltage in the backscattered electron mode.

References

- [1] R. Hannachi, D. Biggio, B. Elsener, M. Fantauzzi, and A. Rossi, "X-ray photoelectron spectroscopy investigation of X60 steel," *Surf. Sci. Spectra*, vol. 31, no. 2, p. 024014, Nov. 2024, doi: 10.1116/6.0003972.
- [2] R. Hannachi, D. Biggio, B. Elsener, M. Fantauzzi, N. Zacchetti, and A. Rossi, "A Contribution of XPS and Electrochemistry to the Understanding of Hydrogen Diffusion in X60 Steel," *Coatings*, vol. 15, no. 4, p. 442, Apr. 2025, doi: 10.3390/coatings15040442.
- [3] R. Hannachi, D. Biggio, B. Elsener, M. Fantauzzi, N. Zacchetti, and A. Rossi, "A Surface Analytical Method for Determining the Porosity of Tungsten Coatings as Hydrogen Permeation Barriers," *Surface and Interface Analysis*, vol. 58, no. 1, pp. 3–8, 2026, doi: 10.1002/sia.70027.
- [4] "API 5L X60 Pipe Specifications (PSL1 & PSL2).
- [5] M. a. V. Devanathan, Z. Stachurski, and F. C. Tompkins, "The adsorption and diffusion of electrolytic hydrogen in palladium," *Proceedings of the Royal Society of London. Series A. Mathematical and Physical Sciences*, vol. 270, no. 1340, pp. 90–102, Jan. 1997, doi: 10.1098/rspa.1962.0205.
- [6] T. Zakroczymski, "Adaptation of the electrochemical permeation technique for studying entry, transport and trapping of hydrogen in metals," *Electrochimica Acta*, vol. 51, no. 11, pp. 2261–2266, Feb. 2006, doi: 10.1016/j.electacta.2005.02.151.

- [7] E. Koren, C. M. H. Hagen, D. Wang, X. Lu, R. Johnsen, and J. Yamabe, “Experimental comparison of gaseous and electrochemical hydrogen charging in X65 pipeline steel using the permeation technique,” *Corrosion Science*, vol. 215, p. 111025, May 2023, doi: 10.1016/j.corsci.2023.111025.
- [8] E. Van den Eeckhout, I. De Baere, T. Depover, and K. Verbeken, “The effect of a constant tensile load on the hydrogen diffusivity in dual phase steel by electrochemical permeation experiments,” *Materials Science and Engineering: A*, vol. 773, p. 138872, Jan. 2020, doi: 10.1016/j.msea.2019.138872.
- [9] V. Nemanič, J. Kovač, C. Lungu, C. Porosnicu, and B. Zajec, “Characterization of tungsten films and their hydrogen permeability,” *Journal of Vacuum Science & Technology A: Vacuum, Surfaces, and Films*, vol. 32, no. 6, p. 061511, 2014, doi: 10.1116/1.4898061.
- [10] Jürgensen, J.; Pohl, M. Local Hydrogen Measurements in Multi-Phase Steel C60E by Means of Electrochemical Microcapillary Cell Technique. *Metals* **2023**, *13*, 1585. <https://doi.org/10.3390/met13091585>
- [11] “ISO 15472:2010,” ISO. Accessed: Feb. 02, 2026. [Online]. Available: <https://www.iso.org/standard/55796.html>
- [12] Fairley, N., Fernandez, V., Richard-Plouet, M., Guillot-Deudon, C., Walton, J., Smith, E., ... & Baltrusaitis, J. (2021). Systematic and collaborative approach to problem solving using X-ray photoelectron spectroscopy. *Applied Surface Science Advances*, *5*, 100112..
- [13] A. Rossi and B. Eisener, “XPS analysis of passive films on the amorphous alloy Fe₇₀Cr₁₀P₁₃C₇: Effect of the applied potential,” *Surface & Interface Analysis*, vol. 18, no. 7, pp. 499–504, Jul. 1992, doi: 10.1002/sia.740180708.
- [14] D. Biggio, B. Eisener, G. Usai, M. Fantauzzi, and A. Rossi, “Surface Chemistry of Passive Films on Ni-Free Stainless Steel: The Effect of Organic Components in Artificial Saliva,” *Langmuir*, vol. 40, no. 13, pp. 6824–6833, Apr. 2024, doi: 10.1021/acs.langmuir.3c03728.
- [15] “Products:XPS/PHI Quantes 1 ULVAC-PHI, Inc.” Accessed: Feb. 02, 2026. [Online]. Available: <https://www.ulvac-phi.com/en/products/xps/quantest/#01>
- [16] “ISO 18115-1:2023
- [17] “ISO 15472:2010,” ISO. Accessed: Feb. 02, 2026. [Online]. Available: <https://www.iso.org/standard/55796.html>
- [18] S. Devesa, A. P. Rooney, M. P. Graça, D. Cooper, and L. C. Costa, “Williamson-hall analysis in estimation of crystallite size and lattice strain in Bi_{1.34}Fe_{0.66}Nb_{1.34}O_{6.35} prepared by the sol-gel method,” *Materials Science and Engineering: B*, vol. 263, p. 114830, Jan. 2021, doi: 10.1016/j.mseb.2020.114830.
- [19] “Lorenzin, G., Jeurgens, L. P., & Cancellieri, C. (2022). Stress tuning in sputter-grown Cu and W films for Cu/W nanomultilayer design. *Journal of Applied Physics*, *131*(22).

[20] “,<https://www.jyu.fi/science/en/physics/research/infrastructures/accelerator-laboratory/pelletron/potku/potku-analysis-software-for-tof-erda>

4. Results

This chapter presents the results obtained from experimental investigations. To achieve a multi-scale evaluation, an unprecedented combination of advanced analytical techniques was employed. These include highly surface-sensitive methods (XPS, HAXPES), localized and near-surface probes (SEM/EDS, microcapillary cell technique, RBS/ERDA), and bulk characterization approaches (XRF, XRD, hydrogen quantification by inert gas fusion analysis, hydrogen permeation testing). Table 4.1 summarizes the scope and spatial sensitivity of each technique utilized in this work.

Table 4.2. Overview of the technique used in this study

Techniques	Type / Region Probed
X-ray Photoelectron Spectroscopy (XPS)	Surface (nanometers)
Hard X-ray Photoelectron Spectroscopy (HAXPES)	Near-surface (tens of nanometers)
SEM-EDS	Surface / Near-surface (micrometers)
Microcapillary cell technique	Localized (surface / near-surface)
Rutherford Backscattering Spectrometry (RBS) / Elastic Recoil Detection Analysis (ERDA)	Near-surface to bulk (depth profile)
X-ray Fluorescence (XRF)	Bulk
Inert gas fusion analysis	Bulk
X-ray Diffraction (XRD)	Bulk / Phase analysis
Hydrogen permeation test	Bulk transport properties
Local hydrogen measurement (microcapillary)	Localized (surface / near-surface)

The results presented in this chapter were elaborated by me, under the supervision and with the support of Prof. Antonella Rossi, Prof. Marzia Fantauzzi, Prof. Bernhard Elsener, Dr. Nicoletta Zacchetti, and Dr. Deborah Biggio. The RBS/ERDA results were processed and interpreted by Dr. Arnold Müller, while the XRD data, acquired by Dr. Claudia Cancellieri, were processed and interpreted by me under her supervision.

The majority of this chapter is taken from my papers:

- 1) Hannachi, R.; Biggio, D.; Elsener, B.; Fantauzzi, M.; Zacchetti, N.; Rossi, A. A Contribution of XPS and Electrochemistry to the Understanding of Hydrogen Diffusion in X60 Steel. *Coatings* **2025**, *15*, 442. <https://doi.org/10.3390/coatings15040442>
- 2) R.Hannachi,D.Biggio,B.Elsener,M.Fantauzzi,N.Zacchetti, and A.Rossi, “A Surface Analytical Method for Determining the Porosity of Tungsten Coatings as Hydrogen Permeation Barriers,” *Surface and Interface Analysis*58, no. 1 (2026): 3–8, <https://doi.org/10.1002/sia.70027>.

The co-authors all participated in discussions, interpretation of data and editing of these papers.

4.1. Diffusion of hydrogen in X60 steel

4.1.1. Sample characterization before hydrogen permeation test

To achieve a comprehensive understanding of hydrogen behavior in X60 steel substrate an array of complementary analytical techniques was employed, each providing unique information regarding surface, near-surface, localized, and bulk properties. The techniques include X-ray Photoelectron Spectroscopy (XPS), Hard X-ray Photoelectron Spectroscopy (HAXPES), Scanning Electron Microscopy with Energy Dispersive Spectroscopy (SEM/EDS), Rutherford Backscattering Spectrometry (RBS), Elastic Recoil Detection Analysis (ERDA), X-ray Fluorescence (XRF), X-ray Diffraction (XRD), Hydrogen Analysis by Inert Gas Fusion, hydrogen permeation testing (Devanathan and Stachurski cell), the microcapillary cell method.

4.1.1.1. X-ray fluorescence (XRF)

X-ray fluorescence (XRF) analysis was performed to determine the elemental composition of the samples, with the resulting data summarized in Table 4.3. Elements that were not detected in the spectra are either absent from the sample matrix or present at concentrations below the instrumental limit of detection (LOD). For most transition metals and heavier elements, the LOD typically ranges from a few parts per million (ppm) to several tens of ppm under standard measurement conditions. In contrast, lighter elements generally exhibit higher detection limits due to their lower fluorescence yields and increased absorption by the sample matrix and detector window. Consequently, the absence of light elements in the acquired data indicates that their concentrations fall below the analytical sensitivity of the XRF instrumentation employed in this study.

Table 4.3. Elemental composition of X60 steel determined by portable X-ray fluorescence spectroscopy; the average wt% calculated on the results obtained on three samples is provided and the standard deviations are given in parentheses.

	Fe	Mn	Cr	Mo	Ni	Cu
wt.%	98.2 (0.1)	1.2 (0.04)	0.20 (0.02)	0.10 (0.01)	0.10 (0.01)	0.10 (0.01)

4.1.1.2. Scanning electron microscopy-Energy dispersive X ray spectroscopy (SEM-EDS)

Scanning electron microscopy coupled with energy dispersive X-ray spectroscopy (SEM-EDS) enables precise elemental analysis of localized microstructural regions, thereby providing detailed compositional information at the microscopic scale. This technique confirms the presence and distribution of elements such as Fe, Mn, Cr, and Si within localized areas (Figure 4.1, Table 4.5). In Figure 4.1, the regions selected on the SEM micrograph for elemental analysis are shown. The image was acquired at a magnification of 100x. Table 4.4 reports the chemical composition (in wt%) obtained from six marked areas, together with corresponding mean values and standard deviations.

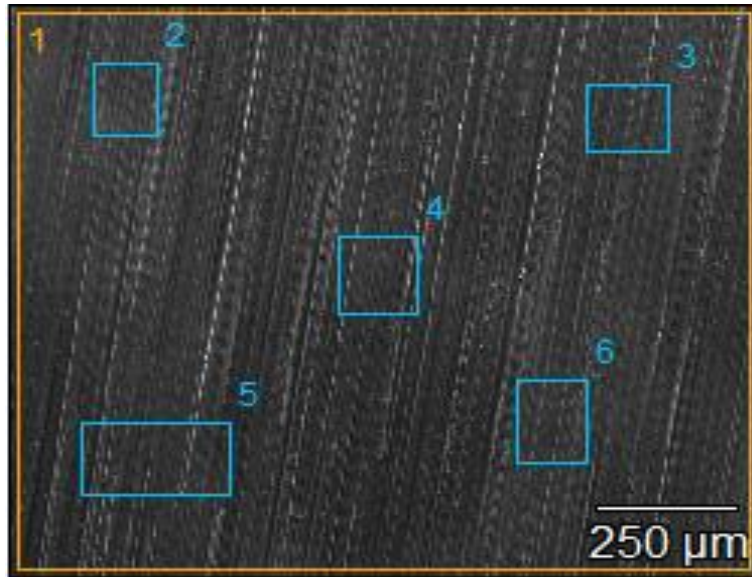


Figure 4.1. SEM micrograph of X60 steel

Table 4.5. Elemental composition (wt.%) obtained by SEM-EDS analysis in six different areas on the sample surface (Figure 4.1).

Wt.%		Fe	Mn	Cr	Si
1		97.9	1.6	0.2	0.3
2		97.7	1.5	0.3	0.4
3		98.3	1.4	0.3	0
4		98.1	1.5	0	0.4
5		98.1	1.5	0	0.4
6		98.2	1.5	0.3	0
Mean value (st. dev.)		98.0 (0.2)	1.5 (0.1)	0.2 (0.2)	0.3 (0.2)

The chemical composition determined by EDS analyses indicates that the investigated alloy is predominantly iron, with an average Fe content of 98.0 wt%, and minor constituents including Mn (1.5 wt%), and Cr (0.20wt.%). Mo, Ni, and Cu that were quantified by XRF, were not detected by SEM-EDS, likely due to their low abundance and the spatial resolution limits of the technique. On the contrary, Si were not identified by p-XRF, due to the low sensitivity of the technique to light elements under the adopted experimental conditions. Collectively, these complementary results confirm that the material consists primarily of iron, with minor amounts of alloying elements.

4.1.1.3 X-ray diffraction (XRD)

The XRD pattern (Figure 4.2) of X60 steel exhibits distinct diffraction peaks at 2θ values of 44.66° , 64.80° , and 82.3° , corresponding to the planes (110), (200), and (121), respectively. The presence of these peaks confirms that the steel has a body-centered cubic (BCC) structure, as indicated on the ICSD 14754 card. Additionally, the peak intensity and sharpness indicate a polycrystalline structure.

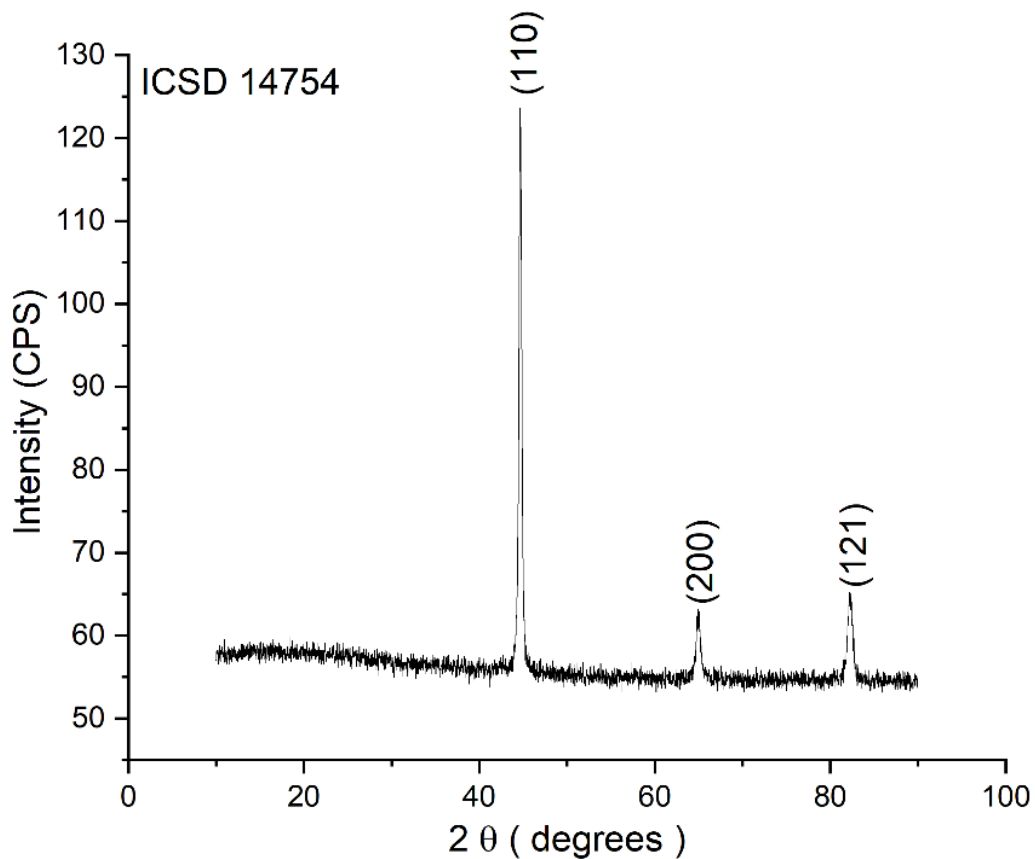


Figure 4.2. XRD pattern of X60 steel

4.1.1.4. X-ray photoelectron spectroscopy (XPS)

The XPS is used to provide information on the surface composition of X60 steel, the chemical state of iron, the thickness of the oxide layer, and the hydrocarbon contamination layer after various sample preparation and heat treatment procedures, including 15 hours at 80°C.

The XPS survey spectrum of the X60 steel following the cleaning procedure under different conditions: cleaned with various solvents (C), heated cleaned (HC), mechanically polished (MP), and heated MP (H MP) shown in Figure 4.3 indicates that iron (Fe) is the primary element present. The signals assigned to oxygen (O) and carbon (C) are likely due to surface oxidation and contamination of the steel's outer layer. The presence of these elements is due to the exposure of the sample surface to the laboratory environment after cleaning, heating, and transferring it to the spectrometer. A detailed description of the samples prior to XPS analysis is given in the experimental chapter three, section 3.2.1

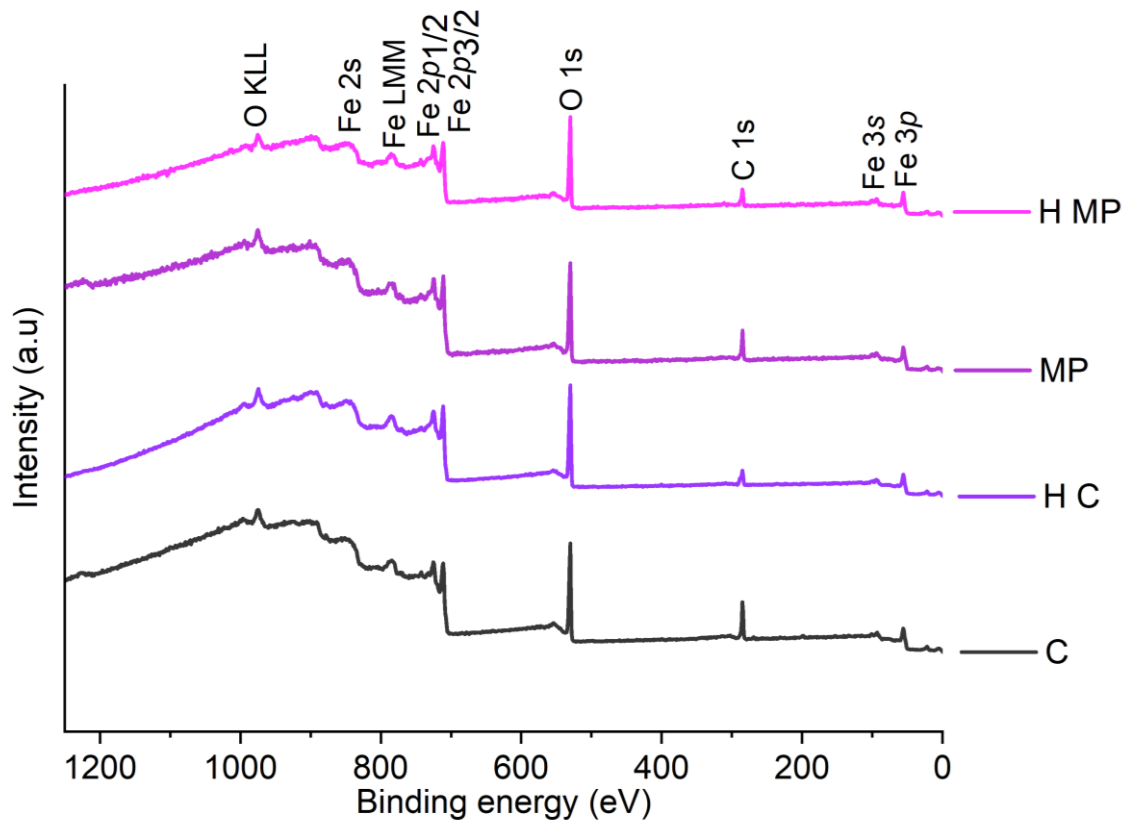


Figure 4.3. The survey spectra for X60 steel following the cleaning procedure under different conditions: cleaned with various solvents (C), heated cleaned (HC), mechanically polished (MP), and heated MP (H MP).

Processing of the high-resolution spectra, as shown in Figure 4.4, for H C and H MP X60 steel, allowed us to distinguish the contributions due to various chemical states of the same element. The curve-fitting parameters for the O 1s and Fe 2p signals are listed in Table 4.6. The Fe 2p_{3/2} peak of both H C X60 steel and H MP X60 steel (Figure 4.4.a and Figure 4.4.b) was fitted according to the literature[5], identifying four distinct components. The peak energy for metallic iron (Fe (0)) was measured at 706.8 (0.1) eV in both the cleaned and MP X60 steel samples, and at 707.0 (0.1) eV in the heated cleaned and heated MP X60 steel samples. The Fe (II) oxide (FeO) component was detected at 709.4 (0.1) eV, with its satellite at 714.9 (0.1) eV. The Fe (III) oxide (Fe₂O₃) peak appeared at 710.6 (0.1) eV, while Fe (III) oxyhydroxides (FeOOH) was identified at a peak energy of 712.5 (0.1) eV[5]. The peak energies are presented in Table 4.7.

The O 1s high-resolution spectra following the fitting procedure showed four components (Figure 4.4.b, Figure 4.4.d); the peak energies of the components are at 530.1 (0.1) eV, 531.4 (0.1), 532.2 (0.1) eV, and 533.5 (0.1) eV, and they are assigned to oxygen present in the iron oxides, hydroxides, adsorbed water, and organic contamination, respectively.[6] The results are summarized in Table 4.7.

Table 4.6. Fitting parameters used for O 1s and Fe 2p_{3/2} high-resolution spectra of X60 steel. Standard deviations are in parentheses. The Fe 2p_{3/2} was fitted according to the literature [5] ,

	FWHM (eV)	Line Shape	Position Constraint (eV)	FWHM Constraint (eV)	Area Constraint
O 1s – Oxide	1.35 (0.04)	GL (40)	—		—
O 1s – Hydroxide	1.35 (0.04)	GL (40)	—	O 1s-oxide*1	—
O 1s – Water	1.35 (0.04)	GL (40)	—	O 1s-oxide*1	—
O 1s – Organic contamination	1.35 (0.04)	GL (40)	—	O 1s-oxide*1	—
Fe 2p _{3/2} – Fe (0)	1.18 (0.03)	GL (85)T(0.8)	707–706	1-1.2	—
Fe 2p _{3/2} – FeO	2.56 (0.04)	GL (30)	709.7–709.3	2.4–2.6	—
Fe 2p _{3/2} – FeO sat	2.56 (0.04)	GL (30)	Fe 2p _{3/2} – FeO +5.5	2.4–2.6	Fe 2p _{3/2} *0.08
Fe 2p _{3/2} – Fe ₂ O ₃	2.47 (0.06)	GL (30)	—	2.4-2.6	1–4
Fe 2p _{3/2} – Fe (III)-OOH	3.02 (0.08)	GL (30)	—	1 - 4	—

Table 4.7. Peak energy values (eV) of O 1s, Fe 2p_{3/2} are reported as mean values the standard deviations are given in parentheses.

		C X60 Steel (eV)	Heated C X60 Steel (eV)	MP X60 Steel (eV)	Heated MP X60 Steel (eV)
O 1s	Iron oxide	530.1 (0.1)	530.2 (0.1)	530.1 (0.1)	530.2 (0.1)
O 1s	Iron hydroxide	531.4 (0.1)	531.4 (0.1)	531.4 (0.1)	531.5 (0.1)
O 1s	Adsorbed water	532.2 (0.2)	532.2 (0.1)	532.2 (0.1)	532.3 (0.1)
O 1s	Organic contamination	533.5 (0.1)	533.4 (0.1)	533.5 (0.1)	533.5 (0.1)
Fe 2p _{3/2}	Fe (0)	706.8 (0.1)	707.0 (0.1)	706.8 (0.1)	707.0 (0.1)
Fe 2p _{3/2}	FeO	709.4 (0.1)	709.4 (0.2)	709.3 (0.1)	709.4 (0.1)
Fe 2p _{3/2}	FeO sat	714.9 (0.1)	714.9 (0.2)	714.8 (0.1)	714.9 (0.1)
Fe 2p _{3/2}	Fe ₂ O ₃	710.6 (0.1)	710.7 (0.1)	710.6 (0.1)	710.6 (0.1)
Fe 2p _{3/2}	Fe(III)-OOH	712.5 (0.1)	712.6 (0.1)	712.5 (0.1)	712.4 (0.1)

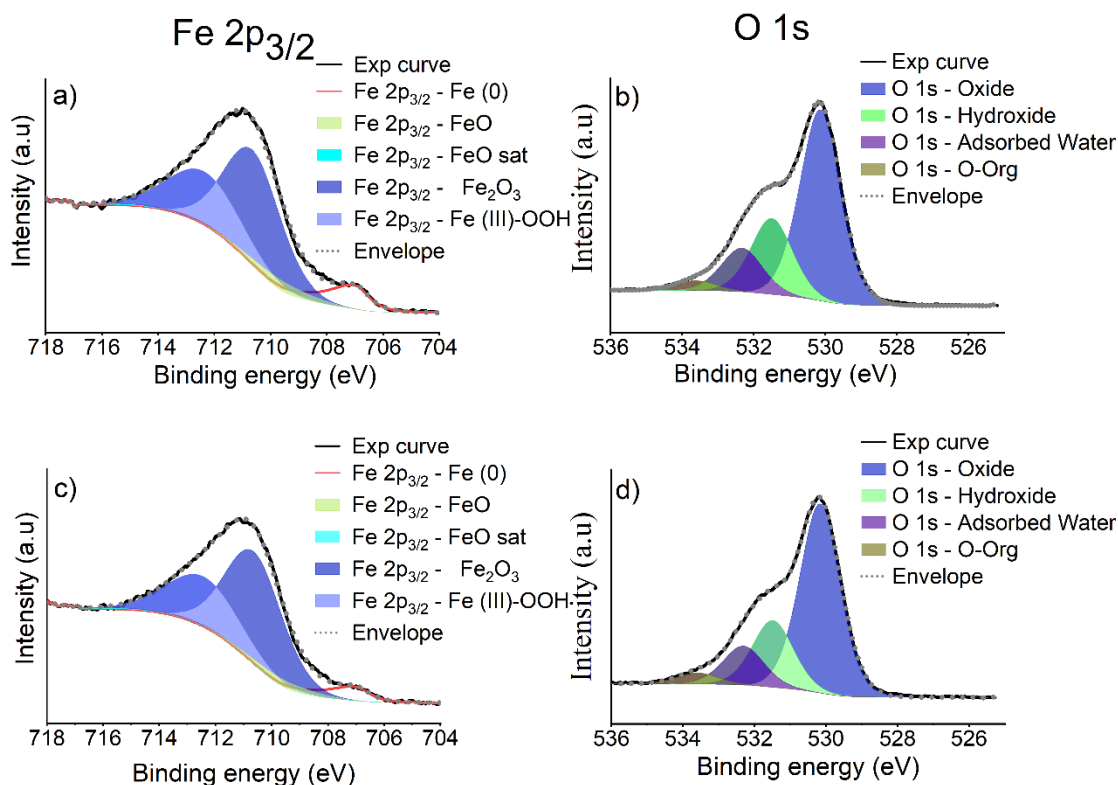


Figure 4.4. High-resolution spectra of Fe 2p_{3/2} and O 1s for HC (a, b) and H MP (c, d) X60 steel.

The composition of the surface layer was determined by considering the oxidized iron species; the results are presented in Table 4.8.

The application of the three-layer model (see experimental section 3.6.1) enabled the estimation of the contamination layer thickness (l_c) and the oxide layer thickness (t), as presented in the bar chart in Figure 4.5.

Upon heating, the FeO content exhibits a significant reduction in both C X60 steel and MP X60 steels, decreasing from approximately 5% to less than 1%. Conversely, the relative atom percentage of Fe₂O₃ and FeOOH remain largely unchanged.

Table 4.8. Atomic percentages of FeO, Fe₂O₃, and FeOOH following the various X60 steel samples conditions.

Atomic %	C X60 steel	Heated C X60 steel	MP X60 steel	Heated MP X60 steel
FeO	5 (2)	0.5 (0.7)	4 (3)	0.9 (0.9)
Fe ₂ O ₃	60 (2)	64 (3)	62 (2)	64 (2)
FeOOH	35 (3)	36 (3)	34 (3)	35 (2)

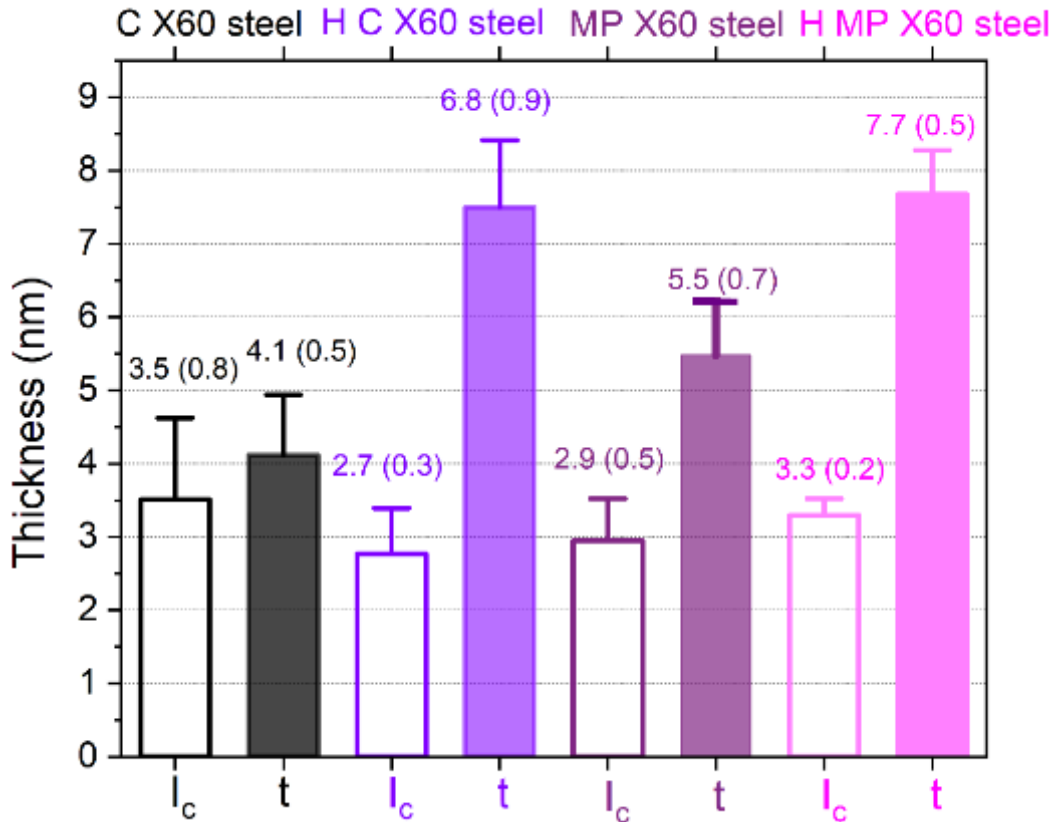


Figure 4.5. Bar chart illustrates the thicknesses of the contamination layer (l_c) and oxide layer (t), as determined by the three-layer model, for the steels' surfaces labeled as Cleaned, MP, H CX60, and H MP X60.

4.1.1.5 Rutherford Backscattering spectrometry/Elastic recoil detection (RBS/ERDA)

Compositional depth profiles of the X60 carbon steel surface were obtained by Rutherford Backscattering Spectrometry (RBS) and Elastic Recoil Detection Analysis (ERDA), with a representative profile presented in Figure 4.6. X60 steel, a low-alloy carbon steel extensively utilized in pipeline applications, is characterized by a high iron content and minor concentrations of carbon, manganese, and other alloying elements that impact its mechanical properties and corrosion resistance. The depth distribution of hydrogen, carbon, oxygen, aluminum, and iron within the near-surface region reveals pronounced compositional gradients. Iron dominates the bulk, while oxygen displays a distinct near-surface enrichment. The concentrations of hydrogen, carbon, and aluminum remain minimal across the entire profile. The RBS/ERDA data indicate that the near-surface region contains a thin oxidized layer enriched in oxygen, as evidenced by a sharp surface-near O peak. The average elemental weight percentages for the regions delineated by the red and blue dashed lines in the depth profile are presented in Table 4.9, beyond this region, iron content rises rapidly to approximately 98.7 wt% and remains stable throughout most of the analyzed depth. Small amounts of hydrogen (0.010 wt%) is detected, the amount of carbon is found to be 0.25 wt%, while aluminum is present at 0.28 wt%; all exhibit low and only slightly varying concentrations with depth. Oxygen content is slightly higher at 0.73 wt%, consistent with the presence of a surface oxide layer.

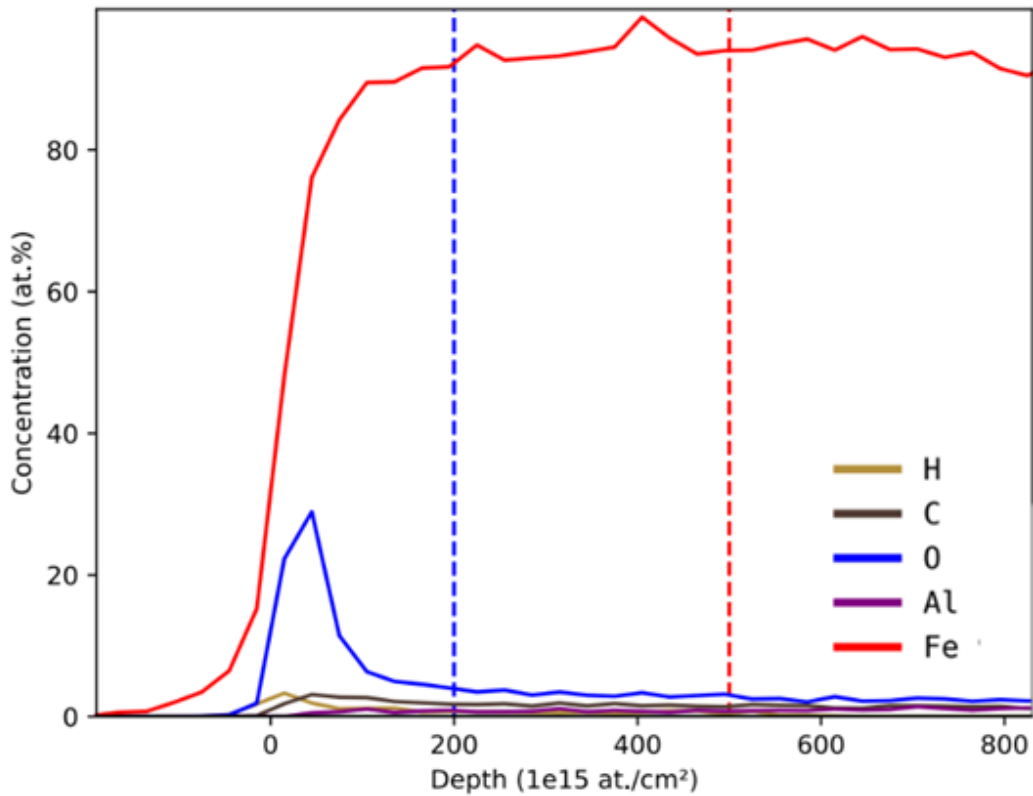


Figure 4.6: composition - depth profiles measured by RBS/ERDA for the X60 steel mechanically polished X60 steel MP. The average elemental composition was determined over the depth range indicated by the blue and red dashed lines.

Table 4.9. The average elemental composition of X60 steel MP was determined over the depth range indicated by the blue and red dashed lines.

	Fe	H	C	O	Al
wt%	98.70 ± 0.01	0.010 ± 0.001	0.25 ± 0.01	0.73 ± 0.01	0.28 ± 0.01

4.1.2 Electrochemical hydrogen permeation results (HPT)

To prepare the steel surface for electrochemical hydrogen measurements, the detection cell was filled with 0.1 M NaOH solution. H C and H MP X60 steel samples were immersed in the electrolyte, and their open circuit potential (OCP) was monitored for one hour to assess surface conditioning. Figure 4.7 show the OCP vs time plot for both surface preparations. Immediately after immersion, the potential is around -270 mV vs Ag/AgCl and increases to about -220 mV vs Ag/AgCl after one hour. The results obtained on H MP X 60 steel are highly reproducible (Figure 4.7.b). The HC X60 sample achieved a slightly higher final OCP compared to MP X60, indicating that heat cleaning produces a more uniform and protective passive film. These results demonstrate that surface preparation has a significant influence on the electrochemical behavior of X60 steel in alkaline media.

After exposure at the OCP, the steels undergo anodic passivation at a potential of +0.3 V versus OCP. This process aims to reduce surface condition variability, prevent oxidation of the specimens, and improve hydrogen atom oxidation efficiency for more consistent data[7]. The passivation current decreases following a power law, reaching values below $0.5 \mu\text{A}$, which is less than $0.1 \mu\text{A}/\text{cm}^2$.

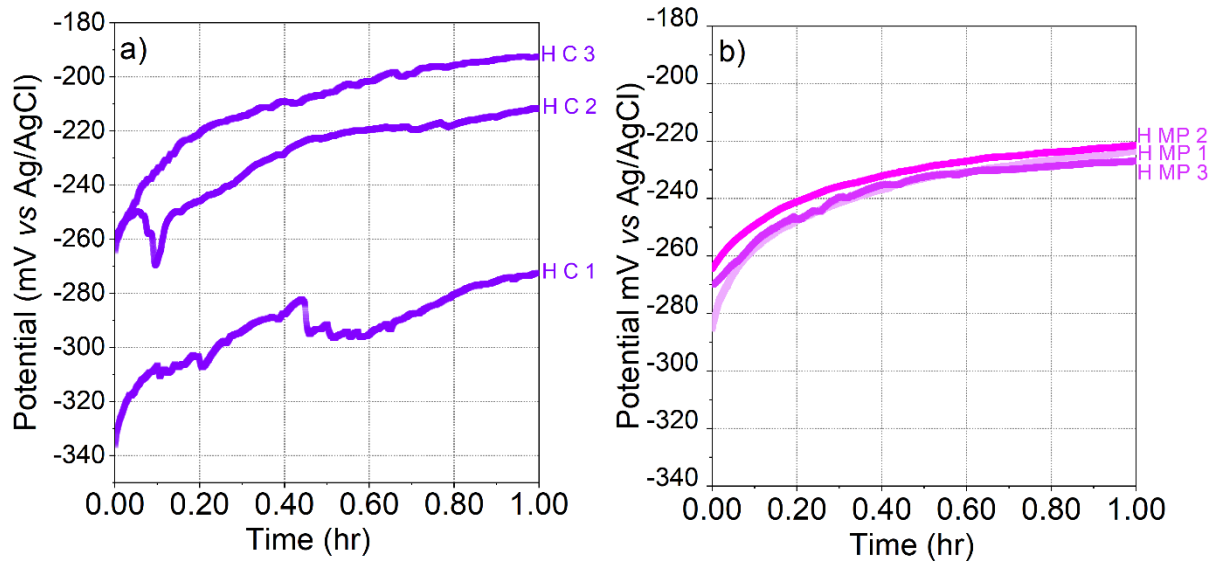


Figure 4.7. Open circuit potential (mV vs. Ag/AgCl) over time for hydrogen permeation, showing a) H C X60 steel (heated cleaned X60 steel), and b) H MP X60 steel (heated, mechanically polished X60 steel).

The production cell was filled with a 0.1 M HCl solution containing 0.2 g/kg of As_2O_3 . Arsenic oxide inhibits the recombination of hydrogen and promotes the formation of hydrogen atoms[8]. The samples were exposed to this solution for 5 minutes, during which the OCP was measured. Afterwards, cathodic hydrogen production was started with a current of -6 mA . The measured OCP values of H C X60 and H MP X60 steel were $-415 (10) \text{ mV vs. Ag/AgCl}$. During cathodic polarization at -6 mA , the potential was $-996 (4) \text{ mV vs. Ag/AgCl}$ for H C X60 steel and $-1067 (83) \text{ mV vs. Ag/AgCl}$ for H MP X60 steel.

Figure 4.8 shows the experimental hydrogen permeation curves as current versus time for both the H C X60 steel and the H MP steel. After the start of hydrogen production, the current initially remained very low (at the passivation current $< 1 \mu\text{A}$); subsequently, it rapidly increased during the build-up phase and reached a nearly steady-state value.

The hydrogen permeation curves from the H C X60 steel samples (Figure 4.8.a) showed consistent results. The hydrogen oxidation current begins to rise, with steady-state current (i_{ss}) values of $29.4 \mu\text{A}$, $35.7 \mu\text{A}$, and $41.8 \mu\text{A}$, for H C 1, H C 2 and H C 3 respectively. Similarly, the curves for three H MP X60 steel samples (Figure 4.8.b) showed similar patterns during both buildup and decay phases. The i_{ss} values of $29.0 \mu\text{A}$, $57.9 \mu\text{A}$, and $35.0 \mu\text{A}$ for H MP 1, H MP 2, and H MP 3, respectively.

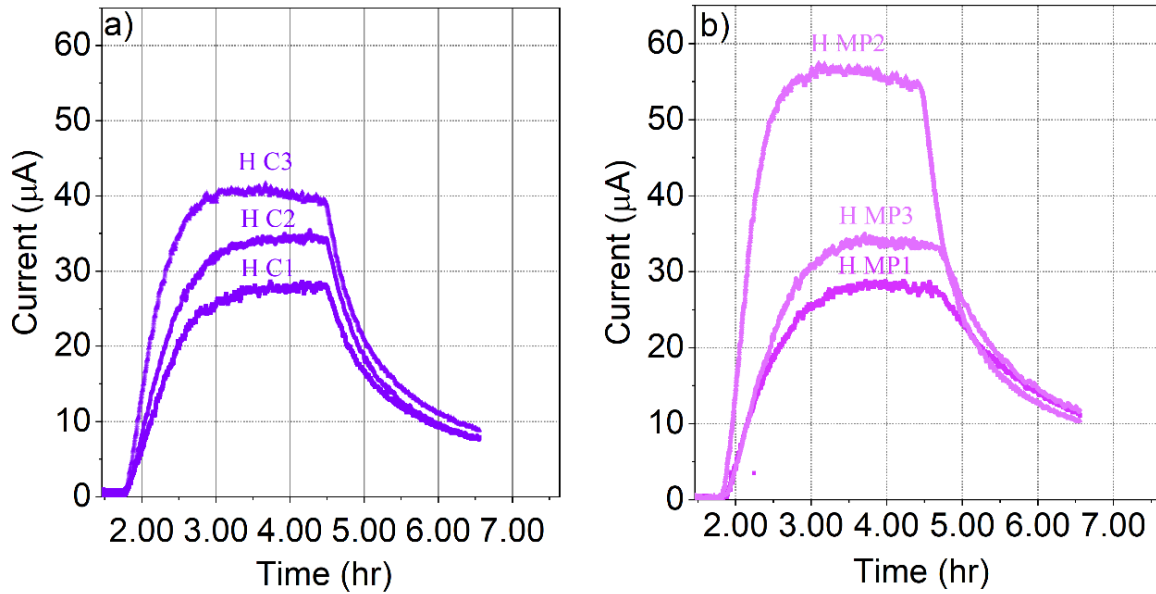


Figure 4.8. Hydrogen permeation curves for a) H C X60 steel and b) H MP X60 steel.

The hydrogen diffusion coefficient was calculated using the time lag t_{lag} (Equation 3.1) and breakthrough t_b (Equation 3.2) methods applied to the build-up region of the hydrogen permeation curve. The results are summarized in Table 4.10.

Table 4.10. Effective diffusion coefficients (D_{eff}) of H C X60 and H MP X60 steels. The results are given as average values calculated over three independent measurements and the standard deviations are reported in parentheses.

Material	$(D_{eff-tlag} (\times 10^{-10} \text{ m}^2/\text{s}))$	$(D_{eff-tb} (\times 10^{-10} \text{ m}^2/\text{s}))$
H C X60 steel	2.4 (0.4)	2.8 (0.2)
H MP X60 steel	2.0 (0.4)	2.9 (0.5)

No significant differences were observed either in the effective diffusion coefficients of H C X60 steel and H MP X60 steel, nor between the two methods.

An alternative approach for evaluating hydrogen diffusion involves fitting the permeation current curve using the analytical solution of Fick's second law, also known as the build-up equation (Equation 3.3). In Figure 4.9.a and Figure 4.9.b the permeation buildup transient for H C X60 and H MP X60 samples is shown ; the effective diffusion coefficient for H C X60 steel was determined to be $2.9 (0.9) \times 10^{-10} \text{ m}^2/\text{s}$, whereas for H MP X60 steel, it was $2.8 (0.6) \times 10^{-10} \text{ m}^2/\text{s}$.

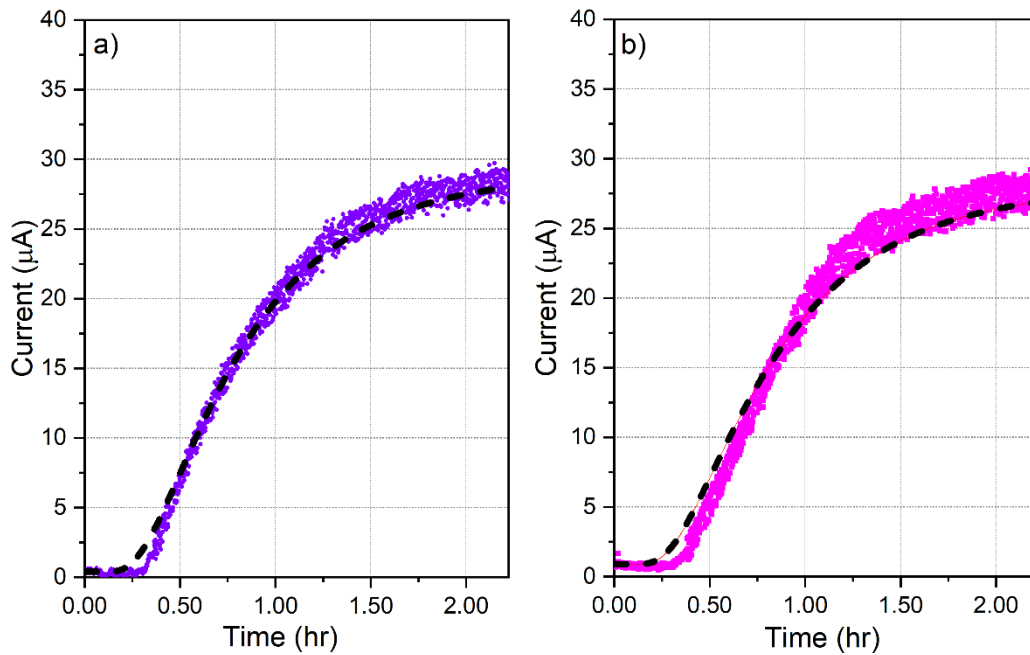


Figure 4.9. Permeation buildup transient for a) H C X60 steel and b) H MP X60 steel vs model fit (black dashed)

These findings are in close agreement with values derived from both the t_{lag} and t_b methods, underscoring the consistency of the diffusion measurements across various analytical methods. The consistency of results confirms the validity of the experimental procedures.

In addition to the hydrogen diffusion coefficient, the hydrogen sub-surface concentration on the production side of the sample can be determined using Equation 3.5. The subsurface concentration is slightly higher in the H MP steel (0.8 (0.1) ppm) compared to the H C X60 steel (0.66 (0.02) ppm).

To quantify the amount of hydrogen trapped within the steel microstructure, the Zakrocynski approach (chapter three section 3.3.2) was employed by analyzing the decay region of the hydrogen permeation curve (Figure 4.9). The quantity of trapped hydrogen (q_{Ht}) was estimated to be $8 (2) \times 10^{-8}$ mol H/cm² for HC X60 steel and $8 (6) \times 10^{-8}$ mol H/cm² for H MP X60 steel.

The reproduced curve was obtained using the decay equation (Equation 3.4) by fixing all the parameters at $I_p^0 = I_{ss}$, and $I_p^\infty = 0$, while fixing the diffusion coefficient D as the diffusion coefficient of the mobile hydrogen ($D_{eff\ mH}$) also called D_L that was determined experimentally by first charging the sample at cathodic current density i_c , where $i_c = -0.5$ mA/cm², then at $i_c = -1$ mA/cm² and is found to be equal to $1.1 \pm 0.2 \times 10^{-9}$ m²/s, thus higher than the effective diffusion coefficients (Table 4.10)

4.1.3 Sample characterization after the hydrogen permeation test

4.1.3.1. Local Hydrogen Measurements: Microcapillary cell technique

The following results show the local hydrogen concentration determined by using the microcapillary cell technique. This method allows us to estimate the absorbed hydrogen concentration in steel within localized areas.

The local hydrogen measurements are presented in Figure 4.10 for uncharged and hydrogen-charged X60 steel across three points. The oxidation current of the uncharged samples are due to passivation of the sample surface during anodic polarization. These values are the “background current” that has to be subtracted and show good reproducibility. The hydrogen concentration of the charged X60 steel was measured at three points. Point 1 was measured after 5 minutes of hydrogen charging, point 2 after 30 minutes and Point 3 after 1 hour and 7 minutes of charging. These measurements show a higher oxidation current attributable to the presence of absorbed hydrogen. The three points show different hydrogen oxidation currents, The diffusion pathways of hydrogen or the increase of the oxidation current at point 2 and point 3 could be attributed to crevice corrosion.

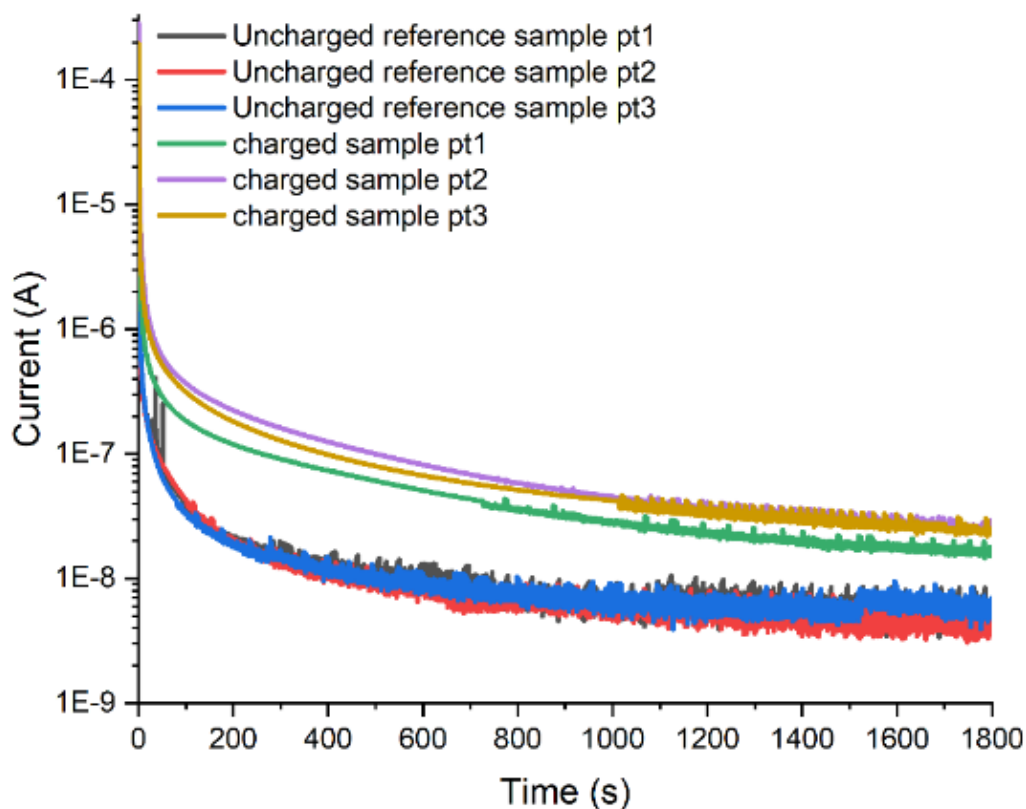


Figure 4.11. Microcapillary results measurements on X60 steel.

The hydrogen concentration was calculated based on the electric charge conversion, following Faraday's second law as described in the chapter three, section 3.4. The results are shown in the Table 4.11:

Table 4.11. Hydrogen concentration CH (ppm) on charged X60 steel, determined on three different points: pt1, pt2 and pt3. These measurements were performed in only three points in one sample.

	Charged X60 steel pt1	Charged X60 steel pt2	Charged X60 steel pt3
C _H (ppm)	0.2	0.4	0.3

The local hydrogen measurements performed using the microcapillary cell technique demonstrated a non-uniform distribution of the hydrogen concentration of diffusible hydrogen across the surface of charged X60 steel. which are 0.2 ppm 0.4 ppm and 0.3 ppm for pt1, pt2 and pt3 respectively.

4.1.3.2. Hydrogen Analysis by Inert Gas Fusion.

The purpose of this analysis is to determine the hydrogen content in X60 steel using the inert gas fusion method. The technique is described in chapter three, section 3.5.

The results are presented in Table 4.12.

Table 4.12. Hydrogen Content in X60 Steel Samples Determined by Inert Gas Fusion

X60 Steel Samples	Mass (g)	Measured Hydrogen Content (ppm)
Uncharged reference X60 Steel Sample 1	1.00 ±0.01	1.50±0.01
Uncharged reference X60 steel Sample 2	1.02±0.01	1.40±0.01
Uncharged reference X60 steel Sample 3	1.02±0.01	1.06±0.01
Charged X60 steel (measured after 7 min of charging)	—	2.20 ±0.03

The uncharged reference samples exhibit hydrogen concentrations ranging from 1.06 to 1.50 ppm that are slightly high for degassed steels and likely reflect the total hydrogen, including both residual bulk hydrogen and hydrogen trapped at microstructural sites.

In contrast, the sample subjected to electrochemical hydrogen charging and measured after 7 minutes displays a significantly higher hydrogen content of 2.17 ppm. This increase, relative to the reference samples, clearly indicates successful hydrogen uptake during the charging process.

4.1.3.3 Rutherford Backscattering spectrometry/Elastic recoil detection (RBS/ERDA)

Compositional depth profiling of the X60 carbon steel surface following hydrogen charging was conducted using Rutherford Backscattering Spectrometry (RBS) in conjunction with Elastic Recoil Detection Analysis (ERDA). A representative elemental depth profile is presented in Figure 4.13. The distribution of hydrogen, carbon, oxygen, aluminum, and iron

within the near-surface region reveals distinct compositional gradients. Iron is the predominant constituent in the bulk material, whereas oxygen exhibits significant enrichment at the near surface. Post-charging analyses indicate a slight increase in hydrogen concentration relative to pre-charging conditions, accompanied by a slight increase in both carbon and oxygen content. These observations suggest that a fraction of the incorporated hydrogen is likely associated with surface oxide (e.g., hydroxides) and carbon species, rather than being present exclusively as lattice-diffusible hydrogen. Notably, a small amount of hydrogen introduced during charging may be bound within the native oxide layer, the thickness of which was estimated to be about 6 nm by XPS data (Figure 4.12). The RBS/ERDA results further indicate that the near-surface region comprises a thin, oxidized layer enriched in oxygen and carbon, as evidenced by pronounced peaks for these elements in the surface-adjacent region of the profile. The mean elemental weight percentages for the regions delineated by the red and blue dashed lines in the depth profile are summarized Table 4.13. Beyond this oxidized surface layer, the iron content rapidly increases to approximately 98.4 wt% and remains constant throughout the analyzed depth.

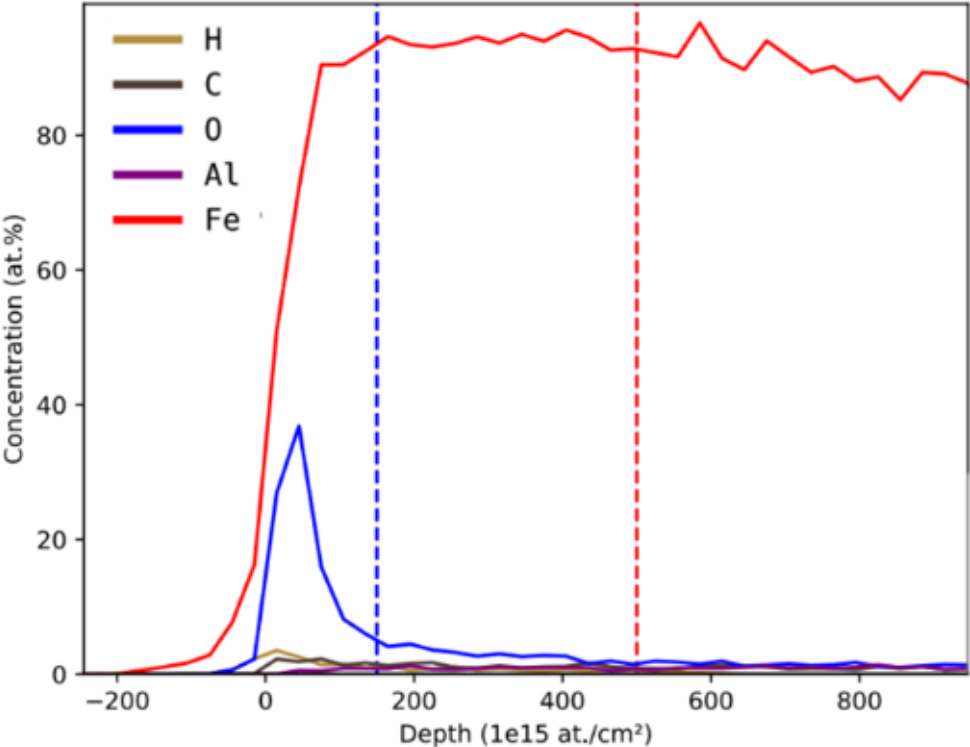


Figure 4.13. composition - depth profiles measured by RBS/ERDA for the X 60 steel mechanically polished X60 steel MP after hydrogen charging. The average elemental composition was determined over the depth range indicated by the blue and red dashed lines.

Table 4.13. The average elemental composition of X60 steel MP after hydrogen charging was determined over the depth range indicated by the blue and red dashed lines.

	Fe	H	C	O	Al
wt%	98.44 ± 0.01	0.014 ± 0.001	0.28 ± 0.01	0.85 ± 0.01	0.43 ± 0.01

4.2. Tungsten coatings as a hydrogen permeation barrier

In this section, the development and characterization of effective hydrogen permeation barriers for high-strength steels is presented. Specifically, this work investigates the application of tungsten coatings on X60 steel that presents both significant scientific challenges and innovative potential. The formation of adherent, and chemically stable tungsten layers capable of impeding hydrogen ingress is a complex task, complicated by issues such as coating uniformity, interfacial integrity, and the preservation of desirable mechanical properties. The innovative aspect of this study lies in the systematic and multi-technique evaluation of tungsten as a hydrogen barrier, employing advanced surface analytical techniques, electrochemical hydrogen permeation cell and bulk characterization methods to obtain a full information's in chemical, structural, and hydrogen diffusion information in the barriers- substrate system. Three distinct series of W-coated X60 steel samples were characterized: each series differs for the deposition and processing conditions. Series 1 was characterized by an average substrate roughness $R_a = 0.4 \mu\text{m}$ and a coating thickness of $3 \mu\text{m}$. Series 2 had an average substrate roughness $R_a = 0.2 \mu\text{m}$ with a coating thickness of $3 \mu\text{m}$, while Series 3 exhibited an average substrate roughness $R_a = 0.2 \mu\text{m}$ and a reduced coating thickness of $1.5 \mu\text{m}$.

4.2.1 Characterization of the coated samples

4.2.1.1 X-ray fluorescence (XRF) results

X-ray fluorescence (XRF) analysis was performed to quantitatively evaluate the surface composition of tungsten-coated X60 steel (W-coated X60 steel) samples from series S1, S2, and S3; the results are summarized in the Table 4.14. Note that the analyzed depth of the sample is in the order of $10 \mu\text{m}$. Series S1 and S2, both characterized by a nominal tungsten coating thickness of $3 \mu\text{m}$, demonstrated high tungsten contents of 87 (1) wt.% and 88.7 wt.%, respectively, accompanied by relatively low iron concentrations of 12 (1) wt.% for S1 and 10.6 (0.7) wt.% for S2. Conversely, series S3, which featured a thinner tungsten coating of $1.5 \mu\text{m}$, exhibited a significantly reduced tungsten content of 61 (1) wt.% and a correspondingly increased iron content of 38 (1) wt.%.

Small amounts of molybdenum (Mo), between 0.12 and 0.16 wt.%, were found in all series. Manganese (Mn) and nickel (Ni) appeared only in S3, with concentrations of 0.44 (0.04) wt.% and 0.33 (0.01) wt.%, respectively.

Table 4.14.XRF results of series 1,2 and 3

wt.%	Series 1 (3 μm coating, $R_a = 0.4 \mu\text{m}$)	Series 2 (3 μm coating, $R_a = 0.2 \mu\text{m}$)	Series 3(1.5 μm coating, $R_a = 0.2 \mu\text{m}$)
Fe	12 (1)	10.6 (0.7)	38 (1)
Mo	0.16 (0.03)	0.12 (0.01)	0.16 (0.01)
W	87 (1)	88.7 (0.1)	61 (1)
Mn			0.44 (0.04)
Ni			0.33 (0.01)

4.2.1.2 Scanning electron microscopy (SEM) results

Scanning electron microscopy (SEM) was used to characterize the cross-sectional morphology of W-coated X60 steel. SEM cross-section micrographs for each series are presented in Figure 4.14, while the measured coating thicknesses, as determined by SEM cross-sectional analysis, are summarized in Table 4.15 and compared with the corresponding nominal coating thicknesses.

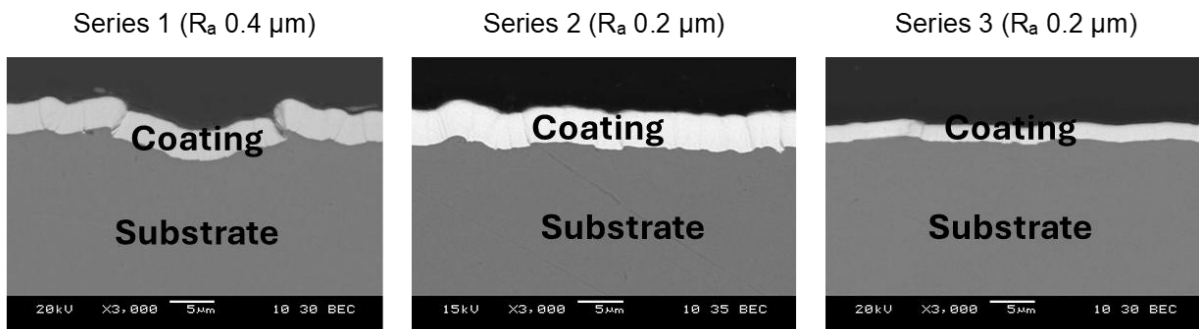


Figure 4.14. SEM cross section micrograph of W coated X60 steel, series 1, series 2 and series3

Table 4.15. Summary of W-coated X60 steel thickness for all sample series. The standard deviations are reported in parentheses.

Series	R_a (μm)	Nominal thickness (μm)	Measured thickness (μm , SD)
1	0.4	3	3.6 (0.7) μm
2	0.2	3	3.350 (0.004) μm
3	0.2	1.5	1.59 (0.04) μm

In Series 1, the substrate exhibited a mean surface roughness (R_a) 0.4 μm , with a nominal W coating thickness of 3 μm . SEM analysis showed the actual coating was 3.6 (0.7) μm thick; the relatively high standard deviation of 0.7 μm indicates that the coating was not uniform. The SEM cross-section micrograph shows that the interface between the coating and substrate was wavy.

For Series 2, the substrate exhibited a mean surface roughness $R_a = 0.2 \mu\text{m}$, while the nominal coating thickness remained at 3 μm . The measured coating thickness was 3.350 (0.004 μm), the small standard deviation of 0.004 μm , indicating excellent thickness uniformity. The interface was much smoother compared to Series 1, with only minor undulations observed.

Series 3, the substrate exhibited a mean surface roughness $R_a = 0.2 \mu\text{m}$, and the nominal coating thickness was 1.5 μm . The measured coating thickness was 1.59 (0.04) μm . SEM cross-section micrograph revealed a smooth and continuous interface, exhibiting a small variation in coating thickness throughout the sample.

4.2.1.3 X-ray diffraction (XRD)

X-ray diffraction (XRD) was performed to investigate the crystallographic characteristics of W-coated X60 steel. The XRD patterns of the series S1, S2 and S3 are presented Figure 4.16.

The XRD analysis of the W-coated X60 steel samples shows clear differences in crystallographic orientation, influenced by substrate roughness (Figure 4.15). In Series S1, with a 3 μm tungsten coating on a substrate with 0.4 μm roughness, three main peaks appear at $2\theta = 40.24^\circ$, 58.28° , and 73.13° , which correspond to the (110), (200), and (211) planes of BCC tungsten (*ICSD 64711 card*). This indicates a polycrystalline coating with various orientations. Conversely, Series S2 (3 μm coating, 0.2 μm roughness) and S3 (1.5 μm coating, 0.2 μm roughness) display strong peaks around 40.2° in 2θ . While the (200) and (211) peaks are present, their intensities are lower than that of the (110) peak, indicating a preferred orientation along the (110) direction, likely due to the smoother substrate surface. Additionally, a slight shift in the 2θ position of the (110) peak occurs between Series S2 and S3, with the (110) reflection at 40.24° in S2 and at 40.03° in S3.

Following the W-H analysis using the equation (Equation 3.13) reported in the chapter three, section 3.7.3, the crystallite size and microstrain were determined for the three series 1, 2 and 3

The W-H analysis from W-H plots (Figure 4.17) provided quantitative estimates of crystallite size and microstrain for all three series. For S1 (3 μm coating, 0.4 μm substrate roughness), the average crystallite size was 35 ± 1 nm, with a microstrain of 0.007 ± 0.001 nm. S2 (3 μm coating, 0.2 μm roughness) showed a slightly larger crystallite size of 37.0 ± 0.6 nm and the same microstrain value (0.007 ± 0.003 nm), indicating that reducing substrate roughness alone does not significantly affect the strain but can promote marginal grain growth. In contrast, S3 (1.5 μm coating, 0.2 μm roughness) exhibited small crystallite size of 14.18 ± 0.01 nm and the highest microstrain (0.010 ± 0.001 nm), indicating that reducing coating thickness results in finer grains and increased lattice strain.

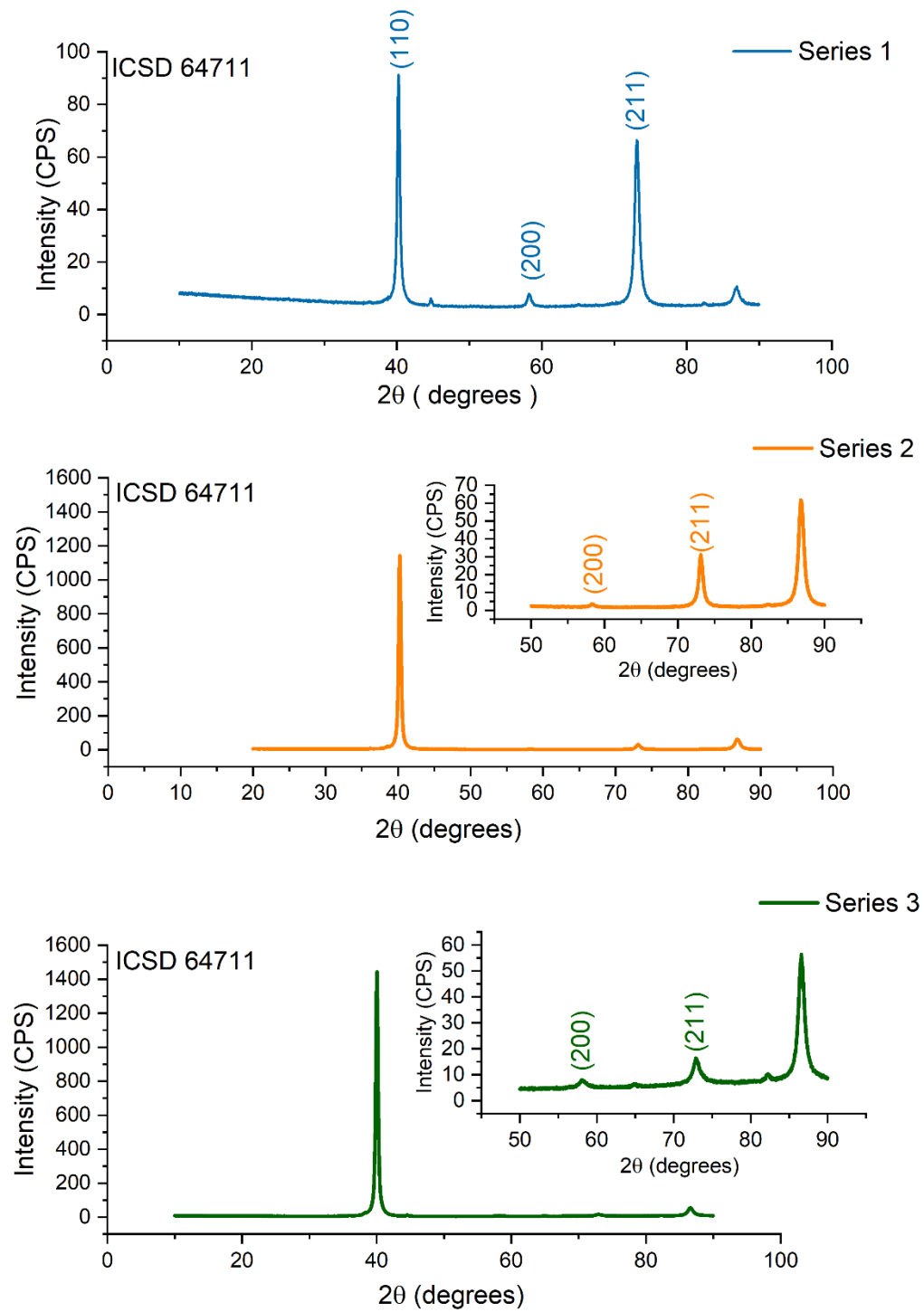


Figure 4.16. XRD pattern of W-coated X60 steel Series 1, Series 2 and Series 3

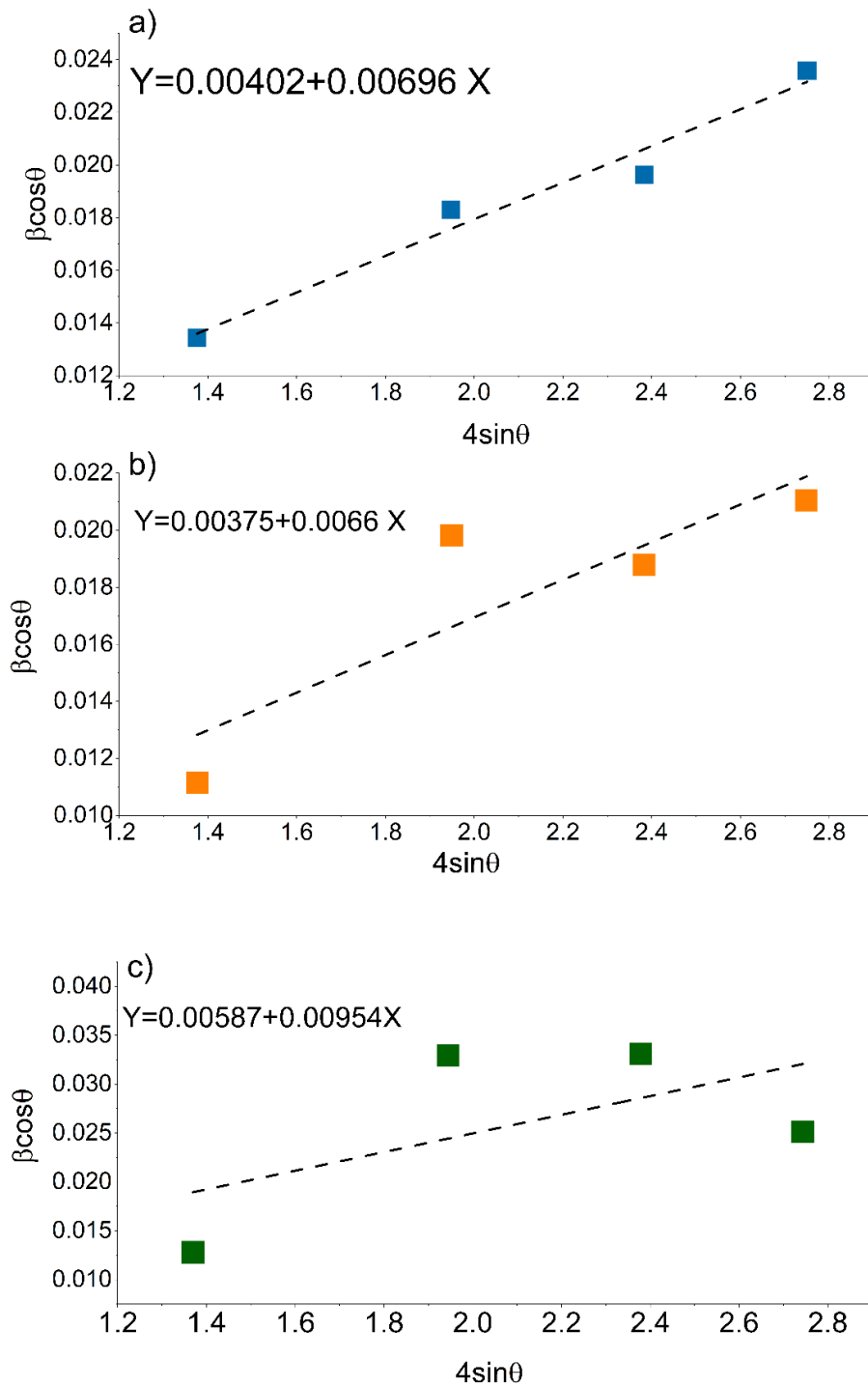


Figure 4.17. W-H plot with linear curve fit (black dashed) of W-coated X60 steel for a) Series 1, b) Series 2 and c) Series 3.

Residual stress in W-coated X60 steel was estimated from XRD analysis. The results are shown in Table 4.16.

Table 4.16. Crystallite size (nm), Microstrain and residual stress values in W-coated X60 steel Series 1, Series 2 and Series 3.

Series	Crystallite size (nm)	Microstrain (ϵ)	Residual stress (MPa)
S1	35 (1)	0.007 \pm 0.001	147.0 \pm 0.4
S2	37 (0.6)	0.007 \pm 0.003	375.4 \pm 0.1
S3	23.6 (0.1)	0.010 0 \pm 0.001	393.9 \pm 0.1

4.2.1.4 Rutherford Backscattering Spectrometry /Elastic recoil detection (RBS/ERDA)

Rutherford Backscattering Spectrometry (RBS) and Elastic Recoil Detection Analysis (ERDA) depth-profile measurements of W-coated X60 steel samples Series 1, Series 2 and Series 3 are presented in Figure 4.18,

Figure 4.19 and Figure 4.20 and reveal a distinct elemental distribution indicative of dense tungsten coatings with surface enrichment of light elements. Across all three series, the near-surface region demonstrates intense signals for oxygen, carbon, and nitrogen, while tungsten predominates in the subsurface and bulk, consistent with the intended coating structure. ERDA detection of hydrogen indicates its presence only in small amounts from the regions delimited by red and blue dashed lines; this is in line with expectations for residual uptake from the deposition environment using RF Magnetron sputtering. The quantitative mass fractions, calculated from measured atomic ratios and summarized in Table 4.17, confirm that despite the atomic abundance of lighter elements, tungsten constitutes the majority of the mass in all coatings.

In Series 1, the depth profile identifies, in addition to tungsten, the presence of quite high amounts of oxygen and small amounts of light elements. As detailed in Table 4.17, the mass composition is strongly tungsten-dominated (W = 97.7 wt%), with oxygen accounting for 1.79 wt%. Nitrogen, carbon, and hydrogen are detected only in small quantities for all series.

For Series 2, RBS/ERDA data indicate a reduced oxygen-enriched surface compared to Series 1. The corresponding weight percentage (Table 4.17,) supports this observation, with tungsten content increasing to 98.10 wt%, the highest among the series, and oxygen decreasing to 1.46 wt%. Nitrogen, carbon, and hydrogen remain present only in small amounts (0.11 wt%, 0.04

wt%, and 0.02 wt%, respectively), thus indicating the presence of a thinner or less developed oxide layer and a more pure tungsten coating compared to samples from Series 1 and 3.

Series 3 exhibits a depth profile similar to Series 1, characterized by a more pronounced oxygen-enriched surface layer than Series 2. Consistent with the compositional depth profile, Table 4.17, reports W = 98.0 wt%, O = 1.79 wt%, N = 0.18 wt%, C = 0.04 wt%, and H = 0.02 wt%. The oxygen mass fraction is nearly identical to that of Series 1, suggesting comparable surface oxidation, while the contributions from hydrogen, carbon, and nitrogen remain negligible.

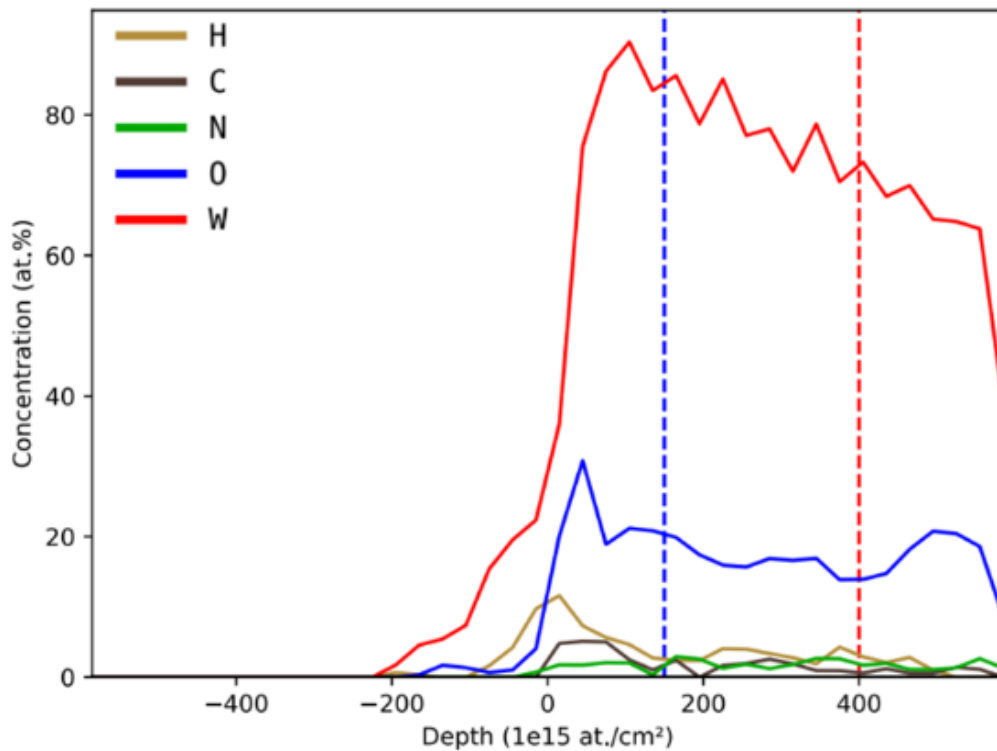


Figure 4.18. composition - depth profiles measured by RBS/ERDA for W-coated X60steel (Series1). The average elemental composition was determined over the depth range indicated by the blue and red dashed lines.

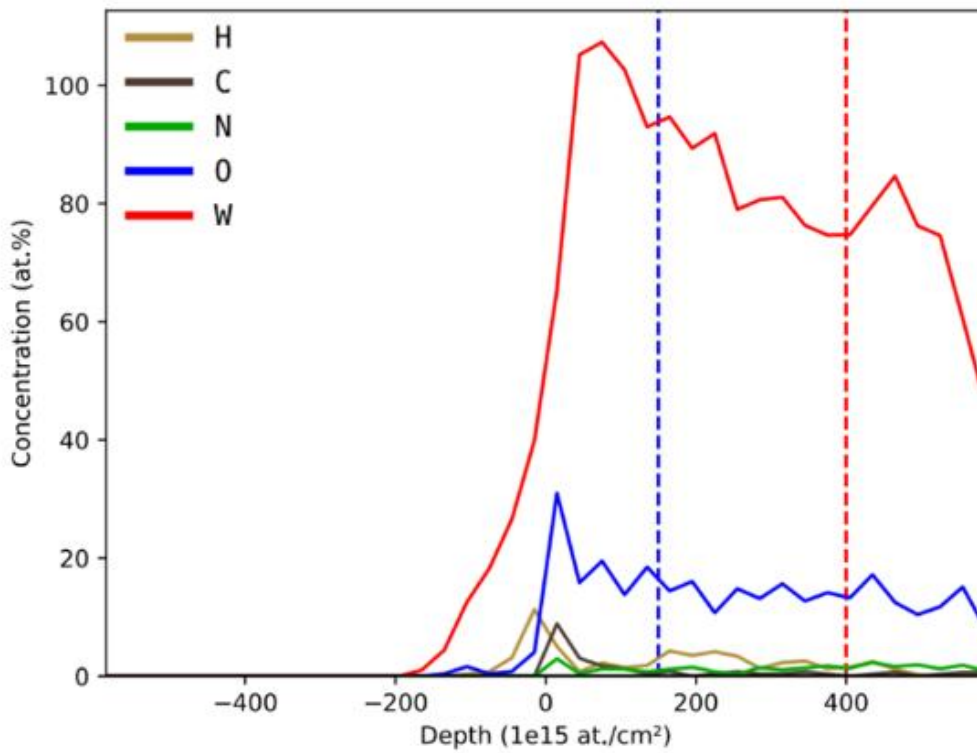


Figure 4.19. composition - depth profiles measured by RBS/ERDA for W-coated X60steel Series 2. The average elemental composition was determined over the depth range indicated by the blue and red dashed lines.

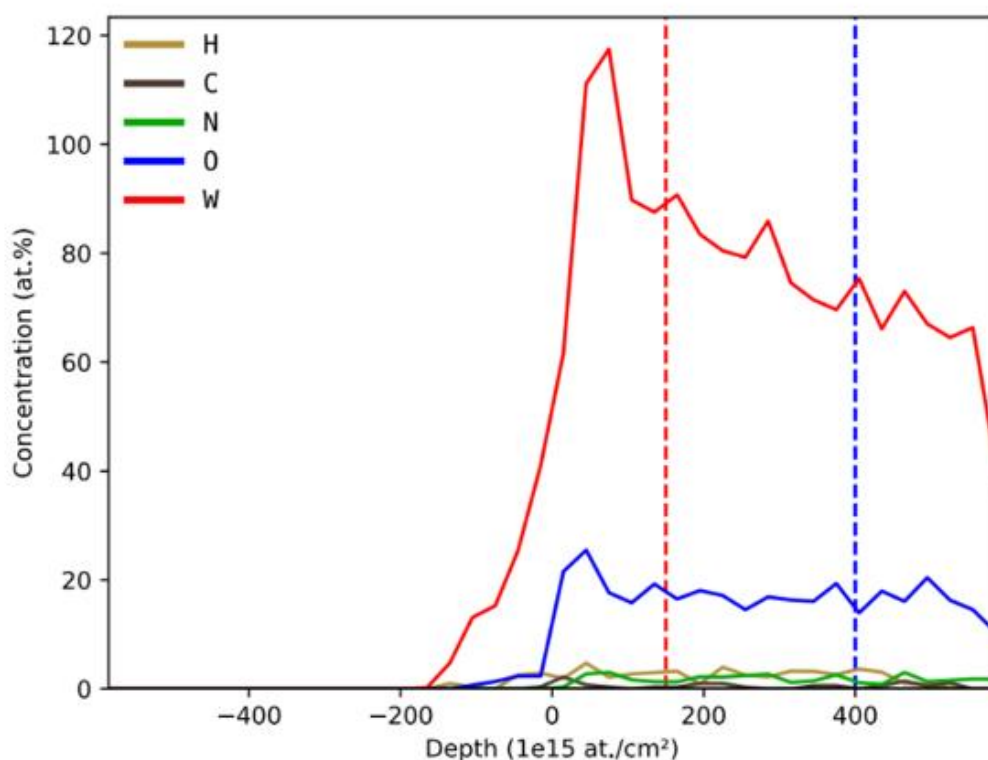


Figure 4.20. composition - depth profiles measured by RBS/ERDA for W-coated X60steel (Series 3). The average elemental composition was determined over the depth range indicated by the blue and red dashed lines.

Table 4.17 . The average elemental composition of W-coated X60 steel (Series 1, Series 2 and Series 3) determined over the depth range indicated by the blue and red dashed lines.

Series	H (wt%)	C (wt%)	N (wt%)	O (wt%)	W (wt%)
Series 1	0.020 ±0.001	0.12 ±0.01	0.20 ±0.01	1.80 ±0.01	97.70 ±0.01
Series 2	0.020 ±0.001	0.04 ±0.01	0.11 ±0.01	1.45 ±0.01	98.10 ±0.01
Series 3	0.020 ±0.001	0.04 ±0.01	0.18 ±0.01	1.79 ±0.01	98.0 ±0.1

4.2.1.4 Porosity measurements on the W-coated X60 steel: Development of a Survey XPS-Based Analytical approach

The application of advanced analytical techniques, such as X-ray Photoelectron Spectroscopy (XPS), is crucial in this study for evaluating the barrier performance of protective coatings, particularly in terms of coating uniformity. XPS offers high surface sensitivity and chemical specificity, enabling detailed characterization of elemental distributions at the outermost layers of the coated steel. Importantly, XPS allows for the analysis of multiple points across the sample surface, thus allowing an evaluation of the uniformity of the coating. In this study, three distinct samples were investigated, with three points measured on each sample. Recognizing the limitations of conventional methods for quantifying coating coverage, my co-authors and I have developed a novel, non-destructive analytical approach based on XPS to accurately determine the porosity of tungsten coatings.

Examples of survey spectra of the three series of coatings, Series 1, Series 2, and Series 3 are presented in the Figure 4.21. In all survey spectra, signals corresponding to tungsten (W 4f, W 4d, W 4p, and W 4s), oxygen (O 1s), and carbon (C 1s) were identified. A signal of Fe 2p from

the steel substrate was detected at all analysis points of Series 1, on sample 2 of Series 3, and no iron was detected in the samples of Series 2.

In each survey spectrum, the area of the Fe 2p signal and of the W 4f signal after Shirley background subtraction and after σ correction was determined the percentage of the through thickness porosity was calculated by dividing the area of the Fe 2p signal by the area of the W 4f signal taking into account the calculated sensitivity factors of the iron Fe 2p (16.42) and W 4f (9.8). The results are reported in Table 4.18.

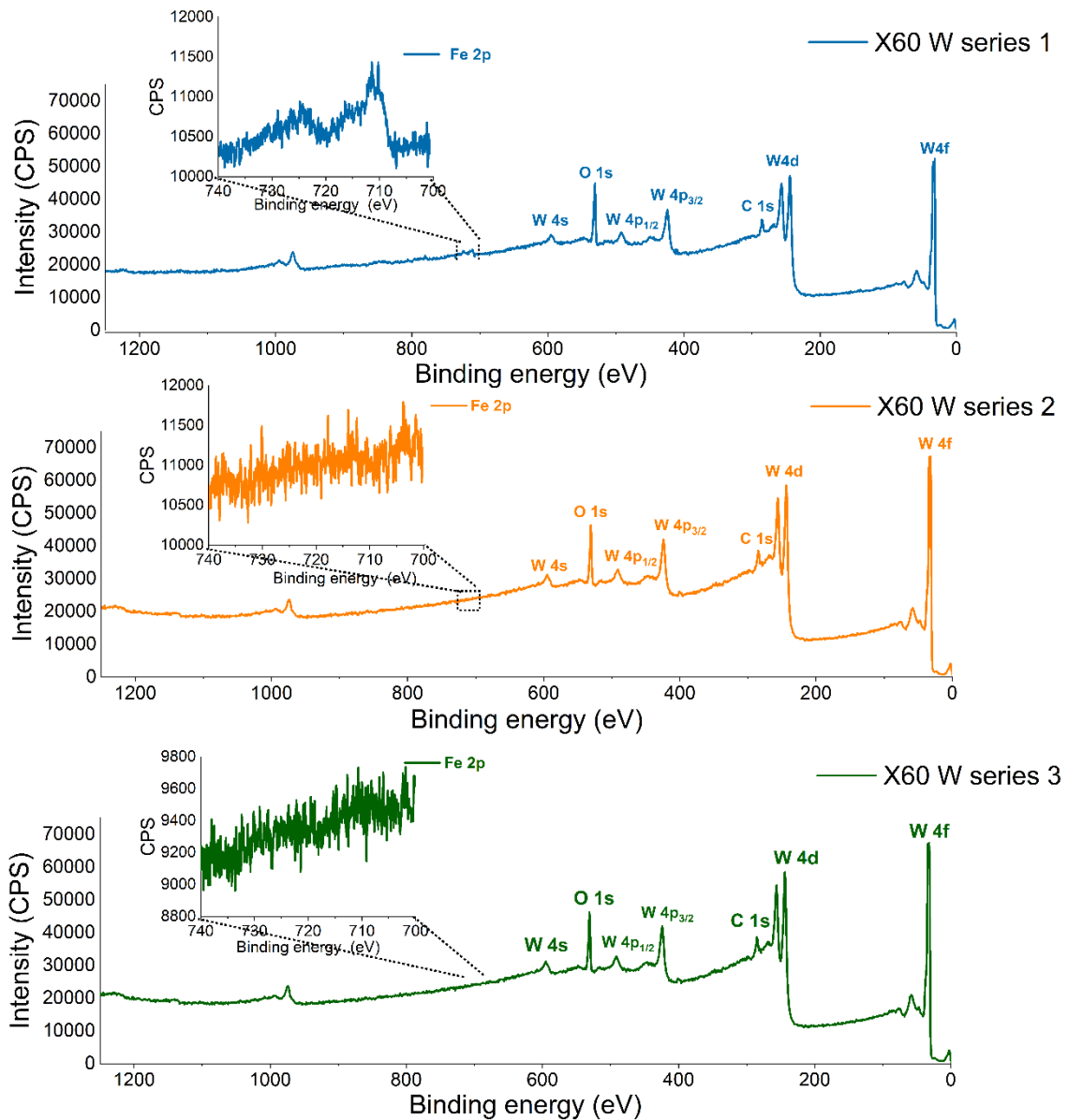


Figure 4.21. Examples of survey spectra of W-coated X60 steel of the three series examined. Insert shows the Fe 2p region. The presence of iron was revealed for all samples of series 1.

Table 4.18. Calculated through-thickness porosity (%) obtained from the survey spectra of the W-coated X60 steels

Sample 1	Sample 2	Sample 3	Average
----------	----------	----------	---------

Series 1	3.0 (1.1)	3.5 (0.7)	4.0 (0.3)	3.5 (0.8)
Series 2	0	0	0	0
Series 3	0	0.5 (0.4)	0	n.d.

Clear differences emerged among the three series analyzed. Series 1 exhibited an average open porosity of 3.5 % (with a standard deviation of 0.8 %), showing small variations between the three replica samples. Sample 1 demonstrated the lowest porosity, but there was a significant difference in the points analyzed. While series 2 presents 0% porosity.

4.2.1.9. XPS high-resolution spectra for chemical state identification.

Previously, bulk-sensitive techniques such as Rutherford Backscattering Spectrometry (RBS) and Elastic Recoil Detection Analysis (ERDA) revealed the presence of oxygen within the W-coated X60 steel samples (Section 4.1.3.3), indicating significant oxygen incorporation throughout the coatings. However, while these methods provide quantitative elemental profiles, they do not offer information regarding the specific chemical states of the incorporated oxygen or tungsten. To address this critical gap, high-resolution X-ray photoelectron spectroscopy (XPS) was employed for its exceptional surface sensitivity and unique capability to distinguish between different oxidation states.

In addition to the survey spectra, which was used to assess porosity and coating uniformity (section 4.2.1.4), high-resolution XPS measurements were performed on Series 1, Series 2, and Series 3 to determine the tungsten oxidation state. The fitting parameters for the W 4f and W 5p_{3/2} core-level signals are presented in Table 4.20. The fitting parameters refer to pure tungsten after ion sputtering and tungsten oxides (WO₃ and WO₂) as reference compounds. The data were recorded using the Theta Probe at UniCA and applying always the same analysis settings described in chapter three, section 3.6.1. The spectra and the fitting parameters are presented in appendix 2. In each series, the W 4f spectra (Figure 4.22.a) displayed a component attributed to elemental tungsten, with the characteristic W 4f_{7/2} and W 4f_{5/2} doublet clearly observed at peak energy 31.9 (0.1) eV and 34.3(0.1) eV respectively. All the samples of the three series exhibit the presence of oxidized tungsten on the surface; in details, W 4f_{7/2} and 4f_{5/2} signals from WO₃ were found at 36.1 (0.1) eV and 38.3 (0.1) eV, respectively; the peaks due to the spin orbit coupling W 4f_{7/2} and W 4f_{5/2} ascribed to WO₂ are found at 33.2 (0.1) eV and 35.1 (0.1) eV (Table 4.19). These values are in good agreement with the literature.[9],[10]

The O 1s signals (Figure 4.22b) showed four components; the peak energies of the components are at 530.9 (0.1) eV, 531.4 (0.2) eV, 533.2 (0.1) eV and 534.4 (0.1) eV, and they are assigned to oxides, hydroxides, adsorbed water, and organic contamination, respectively (Table 4.19).

Table 4.19. Peak energy values (eV) of O 1s, W 4f, and W 5p_{3/2} are reported as mean values, and the standard deviations are given in parentheses.

Peak energy (eV)	Series 1	Series 2	Series 3
O 1s - Oxide	530.7 (0.4)	530.9 (0.1)	530.8 (0.2)
O 1s - Hydroxide	531.4 (0.2)	531.4 (0.2)	531.4 (0.1)
O 1s - adsorbed water	533.2 (0.1)	533.2(0.1)	533.2 (0.1)
O 1s- organic contamination	534.4 (0.1)	534.7 (0.2)	534.7 (0.1)
W 4f _{7/2} – W (0)	32.0 (0.1)	31.7 (0.3)	31.8(0.1)
W 4f _{5/2} – W (0)	34.2(0.1)	33.8 (0.1)	33.9 (0.1)
W 5p _{3/2} - W (0)	37.6 (0.1)	37.2 (0.1)	37.3 (0.1)

W 4f _{7/2} - WO ₃	36.1 (0.1)	36.0 (0.1)	36.0 (0.1)
W 4f _{5/2} - WO ₃	38.3 (0.1)	38.2 (0.1)	38.2(0.1)
W 4f _{7/2} - WO ₂	33.2 (0.1)	33.0 (0.1)	33.0(0.1)
W 4f _{5/2} - WO ₂	35.1 (0.1)	34.9 (0.2)	34.9 (0.1)

Table 4.20. Fitting parameters used for O 1s and W 4f and W 5p_{3/2} high-resolution spectra of W-coated X60 steel. The FWHM are reported as average values over three independent measurements and the standard deviations are in parentheses. The W 4f curve fitting parameters are established by analysing pure tungsten after ion sputtering and pure tungsten oxides as reference compounds (the XPS spectra of the analysed regions are presented in Appendix 2).

	Line shape	Position constraint	FWHM (eV)	FWHM constraint	Area constraint
O 1s Oxide	GL (30)	-	1.49 (0.1)	-	-
O 1s-hydroxide	GL (30)	-	1.49 (0.1)	O1s - oxide *1	-
O 1s – adsorbed water	GL(30)		1.49 (0.1)		
O 1s- organic contamination	GL (30)	-	1.49 (0.1)	O1s - oxide *1	-
W 4f _{7/2} W0)	GL (35)T(1.6)	-	0.84 (0.01)	-	-
W 4f _{5/2} W(0)	GL (35)T(1.6)	W 4f _{7/2} - W (0)*+2.15	0.84 (0.01)	W 4f _{7/2} - W (0) *1	W 4f _{7/2} - W (0) *0.76
W 5p _{3/2}	GL (45)	W 4f _{7/2} - W (0)*+5.5	2.1(0.1)	2-2.9	W 4f _{7/2} - W (0) *0.12
W 4f _{7/2} (WO ₃)	GL (45)		1.5(0.2)	-	
W 4f _{5/2} (WO ₃)	GL (45)	W 4f _{7/2} - WO ₃ +2.15	1.5(0.2)	W 4f _{7/2} - WO ₃ *1	W 4f _{7/2} - WO ₃ *0.76
W 4f _{7/2} (WO ₂)	GL (45)		1.40 (0.01)		
W 4f _{5/2} (WO ₂)	GL (45)	W 4f _{7/2} - WO ₂ +2.15	1.40 (0.01)	W 4f _{7/2} - WO ₂ *1	W 4f _{7/2} - WO ₂ *0.76

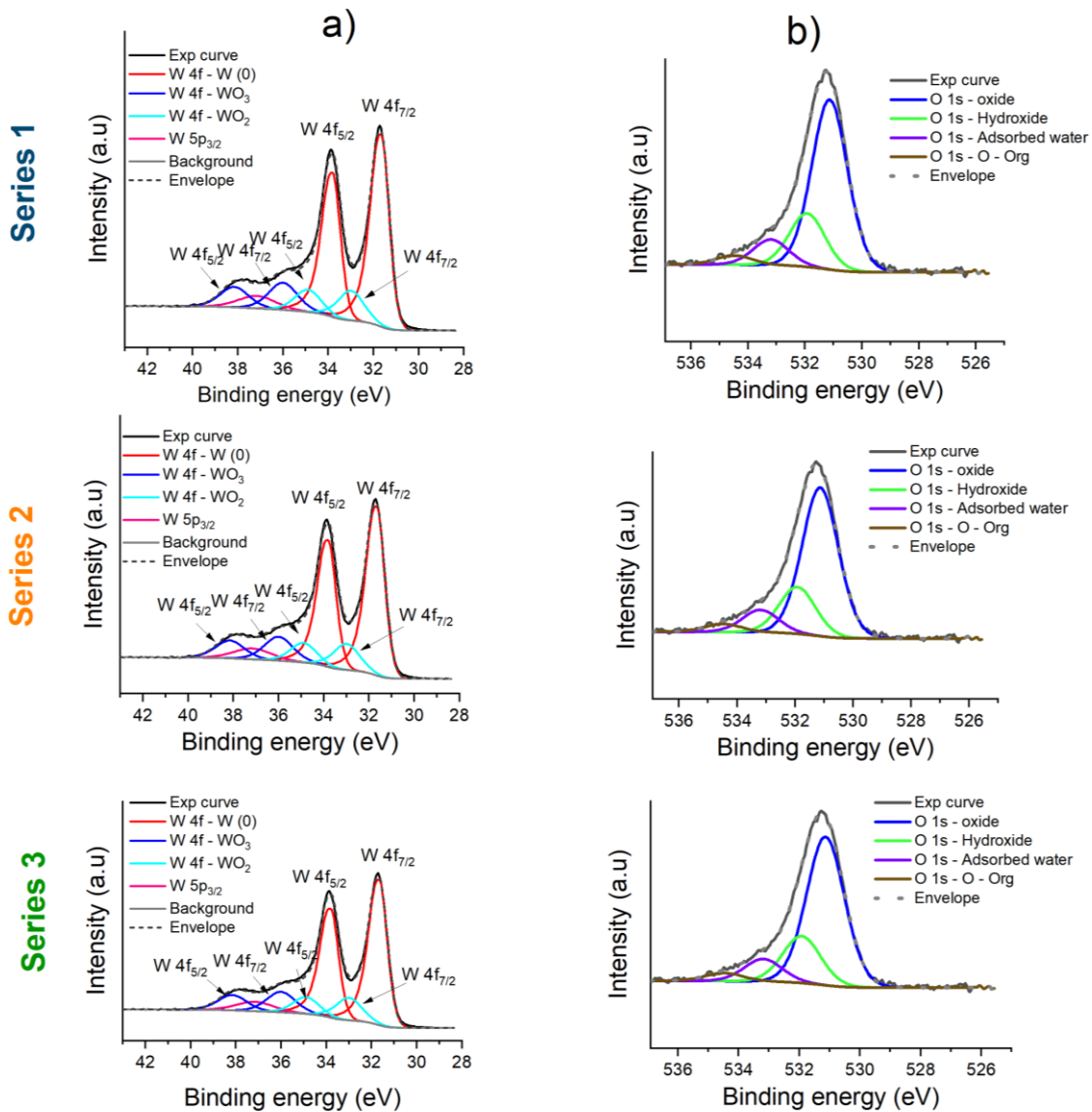


Figure 4.22.a) W 4f, W 5p_{3/2}, and b) O 1s XP- high-resolution spectra of Series 1, Series 2, and Series 3

The angle resolved XPS has been used as well for the W-coated X60 steel series 2. The Figure 4.23 shows the atomic percentage of tungsten and tungsten oxides at different emission angles. For tungsten, it can be observed that the atomic percentages decrease at higher emission angles and the atomic percentages of tungsten oxides increase at higher emission angles, and decrease at lower emission angles, indicating that an oxide layer is present at the W surface.

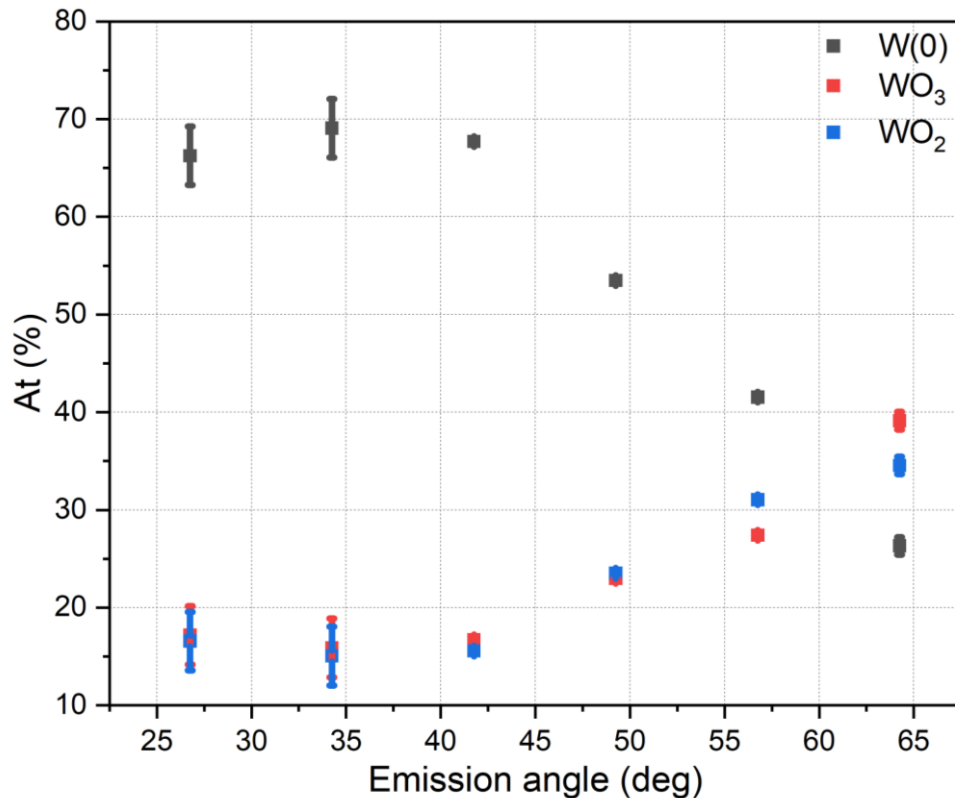


Figure 4.23. Atomic percentage versus emission angle for tungsten and tungsten oxides

4.2.1.6 Combined X – ray photoelectron spectroscopy and hard X-ray photoelectron spectroscopy (XPS/HAXPS)

To achieve a depth-resolved assessment of the chemical states within the W-coated X60 steel samples, the combined X -ray photoelectron spectroscopy and hard X-ray photoelectron spectroscopy (HAXPES) was employed. Measurements were performed using Al $K\alpha$ source Cr $K\alpha$ excitation sources respectively.

The high-resolution spectra of W 4f and W 5p_{3/2} acquired using the Al $K\alpha$ source are presented in Figure 21.a. Five peaks (1, 2, 3, 4, and 5) are observed, corresponding to W 4f_{7/2}– W(0), W 4f_{5/2} – W(0), W 4f_{7/2} – WO₃, W 5p_{3/2}, and W 4f_{5/2}– WO₃, respectively. The high-resolution W 4f spectra acquired with the Cr $K\alpha$ source, shown in Figure 4.24.b, reveal the presence of metallic tungsten (W(0)) . Signals 1, 2, and 3 are attributed to metallic tungsten W 4f_{7/2} and W 5p_{3/2}, respectively. The O 1s high-resolution spectrum presented in Figure 4.24.c, obtained using the Al $K\alpha$ source, shows four peaks (1, 2, 3, and 4) attributed to tungsten oxides, hydroxides, adsorbed water, and organic contamination, respectively. In contrast, the O 1s spectrum shown in Figure 4.24.d (acquired using the Cr $K\alpha$ source) displays two peaks: peak 1 corresponds to tungsten oxide, and peak 2 to adsorbed water. No attempt of curve-fitting these data was performed.

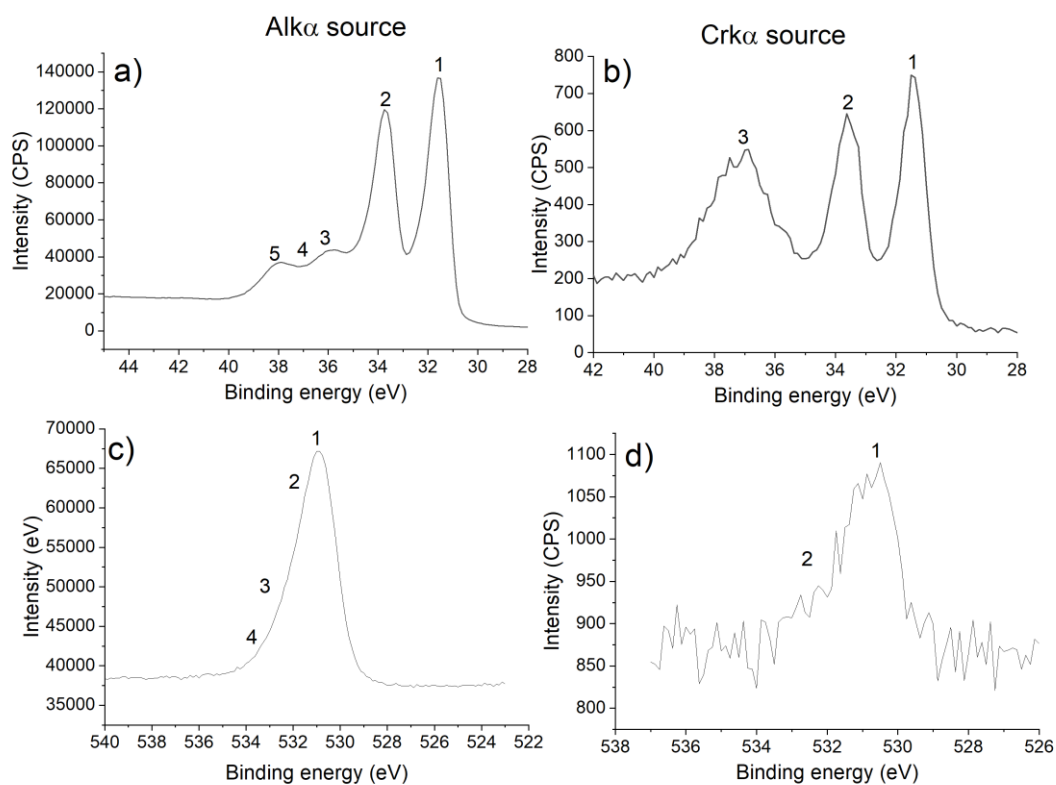


Figure 4.24. High-resolution XPS spectra of (a, c) W 4f, W 5p_{3/2}, and O 1s acquired using the Al Kα source, and (b, d) W 4f, W 5p_{3/2}, and O 1s acquired using the Cr Kα source.

4.2.2 Electrochemical hydrogen permeation results (HPT)

Hydrogen permeation experiments were performed to evaluate the barrier properties of the W-coated X60 steel samples (Series 1, Series 2, and Series 3). Figure 4.25 shows the typical hydrogen permeation curves for the three series, where the anodic current is plotted as a function of time. Three replicates of the hydrogen permeation measurements were performed for each series of coating.

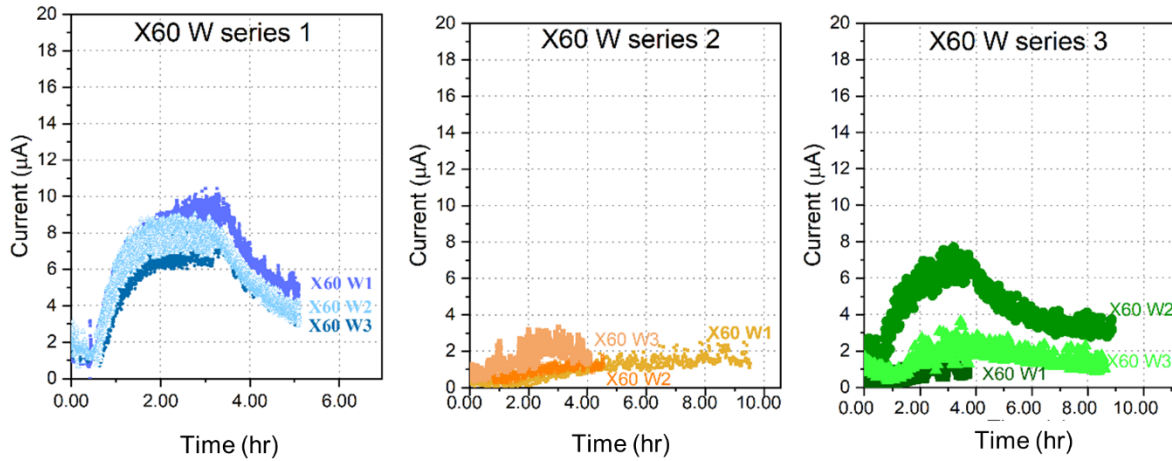


Figure 4.26. Hydrogen permeation curves for a) X60 W series 1, b) X60 W series 2 and c) X60 W series

The hydrogen detection current of the W-coatings of series 1 (Fig. 15 a) reaches values between 7 and 10 μA . For series 2 (thickness 3 μm) and series 3 (thickness 1.5 μm) the current initially remained very low (at the passivation current $< 0.1 \mu\text{A}$); subsequently, it increased during the build-up phase and reached a nearly steady-state value at low values of 1 – 2 μA , indicating a good hydrogen permeation barrier behavior of the tungsten coating.

The permeation reduction factor (PRF) and the effective diffusion coefficient (D_{eff}) for hydrogen permeation through the coated samples was determined and presented in Table 4.21

Table 4.21. Effective diffusion coefficients (D_{eff}) of W coatings on X60 steels for series 1, 2 and 3. The results are given as mean values with the respective standard deviations and are reported in parentheses

Material	Thickness μm	PRF	$D_{\text{eff-tlag}}$ (m^2/s)	$D_{\text{eff-tb}}$ (m^2/s)
X60 steel	-	-	$2.4 (0.4) 10^{-10}$	$2.8 (0.2)$
W coat. Series 1	3.0	4	$3.5 (0.5) 10^{-10}$	
W coat. Series 2	3.0	35 - 40	$4.9 (0.2) 10^{-11}$	
W coat. Series 3	1.5	25 - 30	$9.1 (0.2) 10^{-11}$	

The permeation reduction factor (PRF) of Series 1 shows a low value of 4. This may be due to the high porosity of the coatings in Series 1 (see Section 4.2.1.5). Series 2 and 3 show high PRF values, indicating good hydrogen permeation barrier effect. The effective diffusion coefficients of the coated samples is four to eight times lower than D_{eff} of the bare X60 steel.

References

- [1] Sun, B., Zhao, H., Dong, X., Teng, C., Zhang, A., Kong, S., ... & Tu, S. T. (2024). Current challenges in the utilization of hydrogen energy—a focused review on the issue of hydrogen-induced damage and embrittlement. *Advances in Applied Energy*, 14, 100168.
- [2] J. Hoschke, M. F. W. Chowdhury, J. Venezuela, and A. Atrens, “A review of hydrogen embrittlement in gas transmission pipeline steels,” *Corrosion Reviews*, vol. 41, no. 3, pp. 277–317, Jun. 2023, doi: 10.1515/corrrev-2022-0052.
- [3] D. Mahajan, K. Tan, T. Venkatesh, P. Kileti, and C. R. Clayton, “Hydrogen Blending in Gas Pipeline Networks—A Review,” *Energies*, vol. 15, no. 10, p. 3582, May 2022, doi: 10.3390/en15103582.
- [4] E. Ohaeri, U. Eduok, and J. Szpunar, “Hydrogen related degradation in pipeline steel: A review,” *International Journal of Hydrogen Energy*, vol. 43, no. 31, pp. 14584–14617, Aug. 2018, doi: 10.1016/j.ijhydene.2018.06.064.
- [5] D. Biggio, B. Elsener, G. Usai, M. Fantauzzi, and A. Rossi, “Surface Chemistry of Passive Films on Ni-Free Stainless Steel: The Effect of Organic Components in Artificial Saliva,” *Langmuir*, vol. 40, no. 13, pp. 6824–6833, Apr. 2024, doi: 10.1021/acs.langmuir.3c03728.
- [6] R. Hannachi, D. Biggio, B. Elsener, M. Fantauzzi, and A. Rossi, “X-ray photoelectron spectroscopy investigation of X60 steel,” *Surface Science Spectra*, vol. 31, no. 2, p. 024014, Dec. 2024, doi: 10.1116/6.0003972.
- [7] T. Casanova and J. Crousier, “The influence of an oxide layer on hydrogen permeation through steel,” *Corrosion Science*, vol. 38, no. 9, pp. 1535–1544, Sep. 1996, doi: 10.1016/0010-938X(96)00045-5.
- [8] F. Bolzoni, L. Paterlini, L. Casanova, and M. Ormellese, “Hydrogen charging of carbon and low alloy steel by electrochemical methods,” *J Appl Electrochem*, vol. 54, no. 1, pp. 103–114, Jan. 2024, doi: 10.1007/s10800-023-01942-8.
- [9] C.-O. A. Olsson, H.-J. Mathieu, and D. Landolt, “Angle-resolved XPS analysis of molybdenum and tungsten in passive films on stainless steel PVD alloys,” *Surface and Interface Analysis*, vol. 34, no. 1, pp. 130–134, 2002, doi: 10.1002/sia.1268.
- [10] J. L. Alay, H. Bender, G. Brijs, A. Demesmaeker, and W. Vandervorst, “Quantitative analysis of W(N), TiW and TiW(N) matrices using XPS, AES, RBS, EPMA and XRD,” *Surface and Interface Analysis*, vol. 17, no. 6, pp. 373–382, 1991, doi: 10.1002/sia.740170613.
- [11] P.-M. Deleuze, N. Gauthier, K. Artyushkova, E. Martinez, and O. Renault, “HAXPES reference spectra of bulk W and WSe₂ with Cr K α excitation,” *Surf. Sci. Spectra*, vol. 30, no. 2, p. 024029, Nov. 2023, doi: 10.1116/6.0003124.

5. Discussion

This chapter provides a comprehensive discussion of the hydrogen diffusion and trapping in X60 steel by correlating surface chemistry, microstructural features, and hydrogen transport properties. Insights are drawn from a series of characterization techniques, including X-ray Photoelectron Spectroscopy (XPS), Scanning Electron Microscopy coupled with Energy Dispersive X-ray Spectroscopy (SEM/EDS), X-ray Diffraction (XRD) as well as hydrogen permeation experiments, LECO hydrogen analysis, Rutherford Backscattering Spectrometry and Elastic Recoil Detection Analysis (RBS/ERDA), as well as microcapillary cell measurements before and after hydrogen charging.

This chapter is based on my personal work under the supervision and with the support of Prof. Antonella Rossi, Prof. Marzia Fantauzzi, Prof. Bernhard Elsener, Dr. Nicoletta Zacchetti, and Dr. Deborah Biggio. Some of the experimental results discussed in sections 5.1 and 5.2. are presented in the paper [1], and in [2].

5.1. Hydrogen diffusion in X60 steel

5.1.1. Surface composition and homogeneity

The XPS spectra were obtained on three independent samples, each with three spots on the steel samples after cleaning, mechanical polishing, and heating (see chapter 4). The binding energy values of Fe (II) oxide, Fe (III) oxide and of Fe (III)-OOH (Table 4.7) agree with the literature [3–5]. They remain unchanged within the experimental uncertainty (± 0.1 eV) for all the samples regardless of the surface treatment.

The thickness of the hydrocarbon contamination layer showed a lower variation for the heated C X60 (labelled as HC (2.7 (0.3) nm)) and for the heated MP (labelled as H MP (3.3. (0.2) nm) X60 steels (Figure 4.5) compared to the same samples before heating. (3.5 (0.8) nm for C X60 steel and 2.9 (0.5) nm) for MP X60 steel). The thickness of the oxide layers of the series of heated samples is higher than that of the same samples before heating. This suggests that the surface layer slightly grows upon heating, as expected. The higher standard deviation of the thickness values of the cleaned samples after heating might be interpreted as an indication of the growth of a non-homogeneous surface film. This indicates that mechanical polishing leads to more reproducible surfaces, as evidenced by the reproducibility of the open-circuit potential versus time curves (Figure 4.7) for mechanically polished surfaces. Studies have shown that mechanically polished steel exhibits better reproducibility of passive film after immersion in aggressive solutions [6].

Based on the binding energies of both the iron and oxygen peaks, we can conclude that the surface film is composed of iron oxyhydroxides. The iron is mainly present as Fe (III) (Table 4.17,). After heating, the atomic percentage of FeO strongly decreases: the Fe (II) component in the fitted Fe 2p_{3/2} spectrum almost disappears and this can explain the high relative uncertainty, which characterizes this contribution to the signal after heating (Table 4.8): from 5 (2) % to about 0.5 (0.7)% for C X60 steel and from 4 (3) % to about 0.9 (0.9) % in the case

of the MP X60 steel). This decrease might be due to the fact that heating promotes oxidation into more stable oxides, such as Fe_2O_3 . This might be substantiated by the trend that indicates an increase in the atomic percentage of Fe_2O_3 .

RBS/ERDA depth profiling confirmed the presence of an oxygen-enriched near-surface region, followed by a rapid transition to an iron-dominated bulk with Fe contents approaching 98.5–98.7 wt%. The oxygen peak detected by RBS/ERDA directly correlates with the oxide layer thickness determined by XPS, providing strong validation and consistency between the two analytical techniques.

5.1.2. Hydrogen content in X60 steel before Hydrogen charging

Before any hydrogen charging, the steel exhibits a low but detectable hydrogen content: 0.010 ± 0.001 wt% hydrogen measured by ERDA analysis. ERDA detects atomic hydrogen in the near surface region i.e. in the 30-50 nm. The inert gas fusion (LECO) technique, which measures the total hydrogen content released as molecular H_2 from the bulk material by integrating all hydrogen released during high-temperature melting of the sample [7] provides values ranging from 1.06 to 1.50 ppm. It is important to note that the hydrogen contents measured by inert gas fusion and ERDA are not expected to be identical, as these two techniques probe different hydrogen depth scales and types. includes lattice-diffusible hydrogen, reversibly trapped hydrogen at microstructural defects (such as dislocations and grain boundaries), as well as more strongly trapped hydrogen.

In contrast, ERDA provides a depth-resolved measurement of hydrogen concentration, typically limited to the near-surface and subsurface regions. [8] ERDA is therefore more sensitive to hydrogen present near the surface and at shallow trapping sites, such as oxides, metal interfaces, and near-surface defects. Additionally, ERDA measurements are influenced by surface chemistry. The presence of a thin native oxide layer, as identified by XPS, can locally increase hydrogen content through hydroxyl functional groups or adsorbed water species. This hydrogen contributes to the ERDA signal but represents only a small fraction of the total hydrogen detected by inert gas fusion. Conversely, hydrogen trapped in the bulk and in deeper microstructural defects contributes more significantly to the inert gas fusion analysis.

The detection of hydrogen in the steel before any hydrogen charging is consistent with findings in the literature, which indicate that hydrogen can be introduced into the steel microstructure during manufacturing processes.[9]

5.1.3. Hydrogen uptake after hydrogen charging

To study the uptake and distribution of hydrogen in steel samples, we employed a combination of depth-resolved analytical techniques, electrochemical methods, and bulk techniques.

- **Near surface hydrogen accumulation and associated with impurities**

RBS/ERDA depth profile (Figure 4.13) acquired after one month from hydrogen charging reveals a slight increase in hydrogen concentration, particularly in the near-surface region (30-50 nm). This result is consistent with previous investigations reporting hydrogen accumulation

close to the surface, where defects and chemically active sites act as effective trapping sites for hydrogen [10]. This is indeed accompanied by slight increases in oxygen and carbon content (Table 4.9, Table 4.13), suggesting that a fraction of the absorbed hydrogen is associated with surface oxides, hydroxides, and carbon-containing species. [11]

- **Electrochemical permeation tests (Devanathan and Stachurski cell (D-S cell))**

Hydrogen diffusion coefficient of X60 determined by D-S cell

The effective hydrogen diffusion coefficient D_{eff} values (Table 4.10) calculated with the t_{lag} and t_b methods are comparable and no influence of the sample preparation method can be revealed. This indicates that the hydrogen diffusion coefficient is governed by the bulk material properties, and it seems that it is not affected by nanometer thick surface layers. These two methods (t_{lag} and t_b), used frequently in the literature [26,27], are based on the assumption that the diffusion of hydrogen in the metal can be described by Fick's laws (Equations 5.1 and Equation 5.2) [14] where j is the hydrogen flux, D_{eff} is the effective hydrogen diffusion coefficient, C the hydrogen concentration, x the distance from the surface and t the time.

$$j(x, t) = -D_{\text{eff}} \frac{\partial C(x,t)}{\partial x}, \quad (\text{Equation 5.1})$$

$$\frac{\partial C}{\partial t} = D_{\text{eff}} \frac{\partial^2 C}{\partial x^2}, \quad (\text{Equation 5.2})$$

The solution of Fick's laws depends on the boundary conditions and the system geometry. For the Devanathan and Stachurski electrochemical double cell (see experimental) the conditions are: 1) a membrane of finite thickness L ; 2) $C = C_0$ at $x = 0$, meaning a constant hydrogen concentration C_0 at the production side, 3) $C = 0$ at $x = L$, meaning that the hydrogen concentration at the detection side of the membrane is zero.

The effective diffusion coefficients calculated for the H C X60 steel ($2.4 (0.4) 10^{-10} \text{ m}^2/\text{s}$) and for the H MP X60 steel ($2.0 (0.4) 10^{-10} \text{ m}^2/\text{s}$) are in the same order of magnitude and are in agreement with literature data [15]. The highest values of D_{eff} are reported for Armco iron ($6.2 10^{-9} \text{ m}^2/\text{s}$) [16] and pure annealed iron ($4 10^{-9} \text{ m}^2/\text{s}$) [17]. The literature data obtained using different steels shows that the hydrogen diffusion coefficient D_{eff} of X60 steel in this work is similar to the one of X65 steel ($2.3 10^{-10} \text{ m}^2/\text{s}$) [15] and $3.5 10^{-10} \text{ m}^2/\text{s}$ [18]. Other studies reported hydrogen diffusion coefficient to be $6.2 10^{-11} \text{ m}^2/\text{s}$ and $5.1 10^{-11} \text{ m}^2/\text{s}$ for different grade high-strength pipeline steels such as X70 C and X80 C steels, respectively [12]. High carbon steel exhibited a D_{eff} value equal to $2.2 10^{-11} \text{ m}^2/\text{s}$ [16], which is lower than that of the D_{eff} of X60 steel; this may be attributed to its relatively higher carbon content, which can delay hydrogen transport and act as a trapping site [16].

In addition, other studies investigated the influence of different tempering temperatures on the hydrogen diffusion on low-alloy high strength steel (LAHSS)[13] showed that the hydrogen diffusion coefficient D_{eff} increased with tempering temperature [13].

Hydrogen sub-surface concentration (C_0) of X60 steel

The study of hydrogen subsurface concentration in steels is critical for understanding hydrogen embrittlement. Hydrogen accumulation near the surface can initiate micro-cracks, which can propagate under mechanical stress, leading to failure [13].

The sub-surface hydrogen concentration C_0 at the production side of the sample was calculated from the hydrogen permeation curves using Equation 3.5.

Table 5.1. Hydrogen subsurface concentration of different steel present in the literature compared with those obtained in this work

	C_0 (ppm)	C_0 mol H /m ³	Ref
Heated C X60 steel	0.66 (0.02)	5.2 (1.4)	This work
Heated MP X60 steel	0.8 (0.1)	6.3 (0.8)	This work
LAHSS steel T640	0.21	<i>1.65</i>	[13]
LAHSS steel T600	0.87	<i>6.85</i>	[13]
LAHSS steel T560	1.52	<i>11.96</i>	[13]
High carbon steel	6.09	<i>47.5</i>	[16]
Weld X80 steel	2.21	17.43	[19]
HAZ X80 steel	2.12	16.71	[19]
Base X80 steel	1.54	12.12	[19]
Annealed iron	0.022	0.17	[17]
Armco Iron	0.085	0.662	[16]

*The values written in italic are converted values

The subsurface hydrogen concentration C_0 of heated C X60 and MP X60 steel is given in Table 5.1 together with the literature data from other steels of different composition, microstructure and heat treatment. two different units are used to report hydrogen concentration: mol H/m³ and ppm (Table 5.1). The conversion factor is the iron density 7.87 g/cm³; for the sake of clarity this discussion uses only ppm. The lowest values of C_0 are reported for annealed iron (0.022 ppm) [17] and annealed Armco iron (0.085 ppm) [16]. The hydrogen concentration C_0 in low alloyed high-strength steel (LAHSS) at different tempering temperatures (560°C, 600 °C and 640°C) was found to be 1.52 ± 0.01 ppm, 0.87 ± 0.08 ppm and 0.21 ± 0.01 ppm, respectively [13]. The influence of welding was tested on X80 steel, the hydrogen concentration C_0 for weld, heat affected zone (HAZ) and base X80 steel was found to be 2.21 ppm, 2.12 ppm and 1.54 ppm, respectively [19].

Trapped Hydrogen in X60 steel

To quantify the amount of hydrogen trapped within the steel microstructure, the Zakrocynski approach (see experimental chapter 3 section 3.3.3) can be used by analyzing the decay region of the hydrogen permeation curve (Figure 5.1.a and Figure 5.2.b). The quantity of trapped hydrogen (q_{H}) was determined to be $8 (2) \times 10^{-8}$ mol H/cm² for HC X60 steel and $8 (6) \times 10^{-8}$ mol H/cm² for H MP X60 steel.

The reproduced curve was obtained using the decay equation (Equation 3.4) by fixing all the parameters at $I_p^0=I_{ss}$, and $I_p^\infty=0$, while fixing the diffusion coefficient D_L using the value obtained experimentally (see experimental section 3.3.2.) as the diffusion coefficient of the mobile hydrogen, also termed as the lattice diffusion

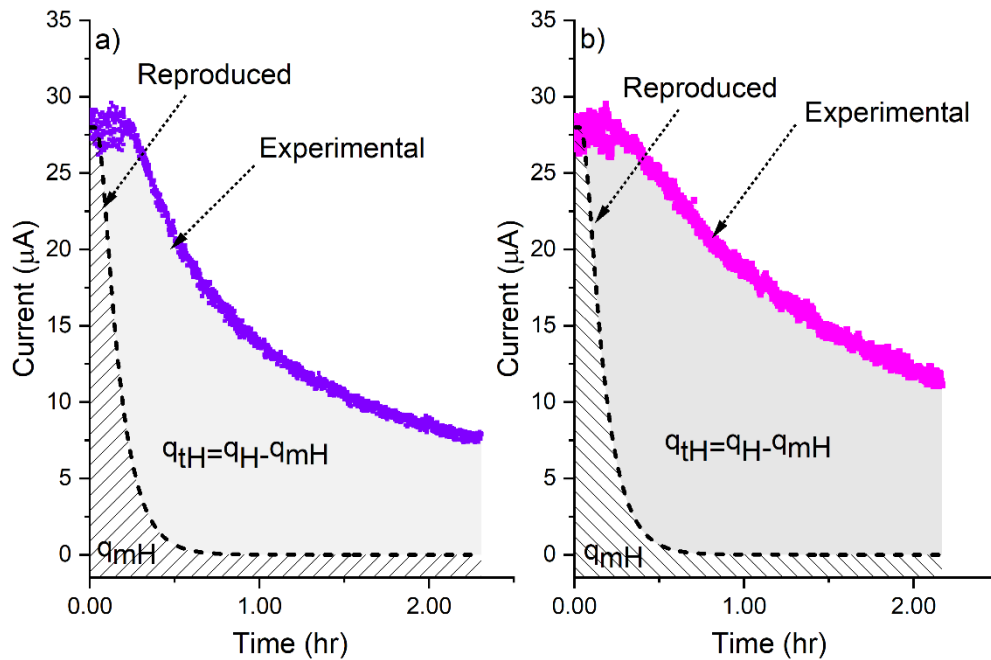


Figure 5.3. An analysis of hydrogen desorption from the steel sample at the detection side (decay region). q_{mH} is the amount of mobile hydrogen, q_{tH} is the amount of trapped hydrogen and q_H is the total amount of hydrogen for a) H cleaned steel and b) H MP steel

By analyzing the decay region according to the Zakroczymski approach, which states that the area between the reproduced and experimental curves is proportional to the amount of trapped hydrogen. The quantity of trapped hydrogen was determined to be approximately $q_{tH} = 8 \cdot 10^{-8}$ mol H·cm⁻² for both heated-cleaned (HC) and heated mechanically polished (H-MP) X60 steel samples. This indicates that surface preparation has a minimal effect on the intrinsic trapping capacity of the material.

The diffusion coefficient of mobile hydrogen ($D_L = (1.1 (0.2) 10^{-9} \text{ m}^2 \cdot \text{s}^{-1})$) was found to be 4–5 times higher than the effective diffusion coefficients obtained from steady-state permeation measurements.

This difference is characteristic of hydrogen trapping: while lattice hydrogen diffuses rapidly, repeated trapping and detrapping at microstructural defects slow the net hydrogen transport, resulting in a lower apparent diffusion coefficient. [20] This finding is in good agreement with the SEM/EDS and XRF results in this research, which confirm the presence of alloying elements in the steel that can serve as hydrogen traps. Additionally, metallographic analysis of the X60 steel after etching with nital solution reveals the presence of ferrite and possibly carbides, both of which can also act as trapping sites for hydrogen.[21]

- **The hydrogen concentration determined using D-S cell vs local hydrogen measurement using the microcapillary cell technique**

Local hydrogen measurements using the microcapillary cell technique reveal significant spatial variability in hydrogen concentration across the X60 steel surface, with values ranging from approximately 0.2 to 0.4 ppm. The three measurement points after hydrogen charging of X60 steel show varying hydrogen oxidation currents, which may be attributed to several factors, including differences in the timing of measurements after hydrogen charging as well as the multiphase microstructure of X60 steel (such as ferrite and bainite or inclusions) [22]. In addition, recent studies in numerical modelling have demonstrated that inclusions within steel microstructures significantly increase local hydrogen concentrations, which promote the accumulation of hydrogen atoms around inclusions. Simulations show that microstructures containing non-metallic inclusions can exhibit local hydrogen concentrations up to 28% higher than those without inclusions, underscoring the critical role of steel purity in hydrogen-induced damage susceptibility [23].

A direct comparison can be made between the local hydrogen concentrations measured by the microcapillary cell and the subsurface hydrogen concentration (C_0) determined from electrochemical hydrogen permeation tests. The permeation experiments yielded subsurface hydrogen concentrations of ($C = 0.66$ (0.02) ppm) for HC X60 steel and (0.80 (0.10) ppm) for H MP X60 steel. These values represent the average concentration of diffusible hydrogen at the entry surface of the steel under steady-state permeation conditions [24], [25].

The local hydrogen concentrations measured by microcapillary technique are consistently lower than the (C_0) values from permeation testing. This is consistent with previous observations and can be explained by the fact that the permeation-derived (C_0) reflects the maximum near-surface concentration of mobile, lattice-diffusible hydrogen during continuous charging [26],[27] whereas the microcapillary cell measures locally oxidizable hydrogen within a confined surface volume after hydrogen charging. [22] The microcapillary technique is thus inherently sensitive to local diffusion, trapping, and potential microstructural heterogeneities at the measurement site.

- **Bulk hydrogen content assessed by inert gas fusion measurements**

Following electrochemical hydrogen charging, the bulk hydrogen concentration measured by inert gas fusion technique increased to approximately 2.17 ppm, confirming the effective electrochemical charging of hydrogen into the steel. Notably, the magnitude of this increase remains modest, highlighting that inert gas fusion measurements of hydrogen provide a bulk-averaged value that integrates hydrogen over the entire sample volume and does not resolve spatial variations or preferential accumulation sites. As a result, the inert gas fusion analysis data primarily reflect the total hydrogen content [28].

- **Influence of steel microstructure and composition on hydrogen uptake in steel**

The steel studied in this work is API 5L X60 steel. API 5L is the standard specification for pipelines of the American Petroleum Institute. The pipelines are made of carbon steel pipes used for oil and gas transmission. The abbreviation “X60” defines the minimum yield strength

(60'000 psi or 415 MPa). This (high) strength is achieved through the addition of alloying elements such as manganese, silicon and chromium. The steels “X65”, “X70” and “X80” have a higher yield strength. X-ray diffraction measurements confirmed that the materials exhibit a body-centered cubic (BCC) and the average crystallite size determined using W-H analysis, indicates a nanocrystalline microstructure of the steel. This microstructure is known to increase the density of grain boundaries.

It is now interesting to evaluate the effective diffusion coefficient D_{eff} and the sub-surface hydrogen concentration C_0 of the different iron-based materials. A high effective diffusion coefficient D_{eff} is related to a very low hydrogen concentration C_0 and vice versa: this appears to be valid for various materials independently from the method applied for the calculation of D_{eff} and C_0 . from annealed and Armco iron [16,17] over the X60 steels studied in this work to X80 base material, welded and heat affected zone (HAZ) [19] as well as LAHSS steel tempered at temperatures between 560°C and 640°C [13]

5.2. Tungsten as a hydrogen permeation barrier

This section addresses the second objective of this study, which is the development and the evaluation of tungsten coatings as hydrogen permeation barriers for X60 steel.

Three main sections are highlighted in this part:

- Study the influence of substrate surface roughness on hydrogen permeation barrier performance.
- Investigate the effect of coating thickness.
- Correlation of the substrate roughness and coating thickness with hydrogen permeation behavior.

5.2. 1. Influence of surface roughness

Three series of W-coated X60 steel samples were prepared (Table 3.2) to study the effects of substrate roughness and coating thickness on hydrogen permeation. XRF and SEM analyses confirm that the selected deposition parameters successfully produced the aimed for coating thickness. Series 1 and Series 2, both with nominal thicknesses of 3 μm , exhibit high tungsten content (>87 wt%), whereas Series 3 displays a significantly lower tungsten fraction as a result of its reduced thickness (1.5 μm) and increased substrate contribution within the XRF information depth. XPS surface analysis of the tungsten coatings showed that the substrate with rougher substrate (Series 1) exhibits a through thickness porosity of 3.5 (0.7) %.

- **Influence of Surface Roughness on Coating Integrity and Microstructure**

SEM cross-sectional imaging (Figure 4.14) reveals the crucial role of substrate roughness in determining coating uniformity and interfacial morphology. The rougher substrate in Series 1

($R_a = 0.4 \mu\text{m}$) results in a wavy interface and substantial thickness variation, while the smoother substrates in Series 2 and Series 3 ($R_a = 0.2 \mu\text{m}$) yield continuous, and uniform interfaces. These results agree with other findings from the literature [29].

XRD analysis in this study reveals that both substrate roughness and coating thickness significantly influence the crystallographic and microstructure of magnetron sputtered tungsten coatings (Figure 4.16). Specifically, series 1 exhibits a polycrystalline microstructure, while Series 2 and Series 3 are characterized by a strong (110) preferred orientation, which can be attributed to the use of smoother substrates. These observations align with previous studies in literature which highlight that the substrate roughness and controlled deposition condition influence the coating performance. [30]. However, our work extends these findings by demonstrating through Williamson and Hall analysis that reduced coating thickness leads to smaller crystallite sizes and increase micro-strain, in particular in series 3 (shows the highest microstrain $0.010 \pm 0.001 \text{ nm}$) (Table 4.16).

- **Influence of surface roughness on the porosity of the coating**

Another particularly innovative aspect of this research is the development of a non-destructive, XPS-based method for quantifying through-thickness porosity in tungsten coatings based on Fe/W signal ratios, which represents a novel methodological advancement. This part of the PhD thesis has already been published [2], the paper is attached as appendix 2.

Clear differences emerged among the three series analyzed. Series 1 exhibited an average open porosity of 3.5% (with a standard deviation of 0.8%), showing notable variations between the three replica samples. Sample 1 demonstrated the lowest porosity, but there was a significant difference in the points analyzed (Table 4.18).

The tungsten coatings on X60 steel produced in series 2 (R_a of the substrate $0.2 \mu\text{m}$, coating thickness $3 \mu\text{m}$) did not show the presence of the iron signal. Thus, the coating had no through-thickness defects. The coating of series 3 with a thickness of $1.5 \mu\text{m}$ showed low through-thickness porosity of about 0.5 % only in one of three replica samples (Table 4.18).

As a reason for the different porosity of the tungsten coating with a thickness of $3 \mu\text{m}$ (series 1 and 2 in Table 4.18), the different surface roughness R_a can be identified: the X60 substrate with higher surface roughness shows 3.5 (0.8) % through-thickness porosity, while the coating on the smoother substrate shows no pores. The effect of the surface roughness of the substrate was tested with TiN/zirconium samples [29]. The increase of surface roughness from $R_a = 0.08$ ($0.03 \mu\text{m}$) to 0.3 ($0.03 \mu\text{m}$), the appearance of the surface became worse and less smooth. Lee et al [31] studied the corrosion behavior of $2.36 \mu\text{m}$ CrN thick films on steel substrate with roughness, R_a of 0.10, 0.20, and $0.31 \mu\text{m}$ and observed that the coating porosity increased with increasing roughness. For a PVD CrN coating, Liu et al.[32] found a decrease in defects as surface roughness decreased with polishing, which changed from 220 grit SiC to a $6 \mu\text{m}$ diamond paste. ISO 4527:2003 [33] recommends a roughness value of R_a lower than $0.2 \mu\text{m}$ to prevent corrosion. A low porosity is even more relevant when using these alloys as HPB, as the

porosity affects hydrogen diffusion. No influence on porosity was revealed for 50 μm thick tantalum coating on steel [34].

Through-coating defects can be revealed by Fe 2p photoelectrons only due to the presence of iron oxide in the pores, resulting from corrosion of the steel substrate during exposure to the atmosphere and mechanical polishing, as confirmed by the analysis of the high-resolution Fe 2p_{3/2} spectra from the W-coated X60 steel sample series 1. Curve fitting was performed according to the literature [2]. The high-resolution spectrum (Figure 5.4) revealed the presence of iron oxides, including FeO with its satellite, and Fe (III)-OOH at peak energies of 709.9 eV, 712.6 eV, and 715.4 eV, respectively (Table 5.2). These results are in good agreement with the results obtained from the X60 steel substrate (see section 4.1.1.4. chapter 4) and published in [37] and with other findings in literature [35] , [36]

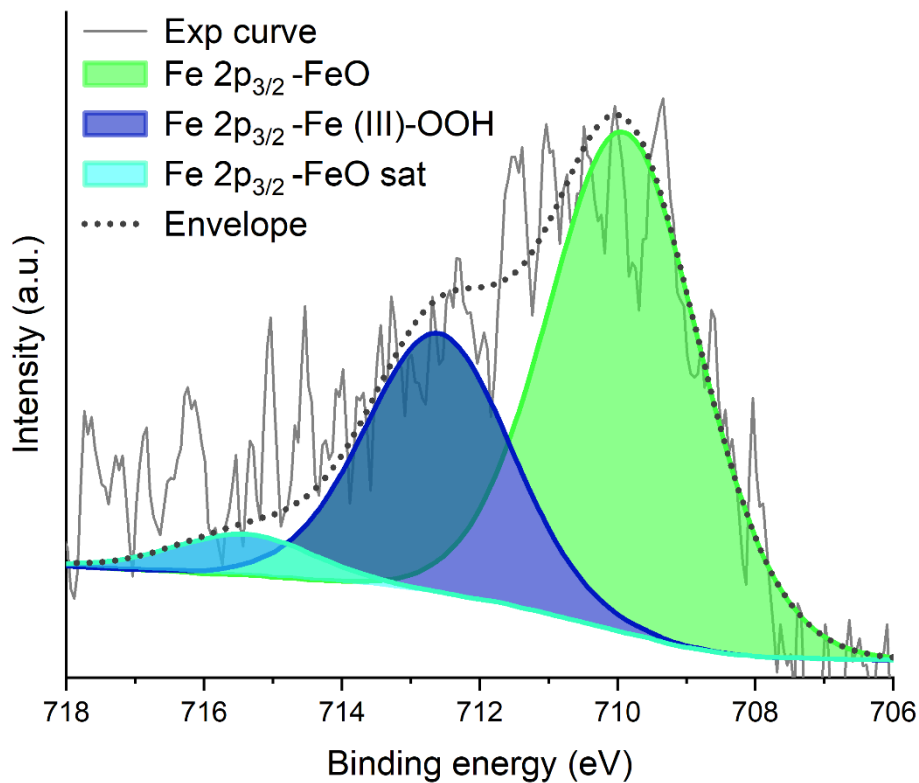


Figure 5.4: Fe 2p_{3/2} high resolution spectra revealed from W-coated X60 steel series 1

Table 5.2. Peak energy values (eV) of F 2p_{3/2} of W coated X60 steel /Series 1) are reported as mean values and the standard deviations given in parentheses; the last three columns list the peak energy values from the literature

Peak energy (eV)	This work- W coated X60 steel (Series 2)	This work -substrate: X60 steel (Table 4.7 and [37])	[35]	[36]
Fe 2p _{3/2} –FeO (Fe ²⁺)	709.9 (0.3)	709.4 (0.2)	709.6 (0.2)	709.7

Fe 2p _{3/2} - OOH	Fe(III)-	712.6 (0.1)	712.6 (0.1)	712.7	712.3
Fe 2p _{3/2} - satellite	FeO	715.4 (0.3)	714.9 (0.2)	715.1 (0.3)	-

- **Surface Chemical Composition and Hydrogen Incorporation in Tungsten Coatings**

RBS/ERDA profiling demonstrates that all coatings are tungsten-rich with the tungsten exceeding 97 wt%, despite the presence of light elements near the surface. Oxygen enrichment is consistently observed in the near-surface region, which might be attributable to post-deposition oxidation and environmental exposure.

Series 2 has the lowest oxygen content, indicative of greater coating density and reduced oxidation susceptibility, consistent with its smoother interface and higher structural uniformity. In fact, these results are consistent those of XPS, indicating that Series 2 exhibits 0% porosity.

Hydrogen was detected across all series; this might suggest that the RF magnetron sputtering process may introduce hydrogen into the coating. The incorporation of hydrogen into tungsten during deposition often occurs due to residual water vapor. It is important to note that hydrogen incorporation during coating is not exclusive to physical vapor deposition techniques; it has also been widely reported in processes such as electrodeposition [38], and in the growth of amorphous Al₂O₃ using thermal atomic layer deposition [39].

The combined use of RBS/ERDA, XPS, and HAXPES provides depth-sensitive chemical analysis that cannot be achieved by any single technique alone. High-resolution W 4f spectra indicate the presence of oxygen as stoichiometric WO₃ and WO₂, as well as metallic tungsten (W (0)) and they remained unchanged within the experimental uncertainty for all the three series and are consistent with values reported in the literature [40], [41], [42]. The identification of both WO₃ and WO₂ can be attributed to post-deposition oxidation processes, which may influence the barrier performance of the coating.

5.2.2. Influence of coating thickness

To isolate the effect of coating thickness, Series 2 and Series 3 were deposited on substrates with identical surface roughness ($R_a = 0.2 \mu\text{m}$) but with different nominal thicknesses (3 μm and 1.5 μm , respectively).

- **Effect on Microstructure and Residual Stress**

The XRD analyses reveals that both Series 2 and Series 3 retain a strong (110) preferred orientation (Figure 4.16), indicating that reducing the coating thickness does not fundamentally alter the crystallographic texture when substrate roughness is controlled. The measured tungsten content closely represents the true composition of the coating, with minimal contribution from substrate iron. In contrast, for Series S3, the W coating thickness of 1.5 μm is comparable to the XRF sampling depth, which allows a substantial portion of the Fe K α X-rays emitted from the substrate to be detected. This results in a lower apparent W fraction and a higher Fe fraction in

the measurement. These findings underscore the necessity of accounting for both XRF sampling depth and X-ray attenuation when interpreting elemental compositions in thin film analyses.

Williamson–Hall analysis indicates that the thinner coating in Series 3 exhibits smaller crystallite sizes and increased micro-strain compared to Series 2 (Table 4.16). This suggests that strain accommodation in thinner coatings occurs through microstructural refinement rather than elastic relaxation, consistent with the higher residual stresses measured in both Series 2 and Series 3.

- Effect on Porosity

Series 3 (thickness 1.5 μm) exhibits very low through-thickness porosity ($\sim 0.5\%$) in only one out of three replicate samples, with the remaining samples displaying no detectable defects. This suggests that reducing the coating thickness does not inherently increase porosity, as long as the substrate surface is sufficiently smooth and deposition parameters are carefully controlled.

Literature findings have been reported in other thin-film systems, where porosity is more strongly influenced by factors such as deposition kinetics, surface mobility, and microstructural evolution than by thickness alone. Y.M. Chen et al [40] have studied TiN films deposited by physical vapor deposition and they found that the porosity of TiN coatings is affected by the combined effects of deposition time, temperature and the process parameters during deposition [43]. In addition, according to classical models such as Thornton’s structure zone model [44], porosity formation is primarily associated with growth under low homologous temperature conditions (Zone 1 [44]), where limited adatom mobility and geometric shadowing dominate film growth, leading to intercolumnar voids and strong inheritance of substrate roughness. When deposition conditions promote enhanced surface diffusion or ion-assisted densification, dense and continuous coatings can be achieved even at reduced thicknesses [29], consistent with the low porosity observed in Series 3.

5.2.3. Correlation of the substrate roughness and coating thickness with hydrogen permeation behavior

The hydrogen permeation tests on the X60 steel substrate were reported in Chapter 4, and the average maximum hydrogen permeation current I_{ss} was found to be around 40 μA , the results of electrochemical hydrogen permeation tests on the W-coated X60 steel samples are summarized in Table 4.21.

From the ratio of the steady state permeation rate through the coated membrane, j_{uncoated} divided the permeation rate through the coated membrane j_{coated} , the permeation reduction factor PRF was calculated. $PRF = \frac{j_{\text{uncoated}}}{j_{\text{coated}}}$

The results are given in Table 4.16. The samples of series 2 did not show very low hydrogen detection current; the permeation reduction factor (PRF) was higher than 40. Samples of series 1 instead showed a PRF of only about 4 - 5. Series 2 (coating 1.5 μm thick) showed two samples with PRF > 40, and one sample (sample 2) exhibited a low PRF. The results are in line with the porosity of the coatings (Table 4.18). Electrochemical hydrogen permeation measurements clearly demonstrate that tungsten coatings can substantially reduce hydrogen transport through X60 steel. However, the extent of this reduction depends strongly on coating integrity rather than thickness alone. Series 1, despite having a thickness similar to Series 2, shows a low permeation reduction factor (PRF \approx 4), attributable to its higher porosity and interfacial irregularities. In contrast, Series 2 exhibits PRF up to 40 and Series 3 exhibit PRF value up to 30, despite the reduced thickness of Series 3 it has higher PRF than the series 1 with a higher thickness (3mm) but with higher porosity.

Before going into details in the study of the diffusion of hydrogen into the tungsten coating, I would like to address the effective hydrogen diffusion coefficients for the three series. It is noteworthy that the effective diffusion coefficient for the coated samples is lower than those for bare X60 steel. This observation confirms that tungsten is an effective hydrogen permeation, establishing his role as a hydrogen diffusion barrier.

To isolate the intrinsic hydrogen diffusion properties of the tungsten coating itself, the diffusion coefficient of the film (D_f) was calculated by considering the multilayer structure of the coated samples. Using a two-layer model (Equation 3.6). This equation is only valid when the coating is free of defects, which is why it is not valid in the cases of series 2. [45]

This equation (Equation 3.6). accounts for both the coating and the steel substrate in series. D_f was estimated from permeation data and the known thicknesses of the coating and substrate. The calculated D_f value for series 2 for the tungsten coatings was significantly lower than the effective diffusion coefficients measured for the entire coated system and is presented in Table 5.3 and these results are consistent with findings reported in the literature, which indicate that the diffusion coefficient of tungsten films, regardless of the deposition method, is typically on the order of $10^{-14} \text{ m}^2/\text{s}$ [46]

Table 5.3 Effective diffusion coefficient D_{eff} and diffusion coefficient of the W coating D_f obtained in this work compared with work in the literature, RF-MS: Radio frequency magnetron sputtering, TVA: thermionic vacuum arc. R_a surface roughness, R = deposition rate.

Studies	Sample Series	Deposition technique	W Thickness (μm)	Conditions	D_{eff} (m^2/s)	(D_f) (m^2/s)
This work	W Coat Series 1	RF MS	3	$R_a=0.4 \mu\text{m}$ $R=0.21\text{nm/s}$	$3.5 (0.5) 10^{-10}$	-
This work	W coat Series 2	RF MS	~ 3 .	$R_a=0.2 \mu\text{m}$ $R=0.21\text{nm/s}$	$4.9 (0.2) \times 10^{-11}$	$0.18 (0.07) \times 10^{-14}$

This work	W Coat Series 3	RF MS	~1.5	$R_a = 0.2 \mu\text{m}$ $R = 0.21 \text{ nm/s}$	$9.1 (0.2) \times 10^{-11}$	$0.8 (0.2) \times 10^{-14}$
[46]	W coat Sample 1	TVA	4.1	R_a (NA) $R = 0.079 \text{ nm/s}$		28×10^{-14}
[46]	W coat Sample 2	TVA	2.7	R_a (NA) $R = 0.045 \text{ nm/s}$		0.21×10^{-14}
[46]	W coat Sample 3	TVA	4.2	R_a (NA) $R = 0.046 \text{ nm/s}$		10×10^{-14}
[46]	W coat Sample 4	TVA	4.2	R_a (NA) $R = 0.046 \text{ nm/s}$		4.1×10^{-14}

By concluding this chapter, it is important to highlight that this work demonstrates a significant innovation in the development of an integrated analytical approach combining advanced electrochemical and spectroscopic techniques to investigate hydrogen uptake in steel and to optimize tungsten as hydrogen permeation barriers. A novel XPS-based methodology was established for the quantitative determination of through-thickness porosity in protective coatings. The results of the electrochemical hydrogen permeation experiment further validate this analytical method, revealing that the conventional bi-layer model applicable only to defect-free, non-porous coatings does not hold for series 1 samples exhibiting through-thickness porosity. This direct experimental evidence confirms both the validity and the practical relevance of the new XPS-based approach introduced in this study, marking a substantial advance in the characterization and optimization of hydrogen permeation barriers.

It should be noted that RF magnetron sputtering was chosen in this work for its ability to produce uniform and well-controlled tungsten coatings, ideal for fundamental studies. However, this technique may not be feasible for large-scale or in situ application within pipelines due to practical constraints. The choice of deposition technique is expected to influence coating microstructure, density, defect distribution, and adhesion all of which are critical determinants of hydrogen permeation resistance. Industrially viable alternatives, such as thermal spraying, chemical vapor deposition (CVD), or electrodeposition, may yield coatings with different characteristics and, consequently, different barrier performances. The analytical methodologies developed and validated in this study, particularly XPS-based porosity assessment and electrochemical permeation testing, are broadly applicable and provide a robust framework for evaluating coatings produced by alternative deposition techniques. This enables systematic optimization and supports the translation of these findings toward practical, real-world applications.

In the present study, hydrogen charging was performed in 0.1 M HCl using a cathodic current of -6 mA . Under these cathodic polarization conditions, the electrode potential is typically well below the region where active dissolution or significant oxidation of tungsten occurs. Literature

reports indicate that tungsten is effectively passivated at low pH and moderate potentials, [47]
Thus, tungsten demonstrates good stability under these experimental conditions.

References

- [1] Hannachi, R.; Biggio, D.; Elsener, B.; Fantauzzi, M.; Zacchetti, N.; Rossi, A. A Contribution of XPS and Electrochemistry to the Understanding of Hydrogen Diffusion in X60 Steel. *Coatings* **2025**, *15*, 442, doi:10.3390/coatings15040442.
- [2] Hannachi, R.; Biggio, D.; Elsener, B.; Fantauzzi, M.; Zacchetti, N.; Rossi, A. A Surface Analytical Method for Determining the Porosity of Tungsten Coatings as Hydrogen Permeation Barriers. *Surface and Interface Analysis* **2026**, *58*, 3–8, doi:10.1002/sia.70027.
- [3] Hannachi, R.; Biggio, D.; Elsener, B.; Fantauzzi, M.; Rossi, A. X-Ray Photoelectron Spectroscopy Investigation of X60 Steel. *Surface Science Spectra* **2024**, *31*, 024014, doi:10.1116/6.0003972.
- [4] Biggio, D.; Elsener, B.; Usai, G.; Fantauzzi, M.; Rossi, A. Surface Chemistry of Passive Films on Ni-Free Stainless Steel: The Effect of Organic Components in Artificial Saliva. *Langmuir* **2024**, *40*, 6824–6833, doi:10.1021/acs.langmuir.3c03728.
- [5] Elsener, B.; Pisu, M.; Fantauzzi, M.; Addari, D.; Rossi, A. Electrochemical and XPS Surface Analytical Study on the Reactivity of Ni-Free Stainless Steel in Artificial Saliva. *Materials and Corrosion* **2016**, *67*, 591–599, doi:10.1002/maco.201608930.
- [6] Rossi, A.; Elsener, B.; Hühner, G.; Textor, M.; Spencer, N.D. XPS, AES and ToF-SIMS Investigation of Surface Films and the Role of Inclusions on Pitting Corrosion in Austenitic Stainless Steels. *Surf. Interface Anal.* **2000**, *29*, 460–467, doi:10.1002/1096-9918(200007)29:7%3C460::AID-SIA889%3E3.0.CO;2-T.
- [7] Holt, B. D., & Goodspeed, H. T. (1963). Determination of Nitrogen, Oxygen, and Hydrogen in Metals by Inert Gas Fusion. A Manometric Method. *Analytical Chemistry*, *35*(10), 1510-1513.
- [8] Weiss, Z. Analysis of Hydrogen in Inorganic Materials and Coatings: A Critical Review. *Hydrogen* **2021**, *2*, 225–245, doi:10.3390/hydrogen2020012.
- [9] Smialowski, M. *Hydrogen in Steel: Effect of Hydrogen on Iron and Steel During Production, Fabrication, and Use*; Elsevier, 2014; ISBN 978-1-4832-1371-2.
- [10]. Oriani, R.A. The Diffusion and Trapping of Hydrogen in Steel. *Acta Metallurgica* **1970**, *18*, 147–157, doi:10.1016/0001-6160(70)90078-7.
- [11]. Becker, Th.; Hövel, St.; Kunat, M.; Boas, Ch.; Burghaus, U.; Wöll, Ch. Interaction of Hydrogen with Metal Oxides: The Case of the Polar ZnO(0 0 1) Surface. *Surface Science* **2001**, *486*, L502–L506, doi:10.1016/S0039-6028(01)01120-7.
- [12] Samanta, S.; Kumari, P.; Mondal, K.; Dutta, M.; Singh, S.B. An Alternative and Comprehensive Approach to Estimate Trapped Hydrogen in Steels Using Electrochemical Permeation Tests. *International Journal of Hydrogen Energy* **2020**, *45*, 26666–26687, doi:10.1016/j.ijhydene.2020.07.131.

- [13] Cheng, X.Y.; Zhang, H.X. A New Perspective on Hydrogen Diffusion and Hydrogen Embrittlement in Low-Alloy High Strength Steel. *Corrosion Science* **2020**, *174*, 108800, doi:10.1016/j.corsci.2020.108800.
- [14] Frappart, S.; Feaugas, X.; Creus, J.; Thebault, F.; Delattre, L.; Marchebois, H. Study of the Hydrogen Diffusion and Segregation into Fe–C–Mo Martensitic HSLA Steel Using Electrochemical Permeation Test. *Journal of Physics and Chemistry of Solids* **2010**, *71*, 1467–1479, doi:10.1016/j.jpccs.2010.07.017.
- [15] Fallahmohammadi, E.; Bolzoni, F.; Lazzari, L. Measurement of Lattice and Apparent Diffusion Coefficient of Hydrogen in X65 and F22 Pipeline Steels. *International Journal of Hydrogen Energy* **2013**, *38*, 2531–2543, doi:10.1016/j.ijhydene.2012.11.059.
- [16] Hadam, U.; Zakroczymski, T. Absorption of Hydrogen in Tensile Strained Iron and High-Carbon Steel Studied by Electrochemical Permeation and Desorption Techniques. *International Journal of Hydrogen Energy* **2009**, *34*, 2449–2459, doi:10.1016/j.ijhydene.2008.12.088.
- [17] Drexler, A.; Siegl, W.; Ecker, W.; Tkadletz, M.; Klösch, G.; Schnideritsch, H.; Mori, G.; Svoboda, J.; Fischer, F.D. Cycled Hydrogen Permeation through Armco Iron – A Joint Experimental and Modeling Approach. *Corrosion Science* **2020**, *176*, 109017, doi:10.1016/j.corsci.2020.109017.
- [18] Yao, C.; Ming, H.; Chen, J.; Wang, J.; Han, E.-H. Effect of Cold Deformation on the Hydrogen Permeation Behavior of X65 Pipeline Steel. *Coatings* **2023**, *13*, 280, doi:10.3390/coatings13020280.
- [19] Xue, H.B.; Cheng, Y.F. Hydrogen Permeation and Electrochemical Corrosion Behavior of the X80 Pipeline Steel Weld. *J. of Materi Eng and Perform* **2013**, *22*, 170–175, doi:10.1007/s11665-012-0216-1.
- [20] Lупpo, M.I.; Ovejero-Garcia, J. The Influence of Microstructure on the Trapping and Diffusion of Hydrogen in a Low Carbon Steel. *Corrosion Science* **1991**, *32*, 1125–1136, doi:10.1016/0010-938X(91)90097-9.
- [21] Hong, G.-W.; Lee, J.-Y. The Interaction of Hydrogen and the Cementite-Ferrite Interface in Carbon Steel. *J Mater Sci* **1983**, *18*, 271–277, doi:10.1007/BF00543835.
- [22] Jürgensen, J.; Pohl, M. Local Hydrogen Measurements in Multi-Phase Steel C60E by Means of Electrochemical Microcapillary Cell Technique. *Metals* **2023**, *13*, 1585. <https://doi.org/10.3390/met13091585>
- [23] Tekkaya, B.; Dölz, M.; Münstermann, S. Modeling of Local Hydrogen Concentration on Microscopic Scale to Characterize the Influence of Stress States and Non-Metallic Inclusions in Pipeline Steels. *International Journal of Hydrogen Energy* **2024**, *50*, 1274–1287, doi:10.1016/j.ijhydene.2023.10.158.
- [24] ISO 17081:2014 <https://www.iso.org/standard/64514.html>

- [25] Zakroczymski, T. Adaptation of the Electrochemical Permeation Technique for Studying Entry, Transport and Trapping of Hydrogen in Metals. *Electrochimica Acta* **2006**, *51*, 2261–2266, doi:10.1016/j.electacta.2005.02.151.
- [26] Pereira, V.; Hincapie, D.; Nishikawa, L.; Goldenstein, H. *Effect of Microstructure on Hydrogen Diffusivity, Trapping and HIC Resistance in Two API X65 Steels*; 2017;
- [27] Marchi, C.S.; Somerday, B.P.; Robinson, S.L. Permeability, Solubility and Diffusivity of Hydrogen Isotopes in Stainless Steels at High Gas Pressures. *International Journal of Hydrogen Energy* **2007**, *32*, 100–116, doi:10.1016/j.ijhydene.2006.05.008.
- [28] ASTM E1447-09. (2009). Standard Test Method for Determination of Hydrogen in Titanium and Titanium Alloys by the Inert Gas Fusion Thermal Conductivity/Infrared Detection Method..
- [29] Xiao, W.; Deng, H.; Zou, S.; Ren, Y.; Tang, D.; Lei, M.; Xiao, C.; Zhou, X.; Chen, Y. Effect of Roughness of Substrate and Sputtering Power on the Properties of TiN Coatings Deposited by Magnetron Sputtering for ATF. *Journal of Nuclear Materials* **2018**, *509*, 542–549, doi:10.1016/j.jnucmat.2018.07.011.
- [30] Jiang, J.; Arnell, R.D. The Effect of Substrate Surface Roughness on the Wear of DLC Coatings. *Wear* **2000**, *239*, 1–9, doi:10.1016/S0043-1648(99)00351-8.
- [31] Lee, S.-C.; Ho, W.-Y.; Lai, F.D. Effect of Substrate Surface Roughness on the Characteristics of CrN Hard Film. *Materials Chemistry and Physics* **1996**, *43*, 266–273, doi:10.1016/0254-0584(95)01636-9.
- [32] Liu, C.; Bi, Q.; Leyland, A.; Matthews, A. An Electrochemical Impedance Spectroscopy Study of the Corrosion Behaviour of PVD Coated Steels in 0.5 N NaCl Aqueous Solution: Part I. Establishment of Equivalent Circuits for EIS Data Modelling. *Corrosion Science* **2003**, *45*, 1243–1256, doi:10.1016/S0010-938X(02)00213-5.
- [33] ISO 4527:2003 - Metallic Coatings — Autocatalytic (Electroless) Nickel-Phosphorus Alloy Coatings — Specification and Test Methods Available online: <https://www.iso.org/standard/36258.html> (accessed on 19 January 2026).
- [34] Maeng, S.M.; Axe, L.; Tyson, T.A.; Gladczyk, L.; Sosnowski, M. Corrosion Behavior of Magnetron Sputtered α -Ta Coatings on Smooth and Rough Steel Substrates. *Surface and Coatings Technology* **2006**, *200*, 5717–5724, doi:10.1016/j.surfcoat.2005.08.128.
- [35] Elsener, B.; Fantauzzi, M.; Rossi, A. Stainless Steels: Passive Film Composition, Pitting Potentials, and Critical Chloride Content in Concrete. *Materials and Corrosion* **2020**, *71*, 797–807, doi:10.1002/maco.202011557.
- [36] Biesinger, M.C.; Payne, B.P.; Grosvenor, A.P.; Lau, L.W.M.; Gerson, A.R.; Smart, R.St.C. Resolving Surface Chemical States in XPS Analysis of First Row Transition Metals, Oxides and Hydroxides: Cr, Mn, Fe, Co and Ni. *Applied Surface Science* **2011**, *257*, 2717–2730, doi:10.1016/j.apsusc.2010.10.051.

- [37] Hannachi, R.; Biggio, D.; Elsener, B.; Fantauzzi, M.; Zacchetti, N.; Rossi, A. A Contribution of XPS and Electrochemistry to the Understanding of Hydrogen Diffusion in X60 Steel. *Coatings* **2025**, *15*, 442, doi:10.3390/coatings15040442.
- [38] Zamanzadeh, M.; Allam, A.; Kato, C.; Ateya, B.; Pickering, H.W. Hydrogen Absorption during Electrodeposition and Hydrogen Charging of Sn and Cd Coatings on Iron. *J. Electrochem. Soc.* **1982**, *129*, 284, doi:10.1149/1.2123813.
- [39] Cancellieri, C.; Gramatte, S.; Politano, O.; Lapeyre, L.; Klimashin, F.F.; Mackosz, K.; Utke, I.; Novotny, Z.; Müller, A.M.; Vockenhuber, C.; et al. Effect of Hydrogen on the Chemical State, Stoichiometry and Density of Amorphous Al₂O₃ Films Grown by Thermal Atomic Layer Deposition. *Surface & Interface Analysis* **2024**, *56*, 293–304, doi:10.1002/sia.7282.
- [40] Olsson, C.-O.A.; Mathieu, H.-J.; Landolt, D. Angle-Resolved XPS Analysis of Molybdenum and Tungsten in Passive Films on Stainless Steel PVD Alloys. *Surface and Interface Analysis* **2002**, *34*, 130–134, doi:10.1002/sia.1268.
- [41] Bussolotti, F.; Lozzi, L.; Passacantando, M.; La Rosa, S.; Santucci, S.; Ottaviano, L. Surface Electronic Properties of Polycrystalline WO₃ Thin Films: A Study by Core Level and Valence Band Photoemission. *Surface Science* **2003**, *538*, 113–123, doi:10.1016/S0039-6028(03)00696-4.
- [42] Briggs, D.; Seah, M.P. *Practical Surface Analysis, Auger and X-Ray Photoelectron Spectroscopy*; Wiley, 1990; ISBN 978-0-471-92081-6.
- [43] Chen, Y.M.; Yu, G.P.; Huang, J.H. On the Porosity of TiN Films Deposited by HCD Ion Plating. *Surface and Coatings Technology* **2002**, *155*, 239–244, doi:10.1016/S0257-8972(02)00049-X.
- [44] Thornton, J.A. High Rate Thick Film Growth. *Annu. Rev. Mater. Sci.* **1977**, *7*, 239–260, doi:10.1146/annurev.ms.07.080177.001323.
- [45] Zajec, B. Hydrogen Permeation Barrier – Recognition of Defective Barrier Film from Transient Permeation Rate. *International Journal of Hydrogen Energy* **2011**, *36*, 7353–7361, doi:10.1016/j.ijhydene.2011.03.068.
- [46] Nemanič, V.; Kovač, J.; Lungu, C.; Porosnicu, C.; Zajec, B. Characterization of Tungsten Films and Their Hydrogen Permeability. *Journal of Vacuum Science & Technology A: Vacuum, Surfaces, and Films* **2014**, *32*, 061511, doi:10.1116/1.4898061.
- [47] Weidman, M. C., Esposito, D. V., Hsu, I. J., & Chen, J. G. (2010). Electrochemical stability of tungsten and tungsten monocarbide (WC) over wide pH and potential ranges. *Journal of The Electrochemical Society*, *157*(12), F179-F188.

6. Conclusions and outlook

This work demonstrates that the developed tungsten coating is suitable for obtaining an effective hydrogen permeation barrier for API 5L X60 pipeline steel. By developing advanced analytical techniques and electrochemical (Devanathan–Stachurski cell), a comprehensive and quantitative assessment of hydrogen transport was achieved, supporting a rigorous evaluation of barrier effectiveness.

In this study, both uncoated X60 steel and samples coated with the tungsten-based hydrogen permeation barrier were investigated. Comparative analyses of the uncoated and coated substrates enabled direct quantification of the barrier's impact on hydrogen diffusion. The application of several different analytical techniques allowed for precise measurement of effective hydrogen diffusion coefficients and subsurface hydrogen concentrations in both configurations, providing clear evidence of the enhanced protective performance conferred by the tungsten coating.

Hydrogen permeation testing provided precise quantification of the effective hydrogen diffusion coefficient (D_{eff}) and subsurface hydrogen concentration (C_0). D_{eff} values, determined through time-lag and breakthrough time methods, were consistent with established literature. The measured subsurface hydrogen concentrations were significantly lower than those reported for higher-strength pipeline steels.

A notable innovation of this study is the rapid, non-destructive quantification of through-thickness porosity in tungsten coatings using a novel analytical approach based on X-ray photoelectron spectroscopy (XPS).

Electrochemical hydrogen permeation experiments established a clear correlation between coating porosity and barrier efficiency. Dense tungsten coatings reduced hydrogen permeability and the effective diffusion coefficient, whereas porous coatings displayed lower barrier performance. These findings demonstrate that coating quality defined by uniformity, defect density, and interfacial integrity is the dominant factor in hydrogen permeation barrier performance, with coating thickness as a secondary parameter.

Depth-profiling analyses, including RBS/ERDA and advanced XPS techniques, revealed an oxygen-enriched near-surface region within the tungsten layer. These chemically modified layers further enhance the hydrogen barrier properties and underscore the importance of combining analytical techniques with electrochemical evaluation to develop next-generation hydrogen permeation barriers.

Future work will aim to deepen the understanding of hydrogen diffusion and trapping in hydrogen permeation barriers and steel by integrating electrochemical hydrogen permeation experiments with multiscale modeling. By coupling Devanathan–Stachurski permeation data with physically based diffusion–trapping models, it will be possible to develop predictive descriptions of hydrogen transport that account for lattice diffusion, reversible trapping at microstructural defects, and the effects of coating integrity. This approach will facilitate quantitative assessment of hydrogen permeation behavior under various charging conditions

and provide greater insight into the interplay between bulk diffusion and surface or interface-controlled processes.

An important direction for future research is the long-term stability of tungsten coatings as hydrogen permeation barriers under realistic service conditions. Further studies should evaluate coating performance under combined mechanical loading, cyclic stress, and corrosive environments that simulate actual pipeline operation. Special emphasis should be placed on monitoring the evolution of coating porosity, interfacial integrity, and residual stress, and understanding how these factors influence hydrogen transport during extended exposure. Such investigations are crucial for assessing the durability and reliability of tungsten-based hydrogen barrier systems in practical applications.

The analytical framework established in this study, combining electrochemical permeation testing with surface-sensitive and depth-resolved characterization, will also be applied to alternative coating materials and different grades of pipeline steel. Expanding this methodology to diverse coating systems and substrate microstructures will help identify general principles for designing hydrogen-resistant materials. These comparative studies will contribute to developing a strong guideline for the selection and optimization of hydrogen permeation barriers, ultimately supporting the safe and efficient implementation of hydrogen transport and storage infrastructure.

7. Appendix

7.1. Techniques overview

This chapter outlines the physical principles of the techniques employed in this research.

7.1.1.. Electrochemical hydrogen permeation test: Devanathan and Stachurski cell

The hydrogen permeation test can be performed using the Devanathan–Stachurski cell, which allows investigating hydrogen transport, uptake, and trapping in steel [1]. In this technique, a metallic sample that acts as a “membrane” separating two electrochemical cells: a hydrogen charging (entry) side and a detection (oxidation) side as depicted in the scheme of Figure 7.1.a.

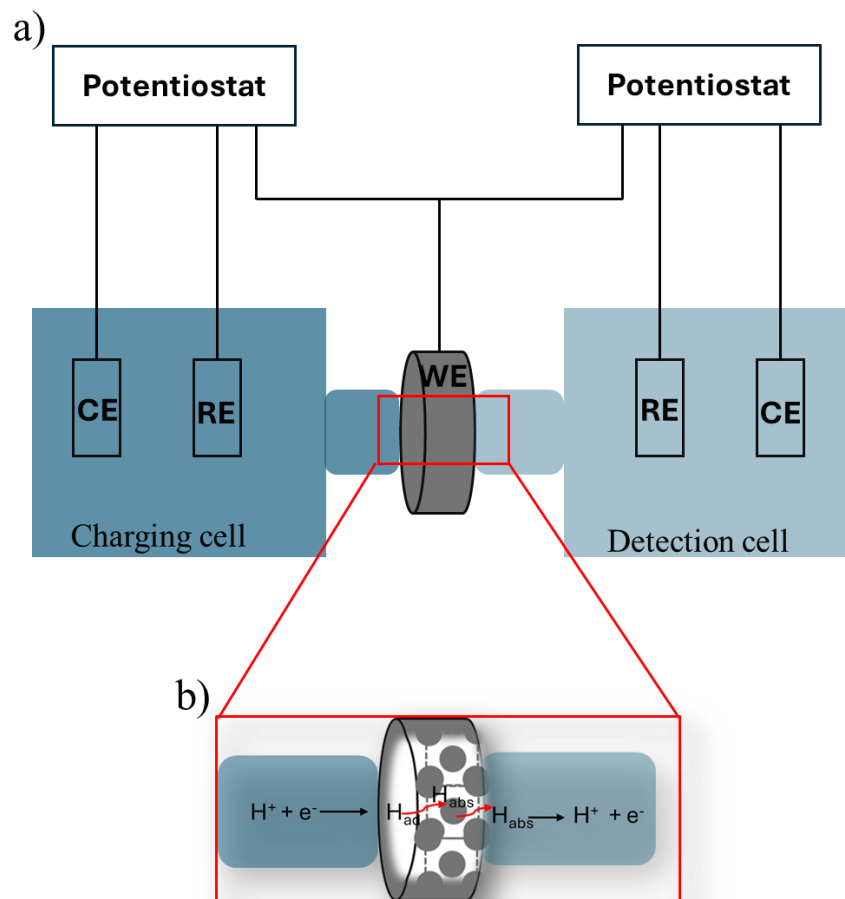
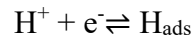


Figure 7.1. a) Electrochemical hydrogen permeation cell setup (Devanathan–Stachurski cell). b) Schematic representation (not to scale) of the hydrogen reactions at the sample surface on the charging side (left), hydrogen diffusion through the steel membrane, and hydrogen oxidation on the detection side (right). Hydrogen ions (H^+) are reduced at the charging side to atomic hydrogen, which is partially absorbed into the steel (H_{abs}) and diffuses through the sample toward the detection side, where it is oxidized to H^+ .

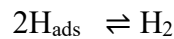
On the charging side, a cathodic current is applied to the sample, which is immersed in an aqueous electrolyte, typically acidified to promote hydrogen evolution. The primary electrochemical reactions are Volmer, Tafel and Heyrovsky reactions [2] :

Volmer Reaction



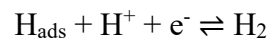
Protons from the electrolyte are reduced to form adsorbed hydrogen atoms on the metal surface.

Tafel Reaction (Recombination):



Two adsorbed hydrogen atoms recombine to form molecular hydrogen

Heyrovsky Reaction



An adsorbed hydrogen atom combines with a proton and an electron to evolve hydrogen gas.

However, the goal in permeation studies is to maximize the fraction of hydrogen that enters the metal lattice as atomic hydrogen $\text{H}_{\text{ads}} \rightleftharpoons \text{H}_{\text{abs}}$, rather than recombining and leaving as gas.

To inhibit the recombination reactions (Tafel and Heyrovsky steps) and promote hydrogen absorption, additives such as arsenic oxide (As_2O_3) known as hydrogen recombination poisons are often added to the charging electrolyte [3].

Hydrogen Diffusion Through the sample

Once hydrogen absorbed (Figure 1.b), hydrogen atoms diffuse through the metal membrane from the entry side to the detection side under a concentration gradient according to Fick's first law:

$$j = -D \frac{dC}{dx} \quad (1)$$

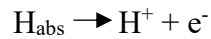
J is the hydrogen flux in $\text{mol cm}^{-2} \text{ s}^{-1}$

D is the diffusion coefficient $\text{cm}^2 \text{ s}^{-1}$

dC/dx is the concentration gradient

Detection and Measurement at the Oxidation Side

At the detection side (oxidation cell), hydrogen atoms emerging at the metal surface are immediately oxidized:



This oxidation reaction generates an anodic current $I(t)$ that is directly proportional to the hydrogen flux ($J(t)$):

$$J(t) = \frac{I(t)/A}{F} \quad (2)$$

F is Faraday's constant ($96,485 \text{ C}\cdot\text{mol}^{-1}$)

A is the exposed area of the sample in the oxidation cell (cm^2)

Data processing: models and calculations

The hydrogen permeation experiment gives a current versus time curve that typically consists of three main regions [4]

Build-Up: Immediately after the start of hydrogen charging, the permeation current increases as hydrogen atoms diffuse through the sample, reaching a steady state.

Steady state: Steady state is reached when the permeation current stays nearly constant. This means the amount of hydrogen entering the detection side is equal to the amount being supplied at the charging side

Decay: After hydrogen charging is stopped, the permeation current decreases as the hydrogen content begins to de-trap.

The time lag method (t_{lag}) and the breakthrough (t_b) method [3] can be used to determine the effective hydrogen diffusion coefficient (D_{eff} (m^2/s)) from the transient region in the permeation curve.

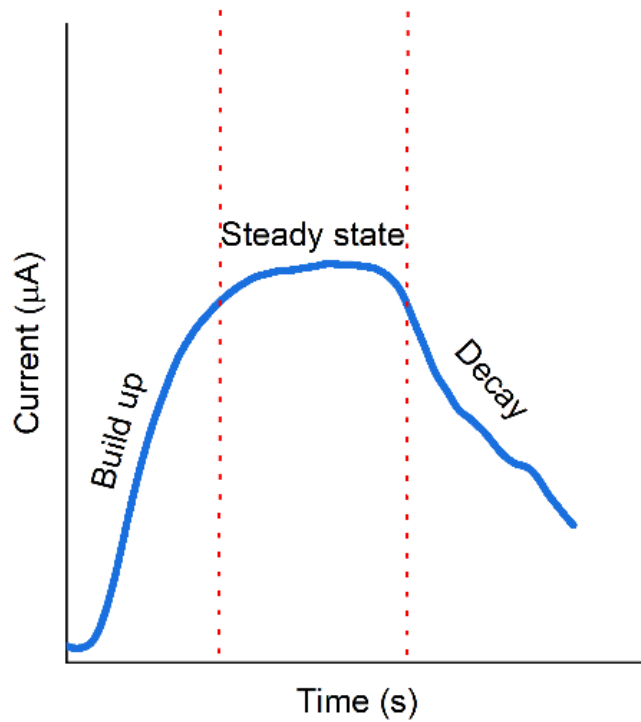


Figure 7.2. A schematic plot of the current–time curve that exhibits three distinct regimes: build-up, steady-state, and decay. During the build-up phase, the measured current (in μA) progressively increases, followed by a steady-state plateau, demarcated by the dashed red lines, where the current remains relatively constant. Upon the stop of hydrogen production, the current enters the decay phase, characterized by hydrogen desorption from the sample.

In the t_{lag} method, D_{eff} is calculated using this equation.

$$D_{\text{eff}} = \frac{L^2}{6t_{\text{lag}}} \quad (3)$$

In the t_b method D is calculated using this equation

$$D_{\text{eff}} = \frac{L^2}{15.3t_b} \quad (4)$$

Where L is the thickness in (m) of the sample, t_{lag} is the time in (s) required to reach 63 % of steady state current density (I_{ss}), and t_b is the breakthrough time in seconds that corresponds to the intersection of the tangent line at the inflection point and the x-axis in the permeation curve. (Figure 7.3)

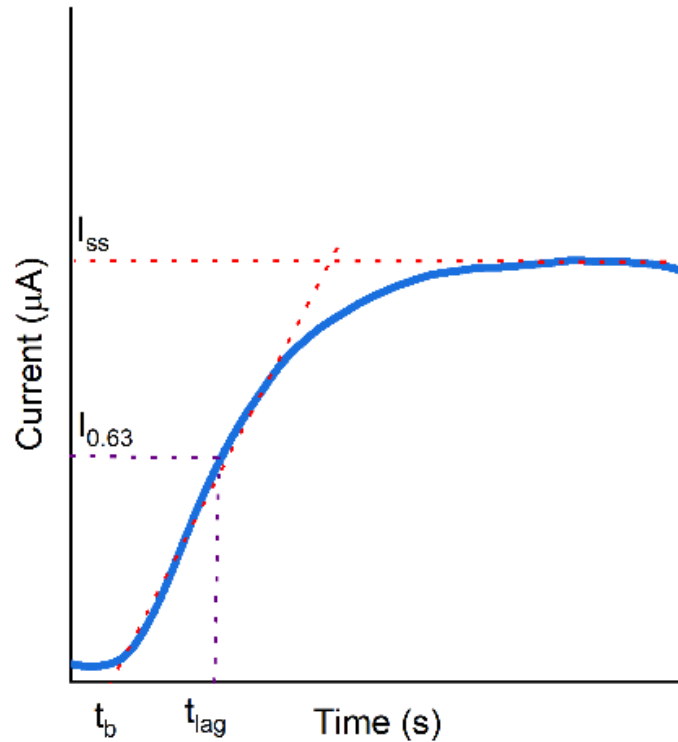


Figure 7.3. Characteristic times for hydrogen diffusion derived from the current–time transient. The steady-state current is represented by the red dashed line. The lag time (t_{lag}) the breakthrough time (t_b) corresponds to the intersection of the tangent to the build-up transient at its inflection point with the time (x) axis.

For greater accuracy, the transient build-up and decay regions can be directly fitted to Fick’s diffusion-based permeation equations [4]

Build-Up Equation:

$$\frac{I_p - I_p^0}{I_p^\infty - I_p^0} = \frac{2L}{\sqrt{\pi D_{eff} t}} \sum_{n=0}^{\infty} \exp\left(-\frac{L^2(2n+1)^2}{4D_{eff} t}\right) \quad (5)$$

Decay Equation:

$$\frac{I - I_p^\infty}{I_p - I_p^\infty} = 1 - \frac{2L}{\sqrt{\pi D_{eff} t}} \sum_{n=0}^{\infty} \exp\left(-\frac{L^2(2n+1)^2}{4D_{eff} t}\right) \quad (6)$$

Where I_p is the permeation current at time t , I_p^0 the initial steady-state current, and I_p^∞ is the new steady-state current after the hydrogen production stops.

In addition, the subsurface hydrogen concentration of mobile hydrogen, C_0 , can be determined by equation (7) [5]

$$C_0 = \frac{i_{ss}L}{FD_{eff}} \frac{M_H}{\rho_{Fe}} 10^6 \quad (7)$$

Where i_{ss} is the steady state permeation current density (A/m^2), L is the thickness of the sample (m), D_{eff} is the effective diffusion coefficient (m^2/s) F is the Faraday constant (96,485 C/mol), M_H is the molar mass of hydrogen (1g/mol), and ρ_{Fe} is the iron density ($7.87 * 10^6 g/m^3$).

The diffusion coefficient within the hydrogen permeation barrier (film) was determined using this model (equation 8) [6]

$$D_f = \frac{D_s D_{eff}(PRF+2)}{D_{eff}(2-3PRF)(\frac{L_s}{L_f})^2 + D_s PRF(1+\frac{L_s}{L_f})^2} \quad (8)$$

where: D_f is the diffusion coefficient of the film (m^2/s), D_s is the diffusion coefficient of the substrate (m^2/s), D_{eff} is the effective diffusion coefficient of the two-layer membrane obtained from time-lag analysis (m^2/s) $= \frac{L_s+L_f}{6t_{lag2}}$, L_s is the substrate thickness (m) and L_f is the film thickness (m).

PRF is the permeation reduction factor determined as the ratio of the steady-state hydrogen flux through the uncoated substrate to the coated sample ($PRF = \frac{J_{uncoated}}{J_{coated}}$).

The amount of trapped hydrogen in the X60 steel samples can be determined using the Zakroczymski approach [4], which consists of analyzing the decay region of the transient hydrogen permeation. The method consists of two main steps:

- **Determination of the diffusion coefficient of mobile hydrogen**

The diffusion coefficient of mobile hydrogen, D_L , can be obtained from permeation transients

The sample must be charged at a specific cathodic charging current density until the anodic current reached steady state. Immediately afterwards, the cathodic charging current have to be increased to generate a second transient. The decay region of the second transient (corresponding to the cathodic current density -1 mA/cm²) can fitted using the build-up equation (equation 5) to determine D_L . This provides the diffusion coefficient of the mobile hydrogen.

- **Analysis of the decay/desorption region to quantify trapped and diffusible hydrogen**

Once D_L is known the decay/desorption region of the transient permeation can be analyzed to distinguish between trapped hydrogen and mobile hydrogen. Basically, the anodic current of the desorption curve $I_H(t)$ corresponds to the sum of the current of the trapped hydrogen $I_{tH}(t)$ and the current of the mobile hydrogen $I_{mH}(t)$ (equation9).

$$I_H(t) = I(t) + I_{tH}(t) \quad (9)$$

Where, $I_{mH}(t)$ is the desorption current of mobile hydrogen and $I_{tH}(t)$ is the desorption current of reversible trapped hydrogen.

Knowing D_L and assuming that the steady-state current I_p^∞ (equivalent to the initial desorption current I_H^0) corresponds to the desorption current of diffusible hydrogen, the desorption current of mobile hydrogen, $I_{mH}(t)$, can be reconstructed using the decay equation (equation 6). Subtracting $I_{mH}(t)$ from the total desorption current $I_H(t)$ gives the trapped hydrogen desorption current.

$$I(t) = I_H(t) - I_{mH}(t) \quad (10)$$

The total hydrogen per unit area is given by the area under the measured curve:

$$q_H = \int I_H(t) dt \quad (11)$$

Similarly:

$$q_{mH} = \int I_{mH}(t) dt \quad (12)$$

$$q_{tH} = \int I_{tH}(t) dt \quad (13)$$

Where q_{mH} is the amount of mobile hydrogen and q_{tH} is the amount of trapped hydrogen

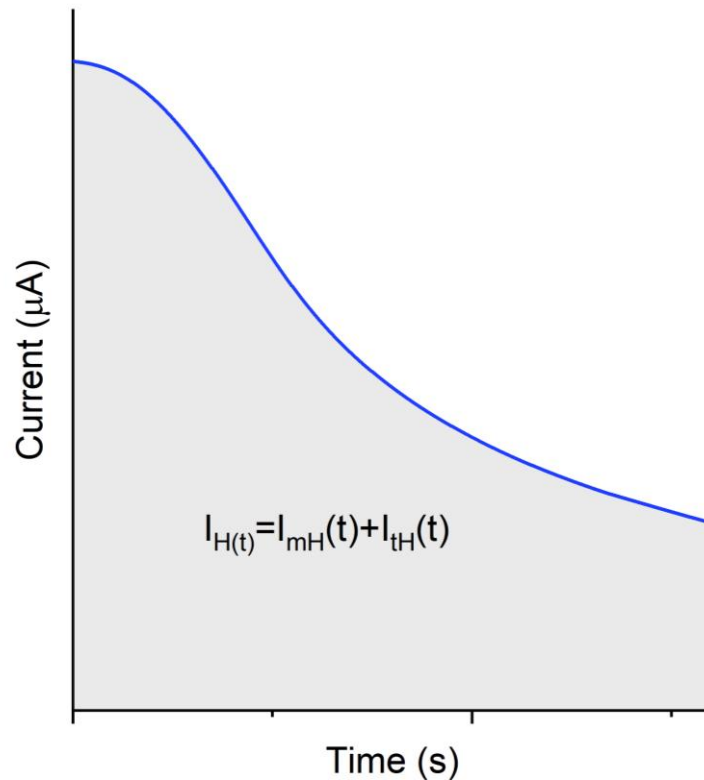


Figure 7.4. Example of the decay curve of steel, $I_H(t)$ is the anodic current of hydrogen, $I_{mH}(t)$ is the desorption current of mobile hydrogen and $I_{tH}(t)$ is the desorption current of reversible trapped hydrogen

7.1.2. The Electrochemical Microcapillary cell technique

The electrochemical microcapillary cell technique represents a significant advancement in the spatially resolved investigation of hydrogen uptake in metallic systems [7],[8], [9].

The microcapillary technique confines the electrolyte to a well-defined microscopic region using a glass capillary with a maximum tip diameter of 1,000 mm [10], the setup (Figure 7.5) forms a localized electrochemical cell on the sample surface, with the capillary opening defining the working electrode area, and integrated reference electrode (RE) and counter electrode (CE) completing the circuit and those are connected to the potentiostat. The rest of the specimen remains electrochemically inactive, ensuring that hydrogen evolution and absorption are exclusively driven and measured within the microregion of the exposed area.

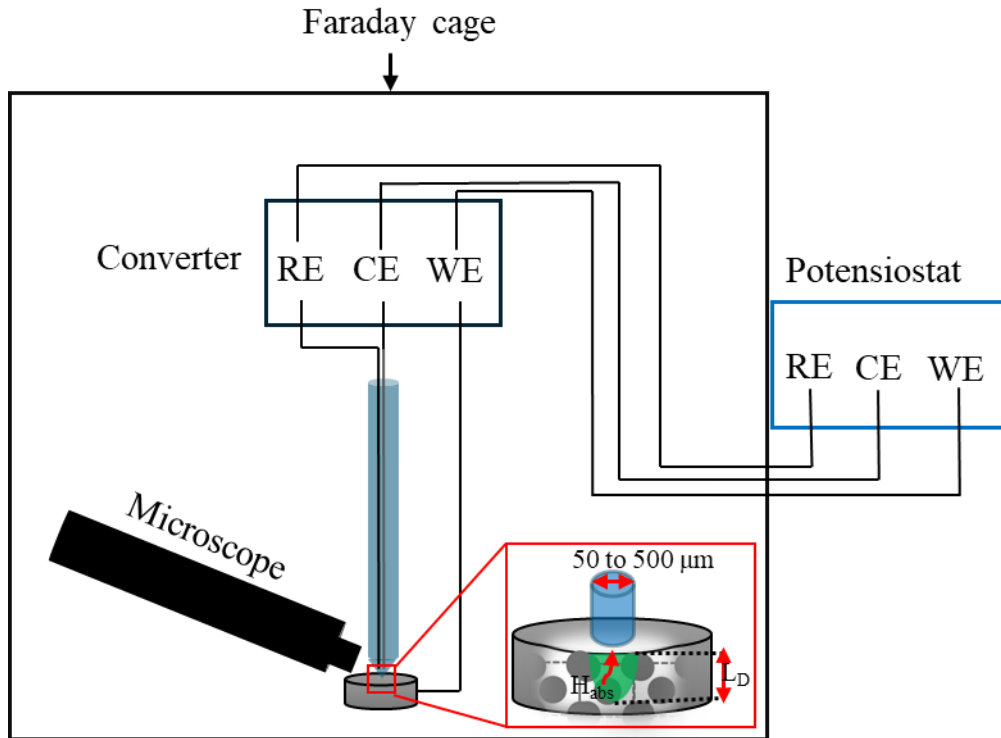


Figure 7.5. Schematic representation of the microcapillary cell technique setup. The microcapillary cell is positioned on the sample surface, defining a localized electrochemical area. The zoomed view highlights the localized hydrogen entry beneath the microcapillary and the subsequent diffusion of hydrogen into the sample thickness, indicated by the arrows.

The microcapillary technique enables accurate measurement of local hydrogen measurement within localized area from which absorbed hydrogen diffuse out from the sample, then the current of the oxidized hydrogen will be measured. The concentration of hydrogen can be quantified for specific microstructural regions. This is critical for correlating hydrogen absorption with localized plastic strain, phase distribution, and microstructural damage factors.

Data processing

The hydrogen concentration can be determined from the microcapillary cell measurements using the approach based on the Faraday second law [8] (Equation 14)

$$c_H = \frac{Q_H - Q_{Ref}}{n.F.V} \quad (14)$$

Where: c_H is the hydrogen concentration in ppm, Q_H is the electric charge in C of the charged sample Q_{ref} is the electric charge in C of the uncharged sample n : Number of oxidized electrons, and V is the effective diffusion volume.

$$V = \frac{4}{3} \cdot (a + LD)^2 L_D \quad (15)$$

Where a is the radius of the microcapillary, L_D is the diffusion distance of hydrogen during the measurement.

7.1. 3.. X-ray photoelectron spectroscopy

The fundamentals of X-ray photoelectron spectroscopy

X-ray photoelectron spectroscopy (XPS) is a powerful surface-sensitive analytical technique used to determine the elemental composition and chemical states of the outermost layers of solid materials [11]. The method is based on the photoelectric effect: when a sample is irradiated with monochromatic X-rays, core-level electrons and valence band are ejected from atoms within the sample. The kinetic energy (KE) of these photoelectrons is measured by the spectrometer, resulting in a spectrum composed of discrete bands that correspond to the binding energies (BE) of electrons in specific atomic orbitals [24]. The relationship between the binding energy, photon energy, and measured kinetic energy of the emitted electron is given by the Einstein relation:[12]

$$BE = hn - KE - \phi^{sp} \quad (24)$$

where hn is the photon energy, ϕ_{sp} is the spectrometer work function, and KE is the measured kinetic energy. The binding energy is referenced to the Fermi level of the sample, allowing for the identification of elements and the determination of their chemical states.

For conductive samples, electrical grounding ensures that the Fermi level of the specimen is aligned with that of the spectrometer (Figure 7.6.a adapted from [12]). Under these conditions, the kinetic energy of a photoemitted electron referenced to the sample's Fermi level is described by

$$KE_1 = hn - BE^F - \phi^s \quad (25)$$

where BE^F is the binding energy of the photoelectron relative to the Fermi level, and ϕ^s denotes the work function of the sample (see Figure 6. a) However, the kinetic energy ultimately measured by the spectrometer, (KE_2), is influenced by the difference between the spectrometer's work function (ϕ^{sp}) and that of the sample, and is given by:

$$KE_2 = hn - BE^F - \phi^s - (\phi^{sp} - \phi^s) \quad (26)$$

The spectrometer work function (ϕ^{sp}) is typically determined through experimental calibration procedures.

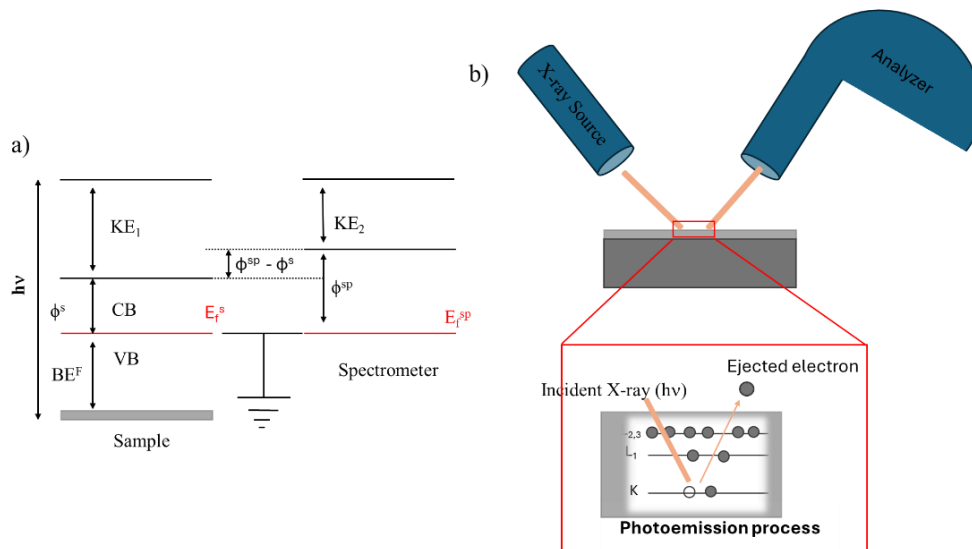


Figure 7.6.a) Schematic representation of the energy level alignment in conductive samples during an XPS experiment adapted from [25] b) Illustration depicting the photoemission process

The photoemission process:

The photoemission process is illustrated schematically in Figure 6.b. This phenomenon occurs when the energy of the incident photon exceeds the binding energy (BE) of the electron, allowing it to be emitted from the material.

The photoionization cross section and sampling depth in XPS:

The relative intensity of spectral peaks in XPS is fundamentally governed by the photoionization cross section (σ), which depends on the atomic number, quantum numbers, and the proximity of the photon energy to the photoemission threshold.[13]

The depth from which XPS can probe, or the sampling depth, is determined by the attenuation length (Λ), which is related to the inelastic mean free path (IMFP, λ) of the photoemitted electrons. The IMFP is defined as “*the average distance an electron with a given kinetic energy can travel within a material before undergoing inelastic scattering*” [12].

The attenuation length further depends on the kinetic energy of the emitted electrons, the material under investigation, and the emission angle ,

The relationship between attenuation length and IMFP is given by equation 27 [12]

$$\Lambda = \lambda \cos \theta \quad (27)$$

The measured photoelectron signal intensity as a function of depth (d) can be described by the exponential attenuation law (equation 28) [12]

$$I_z = I_0 \exp \frac{-z}{\lambda \cos \theta} \quad (28)$$

where (I_0) is the intensity originating from depth z and λ is the inelastic mean free path and θ is the emission angle. the sampling depth is estimated to be

$$d = 3\lambda \cos \theta \quad (29)$$

Several models have been developed to estimate IMFP values based on the kinetic energy of electrons and the properties of the material. One of the most widely used empirical formulations is that of Seah and Dench [14] , who analyzed a broad range of experimental data to derive a simple equation for IMFP (λ) as a function of electron kinetic energy (KE):

$$\lambda = \frac{A}{KE^2} + B\sqrt{KE} \quad (30)$$

where (A) and (B) are empirical parameters that vary depending on the material (e.g., elements, organics, inorganics), and KE is given in electron volts. Typical parameter values are (A = 143) and (B = 0.054) for elements, (A = 31) and (B = 0.087) for organics, and (A = 641) and (B = 0.046) for inorganics. [27]

In addition to empirical approaches, more physically based predictive models, such as the TPP-2M model developed by Tanuma, Powell, and Penn, have been introduced.

The TPP-2M equation [15] takes into account material-specific electronic properties and is expressed as:

$$\lambda = \frac{E}{E_p^2 [\beta \ln(\gamma E) - CE^{-1} + CE^{-2}]}, E_p = 28.8 \left(\frac{N_V \rho}{M}\right)^{1/2} \quad (31)$$

where (ρ) is the material density (g/cm^3), (M) is the atomic or molecular weight, (E_p) is the free electron plasmon energy, (N_V) is the number of valence electrons per atom (elements) or molecule (compounds), The TPP-2M model is widely regarded for its reliability across a broad range of materials, as it incorporates both fundamental physical parameters and empirical fitting [28].

Data interpretation

XPS provides qualitative and quantitative surface chemical analysis, making it essential for studying thin films, surface modifications, and barrier layer compositions in advanced material systems.

Survey and High-Resolution Spectra in XPS Analysis

Elemental characterization of a sample's surface chemistry is initially performed by acquiring a survey spectrum, typically recorded over the binding energy range of 0 to 1400 eV. This spectrum encompasses both photoelectron and Auger electron peaks, with their relative intensities primarily governed by the photoionization cross section of each element [13]. Elemental identification is achieved by comparing the experimentally determined binding energy (BE) values with those reported in standard reference tables and electronic databases [16,17].

Following the survey scan, high-resolution spectra also referred to as narrow-scan or detailed spectra are collected for each element of interest. These spectra are subjected to curve fitting procedures, wherein synthetic peak shapes, derived from reference standard elements or compounds, are fitted to the experimental data to extract information on the chemical states of the detected elements. The curve-fitting procedure typically follows a commonly adopted approach in which the background is first subtracted, and the spectral features are then modeled using a combination of Gaussian and Lorentzian line shapes. It should be noted, however, that this represents one possible methodology; alternative approaches exist in which the background is included as part of the fitting process, particularly for multilayer or complex systems. After fitting, the chemical states are elucidated based on the binding energies of the resolved components and comparison with reference data.

Three-layer model [18]

For the quantitative analysis of nanometer-thick surface films and the film/substrate interface, the three-layer model can be applied. This model assumes the absence of concentration gradients and the lateral homogeneity of each layer. The photo-emitted electrons deriving from the bulk are exponentially attenuated by the oxide and the contamination layer, while the electrons emitted in the oxide layer are attenuated by the contamination layer. By the following equations, according to these assumptions, it is possible to determine the thickness and chemical composition of the layers:

$$I_i^{ox} = \left[\frac{(g_i \sigma_i^{ox} C_i^{ox} \rho_i^{ox} \Lambda_i^{ox})}{g_i} \right] \cdot [1 - \exp(-t/\Lambda_i^{ox})] \cdot \exp(-l_c / \Lambda_i^{con}) \quad (32)$$

$$I_i^{ox} = \left[\frac{(g_i \sigma_j^m C_j^m \rho_j^m \Lambda_j^m)}{A_j} \right] \cdot [1 - \exp(-t/\Lambda_j^{ox})] \cdot \exp(-l_c / \Lambda_i^{con}) \quad (33)$$

Where A is the atomic weight, g is the transmission function of the spectrometer, t is film thickness, l c is the thickness of the contamination layer and ρ is the density (g/cm³).

7.1.4. Combined X-ray photoelectron spectroscopy /Hard X-ray photoelectron spectroscopy (XPS/HAXPES)

Combined X-ray Photoelectron Spectroscopy (XPS) and Hard X-ray Photoelectron Spectroscopy (HAXPES) represent an advanced approach for probing the chemical composition of materials [19]. XPS employs soft X-ray sources, typically Al K α (1486.6 eV) or Mg K α (1253.6 eV), resulting in the emission of photoelectrons with relatively low kinetic energies. These photoelectrons have short inelastic mean free paths (IMFPs) and therefore originate predominantly from the top 5–10 nanometers of a sample, making XPS intrinsically surface sensitive [12].

In contrast, HAXPES utilizes hard X-ray sources (photon energies in the range of 2–15 keV), which impart greater kinetic energy to the emitted photoelectrons. The increased kinetic energy substantially extends the IMFP, thus allowing electrons from deeper within the material—sometimes up to 50–100 nanometers—to escape without significant inelastic scattering [32]. By varying the incident X-ray energy, combined XPS/HAXPES enables depth-profiling of chemical states, allowing researchers to distinguish between surface, subsurface, and bulk phenomena without the need for sputtering or destructive sample preparation [32].

The principle underlying both techniques is the photoelectric effect as described in more detail in the previous section (Section 7.1.3.); irradiation of the sample by monochromatic X-rays causes core-level electrons to be ejected, with their kinetic energy (KE) measured by the spectrometer.

The XPS/HAXPES approach is particularly powerful for studies involving functional thin films, engineered interfaces, and complex heterostructures, as it enables non-destructive, depth-resolved chemical analysis that is essential for understanding interfacial chemistry, diffusion processes, and the evolution of buried layers in advanced materials [19].

The probing depth in hard X-ray photoelectron spectroscopy (HAXPES) [32].

The probing depth in hard X-ray photoelectron spectroscopy (HAXPES) is principally determined by the inelastic mean free path (IMFP) of the emitted electrons, which increases substantially with electron kinetic energy. Calculations based on optical data and the TPP-2M formalism for 41 elements have demonstrated that employing photon energies greater than 2 keV extends the analysis depth well beyond the few-nanometer surface sensitivity characteristic of conventional soft X-ray photoemission experiments.

However, the photoionization cross section decreases sharply with increasing photon energy, exhibiting an approximate asymptotic dependence. This implies a reduction in the measured photoelectron intensity at higher photon energies.

Illustrative example: Energy Dependence of the O 1s Photoionization Cross Section and IMFP

Figure 7.7.b presents the variation of the O 1s photoionization cross section as a function of photon energy, constructed using the theoretical values reported by Scofield [20]. The data clearly demonstrates the asymptotic decline in cross-section with increasing photon energy. Specifically, the Scofield photoionization cross section for O 1s at a soft X-ray energy of 1486.6 eV (Al K α) is approximately 1.5 orders of magnitude greater than that at a hard X-ray energy of 5414.7 eV (Cr K α). This decrease in cross section is consistent with the simultaneous increase in inelastic mean free path (IMFP) of O 1s photoelectrons, as calculated using the TPP-2M model and shown in Figure 7.7.a for example, the IMFP increases from 2.7 nm at 1486.6 eV to 10.2 nm at 5414.7 eV, reflecting the enhanced probing depth achievable with hard X-ray excitation.

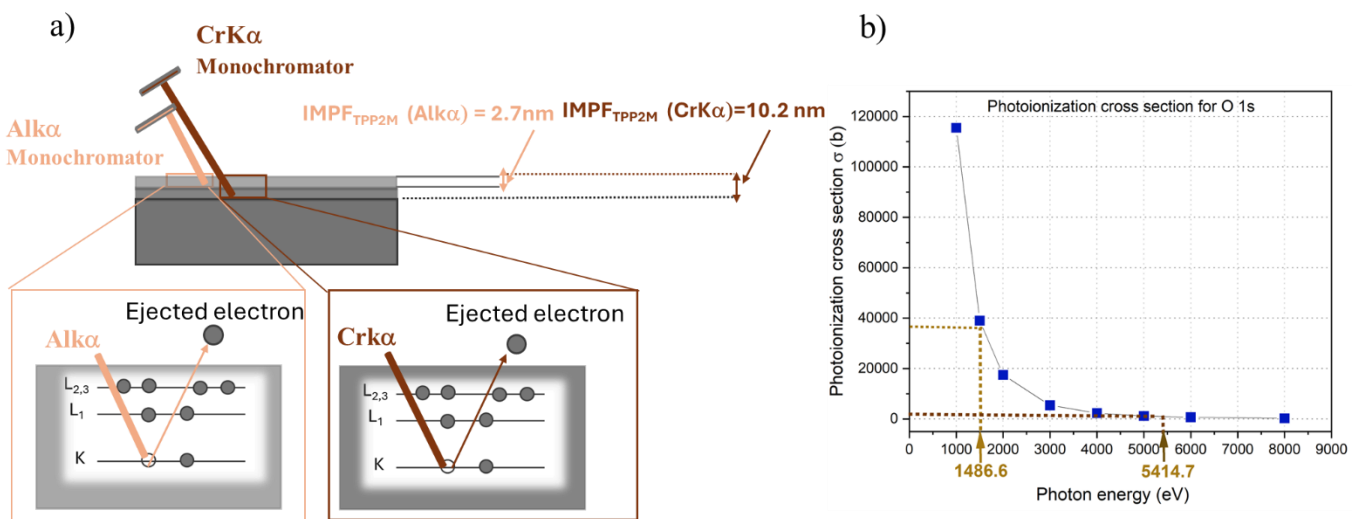


Figure 7.7. a) Illustration of the photoemission process and the inelastic mean free path (IMFP) of O 1s electrons at 1486.6 eV (Al K α) and 5414.7 eV (Cr K α). b) Plot of the O 1s photoionization cross section as a function of photon energy, based on theoretical values reported by Scofield. [33].

7.1. 4.. Rutherford Backscattering Spectrometry (RBS) and Elastic Recoil Detection Analysis (RBS/ERDA)

Fundamental of the Ion beam analysis and theoretical background

Ion beam analysis (IBA) includes an important family of analytical techniques based on the interactions, both atomic and nuclear, between accelerated charged particles (projectiles) and the atoms of a target material. When a high-energy projectile, such as a proton or alpha particle, impinges on a material, it undergoes a series of interactions with the electrons (inelastic collisions) and nuclei (elastic or inelastic collisions) of the sample. These interactions result in the progressive loss of the projectile's kinetic energy as it traverses the material, a process known as stopping power, typically quantified as the energy lost per unit path length [21].

The ion beam analysis and data elaboration in this work were carried out by a technician at the Laboratory of Ion Beam Physics in ETH Zurich.

Rutherford Backscattering Spectroscopy (RBS)

Rutherford Backscattering Spectrometry (RBS) is an analytical technique within the family of ion beam analysis methods. In RBS, a monoenergetic ion beam most commonly comprising helium ions (He^+) in the MeV energy range is directed at the sample, where the ions are elastically scattered by atomic nuclei. The probability of scattering at a particular angle is governed by the Rutherford differential cross section:

$$\frac{d\sigma}{d\Omega} = \frac{Z_1 Z_2}{4E} \frac{1}{\sin^4(\theta/2)} \quad (16)$$

where Z_1 and Z_2 are the atomic numbers of the target and projectile, E is the incident energy, and θ is the scattering angle. [11]

The energy of the backscattered ion, (E_s), is determined by the kinematic factor (K):

$$E_s = k \cdot E_0, \quad K = \left[\frac{(M_2^2 - M_1^2 \sin^2 \theta)^{1/2} + M_1 \cos \theta}{M_1 + M_2} \right]^2 \quad (17)$$

where M_1 and M_2 are the masses of the incident ion and target atom, and E_0 is the initial ion energy. As the ions penetrate the material, they lose energy through interactions with electrons and nuclei a process described by the stopping power (dE/dx). This energy loss enables the conversion of the measured energy spectrum into a quantitative depth profile:

$$E(x) = E_s - \left(\frac{dE}{dx} \right) x \quad (18)$$

By analyzing the RBS spectrum, one can determine elemental composition, areal density, layer thickness, and depth profiles, with particularly high mass resolution for heavy elements in lighter matrices. [11].

3.3.3. Elastic Recoil Detection Analysis: the physical principle

Elastic Recoil Detection Analysis (ERDA) is a quantitative ion beam analysis technique optimized for the detection and depth profiling of light elements in solid materials. In ERDA, an energetic ion beam, typically consisting of helium accelerated to MeV energies and strikes the sample at a specific angle. Through elastic binary collisions, the incident ions transfer momentum to target atoms, causing light elements such as hydrogen, carbon, nitrogen, and oxygen to recoil forward and escape from the sample surface. These recoiled atoms are

detected at a forward angle, and their measured energy (E_2) is related to the incident ion energy (E_0) by the kinematic factor (K)[22]:

$$E_2 = K * E_0 \quad (19)$$

$$K = \frac{4m_1m_2}{(m_1+m_2)^2} \cos^2\theta \quad (20) \quad (\text{equation adapted from [22]})$$

where (m_1) and (m_2) are the masses of the incident ion and the target atom, respectively, and θ is the recoil angle.

7.1.5. . Inert Gas Fusion (LECO ONH836)

The inert gas fusion method, as employed by instruments like the LECO ONH836, The LECO RHEN600 and RHEN602 are hydrogen determinators that utilize an electrode furnace, an argon carrier gas, and thermal conductivity detection to measure the quantity of hydrogen on materials in ppm.[23] and [24]

1. The procedure consists placing the sample on a graphite crucible which heated to release analyte gas. Oxygen present in the sample reacts with graphite crucible to form CO and CO₂. Nitrogen and hydrogen are extracted as N₂ and H₂ respectively.
2. Argon carrier sweeps the liberated analyte gases out of the furnace.
3. The gas flows through Schütze reagent (Schütze reagent, typically based on iodine pentoxide, is used to oxidize hydrogen (H₂) to water (H₂O) for quantitative hydrogen detection in gas streams)where the CO is oxidized to form CO₂. The CO₂ and any H₂O present are then scrubbed out of the carrier gas stream leaving nitrogen and hydrogen.
4. A molecular sieve column separates the nitrogen from the hydrogen, the smaller hydrogen molecules pass through the sieve more quickly than the larger nitrogen molecules and is detected using thermal conductivity detector (TC) detector.

The intensity of the signal is proportional to the concentration of hydrogen present in the sample. Calibration is performed using certified reference materials with known hydrogen content, allowing for accurate quantification on the order of parts per million (ppm) or even lower [23,24].

7.1. 6.. X-ray diffraction

X-ray diffraction (XRD) is an essential technique for the structural characterization of crystalline materials. Its principle is based on the elastic scattering of monochromatic X-rays by the periodic atomic planes within a crystal lattice. When X-rays of wavelength λ impinge on a crystal at an incident angle q , constructive interference of the scattered waves occurs only if the path difference between rays reflected from adjacent planes equals an integer multiple of the wavelength. This condition is described by Bragg's law:

$$n\lambda = 2d\sin\theta \quad (21)$$

where n is an integer (the order of reflection), d is the interplanar spacing, and q is the Bragg angle,[25].

In a typical XRD experiment, a goniometer scans the sample and detector through a range of $2q$ angles, and the resulting diffraction pattern is recorded as intensity versus $2q$. The positions of the diffraction peaks correspond to specific lattice spacings and are used to identify phases present by comparison with reference databases. The relative intensities of the diffraction peaks provide information about crystallographic texture and preferred orientation. Peak broadening and shifts can be analyzed to extract microstructural information, such as crystallite size and micro strain. Williamson–Hall (W-H) analysis W-H (equation 22) [26], and lattice parameter changes due to alloying or hydrogen absorption

$$b \cos q = K\lambda/D + 4\epsilon \sin \theta \quad (22)$$

plot of $b \cos \theta$ versus $4 \sin \theta$ was constructed, and the crystallite size was obtained from the intercept, while the strain was extracted from the slope. The meaning of the symbols is missing, please add the meaning.

In addition stress analysis can be performed by XRD using the $\sin^2\psi$ method which is used for determining residual stresses. It is based on measuring the variation in the spacing of specific crystallographic planes (d_{hkl}) as the sample is tilted at different angles to the incident X-ray beam on the (211) planar.

When a material is stressed, the interplanar spacing changes depending on the direction of measurement. By collecting diffraction data at multiple ψ tilt angles, the change in lattice spacing can be plotted as d_{hkl} versus $\sin^2\psi$.

From the slope of this plot, the residual stress σ (GPa) can be calculated using the general relationship:[27]

$$\sigma = \frac{E}{1+\nu} m \quad (23)$$

where: σ ; the residual stress ψ is tilt angles E is the Young's modulus, ν is the Poisson's ratio, and m is the slope of the d_{hkl} vs $\sin^2\psi$ plot. A positive slope indicates tensile stress, whereas a negative slope indicates compressive stress.

7.2. Supplementary data on X-ray Photoelectron Spectroscopy (XPS) Results

2.1. XPS results of the ion sputtered pure tungsten

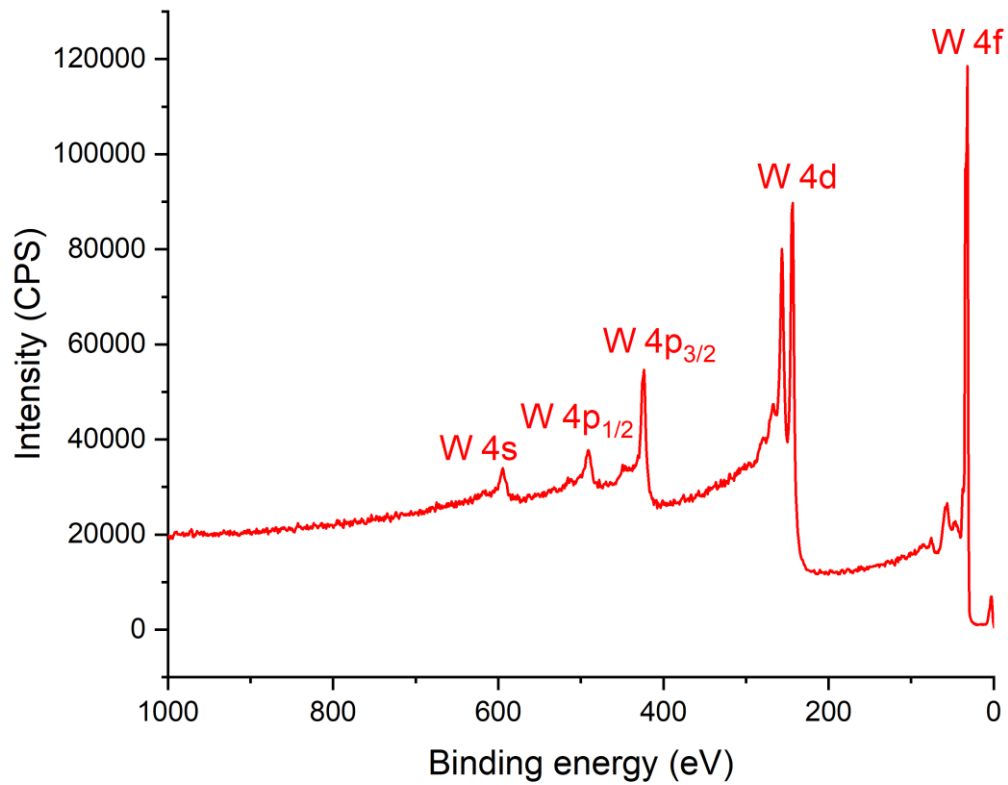


Figure 7.8. Survey spectrum of ion sputtered pure tungsten

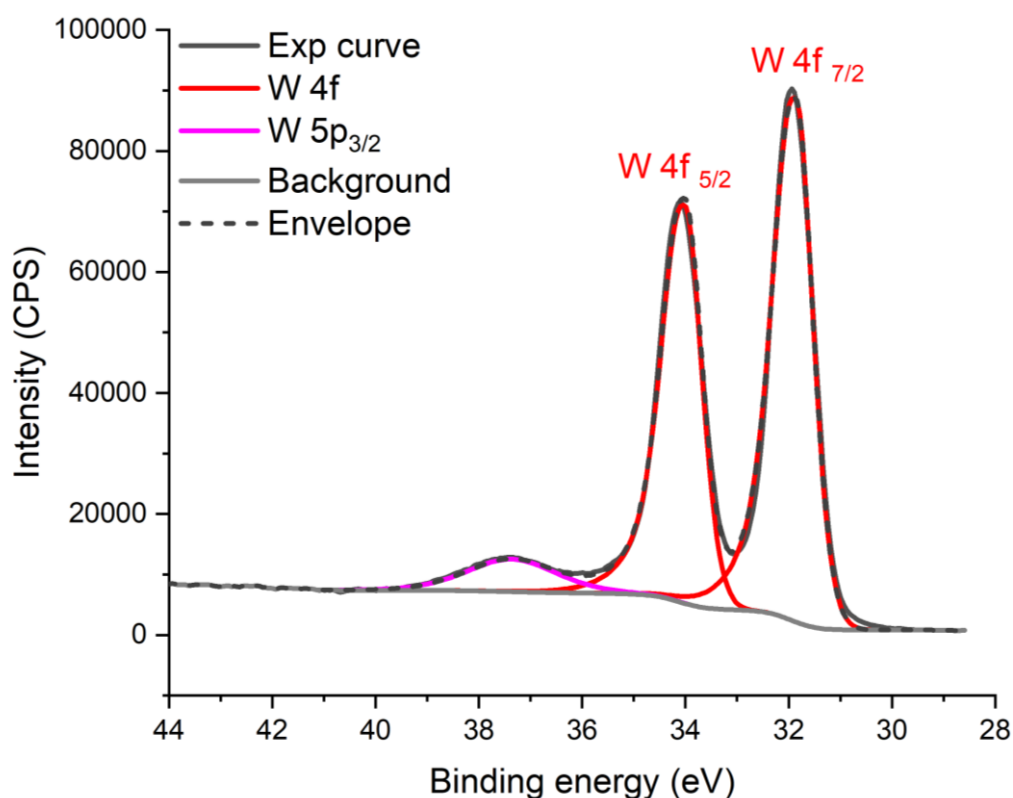


Figure 7.9. W4f and W 5p_{3/2} XP high resolution spectra of ion sputtered pure tungsten, Shirley background subtraction was used

Table 7.1. W 4f_{7/2} and W 5p_{3/2} fitting parameters of ion sputtered pure tungsten

	Line shape	Peak energy (eV)	Peak energy constraint (eV)	FWHM (eV)	FWHM constraint	Area constraint
W 4f _{7/2}	GL (45)	31.90 (0.04)		0.8 (0.01)		
W 4f _{5/2}	GL (45)	34.04 (0.04)	W 4f _{7/2} + 2.15 (0.01)	0.8 (0.01)	W 4f _{7/2} * 1.1 (0.1)	W 4f _{7/2} * 0.76 (0.01)
W 5p _{3/2}	GL (45)	37.40 (0.04)	W 4f _{7/2} + 5.5 (0.1)	2.1 (0.1)		W 4f _{7/2} * 0.76 (0.01)

2.2. XPS results of the pure tungsten trioxide

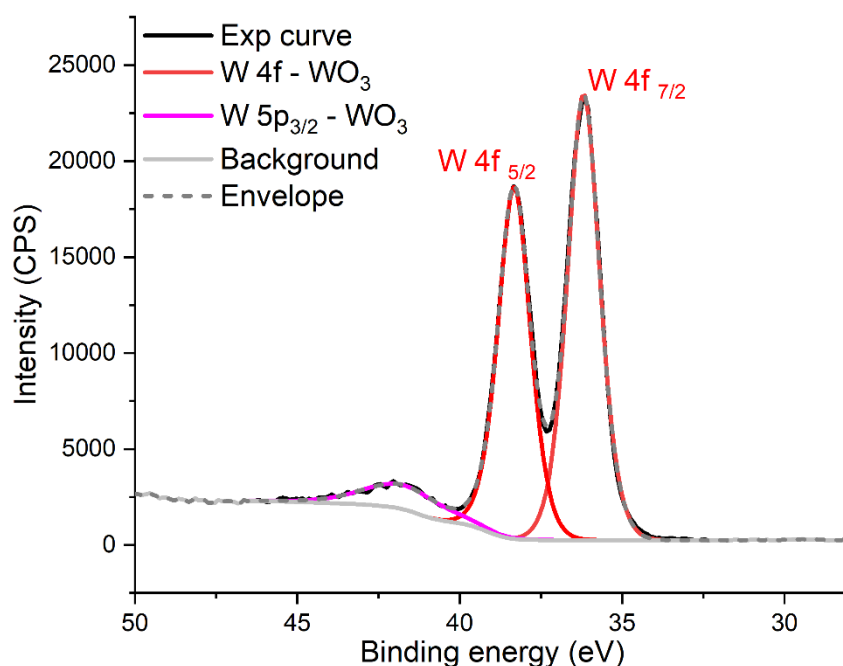


Figure 7.10. W4f and W 5p_{3/2} XP high resolution spectra of ion sputtered pure tungsten, Shirley background subtraction was used U 3 Tougaard background subtraction was used.

2.2. XPS results of the pure tungsten dioxide

Table 7.2. W 4f_{7/2} and W 5p_{3/2} fitting parameters of pure tungsten trioxide (WO₃)

	Line shape	Peak energy (eV)	Peak energy constraint (eV)	FWHM (eV)	FWHM constraint	Area constraint
W 4f _{7/2} - WO ₂	GL(45)	36.10 (0.01)(0.04)		1.20 (0.01)		
W 4f _{5/2} - WO ₂	GL(45)	38.3 (0.1)	W 4f _{7/2} +2.15(0.01)	1.20 (0.01)	W 4f _{7/2} *1	W 4f _{7/2} *0.76 (0.01)
W 5p _{3/2} - WO ₂	GL(45)	41.1 (0.1)	W 4f _{7/2} +5.5 (0.1)	2.5 (0.1)		W 4f _{7/2} *0.76 (0.01)

Table 7.3. W 4f_{7/2} and W 5p_{3/2} fitting parameters of pure tungsten dioxide (WO₂)

	Line shape	Peak energy (eV)	Peak energy constraints	FWHM (eV)	FWHM constraint	Area constraints
W 4f _{7/2} (WO ₂)	GL (45)	(33.2 (0.2)))	1.38 (0.02)		
W 4f _{5/2} (WO ₂)	GL (45)	35.4 (0.2)	W 4f _{7/2} – WO ₂ +2.15(0.01)	1.38 (0.01)	W 4f _{7/2} – WO ₂ *1	W 4f _{7/2} – WO ₂ *0.76(0.01)
W 5p _{3/2} (WO ₂)	GL (45)	38.8 (0.1)	W 4f _{7/2} – WO ₂ + 5.5(0.1)	2.1 (0.1)	W 4f _{7/2} – WO ₂ *1	W 4f _{7/2} – WO ₂ *0.12 (0.01)

References

1. Devanathan, M.A.V.; Stachurski, Z. The Adsorption and Diffusion of Electrolytic Hydrogen in Palladium. *Proc. A* **1962**, *270*, 90–102, doi:10.1098/rspa.1962.0205.
2. Truschner, M.; Trautmann, A.; Mori, G. The Basics of Hydrogen Uptake in Iron and Steel. *Berg Huetttenmaenn Monatsh* **2021**, *166*, 443–449, doi:10.1007/s00501-021-01142-x.
3. Samanta, S.; Kumari, P.; Mondal, K.; Dutta, M.; Singh, S.B. An Alternative and Comprehensive Approach to Estimate Trapped Hydrogen in Steels Using Electrochemical Permeation Tests. *International Journal of Hydrogen Energy* **2020**, *45*, 26666–26687, doi:10.1016/j.ijhydene.2020.07.131.
4. Zakroczymski, T. Adaptation of the Electrochemical Permeation Technique for Studying Entry, Transport and Trapping of Hydrogen in Metals. *Electrochimica Acta* **2006**, *51*, 2261–2266, doi:10.1016/j.electacta.2005.02.151.
5. Van Den Eeckhout, E.; De Baere, I.; Depover, T.; Verbeken, K. The Effect of a Constant Tensile Load on the Hydrogen Diffusivity in Dual Phase Steel by Electrochemical Permeation Experiments. *Materials Science and Engineering: A* **2020**, *773*, 138872, doi:10.1016/j.msea.2019.138872.
6. Nemanič, V.; Kovač, J.; Lungu, C.; Porosnicu, C.; Zajec, B. Characterization of Tungsten Films and Their Hydrogen Permeability. *Journal of Vacuum Science & Technology A: Vacuum, Surfaces, and Films* **2014**, *32*, 061511, doi:10.1116/1.4898061.
7. Ozdirik, B.; Suter, T.; Hans, U.; Depover, T.; Verbeken, K.; Schmutz, P.; Jeurgens, L.P.H.; Terry, H.; De Graeve, I. Study of the Hydrogen Uptake in Deformed Steel Using the Microcapillary Cell Technique. *Corrosion Science* **2019**, *155*, 55–66, doi:10.1016/j.corsci.2019.04.029.
8. Jürgensen, J.; Pohl, M. Local Hydrogen Measurements in Multi-Phase Steel C60E by Means of Electrochemical Microcapillary Cell Technique. *Metals* **2023**, *13*, 1585, doi:10.3390/met13091585.
9. Fushimi, K.; Jin, M.; Kitagawa, Y.; Nakanishi, T.; Hasegawa, Y. Hydrogen Permeation into a Carbon Steel Sheet Observed by a Micro-Capillary Combined with a Devanathan-Stachurski Cell. *ISIJ International* **2016**, *56*, 431–435, doi:10.2355/isijinternational.ISIJINT-2015-191.
10. Arjmand, F.; Adriaens, A. Microcapillary Electrochemical Droplet Cells: Applications in Solid-State Surface Analysis. *J Solid State Electrochem* **2014**, *18*, 1779–1788, doi:10.1007/s10008-014-2413-3.
11. Briggs, D.; Grant, J.T. *Surface Analysis by Auger and X-Ray Photoelectron Spectroscopy*; Surface Spectra, 2003; ISBN 978-1-901019-04-9.
12. *Surface Analysis: The Principal Techniques*; Gilmore, I.S., Vickerman, J.C., Eds.; John Wiley & Sons: Hoboken, NJ, 2009; ISBN 9780470017630.
13. Scofield, J.H. Hartree-Slater Subshell Photoionization Cross-Sections at 1254 and 1487 eV. *Journal of Electron Spectroscopy and Related Phenomena* **1976**, *8*, 129–137, doi:10.1016/0368-2048(76)80015-1.
14. Seah, M.P.; Dench, W.A. Quantitative Electron Spectroscopy of Surfaces: A Standard Data Base for Electron Inelastic Mean Free Paths in Solids. *Surface and Interface Analysis* **1979**, *1*, 2–11, doi:10.1002/sia.740010103.
15. Tanuma, S.; Powell, C.J.; Penn, D.R. Calculations of Electron Inelastic Mean Free Paths. V. Data for 14 Organic Compounds over the 50–2000 eV Range. *Surface and Interface Analysis* **1994**, *21*, 165–176, doi:10.1002/sia.740210302.
16. Moulder, J.F. *Handbook of X-Ray Photoelectron Spectroscopy: A Reference Book of Standard Spectra for Identification and Interpretation of XPS Data*; Physical Electronics Division, Perkin-Elmer Corporation, 1992; ISBN 978-0-9627026-2-4.

17. Justin Gorham NIST X-Ray Photoelectron Spectroscopy Database - SRD 20 2012.
18. Rossi, A.; Eisener, B. XPS Analysis of Passive Films on the Amorphous Alloy Fe₇₀ Cr₁₀ P₁₃ C₇ : Effect of the Applied Potential. *Surface & Interface Analysis* **1992**, *18*, 499–504, doi:10.1002/sia.740180708.
19. *Hard X-Ray Photoelectron Spectroscopy (HAXPES)*; Woicik, J., Ed.; Springer Series in Surface Sciences; Springer International Publishing: Cham, 2016; Vol. 59; ISBN 978-3-319-24041-1.
20. Scofield, J.H. THEORETICAL PHOTOIONIZATION CROSS SECTIONS FROM I TO 1500 keV.
21. Wang, Y.; Nastasi, M. *Handbook of Modern Ion Beam Materials Analysis*; Materials Research Society, 2010; ISBN 978-1-60511-215-2.
22. Tengdelius, L. ZrB₂ Thin Films : Growth and Characterization. **2016**.
23. 836 Series. *LECO Corporation*.
24. Yvon, J. Hydrogen Analysis in Steel and Metals.
25. Epp, J. X-Ray Diffraction (XRD) Techniques for Materials Characterization. In *Materials characterization using nondestructive evaluation (NDE) methods*; Elsevier, 2016; pp. 81–124.
26. Mote, V.D.; Purushotham, Y.; Dole, B.N. Williamson-Hall Analysis in Estimation of Lattice Strain in Nanometer-Sized ZnO Particles. *Journal of Theoretical and Applied Physics* **2012**, *6*, doi:10.1186/2251-7235-6-6.
27. Lorenzin, G.; Jeurgens, L.P.H.; Cancellieri, C. Stress Tuning in Sputter-Grown Cu and W Films for Cu/W Nanomultilayer Design. *J. Appl. Phys.* **2022**, *131*, 225304, doi:10.1063/5.0088203.

7.3. Published papers

7.3.1.Integration of PhD Manuscript: : Paper 1

RESEARCH ARTICLE | NOVEMBER 26 2024

X-ray photoelectron spectroscopy investigation of X60 steel

Special Collection: [Materials for Energy and the Environment](#)

Raouaa Hannachi ; Deborah Biggio ; Bernhard Elsener ; Marzia Fantauzzi ; Antonella Rossi 



Surf. Sci. Spectra 31, 024014 (2024)

<https://doi.org/10.1116/6.0003972>



Articles You May Be Interested In

XPS spectra of chitosan powder and film acquired by monochromatic Al K_{α} x-ray source

Surf. Sci. Spectra (September 2025)

Sardinian limestone and Carrara marble by XPS

Surf. Sci. Spectra (June 2025)

XPS study of electroless NiP coating on iron substrate

Surf. Sci. Spectra (August 2024)

01 April 2026 12:33:06



HIDEN
ANALYTICAL

Surface Composition, Imaging & Depth Profiling

Advanced SIMS solutions for surface science studies

Trusted in Research for over 40 years

Find SIMS Solutions

X-ray photoelectron spectroscopy investigation of X60 steel

Cite as: Surf. Sci. Spectra 31, 024014 (2024); doi: 10.1116/6.0003972

Submitted: 8 August 2024 · Accepted: 25 October 2024 ·

Published Online: 26 November 2024



Raouaa Hannachi, Deborah Biggio, Bernhard Elsener, Marzia Fantauzzi, and Antonella Rossi

AFFILIATIONS

Dipartimento di Scienze Chimiche e Geologiche, Università di Cagliari, Cittadella Universitaria, Monserrato, Cagliari 09042, Italy

Note: This paper is part of the 2024 Special Topic Collection on Materials for Energy and the Environment.

ABSTRACT

XPS is used to characterize the surface of commercial X60 pipeline steel after chemical cleaning with a sequence of five solvents and following mechanical polishing. This steel is used as material for pipeline construction aiming to green hydrogen transportation.

© 2024 Author(s). All article content, except where otherwise noted, is licensed under a Creative Commons Attribution (CC BY) license (<https://creativecommons.org/licenses/by/4.0/>). <https://doi.org/10.1116/6.0003972>

Accession #: 01976 and 01977

Technique: XPS

Specimen: X60 steel cleaned with five solvents (cleaned X60 steel) and mechanically polished X60 steel (MP X60 steel)

Instrument: Thermo Scientific Theta Probe

Major Elements in Spectra: Fe, O, and C

Minor Elements in Spectra: None

Published Spectra: 8

Spectral Category: Comparison

INTRODUCTION

API 5L grade X60 steel (standardized by American Petroleum Institute) has been used since long time as steel for natural gas and petroleum pipelines and in oil and gas applications. Recently, the material has gained interest for hydrogen storage and transportation (Ref. 1). The surface chemistry of X60 steel plays an important role when performing electrochemical hydrogen permeation tests (Ref. 2) because it might affect the hydrogen production and detection kinetics. In this work, x-ray photoelectron spectroscopy was used for characterizing the surface of X60 steel after a thorough cleaning procedure and following mechanical polishing. No significant changes in the chemical state of the elements are detected between the samples upon the different sample preparation procedures. The mechanical polishing reduces the thickness of the natural oxide layer present on the steel surface.

SPECIMEN DESCRIPTION (ACCESSION # 01976 and 01977)

Specimen: X60 steel, thickness 2 mm, diameter 5 cm; cleaned (# 01976) and mechanically polished (# 01977)

CAS Registry #: Unknown

Specimen Characteristics: Homogeneous; solid; polycrystalline; conductor; metal;

Chemical Name: API 5L grade steel X60

Source: RINA Consulting—CSM S.p.A.

Composition: Fe, Mn < 1.4%, Cr, Mo, Ni, Cu, C < 0.28%, and Si < 0.45% (Ref. 3)

Form: X60 steel disk 50 × 2 mm² (diameter × thickness)

Structure: XRD results performed by Rina consulting CSM S.p.A. showed that X60 steel has body centered cubic (BCC) structure. SEM cross-sectional analysis of X60 steel (etched with 2% Nital solution for 5 s) conducted in the Metallography Laboratory of Rina consulting CSM S.p.A. showed that X60 steel has tempered martensite and bainite microstructures with the distribution of precipitated carbides.

History and Significance: The X60 steel was cut from a pipeline tube to obtain disks of 2 mm thickness and a diameter of 50 mm. The surface roughness determined by a SV-3200 surface roughness tester was 0.3–0.4 μm.

As Received Condition: The “as received” X60 steel after cutting is covered with an oil/grease film.

Analyzed Region: Center and at least two other analysis points of the sample surface

01 APRIL 2026 13:32:06

Ex Situ Preparation/Mounting: Two different procedures were applied:

Five solvents' cleaning (# 01976): The as received samples were cleaned by following the described procedure in ultrasonic bath at 40 °C: butan-2-one (5 min), acetone (5 min), ethanol (5 min), petroleum ether (5 min), and double distilled water [specific conductivity = 1.5(0.1) $\mu\text{S}/\text{cm}$] (10 min). After the cleaning procedure with five solvents, the sample was dried under an argon stream and analyzed by XPS. The time between the drying step and the sample insertion into the fast entry air lock of the spectrometer is less than 1 min.

Five solvents' cleaning and mechanical polishing (# 01977): XPS characterization was also carried out on the X60 sample following cleaning with five solvents and mechanical polishing using SiC 4000-mesh paper in the presence of ethanol as lubricant for 3 min and 30 s. After grinding, the samples were immersed in ultrasonic bath at 40 °C in ethanol for 5 min and in double distilled water for 10 min. Also, in this case, the samples were dried under an argon stream. The time between the drying step and the sample insertion into the fast entry air lock of the spectrometer was less than 1 min.

In Situ Preparation: None

Charge Control: No charge control

Temp. During Analysis: 300 K

Pressure During Analysis: $<1 \times 10^{-7}$ Pa

Preanalysis Beam Exposure: 0 s

INSTRUMENT DESCRIPTION

Manufacturer and Model: Thermo Scientific Theta Probe

Analyzer Type: Spherical sector

Detector: Other, multichannel plate detector

Number of Detector Elements: 128

INSTRUMENT PARAMETERS COMMON TO ALL SPECTRA

Spectrometer

Analyzer Mode: Constant pass energy

Throughput ($T = E^N$): The energy dependence can be determined

by the following equation: $\frac{A}{E_p} = \left(\frac{a^2}{(a^2 + R^2)}\right)^b$, where a and b are constants, E_p is the pass energy, A is the peak area, and R is the retard ratio equal to E/E_p , where E is the kinetic energy. Three spectral regions [Cu 2p (925–940 eV), Cu 3p (68–82 eV), and Cu $L_{3,4,5}M_{4,5}$ (561–577 eV)] are recorded on a sputter cleaned copper sample at different pass energies (10, 20, 50, 100, 125, 150, 200, 300, and 400 eV). The values of a and b are then determined to be 26.66 and 1.11, respectively, by a linear least square fit of the data applying the equation described above (Ref. 4).

Excitation Source Window: None

Excitation Source: Al K_{α} monochromatic

Source Energy: 1486.6 eV

Source Strength: 100 W

Source Beam Size: Nominal spot size: $400 \times 400 \mu\text{m}^2$ spot size measured by analyzing Au/Si fresh cleaved sample using line scan measurement resulted to be equal to $355.8 \times 219.2 \mu\text{m}^2$.

Signal Mode: Pulse single channel

Geometry

Incident Angle: 30°

Source-to-Analyzer Angle: 67.38°

Emission Angle: 53°

Specimen Azimuthal Angle: 70°

Acceptance Angle from Analyzer Axis: 60°

Analyzer Angular Acceptance Width: 30° \times 30°

Ion Gun

Manufacturer and Model: Thermo Scientific EX050

Energy: 3000 eV

Current: 0.002 mA

Current Measurement Method: Biased stage

Sputtering Species and Charge: Ar⁺

Spot Size (unrastered): 200 μm

Raster Size: 3000 \times 3000 μm^2

Incident Angle: 45.00°

Polar Angle: 58.43°

Azimuthal Angle: 24.20°

Comment: Sputtering of Ag, Au, and Cu samples was performed before checking the linearity of the binding energy scale.

DATA ANALYSIS METHOD

Energy Scale Correction: Linearity of the energy scale was performed recording the binding energy of Cu 2p_{3/2}, Ag 3d_{5/2}, and Au 4f_{7/2} signals on sputter cleaned high purity copper, silver, and gold foils (Goodfellow, Cambridge, UK). The binding energy values were compared with those reported in ISO 15472:2010. The C 1s of aliphatic carbon at 285.0 eV was taken as internal reference.

Recommended Energy Scale Shift: −0.16 eV for the five solvents' cleaned sample (# 01976) and −0.1 eV for the mechanically polished sample (# 01977).

Peak Shape and Background Method: Spectra were processed using CasaXPS software (V.2.3.25PR1.0) (Ref. 5). Shirley background subtraction was applied before curve fitting; the curve-fitting was carried out using mixed Gaussian - Lorentzian product function as line shape. In the case of Fe 2p_{3/2}, the metallic component was fitted adding the tail for taking into account the asymmetry of the signal (Ref. 6).

Quantitation Method: N/A

ACKNOWLEDGMENTS

This study was carried out under the project "e.INS, Ecosystem of Innovation for Next Generation Sardinia," funded by the National Recovery and Resilience Plan (PNRR)—Mission 4, Component 2, "From research to business" Investment 1.5, "Creation and strengthening of Ecosystems of innovation" and construction of "Territorial R&D Leaders" (No. CUP F53C22000430001). The Ph.D. fellowship of Raouaa Hannachi is cofunded by Ministero dell'Università e della ricerca (MUR)—Italy (No. CUP F22B22000560005) and by RINA Consulting—CSM S.p.A.

AUTHOR DECLARATIONS

Conflict of Interest

The authors have no conflicts to disclose.

Author Contributions

Raouaa Hannachi: Data curation (equal); Investigation (equal); Writing – original draft (equal); Writing – review & editing (equal). **Deborah Biggio:** Data curation (equal); Investigation (equal); Writing – review & editing (equal). **Bernhard Elsener:** Conceptualization (equal); Data curation (equal); Investigation (equal); Methodology (equal); Writing – review & editing (equal). **Marzia Fantauzzi:** Conceptualization (equal); Data curation (equal); Investigation (equal); Methodology (equal); Writing – review & editing (equal). **Antonella Rossi:** Conceptualization (equal); Funding acquisition (equal); Investigation (equal); Methodology (equal); Project administration (equal); Supervision (equal); Writing – review & editing (equal).

DATA AVAILABILITY

The data that support the findings of this study are available within the article and its [supplementary material](#).

REFERENCES

- ¹Global Hydrogen Review, Hydrogen Transport by Pipeline (International Energy Agency, 2022), p. 108 ff, see <https://www.iea.org/reports/global-hydrogen-review-2022>.
- ²E. Van den Eeckhout, K. Verbeken, and T. Depover, *Int. J. Hydrogen Energy* **48**, 30585 (2023).
- ³See <https://www.epowermetals.com/a-comprehensive-guide-to-x60-steel.html> for the nominal composition of X60 steel has been provided by RINA Consulting - CSM-SpA which referred to e-Power Metal web site.
- ⁴K. Berresheim, M. Matter-Klosson, and M. Wilmers, *Fresenius J. Anal. Chem.* **341**, 121 (1991).
- ⁵N. Fairley *et al.*, *Appl. Surf. Sci. Adv.* **5**, 100112 (2021).
- ⁶D. Biggio, B. Elsener, G. Usai, M. Fantauzzi, and A. Rossi, *Langmuir* **40**, 6824 (2024).
- ⁷D. Addari, D. Atzei, B. Elsener, and A. Rossi, *Surf. Sci. Spectra* **9**, 275 (2002).
- ⁸S. Diodati and S. Gross, *Surf. Sci. Spectra* **20**, 17 (2013).
- ⁹B. Elsener, D. Addari, S. Coray, and A. Rossi, *Electrochim. Acta* **56**, 4489 (2011).
- ¹⁰A. P. Grosvenor, B. A. Kobe, M. C. Biesinger, and N. S. McIntyre, *Surf. Interface Anal.* **36**, 1564 (2004).

SPECTRAL FEATURES TABLE

Spectrum ID #	Element/Transition	Peak Energy (eV)	Peak Width FWHM (eV)	Peak Area (eV × counts)	Sensitivity Factor	Concentration (at. %)	Peak Assignment
01976-02	Fe 2p _{3/2}	Fe 2p high resolution spectrum
01976-02	Fe 2p _{3/2}	706.9	1.2	3 770.8	10.77	...	1-Fe (0)
01976-02	Fe 2p _{3/2}	710.6	2.3	17 332.5	19.16	...	2-iron oxide Fe ₂ O ₃
01976-02	Fe 2p _{3/2}	712.4	3.1	12 896.6	19.16	...	3-iron oxy hydroxide
01976-02	Fe 2p _{1/2}
01976-02	Fe 2p _{1/2}	720.0	4-Fe (0)
01976-02	Fe 2p _{1/2}	724.2	5-iron oxide Fe ₂ O ₃
01976-02	Fe 2p _{1/2}	725.9	6-iron oxy hydroxide
01976-03	C 1s	C 1s high resolution spectrum
01976-03	C 1s	285.0	1.5	6 770.3	1.89	...	1-aliphatic carbon
01976-03	C 1s	286.7	1.5	2 274.8	1.89	...	2-alcohol C—OH
01976-03	C 1s	288.1	1.5	1 105.8	1.89	...	3-carbonyl C=O
01976-03	C 1s	289.2	1.5	930.4	1.89	...	4-CO ₃ ²⁻ and/or carboxylic acid —COOH
01976-04	O 1s	O 1s high resolution spectrum
01976-04	O 1s	530.1	1.4	27 482.1	5.85	...	1-oxide
01976-04	O 1s	531.6	1.4	14 238.8	5.85	...	2-hydroxide
01976-04	O 1s	532.8	1.4	4 963.5	5.85	...	3-CO ₃ ²⁻ and/or organic contamination
01976-04	O 1s	534.1	1.4	2 571.9	5.85	...	4-adsorbed water
01977-02	Fe 2p _{3/2}	Fe 2p high resolution spectrum
01977-02	Fe 2p _{3/2}	706.8	1.3	5 940.6	10.77	...	1-Fe (0)
01977-02	Fe 2p _{3/2}	710.5	2.5	17 603.0	19.16	...	2-iron oxide Fe ₂ O ₃
01977-02	Fe 2p _{3/2}	712.4	3.3	10 943.4	19.16	...	3-iron oxy hydroxide
01977-02	Fe 2p _{1/2}
01977-02	Fe 2p _{1/2}	719.9	4-Fe (0)
01977-02	Fe 2p _{1/2}	724.1	5-iron oxide Fe ₂ O ₃
01977-02	Fe 2p _{1/2}	725.9	6-iron oxy hydroxide
01977-03	C 1s	C 1s high resolution spectrum
01977-03	C 1s	285.0	1.4	8 069.5	1.89	...	1-aliphatic carbon
01977-03	C 1s	286.6	1.4	1 722.0	1.89	...	2-alcohol C—OH
01977-03	C 1s	287.8	1.4	395.8	1.89	...	3-carbonyl C=O
01977-03	C 1s	289.1	1.4	894.3	1.89	...	4-CO ₃ ²⁻ and/or carboxylic acid —COOH
01977-04	O 1s	O 1s high resolution spectrum
01977-04	O 1s	530.1	1.4	24 447.5	5.85	...	1-oxide
01977-04	O 1s	531.5	1.4	10 460.7	5.85	...	2-hydroxide

01 April 2024 13:32:06

(Continued.)

Spectrum ID #	Element/Transition	Peak Energy (eV)	Peak Width FWHM (eV)	Peak Area (eV × counts)	Sensitivity Factor	Concentration (at. %)	Peak Assignment
01977-04	O 1s	532.5	1.4	4 882.0	5.85	...	3-CO ₃ ²⁻ and/or organic contamination
01977-04	O 1s	533.7	1.4	2 260.2	5.85	...	4-Adsorbed water

Comment to Spectral Features Table: The oxygen and carbon components listed in the table are due to the oxo-hydroxide layer and to surface contamination. The composition is not given because the assumption of homogeneity is not fulfilled.

Footnote to Spectrum # 01976-02: The Fe 2p spectrum consists of a Fe 2p_{3/2} and Fe 2p_{1/2} doublet due spin-orbit coupling. The Fe 2p_{3/2} signal shows three peaks located at 706.8, 710.5, and 712.4 eV that correspond to Fe (0) (Ref. 6) Fe₂O₃ and FeOOH, respectively (Ref. 6–10). The Fe 2p_{1/2} signal presents three peaks located at 720.0, 724.2, and 725.9 eV that are due to the presence of Fe (0), Fe₂O₃, and FeOOH, respectively.

Footnote to Spectrum # 01976-03: The presence of carbon is attributed to the organic contamination layer and, consequently, it is not considered in the steel composition. In the C 1s spectrum, peaks 1, 2, 3, and 4 correspond to C 1s aliphatic (BE = 285.0 eV), C—OH (BE = 286.7 eV), C=O (BE = 288.1 eV), and COOH (BE = 289.2 eV), respectively.

Footnote to Spectrum # 01976-04: The O 1s spectrum shows four peaks (1, 2, 3, and 4) that correspond to oxide (BE = 530.0 eV), hydroxide (BE = 531.4 eV), oxygen in CO₃²⁻ and/or organic contamination (BE = 532.2 eV), and adsorbed water (BE = 533.6 eV).

Footnote to Spectrum # 01977-02: The Fe 2p spectrum of MP X60 steel consists of a Fe 2p_{3/2} and Fe 2p_{1/2} doublet due spin-orbit coupling. Also in this case, Fe 2p_{3/2} signal shows three peaks located at 706.8, 710.5, and 712.4 eV that are assigned to Fe (0), Fe₂O₃, and FeOOH, respectively. The Fe 2p_{1/2} signal consists of three peaks located at 719.9, 724.1, and 725.9 eV due to Fe (0), Fe₂O₃, and FeOOH, respectively. No differences in the chemical state of iron are observed for the cleaned and MP X60 samples.

Footnote to Spectrum # 01977-03: The C 1s spectrum of the MP X60 steel presents four peaks 1, 2, 3, and 4 that correspond to C 1s aliphatic (BE = 285.0 eV), C—OH (BE = 286.6 eV), C=O (BE = 287.8 eV), and COOH (BE = 289.1 eV), respectively. When comparing the cleaned X60 steel to the MP X60 steel, it can be observed that the measured binding energies are equal within experimental uncertainty (0.1 eV).

Footnote to Spectrum # 01977-04: The O 1s spectrum of the MP X60 steel shows four peaks (1, 2, 3, and 4) that correspond to oxide (BE = 530.0 eV), hydroxide (BE = 531.5 eV), oxygen in organic compounds from CO₃²⁻ and/or organic contamination layer (BE = 532.5 eV), and adsorbed water (BE = 533.7 eV), respectively.

No significant difference in the chemical state of the elements is detected between the cleaned and mechanically polished samples.

ANALYZER CALIBRATION TABLE

Spectrum ID #	Element/Transition	Peak Energy (eV)	Peak Width FWHM (eV)	Peak Area (eV × counts)	Sensitivity Factor	Concentration (at. %)	Peak Assignment
...	Au 4f _{7/2}	83.95	1.04	191 600	Gold metal
...	Ag 3d _{5/2}	368.26	0.96	197 000	Silver metal
...	Cu 2p _{3/2}	932.61	1.24	143 000	Copper metal

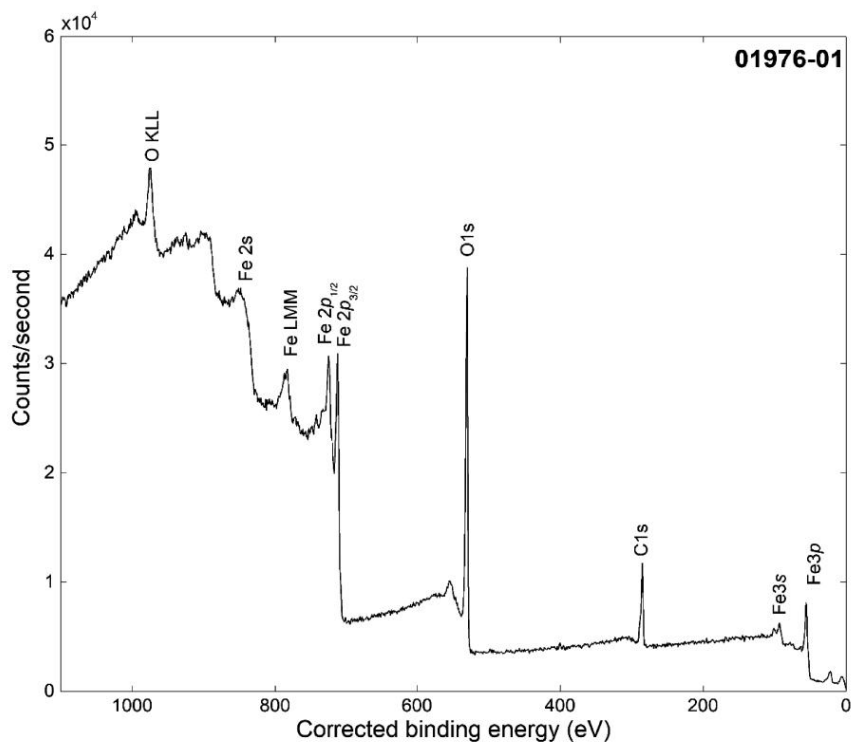
Comment to Analyzer Calibration Table: The spectra were acquired after Ar⁺ ion etching.

GUIDE TO FIGURES

Spectrum ID #	Element/Transition	Voltage Shift ^a	Multiplier	Baseline	Comment #
01976-01	Survey	0.16	1	0	...
01976-02	Fe 2p	0.16	1	0	...
01976-03	C 1s	0.16	1	0	...
01976-04	O 1s	0.16	1	0	...
01977-01	Survey	0.1	1	0	...
01977-02	Fe 2p	0.1	1	0	...
01977-03	C 1s	0.1	1	0	...
01977-04	O 1s	0.1	1	0	...

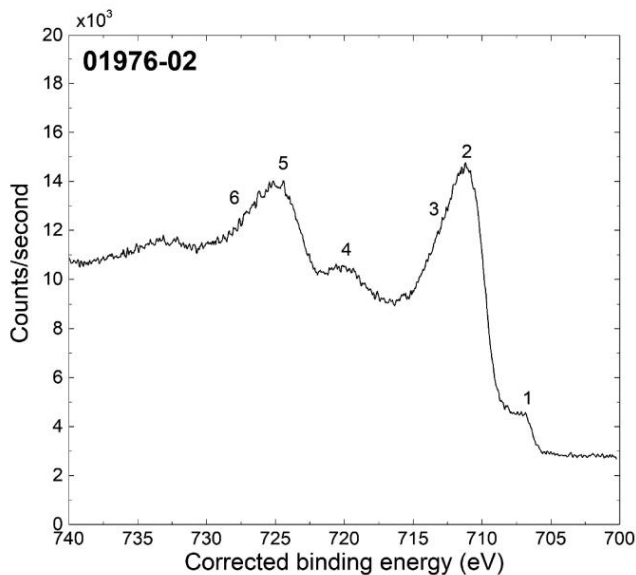
^aVoltage shift of the archived (as-measured) spectrum relative to the printed figure. The figure reflects the recommended energy scale correction due to a calibration correction, sample charging, flood gun, or other phenomenon.

01 April 2024 13:31:06



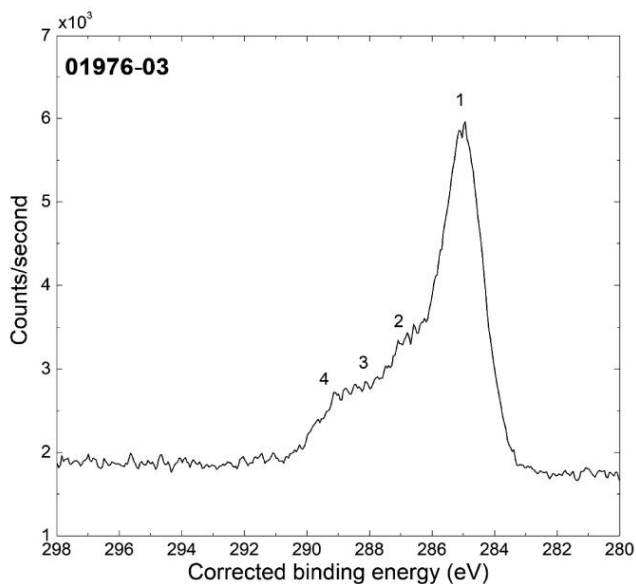
01 April 2026 13:31:06

Accession #:	01976-01
Specimen:	Cleaned X60 steel
Technique:	XPS
Spectral Region:	Survey
Instrument:	Thermo Scientific Theta Probe
Excitation Source:	Al K _α monochromatic
Source Energy:	1486.6 eV
Source Strength:	100 W
Source Size:	0.4 × 0.4 mm ²
Analyzer Type:	Spherical sector analyzer
Incident Angle:	30°
Emission Angle:	53°
Analyzer Pass Energy:	200 eV
Instrument Resolution:	1.5 eV
Total Signal Accumulation Time:	612 s
Total Elapsed Time:	985 s
Number of Scans:	9



■ Accession #: 01976-02
 ■ Specimen: Cleaned X60 steel
 ■ Technique: XPS
 ■ Spectral Region: Fe 2p

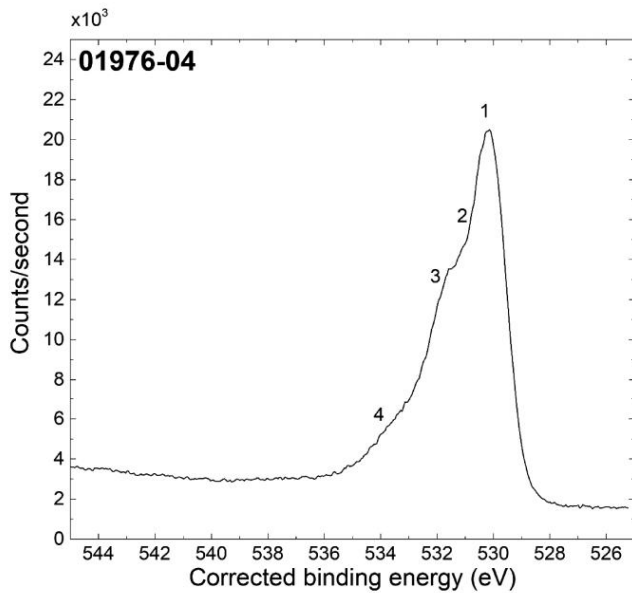
Instrument: Thermo Scientific Theta Probe
 Excitation Source: Al K_{α} monochromatic
 Source Energy: 1486.6 eV
 Source Strength: 100 W
 Source Size: $0.4 \times 0.4 \text{ mm}^2$
 Analyzer Type: Spherical sector
 Incident Angle: 30°
 Emission Angle: 53°
 Analyzer Pass Energy: 100 eV
 Instrument Resolution: 0.96 eV
 Total Signal Accumulation Time: 360 s
 Total Elapsed Time: 647 s
 Number of Scans: 9
 Comments: See the table's footnotes



■ Accession #: 01976-03
 ■ Specimen: Cleaned X60 steel
 ■ Technique: XPS
 ■ Spectral Region: C 1s

Instrument: Thermo Scientific Theta Probe
 Excitation Source: Al K_{α} monochromatic
 Source Energy: 1486.6 eV
 Source Strength: 100 W
 Source Size: $0.4 \times 0.4 \text{ mm}^2$
 Analyzer Type: Spherical sector
 Incident Angle: 30°
 Emission Angle: 53°
 Analyzer Pass Energy: 100 eV
 Instrument Resolution: 0.96 eV
 Total Signal Accumulation Time: 171 s
 Total Elapsed Time: 383 s
 Number of Scans: 9
 Comments: See the table's footnotes

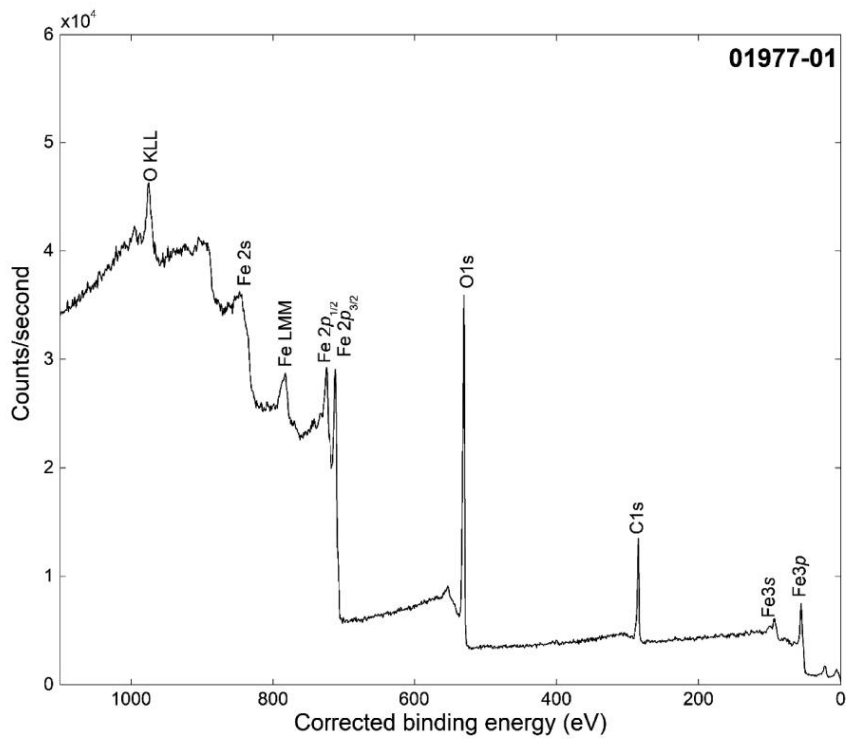
01 April 2024 13:32:06



- Accession #: 01976-04
- Specimen: Cleaned X60 steel
- Technique: XPS
- Spectral Region: O 1s

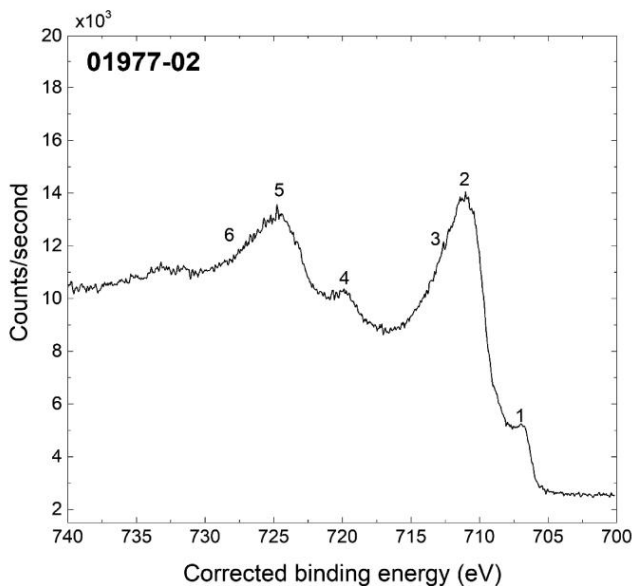
Instrument: Thermo Scientific Theta Probe
 Excitation Source: Al K_{α} monochromatic
 Source Energy: 1486.6 eV
 Source Strength: 100 W
 Source Size: 0.4 × 0.4 mm²
 Analyzer Type: Spherical sector
 Incident Angle: 30°
 Emission Angle: 53°
 Analyzer Pass Energy: 100 eV
 Instrument Resolution: 0.96 eV
 Total Signal Accumulation Time: 180 s
 Total Elapsed Time: 389 s
 Number of Scans: 9
 Comments: See the table's footnotes

01 April 2024 13:32:06



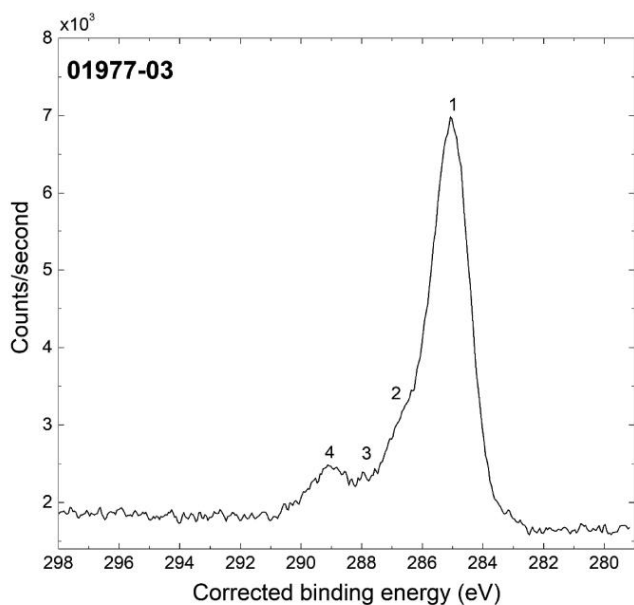
01 April 2026 13:31:06

Accession #:	01977-01
■ Specimen:	MP X60 steel
■ Technique:	XPS
■ Spectral Region:	Survey
Instrument:	Thermo Scientific Theta Probe
Excitation Source:	Al K_{α} monochromatic
Source Energy:	1486.6 eV
Source Strength:	100 W
Source Size:	0.4 × 0.4 mm ²
Analyzer Type:	Spherical sector analyzer
Incident Angle:	30°
Emission Angle:	53°
Analyzer Pass Energy:	200 eV
Instrument Resolution:	1.5 eV
Total Signal Accumulation Time:	612 s
Total Elapsed Time:	985 s
Number of Scans:	9



■ Accession #: 01977-02
 ■ Specimen: MP X60 steel
 ■ Technique: XPS
 ■ Spectral Region: Fe 2p

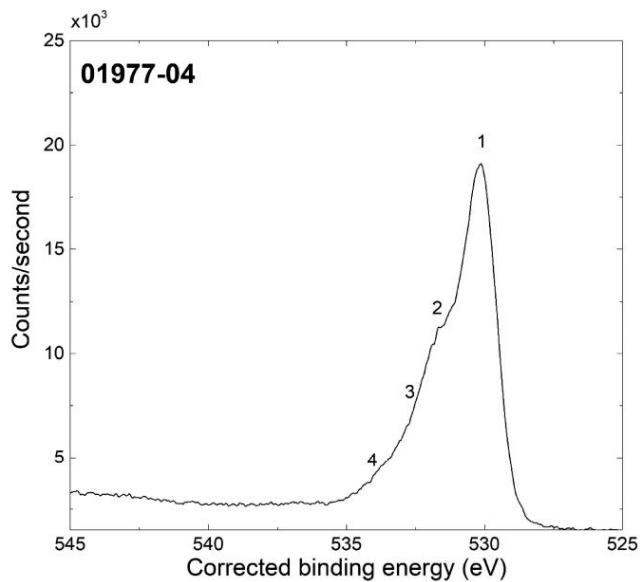
Instrument: Thermo Scientific Theta Probe
 Excitation Source: Al K_{α} monochromatic
 Source Energy: 1486.6 eV
 Source Strength: 100 W
 Source Size: $0.4 \times 0.4 \text{ mm}^2$
 Analyzer Type: Spherical sector
 Incident Angle: 30°
 Emission Angle: 53°
 Analyzer Pass Energy: 100 eV
 Instrument Resolution: 0.96 eV
 Total Signal Accumulation Time: 360 s
 Total Elapsed Time: 647 s
 Number of Scans: 9
 Comments: See the table's footnotes



■ Accession #: 01977-03
 ■ Specimen: MP X60 steel
 ■ Technique: XPS
 ■ Spectral Region: C 1s

Instrument: Thermo Scientific Theta Probe
 Excitation Source: Al K_{α} monochromatic
 Source Energy: 1486.6 eV
 Source Strength: 100 W
 Source Size: $0.4 \times 0.4 \text{ mm}^2$
 Analyzer Type: Spherical sector
 Incident Angle: 30°
 Emission Angle: 53°
 Analyzer Pass Energy: 100 eV
 Instrument Resolution: 0.96 eV
 Total Signal Accumulation Time: 171 s
 Total Elapsed Time: 383 s
 Number of Scans: 9
 Comments: See the table's footnotes

01 April 2024 13:31:06



■ Accession #: 01977-04
 ■ Specimen: MP X60 steel
 ■ Technique: XPS
 ■ Spectral Region: O 1s

Instrument: Thermo Scientific Theta Probe
 Excitation Source: Al K_{α} monochromatic
 Source Energy: 1486.6 eV
 Source Strength: 100 W
 Source Size: 0.4 × 0.4 mm²
 Analyzer Type: Spherical sector
 Incident Angle: 30°
 Emission Angle: 53°
 Analyzer Pass Energy: 100 eV
 Instrument Resolution: 0.96 eV
 Total Signal Accumulation Time: 180 s
 Total Elapsed Time: 389 s
 Number of Scans: 9
 Comments: See the table's footnotes

01 April 2024 13:32:06

7.3.2. Integration of PhD Manuscript: Paper 2



Article

A Contribution of XPS and Electrochemistry to the Understanding of Hydrogen Diffusion in X60 Steel

Raouaa Hannachi ¹, Deborah Biggio ¹, Bernhard Elsener ¹, Marzia Fantauzzi ¹, Nicoletta Zacchetti ² and Antonella Rossi ^{1,*}

¹ Department of Chemical and Geological Sciences, Campus of Monserrato, State University of Cagliari, 09042 Monserrato, (Cagliari), Italy; raouaa.hannachi@unica.it (R.H.); deborah.biggio@unica.it (D.B.); bernhard.elsener@unica.it (B.E.); fantauzzi@unica.it (M.F.)

² RINA Consulting-CSM S.p.A., Via di Castel Romano 100, 00128 Rome, Italy; nicoletta.zacchetti@rina.org

* Correspondence: rossi@unica.it

Abstract: Sustainable storage and transport of hydrogen are challenges in the transition to renewable energy sources. Hydrogen embrittlement (HE), caused by atomic hydrogen absorption and diffusion into steel, influences the mechanical properties of steel pipelines and reservoirs. This work focuses on the hydrogen diffusion on X60 pipeline steel using electrochemical measurements and X-ray photoelectron spectroscopy (XPS). The hydrogen permeation tests (HPT) were performed to estimate the effective hydrogen diffusion coefficient D_{eff} and the subsurface hydrogen concentration C_0 in cleaned and mechanically polished X60 steel. XPS analysis confirmed the presence of a 6 nm thick film of Fe (II) oxide, Fe (III) oxide, and Fe (III) oxyhydroxide. Mechanical polishing improved oxide layer uniformity, ensuring reproducible electrochemical behavior. The effective hydrogen diffusion coefficient D_{eff} was determined for X60 steel using t_{lag} and t_b methods. It was found in the range from $2.0 (0.4) 10^{-10} \text{ m}^2/\text{s}$ to $2.9 (0.5) 10^{-10} \text{ m}^2/\text{s}$. The subsurface hydrogen concentration, C_0 , was found to be $0.7 (0.1) \text{ ppm}$ for X60 steel. The hydrogen diffusion in X60 steel depends on its bulk properties; it is unaffected by surface preparation methods, and it is confirmed to be lower than in high-carbon and other high-strength steels.

Keywords: XPS; electrochemical hydrogen permeation test (HPT); hydrogen embrittlement (HE); X60 steel; iron speciation; thin film thickness



Academic Editor: Christos Argiris

Received: 19 February 2025

Revised: 31 March 2025

Accepted: 5 April 2025

Published: 8 April 2025

Citation: Hannachi, R.; Biggio, D.; Elsener, B.; Fantauzzi, M.; Zacchetti, N.; Rossi, A. A Contribution of XPS and Electrochemistry to the Understanding of Hydrogen Diffusion in X60 Steel. *Coatings* **2025**, *15*, 442. <https://doi.org/10.3390/coatings15040442>

Copyright: © 2025 by the authors. Licensee MDPI, Basel, Switzerland. This article is an open access article distributed under the terms and conditions of the Creative Commons Attribution (CC BY) license (<https://creativecommons.org/licenses/by/4.0/>).

1. Introduction

One of the main problems of sustainable energy production is the discrepancy between electricity production and electricity consumption [1]. Typical examples are the high production of electricity by solar cells in the summer and the demand for electricity in the winter. Therefore, solutions are needed to store renewable energy from summer to winter. As electrical energy cannot be stored in sufficiently high quantities in batteries, other seasonal energy storage solutions have to be found. One frequently used way to store electrical energy is electrolysis, which produces “green hydrogen” (hydrogen produced by sustainable energy sources) from cheap or even excess solar power in the summer and uses it to generate electricity in the winter. Efforts are underway to address the challenges associated with the efficient storage and transport of hydrogen; the traditional way to store hydrogen both in liquid form at cryogenic temperatures and as pressurized hydrogen gas in tanks is expensive and not very efficient. Different ways of storage are proposed in the literature; researchers propose a chemical storage way, relying on the steam-iron process [1]; an alternative to seasonal energy storage is “power to aluminum” [2]. Excess

electrical current is used to reduce aluminum hydroxide to elemental aluminum; during the reverse process, Al is oxidized to aluminum oxide or hydroxide, and hydrogen gas and heat are released.

For hydrogen transport over longer distances, steel pipelines are the favored choice due to their lower cost, high efficiency, and safety [3,4]. However, atomic hydrogen can absorb and diffuse into steel and potentially degrade its mechanical properties; this phenomenon is known as hydrogen embrittlement (HE) [5,6]. A laboratory study showed that hydrogen accelerated the fatigue of API X60 pipeline steel and its welds; it was found that hydrogen accelerated the crack growth phase in API X60 steel by a factor of 8 [7], which might seriously reduce the time of operation of the pipelines. The stress corrosion cracking (SCC) susceptibility of X60 steel was studied with slow strain rate tests in a solution simulating groundwater; it was found that the failure process was controlled by hydrogen embrittlement and anodic dissolution [8]. When repurposing existing gas pipelines for blended hydrogen or pure hydrogen transport, the hydrogen embrittlement sensitivity of the steels used has to be evaluated. Hydrogen embrittlement of X60 steel became more severe in 100% pure hydrogen, and the formation of secondary cracks was observed [9]. Hydrogen induced cracking susceptibility of X60 steel was studied, and the tensile test results showed that the ductility dropped by 83% in the hydrogen-charging environment [10].

Hydrogen embrittlement affects the performance of the steel pipelines, resulting in material degradation that leads to hydrogen leakage, which can cause combustion and possible explosion due to the wide range of flammability of hydrogen [11,12]. In addition, HE impacts the reliability and safety of metal structures in several other industries, such as aerospace, automotive, and construction [13], with possibly catastrophic consequences, especially in energy facilities such as power plants and nuclear plants [14].

For this reason, further investigations on materials are required for safely transporting hydrogen gas via steel pipelines. Key factors influencing HE are the diffusion behavior of absorbed atomic hydrogen within the material and its impact on the cohesive forces within the steel's crystal lattice [5]. The HE mechanism is mainly determined by the interaction between the absorbed hydrogen and the traps, such as grain boundaries, dislocations, and vacancies [6].

Techniques for investigating hydrogen diffusion in steel are essential. The electrochemical permeation test is performed using a Devanathan–Stachurski cell [15], which is a powerful electrochemical technique that provides information not only on the diffusion coefficient but also on the trapping of hydrogen in steel [16]. It consists of two electrochemical cells, the hydrogen production and the detection cells, separated by the sample clamped in between (working electrode: WE). In this study, an analytical approach based on in-situ techniques, such as the hydrogen permeation test (HPT), and surface analytical ex-situ techniques, X-ray photoelectron spectroscopy (XPS), was used on cleaned and mechanically polished X60 steels to clarify whether different surface treatments influence the hydrogen permeation results. HPT was also utilized to determine the effective diffusion coefficient and the subsurface concentration of hydrogen in steel. This work aims to develop an analytical method and investigate the hydrogen permeation in X60 pipeline steel to estimate the effective diffusion coefficient and the hydrogen subsurface concentration. The results of this work are the basis for future studies on X60 steel with hydrogen permeation barrier (HPB) coatings.

2. Materials and Methods

2.1. Materials

The steel studied in this work is API 5L X60QS steel. API 5L is the standard specification of the American Petroleum Institute for seamless and welded pipelines. The pipelines are made of carbon steel pipes used for oil and natural gas transportation. The abbreviation “X60” defines the minimum yield strength (60,000 psi or 415 MPa). This (high) strength is achieved through the addition of alloying elements such as manganese, silicon, and chromium. The steels “X65”, “X70”, and “X80” have a higher yield strength. Q refers to the production process, such as R: as rolled, N: normalized, Q: quenched and tempered, M: thermomechanical rolled, whereas S refers to the sour service use. The X60 steel samples were cut from a section of an as-produced carbon steel API 5L X60QS seamless pipe. According to API specifications [17], the chemical composition of an API 5L X60Q steel is reported in Annex H, paragraph H.4.1, table H1, page 126.

The diameter and thickness of the disk samples were 50 mm and 2 mm, respectively. The bulk composition of the X60 steel sample determined by portable X-ray fluorescence spectroscopy is provided in Table 1. P and S are below the limits of detection (LoD) of the pXRF. The instrument used was the hand-held SPECTRO xSORT (Spectro Analytical Instruments GmbH, Kleve, Germany); the analysis conditions were suggested by the supplier for the method named “precious metals” [18].

Table 1. Bulk composition (mean values, wt.%) of X60 steel determined by portable X-ray fluorescence spectroscopy. Standard deviations are in parentheses. P and S are below the limits of detection (LoD) of the p-XRF.

	Fe	Mn	Cr	Mo	Ni	Cu	S	P
Wt. %	98.2 (0.1)	1.20 (0.04)	0.20 (0.02)	0.10 (0.01)	0.10 (0.01)	0.10 (0.01)	<LoD	<LoD

It is noteworthy that all elements were found to be below the maximum concentration specified for an API 5L steel. The concentration of C could not be revealed by X-ray fluorescence spectroscopy.

The metallographic examinations of the cross-section of X60QS steel (etched with 2% Nital solution for 5 s) revealed an irregular grain size and shape with globular carbides along the grain boundaries, thus confirming a bainite/martensite microstructure as expected on a quenched and tempered product (Figure S1).

2.2. Sample Preparation

After cutting, the “as received” X60 steel was covered with an oil/grease film. Two different procedures were adopted for the surface preparation on both sides of the X60 steel disks:

- Procedure 1: Five solvent cleaning.

The as-received samples were covered with grease from the cutting process. They were cleaned in an ultrasonic bath at 40 °C using five solvents for 5 min each: butan-2-one (purity > 99.5% (CAS Nr. 78-93-3) purchased from Chem-lab, Zedelgem, Belgium), acetone ≥ 95.5% (CAS Nr. 67-64-1), ethanol absolute ≥ 99.8% (CAS Nr. 64-17-5, purchased from Honeywell, Offenbach, Germany), petroleum ether (CAS Nr. 650-001-01, purchased from Carlo Erba Reagents S.r.l, Cornaredo, (MI) Italy), and double distilled water (specific conductivity equal to 1.5 (0.1) μS/cm). Organic solvents were used to reduce the carbon signal, C1s, present on the sample surface. A polar solvent, double-distilled water, was used to remove the deposits of inorganic salts (e.g., Ca²⁺, Zn²⁺). The XP-spectra was

obtained after washing the sample with each solvent to monitor the removal of the organic compounds. This protocol was established in this work to achieve reproducible electrochemical measurements.

- Procedure 2: Five solvents cleaning and mechanical polishing

The samples were cleaned with five solvents as described above and mechanically polished using 4000-mesh SiC paper (Struers, Ballerup (DK)) and ethanol as lubricant for three minutes and thirty seconds. After mechanical polishing, the samples were immersed in an ultrasonic bath at 40 °C in ethanol for five minutes and in double-distilled water for ten minutes.

Following the cleaning and/or the mechanical polishing, the disks were heated at 80 °C for 15 h to remove any hydrogen that might be trapped in the steel following the manufacturing.

2.3. XPS Analysis

The surface composition of cleaned and mechanically polished X60 steel was investigated by XPS using a Theta Probe spectrometer (Thermo Fisher Scientific, East Grinstead (UK)). Survey and high-resolution spectra were acquired with a monochromatic Al K α source (1486.6 eV) and a nominal spot size of 400 μ m. The pass energy was set at 200 eV for the survey and 100 eV for the high-resolution spectra, respectively. The spectrometer was calibrated according to ISO 15472:2010 [19]. Data were processed using the CasaXPS software (V.2.3.25PR1.0) [20]. The energy resolution with a pass energy of 100 eV was determined using the Ag 3d_{5/2} signal, which has a full width at half-maximum (FWHM) of the peak height equal to 0.96 (0.05) eV. The angle between the source and the axis of the lens is 67.38°, and the angle between the axis of the source and the normal to the surface of the sample is 53°. More information is provided by Hannachi et al. [21]. The three-layer model [22] was applied to determine the thickness of the contamination layer, l_c , and the thickness of the oxide layer, t , which were simultaneously calculated by solving a system of nonlinear equations using a Newton–Raphson method [23]. The composition of the oxide film is given as an atomic percentage of the different oxidized iron species based on the integrated peak areas following the background subtraction according to iterative Shirley [20] and the curve fitting using Gaussian/Lorentzian product functions, as reported below in the results sections.

2.4. Electrochemical Permeation Test

The electrochemical permeation test is used to investigate the hydrogen diffusion in steel, and it was conducted using a hydrogen permeation cell (Devanathan and Stachurski cell) [15] consisting of two compartments (Figure 1a): the charging (or cathodic) cell where hydrogen is produced and the detection (or anodic) cell where hydrogen is detected. The surface of the sample exposed to the anodic and cathodic cell is 6.95 cm² (diameter 3 cm). Both cells are equipped with three electrodes: Ag/AgCl (KCl sat) as reference electrode (RE), platinum as counter electrode (CE), and the sample under analysis as working electrode (WE). The three electrodes in the anodic and cathodic cell were connected to a potentiostat, respectively, which was operated in floating mode (Figure 1a).

The charging cell was filled with 0.1 M HCl (CAS Nr. 7647-01-0 Honeywell, Offenbach, Germany) containing 0.2 g/L As₂O₃ (CAS Nr. 033-002-00-5, Carlo Erba Reagents S.r.l, Cornaredo, (MI), Italy). The detection cell was filled with 0.1 M NaOH (CAS Nr. 1310-73-2 Chem-lab, Zedelgem, Belgium). The measurements were conducted with the solutions open to the air.

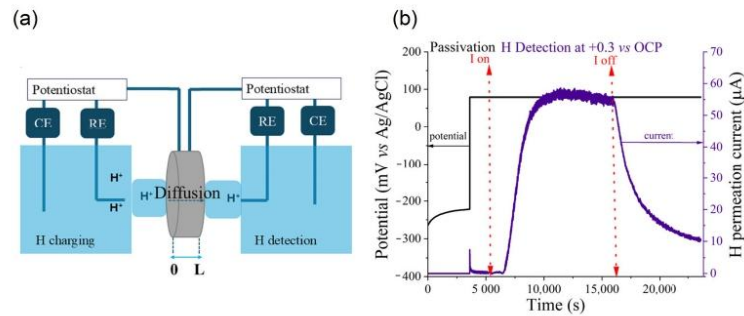


Figure 1. (a) Scheme of the electrochemical hydrogen permeation test set-up; (b) example of hydrogen permeation curve and timing.

The hydrogen permeation experiments followed precise timing (Figure 1b). First, the H-detection cell was filled with 0.1 M NaOH solution, and the open circuit potential (OCP) of the sample was recorded for 3600 s. Then, an anodic potential of +0.3 V vs. OCP was applied in the detection cell. The passivation current decreased with time, reaching values lower than $0.1 \mu\text{A}/\text{cm}^2$. Then, the charging cell was filled with 0.1 M HCl and 0.2 g/L As_2O_3 solution, and the OCP of the steel was measured for 300 s; this was followed by a galvanostatic cathodic polarization applying a current equal to -6 mA . The area of the sample exposed to the solutions is 6.95 cm^2 . After 3600 s at the OCP, a potential of +0.3 V vs. OCP was applied; a sudden increase in the current was recorded, and it was necessary to wait until 6000 s to reach a stable and low current value (about $1 \mu\text{A}$) at the detection side before applying the H production current.

The hydrogen permeation curve consists of three phases [16]: build-up, in which hydrogen entry and diffusion occur with an associated increase in current (i) until reaching a plateau, called steady state (i_{ss}). A decay is then observed, in which hydrogen de-trapping occurs.

From the permeation curve, the diffusion coefficient (D_{eff} (m^2/s)) can be calculated using two methods, the time lag method (Equation (1)) and the breakthrough time method (Equation (2)) [24]:

t_{lag} method:

$$D_{\text{eff}} = \frac{L^2}{6t_{\text{lag}}}, \quad (1)$$

Breakthrough method:

$$D_{\text{eff}} = \frac{L^2}{15.3t_b}, \quad (2)$$

where L is the thickness in meters of the sample, t_{lag} is the time (s) required to achieve 63% of steady state current density (i_{ss}), and t_b is the breakthrough time (s) that corresponds to the intersection of the tangent line at the inflection point and the x-axis in the permeation curve.

The subsurface concentration of diffusible hydrogen, C_0 , can be determined by Equation (3) [25]:

$$C_0 = \frac{i_{ss}L}{FD_{\text{eff}}} \frac{M_{\text{H}}}{\rho_{\text{Fe}}} 10^6, \quad (3)$$

where i_{ss} is the steady state permeation current density (A/m^2), L is the thickness of the sample (m), D_{eff} is the effective diffusion coefficient (m^2/s), F is the Faraday constant ($96,485 \text{ C}/\text{mol}$), M_{H} is the molar mass of hydrogen ($1 \text{ g}/\text{mol}$), and ρ_{Fe} is the iron density ($7.87 \times 10^6 \text{ g}/\text{m}^3$).

The data reported in this work are the mean values over at least three independent measurements. The standard deviations are given in parentheses in agreement with the guidelines published in [26].

3. Results

3.1. Conditioning of the Sample Surface Exposed to the Detection Side

The detection cell is filled with 0.1 M NaOH. The samples were conditioned by first exposing them to the NaOH solution and measuring for one hour the open circuit potential (OCP). The OCP versus exposure time curves for heated cleaned (H C X60) and mechanically polished (H MP X60) steel are shown in Figure 2. The open circuit potential increases asymptotically over time.

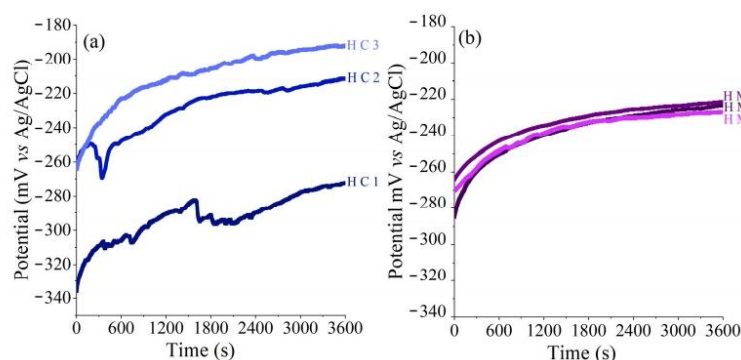


Figure 2. Open circuit potential (mV vs. Ag/AgCl) vs. time curves for hydrogen permeation curves (hydrogen detection current vs. time) for (a) three cleaned X60 steel samples after heating (H C 1, H C 2, H C 3), (b) three mechanically polished X60 steel after heating (H MP 1, H MP 2, H MP 3). H means heated; C means cleaned; MP means mechanically polished.

The potential immediately after immersion is at about -270 mV Ag/AgCl and reaches about -220 mV Ag/AgCl after one hour. The samples H MP X 60 steel are very reproducible (Figure 2b), and the H cleaned steel C X60 shows one outlier (Figure 2a).

Following the OCP measurement, the steels are passivated anodically at a potential $+0.3$ V vs. OCP. This procedure shall minimize the variation in surface conditions of the steel, prevent specimen oxidation, and increase the efficiency of the hydrogen atom oxidation reaction for more repeatable data [27]. The passivation current decreased following a power law and reached values below 0.5 μ A, thus lower than 0.1 μ A/cm² (Table 2).

Table 2. Open circuit potential (mV vs. Ag/AgCl) measured after 1 h of exposure to the solution and current after 1 h of passivation; standard deviations calculated over three independent measurements are in parentheses.

	OCP (1 h, 0.1 M NaOH) (mV vs. Ag/AgCl)	Passivation Current (After 1 h) (μ A)
H C X60 steel	-226 (42)	0.4 (0.3)
H MP X60 steel	-224 (3)	0.5 (0.2)

3.2. Conditioning of the Sample Surface Exposed to the Production Side

The production cell was filled with 0.1 M HCl solution containing 0.2 g/L As₂O₃; arsenic oxide inhibits the recombination reaction of hydrogen and promotes the formation of hydrogen atoms. The samples were exposed for 5 min to this solution, and also, in this

case, the OCP was measured. Afterward, the cathodic hydrogen production with a current of -6 mA was started. The value measured on H C X60 steel in 0.1 M HCl (-435 (5) mV vs. Ag/AgCl) is slightly lower than the OCP value recorded on H MP X60 steel (-415 (10) mV vs. Ag/AgCl). The potential during cathodic polarization with a current of -6 mA was found at -996 (4) mV vs. Ag/AgCl for H C X60 steel and at -1067 (83) mV vs. Ag/AgCl for H MP X60 steel.

3.3. Hydrogen Permeation Results

The anodic current at the detection cell was recorded continuously (Figure 3). After the start of hydrogen production, the current first remained very low, being almost 0 μ A; afterward, it rapidly increased during the build-up phase and reached a nearly steady-state value.

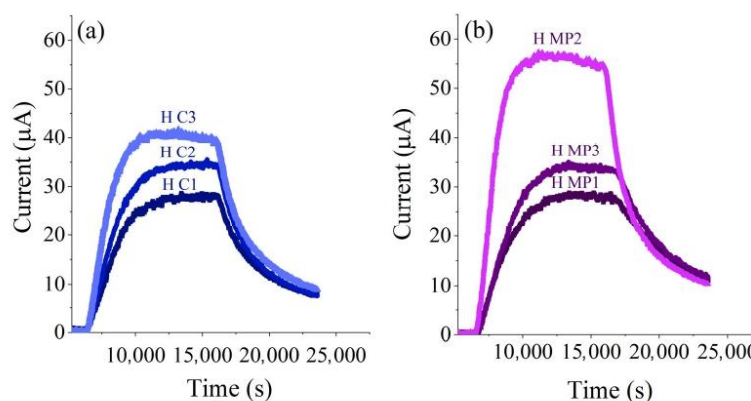


Figure 3. Hydrogen permeation curves (hydrogen detection current vs. time) for (a) three cleaned X60 steel samples (H C1, H C2, H C3), (b) three mechanically polished X60 steel (H MP1, H MP2, H MP3). H means heated; C means cleaned; MP means mechanically polished. The start of hydrogen production is at $t = 0$ (refer to Figure 1b at 6000 s).

After switching off the hydrogen production current, the anodic current in the detection cell decreased (decay phase).

The hydrogen permeation curves obtained on the cleaned H C X60 steel samples (Figure 3a) showed good reproducibility; the current due to hydrogen oxidation starts to increase, and the values of the steady state current, i_{ss} , are found to be 29.4 μ A, 35.7 μ A, and 41.8 μ A for three repeated measurements. The hydrogen permeation curves of three mechanically polished MP X60 steel samples (Figure 3b) showed a similar behavior of the build-up and decay phases. The current due to hydrogen oxidation starts to increase; the i_{ss} values are found to be 29.0 μ A, 57.9 μ A, and 35.0 μ A for the three samples.

The effective hydrogen diffusion coefficient was calculated for each permeation test using the time lag (t_{lag}) and the breakthrough (t_b) methods according to Equations (1) and (2); the results are reported in Table 3. The values of the effective diffusion coefficient D_{eff} are found to be about 2×10^{-10} m^2/s . No significant differences have been observed in the diffusion coefficient values for the cleaned and mechanically polished samples and between the two methods.

The subsurface concentration of hydrogen calculated using Equation (3) is shown in Table 3; the subsurface hydrogen concentration is slightly higher in the H MP X60 steel (0.8 (0.1) ppm) than in H C X60 steel (0.66 (0.02) ppm).

Table 3. Effective diffusion coefficients (D_{eff}) and subsurface concentration C_0 values for H C X60 and H MP X60 steels. The results are reported as mean values over three independent measurements, and the standard deviations are given in parentheses.

	$D_{eff} \cdot t_{lag}$ ($10^{-10} \text{ m}^2/\text{s}$)	Method	$D_{eff} \cdot t_b$ ($10^{-10} \text{ m}^2/\text{s}$)	Method	C_0 (ppm ^a)
H C X60 steel	2.4 (0.4)		2.8 (0.2)		0.66 (0.02)
H MP X60 steel	2.0 (0.4)		2.9 (0.5)		0.8 (0.1)

^a ppm: parts per million represent the mass fraction of hydrogen in iron, measured as milligrams of hydrogen per kilogram of iron.

3.4. XPS Results

The surface of X60 steel samples was analyzed by XPS. This technique provides information on the composition of the surface, the chemical state of iron, the thickness of the oxide layer, and the hydrocarbon contamination layer following the different steps of the sample preparation, such as cleaning, mechanical polishing, and heat treatment for 15 h at 80 °C.

The survey spectra provide an initial overview (Figure 4). Fe signals are detected at the surface of cleaned and mechanically polished X60 samples both before and after heating at 80 °C for 15 h. In addition, C and O signals are observed. Their presence can be ascribed to surface contamination and oxidation of the outer layer of the steel due to the exposure of the samples' surface to the ambient following the cleaning, heating procedures, and the sample transfer to the spectrometer.

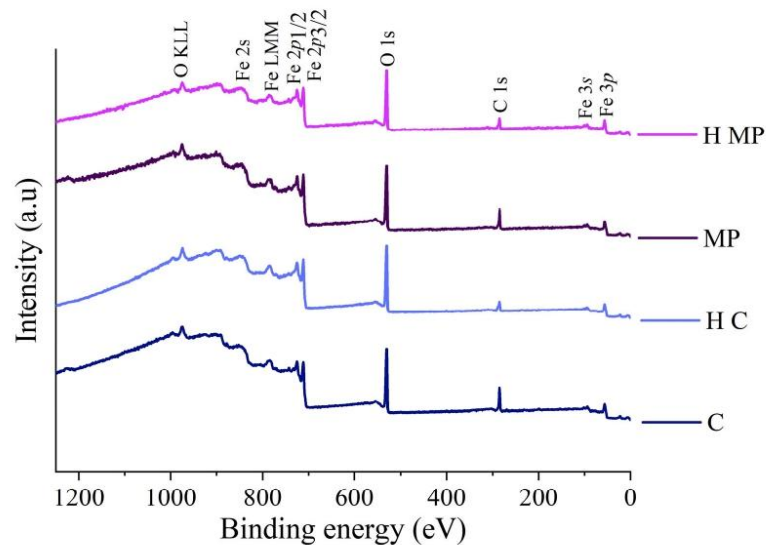


Figure 4. Survey spectra for cleaned (C), heated cleaned (H C), mechanically polished (MP), and heated MP (H MP) X60 steel.

Detailed information was obtained from the curve fitting of the high-resolution spectra (Figure 5). The curve fitting parameters of O 1s and Fe 2p signals are listed in Table S1 (Supporting Information). The Fe 2p_{3/2} peak of the H C X60 steel and H MP X60 steel (Figure 5a,c) were curve-fitted according to the literature [28] and showed four components. The peak energy of metallic iron (Fe (0)) was found to be 706.8 (0.1) eV for both cleaned and MP X60 steel and 707.0 (0.1) eV for heated cleaned and heated MP X60 steel; Fe (II)

oxide (FeO) was found at an energy value of 709.4 (0.1) eV with its satellite at 714.9 (0.1) eV; the peak energy of Fe (III) oxide (Fe₂O₃) was 710.6 (0.1) eV and for Fe (III) oxy-hydroxides (FeOOH) it was found to be 712.5 (0.1) eV [28].

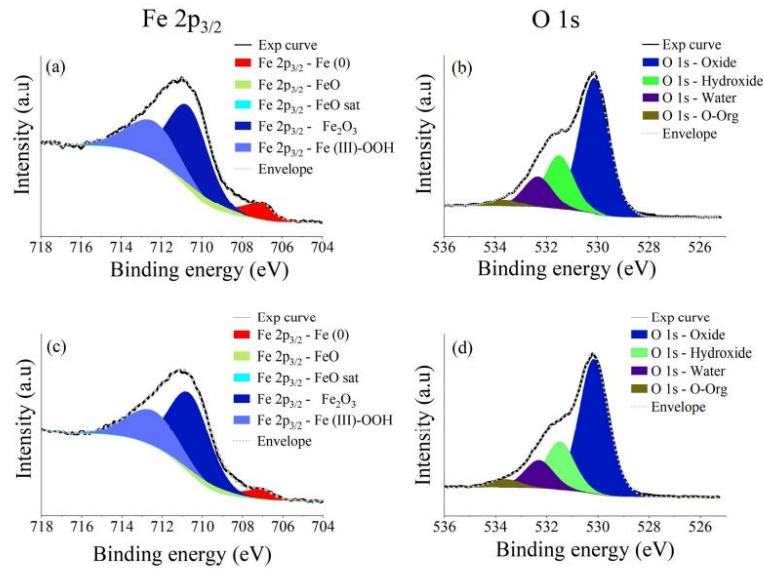


Figure 5. Fe 2p_{3/2} and O 1s peaks recorded on H C X60 steel (a,b) and H MP X60 steel (c,d).

The peak energies of each component are reported in Table 4 as mean values over three independent samples and analyzed in three areas each. The standard deviation in the text and in the table are given in parenthesis, as stated in the reference [26].

Table 4. Peak energy values (eV) of O 1s, Fe 2p_{3/2} XPS-signals of X60 steel reported as mean values over three independent measurements. The standard deviations are given in parentheses.

Elements	C X60 Steel Peak Energy (eV)	Heated C X60 Steel Peak Energy (eV)	MP X60 Steel Peak Energy (eV)	Heated C X60 Steel Peak Energy (eV)
O 1s–Oxide	530.1 (0.1)	530.2 (0.1)	530.1 (0.1)	530.2 (0.1)
O 1s–Hydroxide	531.4 (0.1)	531.4 (0.1)	531.4 (0.1)	531.5 (0.1)
O 1s–Water	532.2 (0.2)	532.2 (0.1)	532.2 (0.1)	532.3 (0.1)
O 1s–Organic contamination	533.5(0.1)	533.4 (0.1)	533.5 (0.1)	533.5 (0.1)
Fe 2p _{3/2} –Fe (0)	706.8 (0.1)	707.0 (0.1)	706.8 (0.1)	707.0 (0.1)
Fe 2p _{3/2} –FeO	709.4 (0.1)	709.4 (0.2)	709.3 (0.1)	709.4 (0.1)
Fe 2p _{3/2} –FeO sat	714.9 (0.1)	714.9 (0.2)	714.8 (0.1)	714.9 (0.1)
Fe 2p _{3/2} –Fe ₂ O ₃	710.6 (0.1)	710.7 (0.1)	710.6 (0.1)	710.6 (0.1)
Fe 2p _{3/2} –Fe (III)-OOH	712.5 (0.1)	712.6 (0.1)	712.5 (0.1)	712.4 (0.1)

The O 1s signals showed four components; the peak energies of the components are at 530.1 (0.1) eV, 531.4 (0.1) eV, 532.2 (0.1) eV, and 533.5 (0.1) eV, and they are assigned to oxides, hydroxides, adsorbed water, and organic contamination, respectively [21] (Figure 5b,d and Table 4). Figure S2 (Supplementary Materials) shows the Fe 2p_{3/2} and O 1s spectra after curve-fitting obtained on the solvent cleaned X60 steel and on the X60 after mechanical polishing but before heating.

The composition of the surface layer was calculated by taking into account the oxidized iron species, and the results are shown in Table 5. The three layers model allows calculating the thickness of the contamination layer (l_c) and of the oxide layer (t). The composition of the iron oxy-hydroxide film is similar in both samples.

Table 5. Thickness of the contamination layer l_c and the oxide layer t calculated applying the three-layer model for Cleaned, MP steel, and H C X60 and H MP X60 steels. Results are reported as mean values over three independent measurements, and the standard deviations are given in parentheses.

	C X60 Steel	Heated C X60 Steel	MP X60 Steel	Heated MP X60 Steel
l_c (nm)	3.5 (0.8)	2.7 (0.3)	2.9 (0.5)	3.3 (0.2)
t (nm)	4.1 (0.5)	6.8 (0.9)	5.5 (0.7)	7.7 (0.5)
Atom % FeO	5 (2)	0.5 (0.7)	4 (3)	0.9 (0.9)
Atom % Fe ₂ O ₃	60 (2)	64 (3)	62 (2)	64 (2)
Atom % FeOOH	35 (3)	36 (3)	34 (3)	35 (2)

4. Discussion

4.1. Surface Composition and Homogeneity

The peak energy values of Fe (II) oxide, Fe (III) oxide, and Fe (III)-OOH are in agreement with the literature [21,28,29], and they remained unchanged within the experimental uncertainty (0.1 eV) for all the samples regardless of the treatment (C X60, H C X60, MP X60 and H MP X60). The results of the peak binding energy values of nine analyzed areas on three independent samples are presented in Figure 6a. The component ascribed to metallic iron was found to be 0.2 eV higher after heating than before heating.

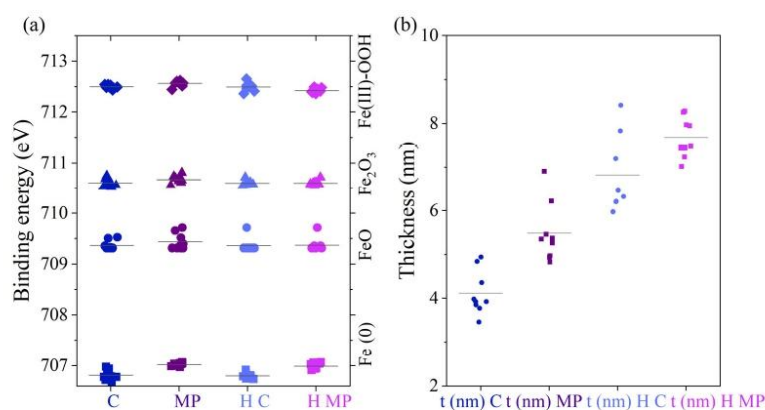


Figure 6. (a) Dot plot of the peak energies of Fe $2p_{3/2}$ components for cleaned (C), Heated C (H C), and MP, Heated MP (H MP) steels. (b) Dot plot of oxide layer thickness (t) calculated using the three-layer model for MP, C, H C and H MP X60 steels.

The thickness of the hydrocarbon contamination layer showed a small variation for the heated C X60 and for the heated MP X60 steels (Table 5) in comparison with the same samples before heating. The thickness of the oxide layers of the series of heated samples following both the cleaning with organic solvents and the mechanical polishing was higher than that of the same samples before heating. This suggests that the surface layer grows upon heating as expected. The standard deviation higher for the thickness values of the cleaned samples after heating might be interpreted as an indication of the growth of a non-homogeneous surface film. A more detailed analysis with a dot plot (Figure 6b) revealed

that there are “outliers” that can be traced back to two points analyzed on two (of three) different samples. This indicates that the procedure of mechanical polishing leads to more reproducible surfaces, as indicated by the reproducibility of the open circuit potential versus time curves (Figure 2) for the mechanically polished surfaces (Figure 2b). Studies have shown that mechanically polished steel exhibits a better reproducibility of passive film after immersion in aggressive solutions [30].

Based on the peak energies of both iron and oxygen signals, we can state that the surface film is made of iron oxyhydroxides. The iron is mainly present as Fe (III) (Table 5). After heating, the atomic percentage of FeO strongly decreases; the Fe (II) component in the fitted Fe 2p_{3/2} spectrum almost disappears, and this can explain the high relative uncertainty, which characterizes this contribution to the signal after heating (Table 5; from 5 (2) % to about 0.5 (0.7) % for C X60 steel and from 4 (3) % to about 0.8 (0.9) % in the case of the MP X60 steel). This decrease might be due to the fact that heating promotes oxidation into more stable oxides, such as Fe₂O₃. This might be substantiated by the trend that indicates an increase in the atomic percentage of Fe₂O₃. This observation is in agreement with the findings that heating can alter oxidation states and reduce reactive species on the surface [31].

4.2. Hydrogen Diffusion Coefficient of X60

The effective hydrogen diffusion coefficient D_{eff} values (Table 3) calculated with the t_{lag} and t_b methods are comparable, and no influence of the sample preparation method can be revealed. This indicates that the hydrogen diffusion coefficient is governed by the bulk material properties and it seems that it is not affected by nanometer thick surface layers. These two methods (t_{lag} and t_b), used frequently in the literature [32,33], are based on the assumption that the diffusion of hydrogen in the metal can be described by Fick’s laws (Equations (4) and (5)) [34] where j is the hydrogen flux, D_{eff} is the effective hydrogen diffusion coefficient, C the hydrogen concentration, x the distance from the surface, and t the time.

$$j(x, t) = -D_{\text{eff}} \frac{\partial C(x, t)}{\partial x}, \quad (4)$$

$$\frac{\partial C}{\partial t} = D_{\text{eff}} \frac{\partial^2 C}{\partial x^2}, \quad (5)$$

The solution of Fick’s laws depends on the boundary conditions and the system geometry. For the Devanathan and Stachurski electrochemical double cell (see experimental), the conditions are (1) a membrane of finite thickness L ; (2) $C = C_0$ at $x = 0$, meaning a constant hydrogen concentration C_0 at the production side; and (3) $C = 0$ at $x = L$, meaning that the hydrogen concentration at the detection side of the membrane is zero.

The effective diffusion coefficients calculated for the H C X60 steel ($2.4 (0.4) 10^{-10} \text{ m}^2/\text{s}$) and for the H MP X60 steel ($2.0 (0.4) 10^{-10} \text{ m}^2/\text{s}$) are in the same order of magnitude (Table 3) and in agreement with literature data (Figure 7) [35]. The fact that D_{eff} determined that the time lag method (63% of steady state current) and the breakthrough method (about 5% of the steady state current) are nearly identical (see Table 3) indicates that the experiments reached the steady state (Figure 3). The highest values of D_{eff} are reported for Armco iron ($6.2 \times 10^{-9} \text{ m}^2/\text{s}$) [36] and pure annealed iron ($4 \times 10^{-9} \text{ m}^2/\text{s}$) [37]. The comparison of the literature data obtained using different steels (Figure 8) shows that the hydrogen diffusion coefficient D_{eff} of X60 steel in this work is similar to the one of X65 steel ($2.3 \times 10^{-10} \text{ m}^2/\text{s}$) [35] and $3.5 \times 10^{-10} \text{ m}^2/\text{s}$ [38]. Previous studies reported hydrogen diffusion coefficient to be $6.2 \times 10^{-11} \text{ m}^2/\text{s}$ and $5.1 \times 10^{-11} \text{ m}^2/\text{s}$ for different grade high-strength pipeline steels such as X70 C and X80 C steels, respectively [32]. High carbon steel exhibited a D_{eff} value equal to $2.2 \times 10^{-11} \text{ m}^2/\text{s}$) [36].

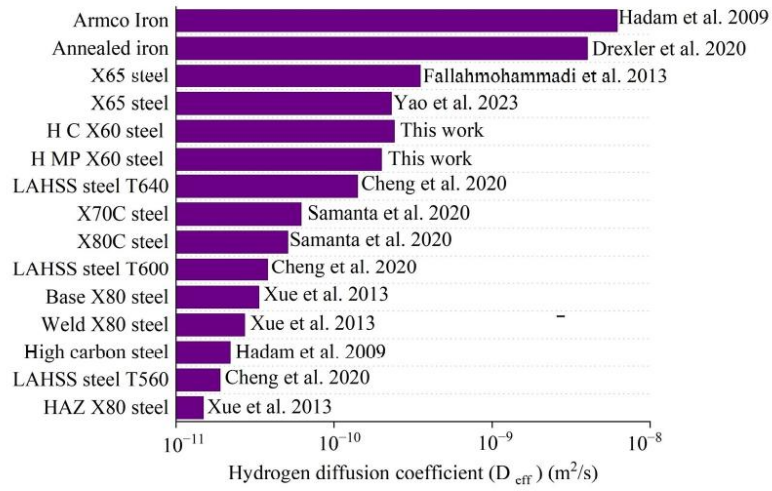


Figure 7. Comparison of literature data on the effective diffusion coefficient of iron, steel, and high-strength steel with the data of this work [32,33,35–39].

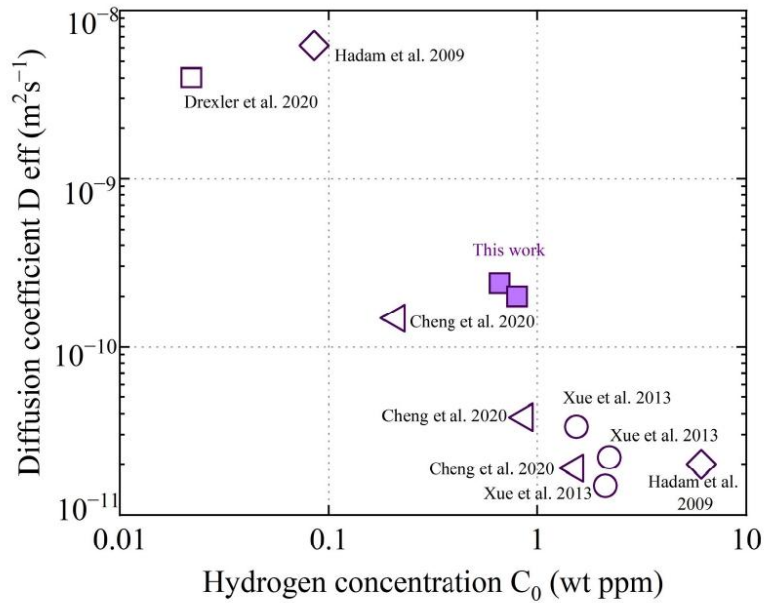


Figure 8. Comparison of the effective diffusion coefficient D_{eff} and the subsurface hydrogen concentration C_0 for different iron and steel grades from literature, \triangleleft [33], \diamond [36], \square [37], \circ [39].

The influence of different tempering temperatures on the hydrogen diffusion on low-alloy high strength steel (LAHSS) [33] showed that the hydrogen diffusion coefficient D_{eff} increased with tempering temperature (Figure 7) [33].

4.3. Hydrogen Sub-Surface Concentration (C_0) of X60 Steel

The study of hydrogen subsurface concentration in steels is critical for understanding hydrogen embrittlement. Hydrogen accumulation near the surface can initiate micro-cracks, which can propagate under mechanical stress, leading to a failure [33].

The sub-surface hydrogen concentration C_0 at the production side of the sample was calculated from the hydrogen permeation curves using Equation (3).

The subsurface hydrogen concentration C_0 of heated C X60 and MP X60 steel is given in Table 6, together with the literature data from other steels of different compositions, microstructure, and heat treatment. In literature, two different units are used to report hydrogen concentration: mol H/m³ and ppm (Table 6). The conversion factor is the iron density of 7.87 g/cm³; for the sake of clarity, this discussion uses only ppm. The lowest values of C_0 are reported for annealed iron (0.022 ppm) [37] and annealed Armco iron (0.085 ppm) [36]. The hydrogen concentration C_0 in low alloyed high-strength steel (LAHSS) at different tempering temperatures (560 °C, 600 °C and 640 °C) was found to be 1.52 ± 0.01 ppm, 0.87 ± 0.08 ppm and 0.21 ± 0.01 ppm, respectively [33]. The influence of welding was tested on X80 steel; the hydrogen concentration C_0 for weld, heat affected zone (HAZ), and base X80 steel were found to be 2.21 ppm, 2.12 ppm, and 1.54 ppm, respectively [39].

Table 6. Hydrogen subsurface concentrations of different steel present in the literature compared with those obtained in this work.

	* C_0 (ppm)	* C_0 mol H/m ³	Ref.
Heated C X60 steel	0.66 (0.02)	5.2 (1.4)	This work
Heated MP X60 steel	0.8 (0.1)	6.3 (0.8)	This work
LAHSS steel T640	0.21	1.65	[33]
LAHSS steel T600	0.87	6.85	[33]
LAHSS steel T560	1.52	11.96	[33]
High carbon steel	6.09	47.5	[36]
Weld X80 steel	2.21	17.43	[39]
HAZ X80 steel	2.12	16.71	[39]
Base X80 steel	1.54	12.12	[39]
Annealed iron	0.022	0.17	[37]
Armco Iron	0.085	0.662	[36]

* The values written in italics are converted values.

4.4. Influence of Steel Microstructure and Composition

The steel studied in this work is API 5L X60 steel. API 5L is the standard specification for pipelines of the American Petroleum Institute. The pipelines are made of carbon steel pipes used for oil and gas transmission. The abbreviation “X60” defines the minimum yield strength (60,000 psi or 415 MPa). This (high) strength is achieved through the addition of alloying elements such as manganese, silicon, and chromium. The steels “X65”, “X70” and “X80” have a higher yield strength.

It is now interesting to evaluate the effective diffusion coefficient D_{eff} and the sub-surface hydrogen concentration C_0 of the different iron-based materials (Figure 8). At first glance, a log-log plot of D_{eff} vs. C_0 results in an approximately linear relationship, representing a power law. A high effective diffusion coefficient D_{eff} is related to a very low hydrogen concentration C_0 and vice versa: this appears to be valid for various materials independently from the method applied for the calculation of D_{eff} and C_0 . It is noteworthy that a wide range of materials, from annealed and Armco iron [36,37] over the X60 steels studied in this work to X80 base material, welded, and heat affected zone (HAZ) [39],

as well as LAHSS steel, tempered at temperatures between 560 and 640 °C [33], are in agreement with this power law.

5. Conclusions

This investigation provides a detailed evaluation of the surface composition and hydrogen permeability of X60 steel in terms of hydrogen diffusion coefficient and subsurface hydrogen concentration. The comparison with the literature data for various steels is also discussed. The following conclusions can be drawn

- XPS analysis revealed the presence of a film composed of Fe (II) oxide, Fe (III) oxide, and Fe (III) oxyhydroxide on the steel substrate on both organic-solvents cleaned and mechanically polished X60 steel samples. The composition and the film thickness formed upon heating at 80 °C for 15 h at the surface of mechanically polished samples are more reproducible than in the case of films present on the steels following the cleaning procedure with organic solvents. The reproducibility of the sample preparation ensures the reproducibility of the electrochemical results.
- The effective diffusion coefficients D_{eff} of both H C X60 and H MP X60 steels, calculated using t_{lag} and t_b methods, are in agreement with the literature data. D_{eff} depends on the bulk properties of the steel; indeed, D_{eff} of X60 steel seems to be unaffected by the presence of a nanometric thick film constituted of iron oxy-hydroxides. The lower D_{eff} value of X60 steel compared to pure iron might be explained by the presence of higher carbon content or other alloying elements changing the microstructure.
- The subsurface hydrogen concentration C_0 in X60 steel was found to be equal to 0.66 (0.02) ppm for C X60 steel and to 0.8 (0.1) ppm for MP X60 steel is lower than in high-carbon steels and other high-strength pipeline steels such as X80. This may be attributed to its specific microstructure, which includes bainite and possible martensite with globular carbides.

Supplementary Materials: The following supporting information can be downloaded at <https://www.mdpi.com/article/10.3390/coatings15040442/s1>: Table S1: Curve fitting parameters used for O 1s, Fe 2p_{3/2} signals of X60. Standard deviations calculated over three independent measurements are in parentheses.; Figure S1: SEM micrograph of X60QS microstructure after etching with 2% Nital solution for 5 s. The X60QS (quenched- tempered and sour) is a product with an expected microstructure consisting in bainite and possible martensite. This SEM cross-section image of the sample reveals an irregular grain size and shape with globular carbides along the grain boundaries, thus, confirming a bainite/martensite microstructure; Figure S2: Fe 2p_{3/2} and O 1s peaks recorded on C X60 steel (a,b) and MP X60 steel (c,d) before heating.

Author Contributions: Conceptualization, A.R. and B.E.; methodology, A.R., B.E. and D.B.; validation, R.H. and D.B.; formal analysis, R.H., B.E. and D.B.; investigation: R.H.; resources, A.R. and N.Z.; data curation, R.H.; writing—original draft preparation, R.H. and B.E.; writing—reviewing and editing, A.R., B.E., M.F., D.B. and N.Z.; supervision, A.R. and N.Z.; project administration, A.R.; funding acquisition, A.R. and N.Z. All authors have read and agreed to the published version of the manuscript.

Funding: The PhD fellowship of Raouaa Hannachi is co-funded by Ministero dell'Università e della ricerca (MUR)—Italy, grant number CUP F22B22000560005) and by RINA Consulting—CSM S.p.A. This research was funded by “e.INS, Ecosystem of Innovation for Next Generation Sardinia”, funded by the National Recovery and Resilience Plan (PNRR)—Mission 4, Component 2, “From research to business” Investment 1.5, “Creation and strengthening of Ecosystems of innovation” and construction of “Territorial R&D Leaders”, grant number CUP F53C22000430001.

Institutional Review Board Statement: Not applicable.

Informed Consent Statement: Informed consent was obtained from all subjects involved in the study.

Data Availability Statement: Data are available on request.

Acknowledgments: Giovanni Emanuele Porcedda is gratefully acknowledged for the maintenance and the calibration of the Theta Probe spectrometer. Material Engineer Mauro Guagnelli is gratefully acknowledged for the interesting discussions on the steel X60QS microstructure. D. Biggio, gratefully acknowledges the financial support of the European Union NextGenerationEU under the National Recovery and Resilience Plan (NRRP) of Ministero dell'Università e della Ricerca (MUR) (Project code PE0000021, Network 4 Energy Sustainable Transition, NEST).

Conflicts of Interest: The authors declare no conflicts of interest.

Abbreviations

The following abbreviations are used in this manuscript:

HE	Hydrogen Embrittlement
HPB	Hydrogen Permeation Barrier
HPT	Hydrogen Permeation Test
t_{lag}	Time lag
t_b	Breakthrough time
D_{eff}	Effective hydrogen diffusion coefficient
C_0	Subsurface hydrogen concentration
OCP	Open Circuit Potential
MP	Mechanically Polished
C	Cleaned
H MP	Heated MP
H C	Heated Cleaned
BCC	Body-centered cubic
XRD	X ray Diffraction
SEM	Scanning Electron Microscopy
XPS	X ray Photoelectron Spectroscopy
FWHM	Full Width at Half-Maximum
BE	Binding Energy

References

1. Heiniger, S.P.; Fan, Z.; Lustenberger, U.B.; Stark, W.J. Safe Seasonal Energy and Hydrogen Storage in a 1: 10 Single-Household-Sized Pilot Reactor Based on the Steam-Iron Process. *Sustain. Energy Fuels* **2024**, *8*, 125–132. [[CrossRef](#)]
2. Haller, M.Y.; Carbonell, D.; Dudita, M.; Zenhäusern, D.; Häberle, A. Seasonal Energy Storage in Aluminium for 100 Percent Solar Heat and Electricity Supply. *Energy Convers. Manage X* **2020**, *5*, 100017. [[CrossRef](#)]
3. Mahajan, D.; Tan, K.; Venkatesh, T.; Kileti, P.; Clayton, C.R. Hydrogen Blending in Gas Pipeline Networks—A Review. *Energies* **2022**, *15*, 3582. [[CrossRef](#)]
4. Ohaeri, E.; Eduok, U.; Szpunar, J. Hydrogen Related Degradation in Pipeline Steel: A Review. *Int. J. Hydrogen Energy* **2018**, *43*, 14584–14617. [[CrossRef](#)]
5. Negi, A.; Elkhodbia, M.; Barsoum, I.; AlFantazi, A. Coupled Analysis of Hydrogen Diffusion, Deformation, and Fracture: A Review. *Int. J. Hydrogen Energy* **2024**, *82*, 281–310. [[CrossRef](#)]
6. He, Y.; Su, Y.; Yu, H.; Chen, C. First-Principles Study of Hydrogen Trapping and Diffusion at Grain Boundaries in γ -Fe. *Int. J. Hydrogen Energy* **2021**, *46*, 7589–7600. [[CrossRef](#)]
7. Faucon, L.E.; Boot, T.; Riemsdag, T.; Scott, S.P.; Liu, P.; Popovich, V. Hydrogen-Accelerated Fatigue of API X60 Pipeline Steel and Its Weld. *Metals* **2023**, *13*, 563. [[CrossRef](#)]
8. Contreras, A.; Hernández, S.L.; Galvan-Martinez, R.; Vega-Becerra, O. Tension Tests Behavior of API 5L X60 Pipeline Steel in a Simulated Soil Solution to Evaluate SCC Susceptibility. *MRS Online Proc. Libr.* **2012**, *1481*, 1–10. [[CrossRef](#)]
9. Walallawita, R.; Hinchliff, M.C.; Sediako, D.; Quinn, J.; Chou, V.; Walker, K.; Hill, M. Evaluating the Effect of Blended and Pure Hydrogen in X60 Pipeline Steel for Low-Pressure Transmission Using Hollow-Specimen Slow-Strain-Rate Tensile Testing. *Metals* **2024**, *14*, 1132. [[CrossRef](#)]
10. Mohtadi-Bonab, M.A.; Eskandari, M.; Rahman, K.M.M.; Ouellet, R.; Szpunar, J.A. An Extensive Study of Hydrogen-Induced Cracking Susceptibility in an API X60 Sour Service Pipeline Steel. *Int. J. Hydrogen Energy* **2016**, *41*, 4185–4197. [[CrossRef](#)]

11. Sun, B.; Zhao, H.; Dong, X.; Teng, C.; Zhang, A.; Kong, S.; Zhou, J.; Zhang, X.-C.; Tu, S.-T. Current Challenges in the Utilization of Hydrogen Energy—a Focused Review on the Issue of Hydrogen-Induced Damage and Embrittlement. *Adv. Appl. Energy* **2024**, *14*, 100168. [CrossRef]
12. Hoschke, J.; Chowdhury, M.F.W.; Venezuela, J.; Atrons, A. A Review of Hydrogen Embrittlement in Gas Transmission Pipeline Steels. *Corros. Rev.* **2023**, *41*, 277–317. [CrossRef]
13. Chen, Y.-S.; Huang, C.; Liu, P.-Y.; Yen, H.-W.; Niu, R.; Burr, P.; Moore, K.L.; Martínez-Pañeda, E.; Atrons, A.; Cairney, J.M. Hydrogen Trapping and Embrittlement in Metals—A Review. *Int. J. Hydrogen Energy* **2024**, *in press*. [CrossRef]
14. Young, G. Hydrogen Embrittlement in Nuclear Power Systems. In *Gaseous Hydrogen Embrittlement of Materials in Energy Technologies*; Woodhead Publishing: Sawston, UK, 2011; ISBN 978-1-84569-673-3.
15. Devanathan, M.A.V.; Stachurski, Z.; Tompkins, F.C. The Adsorption and Diffusion of Electrolytic Hydrogen in Palladium. *Proc. R. Soc. London. Ser. A Math. Phys. Sci.* **1997**, *270*, 90–102. [CrossRef]
16. Zakroczyński, T. Adaptation of the Electrochemical Permeation Technique for Studying Entry, Transport and Trapping of Hydrogen in Metals. *Electrochim. Acta* **2006**, *51*, 2261–2266. [CrossRef]
17. API 5L X60 Pipe Specifications (PSL1 & PSL2)—Octal Steel. Available online: <https://www.octalsteel.com/resources/api-5l-gr-x60-pipe/> (accessed on 18 March 2025).
18. SPECTRO xSORT XHH03 XRF Handheld Analyzer. Available online: <https://www.spectro.com/products/xrf-handheld-analyzer/www.spectro.com/products/xrf-handheld-analyzer/xsort-xhh03> (accessed on 18 March 2025).
19. ISO 15472:2010; Surface Chemical Analysis—X-Ray Photoelectron Spectrometers—Calibration of Energy Scales. International Organization for Standardization: Geneva, Switzerland, 2010. Available online: <https://www.iso.org/standard/55796.html> (accessed on 30 January 2025).
20. Fairley, N.; Fernandez, V.; Richard-Plouet, M.; Guillot-Deudon, C.; Walton, J.; Smith, E.; Flahaut, D.; Greiner, M.; Biesinger, M.; Tougaard, S.; et al. Systematic and Collaborative Approach to Problem Solving Using X-Ray Photoelectron Spectroscopy. *Appl. Surf. Sci. Adv.* **2021**, *5*, 100112. [CrossRef]
21. Hannachi, R.; Biggio, D.; Elsener, B.; Fantauzzi, M.; Rossi, A. X-Ray Photoelectron Spectroscopy Investigation of X60 Steel. *Surf. Sci. Spectra* **2024**, *31*, 024014. [CrossRef]
22. Rossi, A.; Eisener, B. XPS Analysis of Passive Films on the Amorphous Alloy Fe₇₀Cr₁₀P₁₃C₇: Effect of the Applied Potential. *Surf. Interface Anal.* **1992**, *18*, 499–504. [CrossRef]
23. Ypma, T.J. Historical Development of the Newton-Raphson Method. *SIAM Rev.* **1995**, *37*, 531–551. [CrossRef]
24. Koren, E.; Hagen, C.M.H.; Wang, D.; Lu, X.; Johnsen, R.; Yamabe, J. Experimental Comparison of Gaseous and Electrochemical Hydrogen Charging in X65 Pipeline Steel Using the Permeation Technique. *Corros. Sci.* **2023**, *215*, 111025. [CrossRef]
25. Van den Eeckhout, E.; De Baere, I.; Depover, T.; Verbeken, K. The Effect of a Constant Tensile Load on the Hydrogen Diffusivity in Dual Phase Steel by Electrochemical Permeation Experiments. *Mater. Sci. Eng. A* **2020**, *773*, 138872. [CrossRef]
26. Ellison, S.L.R.; Williams, A. *Eurachem/CITAC Guide: Quantifying Uncertainty in Analytical Measurement*, 3rd ed.; Eurachem/CITAC: Teddington, UK, 2012; ISBN 978-0-948926-30-3.
27. Casanova, T.; Crousier, J. The Influence of an Oxide Layer on Hydrogen Permeation through Steel. *Corros. Sci.* **1996**, *38*, 1535–1544. [CrossRef]
28. Biggio, D.; Elsener, B.; Usai, G.; Fantauzzi, M.; Rossi, A. Surface Chemistry of Passive Films on Ni-Free Stainless Steel: The Effect of Organic Components in Artificial Saliva. *Langmuir* **2024**, *40*, 6824–6833. [CrossRef] [PubMed]
29. Elsener, B.; Pisu, M.; Fantauzzi, M.; Addari, D.; Rossi, A. Electrochemical and XPS Surface Analytical Study on the Reactivity of Ni-Free Stainless Steel in Artificial Saliva. *Mater. Corros.* **2016**, *67*, 591–599. [CrossRef]
30. Rossi, A.; Elsener, B.; Hähner, G.; Textor, M.; Spencer, N.D. XPS, AES and ToF-SIMS Investigation of Surface Films and the Role of Inclusions on Pitting Corrosion in Austenitic Stainless Steels. *Surf. Interface Anal.* **2000**, *29*, 460–467. [CrossRef]
31. Rossi, A.; Elsener, B.; Spencer, N.D. *XPS Surface Analysis: Imaging and Spectroscopy of Metal and Polymer Surfaces*; Spectroscopy Europe/World: West Sussex, UK, 2004; Volume 16.
32. Samanta, S.; Kumari, P.; Mondal, K.; Dutta, M.; Singh, S.B. An Alternative and Comprehensive Approach to Estimate Trapped Hydrogen in Steels Using Electrochemical Permeation Tests. *Int. J. Hydrogen Energy* **2020**, *45*, 26666–26687. [CrossRef]
33. Cheng, X.Y.; Zhang, H.X. A New Perspective on Hydrogen Diffusion and Hydrogen Embrittlement in Low-Alloy High Strength Steel. *Corros. Sci.* **2020**, *174*, 108800. [CrossRef]
34. Frappart, S.; Feaugas, X.; Creus, J.; Thebault, F.; Delattre, L.; Marchebois, H. Study of the Hydrogen Diffusion and Segregation into Fe–C–Mo Martensitic HSLA Steel Using Electrochemical Permeation Test. *J. Phys. Chem. Solids* **2010**, *71*, 1467–1479. [CrossRef]
35. Fallahmohammadi, E.; Bolzoni, F.; Lazzari, L. Measurement of Lattice and Apparent Diffusion Coefficient of Hydrogen in X65 and F22 Pipeline Steels. *Int. J. Hydrogen Energy* **2013**, *38*, 2531–2543. [CrossRef]
36. Hadam, U.; Zakroczyński, T. Absorption of Hydrogen in Tensile Strained Iron and High-Carbon Steel Studied by Electrochemical Permeation and Desorption Techniques. *Int. J. Hydrogen Energy* **2009**, *34*, 2449–2459. [CrossRef]

37. Drexler, A.; Siegl, W.; Ecker, W.; Tkadletz, M.; Klösch, G.; Schnideritsch, H.; Mori, G.; Svoboda, J.; Fischer, F.D. Cycled Hydrogen Permeation through Armco Iron—A Joint Experimental and Modeling Approach. *Corros. Sci.* **2020**, *176*, 109017. [[CrossRef](#)]
38. Yao, C.; Ming, H.; Chen, J.; Wang, J.; Han, E.-H. Effect of Cold Deformation on the Hydrogen Permeation Behavior of X65 Pipeline Steel. *Coatings* **2023**, *13*, 280. [[CrossRef](#)]
39. Xue, H.B.; Cheng, Y.F. Hydrogen Permeation and Electrochemical Corrosion Behavior of the X80 Pipeline Steel Weld. *J. Mater. Eng Perform* **2013**, *22*, 170–175. [[CrossRef](#)]

Disclaimer/Publisher's Note: The statements, opinions and data contained in all publications are solely those of the individual author(s) and contributor(s) and not of MDPI and/or the editor(s). MDPI and/or the editor(s) disclaim responsibility for any injury to people or property resulting from any ideas, methods, instructions or products referred to in the content.

7.3.2. Integration of PhD Manuscript: Paper 3



RESEARCH ARTICLE OPEN ACCESS

A Surface Analytical Method for Determining the Porosity of Tungsten Coatings as Hydrogen Permeation Barriers

R. Hannachi¹ | D. Biggio¹ | B. Elsener¹ | M. Fantauzzi¹ | N. Zacchetti² | A. Rossi¹

¹Department of Chemical and Geological Sciences, University of Cagliari, Cagliari, Monserrato, Italy | ²RINA Consulting—CSM S.P.A., Rome, Italy

Correspondence: A. Rossi (rossi@unica.it)

Received: 19 July 2025 | Revised: 23 September 2025 | Accepted: 30 September 2025

Funding: This research was supported by E.INS, Ecosystem of Innovation for Next Generation Sardinia, funded by the National Recovery and Resilience Plan (PNRR)—Mission 4, Component 2, From Research to Business Investment 1.5. Creation and Strengthening of Ecosystems of Innovation, and construction of Territorial R&D Leaders, grant number CUP F53C22000430001. The PhD fellowship of Ms. Raouaa Hannachi is co-funded by Ministero dell'Università e della ricerca (MUR)—Italy, grant number CUP F22B22000560005 and by RINA Consulting—CSM S.p.A.

Keywords: hydrogen permeation barrier (HPB) | roughness | tungsten-coating on X60 steel | X-ray photoelectron spectroscopy

ABSTRACT

Fast and reliable methods that permit the determination of the through-thickness coating porosity are required to develop optimized coating–substrate systems that act as hydrogen permeation barriers. In this work, we present an analytical approach for determining the porosity of tungsten coatings that are 1.5 and 3 μm thick. The coatings are applied to X60QS API 5L pipeline steel, which has a surface roughness of R_a 0.4 μm , as well as to polished substrates with a roughness of R_a 0.2 μm . The method utilizes X-ray photoelectron spectroscopy (XPS) measurements for the coating analysis. The W-coatings were produced by radio frequency magnetron sputtering. The through-thickness porosity was calculated as the ratio of the Fe 2p to W 4f signals from the XPS survey spectra corrected for the respective sensitivity factors. The results from three different samples, for each of which three different areas were analyzed, showed a high porosity of 3.5 (0.8) % for the 3- μm -thick W-coating on the rough substrate, no pores for the 3- μm -thick W-coating on the smooth substrate, and less than 0.5% porosity on one out of three samples of the 1.5- μm coating on the smooth substrate. These results correlate well with the intensity of the hydrogen permeation current.

1 | Introduction

During the production, storage, and transportation of hydrogen used as a sustainable energy carrier, hydrogen atoms can enter the steel and cause hydrogen embrittlement (HE) [1, 2]. This is a major concern in the hydrogen industry, as HE can deteriorate mechanical properties, lead to cracks, hydrogen leaks, and failures [3]. To avoid or at least reduce hydrogen ingress into the steel substrate, hydrogen permeation barriers (HPBs) are applied [4, 5]. Tungsten has a very low hydrogen diffusion coefficient [6]; thus, tungsten coatings are promising candidates for HPBs [7]. The production of the W-coatings by magnetron sputtering on technical substrates such as steel is challenging: it requires a reproducible surface preparation of the substrate, well-defined coating procedures, and controlled deposition

parameters. Despite these efforts, the coatings might show through-thickness defects and open channels between the substrate and the electrolyte through the coating that adversely affect the hydrogen permeation reduction efficiency.

The quantitative characterization of open porosity is thus of great interest to researchers and the industry. An (ideally non-destructive) test procedure to determine through-thickness defects of the coating is required. There are many methods to determine the open porosity in coatings, mainly applied to investigating corrosion resistance [8, 9]. Frequently, electrochemical methods are applied to analyze the whole surface under test [10, 11] or use scanning electrochemical microscopy [12] to determine local pores by detecting the iron ions from the dissolution of the substrate. All these methods require electrochemical

This is an open access article under the terms of the [Creative Commons Attribution License](#), which permits use, distribution and reproduction in any medium, provided the original work is properly cited.

© 2025 The Author(s). *Surface and Interface Analysis* published by John Wiley & Sons Ltd.

Surface and Interface Analysis, 2026; 58:3–8
<https://doi.org/10.1002/sia.70027>

3

instrumentation and immersion of the samples under test in an aggressive electrolyte where the substrate material at the through-coating pores is corroding. This work proposes X-ray photoelectron spectroscopy (XPS) as a nondestructive test procedure to verify the open porosity in the tungsten coatings.

2 | Experimental

2.1 | The Substrate: X60 Steel

The base material (substrate) of the samples was API 5L X60QS steel. API 5L is the standard specification for pipelines of the American Petroleum Institute. The abbreviation "X60" defines the minimum yield strength (60,000 psi or 415 MPa). Q refers to the production process and means Quenched and tempered; S refers to the Sour Service use. In the following, the acronym X60 is used. The chemical composition determined by portable X-ray fluorescence spectroscopy (p-XRF) is given in Table 1 and the content of the main constituents is in accordance with the value reported in the API 5L pipe specification [13]. C, P, and S could not be detected by the handheld SPECTRO xSORT (Spectro Analytical Instruments GmbH, Kleve, Germany) used in this work; C was not revealed since the instrument allows the quantification of elements with Z higher than 11; P and S are below the detection limits under the adopted conditions that are estimated to be 0.03 wt % and 0.02 wt %, respectively, according to the information provided by the instrument manufacturer for these elements in iron-based alloys.

Before coating deposition, the steel samples were degreased in ethanol, rinsed with acetone in an ultrasonic bath, and washed with isopropanol. The surface roughness of the samples was measured by a Mitutoyo SV-3200 H4 surface roughness tester and found to be about R_a 0.4 μm for Series 1. Further samples (Series 2 and 3) were mechanically polished with SIC 2000 (grain size = 8–5 μm) abrasive paper supplied by Struers and had a roughness of R_a 0.2 μm .

2.2 | Deposition of Tungsten Coatings

Prior to W-coating deposition, the X60 steel samples were heated to 350°C to outgas and remove intrinsic residual gas, such as oxygen, nitrogen, and hydrogen, which might negatively affect the W film deposited [14].

The tungsten coatings were deposited by radio frequency (RF) magnetron sputtering in a dedicated sputtering chamber in Ar⁺ plasma. Before the coating formation, the sample had a 6-min glow, 11-min ramp-up, and 5-min cleaning time. Sputtering targets of pure tungsten (purity > 99.95%) were used. Radio frequency magnetron sputtering (RF) with a power of 800 W

was applied. The deposition temperature was 350°C, and the total pressure in the chamber was 10⁻² bar. The substrates were mounted on a substrate holder and installed 75 mm from the target surface. Three series of tungsten coatings were produced, each differing in substrate roughness and coating thickness (Table 2). The coating deposition time was 4 h for the 3- μm -thick coating and 2 h for the 1.5- μm one.

Scanning electron microscopy investigations were conducted at the advanced metallography laboratory at Rina consulting CSM SpA, Castel Romano, Rome with a SEM Zeiss EVO M 15 using a 15- to 20-kV electron beam voltage in the backscattered electron mode. Typical cross sections of the W coated X-60 steel samples are shown in Figure 1. The coatings of Series 2 and 3 look dense and have good adhesion to the substrate; a columnar substructure in the coatings with grain size lower than 1 μm can be observed. The coating of Series 1 with the higher surface roughness (R_a 0.4 μm) shows local irregularities and partial detachment (buckling). The porosity (or inhomogeneity) of the sample of series one and the buckling of the W-coating are possibly due to internal stress and poor adhesion due to the high roughness R_a = 0.4 μm of the substrate.

2.3 | XPS Surface Analysis

The surface composition of the W-coatings on X60 steel was investigated by XPS using a Theta Probe spectrometer (Thermo Fisher Scientific). The base pressure during analysis was always lower than 5 × 10⁻⁷ Pa (i.e., 5 × 10⁻⁹ mbar/3.75 × 10⁻⁹ Torr). All spectra were acquired with a monochromatic Al K α source (1486.6 eV). Lateral resolution, i.e., the smallest distance by which two features have to be spaced in order to be resolved as separate, was experimentally determined, and it was found to be 414 μm . This measurement was performed considering the distance through which a gold-coated Si wafer

TABLE 2 | Tungsten coatings prepared by RF magnetron sputtering used in this study.

Coating	Substrate surface roughness R_a	Nominal coating thickness	Coating thickness determined by SEM
			Mean value (SD)
Series 1	0.4 μm	3 μm	3.6 (0.7) μm
Series 2	0.2 μm	3 μm	3.350 (0.004) μm
Series 3	0.2 μm	1.5 μm	1.59 (0.04) μm

TABLE 1 | Chemical composition (wt %) of API 5L X60 steel by p-XRF.

	Fe	Mn	Cr	Mo	Ni	Cu	C	P	S
API specification	Balance	≤ 1.40	≤ 0.50	≤ 0.15	≤ 0.50	≤ 0.50	≤ 0.28	≤ 0.03	≤ 0.03
p-XRF results	98.2 (0.1)	1.20 (0.04)	0.20 (0.02)	0.10 (0.01)	0.10 (0.01)	0.10 (0.01)	—	< 0.02	< 0.03

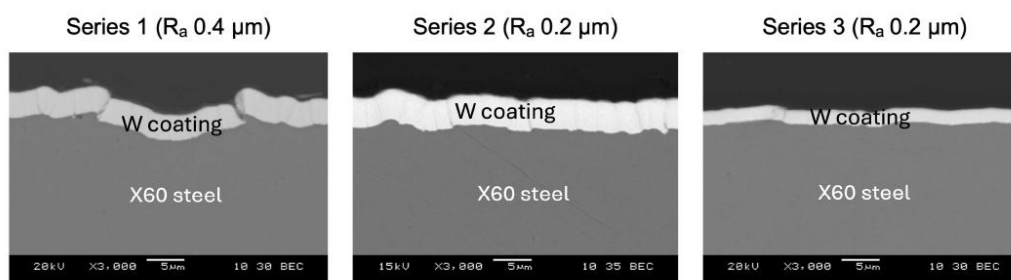


FIGURE 1 | SEM micrographs of the cross section of W coated X60 steels.

edge is translated across the analysis area and the intensity of the Au $4f_{7/2}$ peak changes from 20% to 80%. The estimated analysis area was 0.5 mm^2 . The pass energy for the survey spectra was set at 200 eV. The energy step size was equal to 1 eV, and the dwell time was 50 ms. The linearity of the binding energy scale was checked according to ISO 15472:2010. Data were processed using CasaXPS software (V.2.3.25PR1.0) [15]. An accurate description of the spectrometer and the analysis setup is provided elsewhere [16]. The iterative Shirley background subtraction was applied. The sensitivity factor was determined considering Scofield's photoionization cross sections (σ) [17] of Fe 2p (16.42) and W 4f (9.8).

3 | Results and Discussion

3.1 | XPS Survey Spectra of W-Coated X60 Steel

For each series of W-coatings (Table 2), three independent samples and three different areas on each sample were analyzed, giving the possibility for a statistical analysis. Examples of survey spectra of each series are shown in Figure 2. In all survey spectra, the signals of tungsten (W 4f, W 4d, W 4p, and W 4s), oxygen (O 1s), and carbon (C 1s) were assigned. No other elements (e.g., due to the presence of contaminants) were detected under these analysis conditions. A small signal of Fe 2p (from the steel) was detected in all analysis points of Series 1 and on sample 2 of Series 3; no iron was detected in the samples of Series 2.

Analyzing the Fe 2p spectrum in more detail, the peak binding energy was found at about 711 eV, indicating the presence of iron oxide and not of a bare steel surface (binding energy at 707.0 eV). It can be reasonably assumed that during the mechanical polishing process and exposure to the atmosphere, the steel substrate at the pores was oxidized. The resulting iron oxide (rust) was filling the pores and was revealed by XPS. The presence and intensity of the Fe 2p signal were used to evaluate the coating porosity further.

3.2 | Determination of the Open Porosity

The Fe 2p signal in the survey spectra of W-coated X60 steel was used to evaluate the through-thickness porosity of the coating more quantitatively. Through-thickness porosity here means

cracks, through-going pores, and defects in the coating that allowed the iron signal to be detected from the X60 steel substrate. These pores and defects would form a direct path from the electrolyte to the steel substrate, thus allowing hydrogen entrance into the steel despite the tungsten coating.

In each survey spectrum, the area of the Fe 2p signal and of the W 4f signal (after background subtraction and after σ correction) was determined. The percentage of through-thickness porosity was calculated by dividing the area of the Fe 2p signal by the area of the W 4f signal (Figure 3), taking into account the calculated sensitivity factors of iron Fe 2p (16.42) and W 4f (9.8). The results are given in Table 3.

Clear differences emerged among the three series analyzed. Series 1 exhibited an average open porosity of 3.5% (with a standard deviation of 0.8%), showing small variations between the three replica samples. Sample 1 demonstrated the lowest porosity, but there was a significant difference in the analyzed points. The probability distribution of the open porosity can be plotted using all nine data points from Series 1 (see Figure 3).

The tungsten coatings on X60 steel produced in Series 2 (R_a of the substrate $0.2 \mu\text{m}$, coating thickness $3 \mu\text{m}$) did not show the presence of the iron signal. Thus, the coating had no through-going defects. The coating of Series 3 with a thickness of $1.5 \mu\text{m}$ showed low through-going porosity of about 0.5% only in one of three replica samples (Table 3).

3.3 | Influence of Surface Roughness

As a reason for the different porosity of tungsten-coating of $3 \mu\text{m}$ thickness (Series 1 and 2 in Table 3), the different surface roughness R_a can be identified: the X60 substrate with higher surface roughness shows 3.5 (0.8)% of through-thickness porosity, while the coating on the smoother substrate (Series 2) showed no pores. The SEM images of the cross sections (Figure 1) show for Series 1 (R_a $0.4 \mu\text{m}$) a rougher and more irregular surface, known as buckling of the coating due to high internal compressive stress. Rough surfaces have microscopic peaks and valleys that can act as stress concentrators, leading to localized deformation of the coating and initiating buckling at weak points. Coatings of Series 2 with the same coating thickness but a lower surface roughness (R_a $0.2 \mu\text{m}$) are smoother than those with higher roughness and do not show buckling.

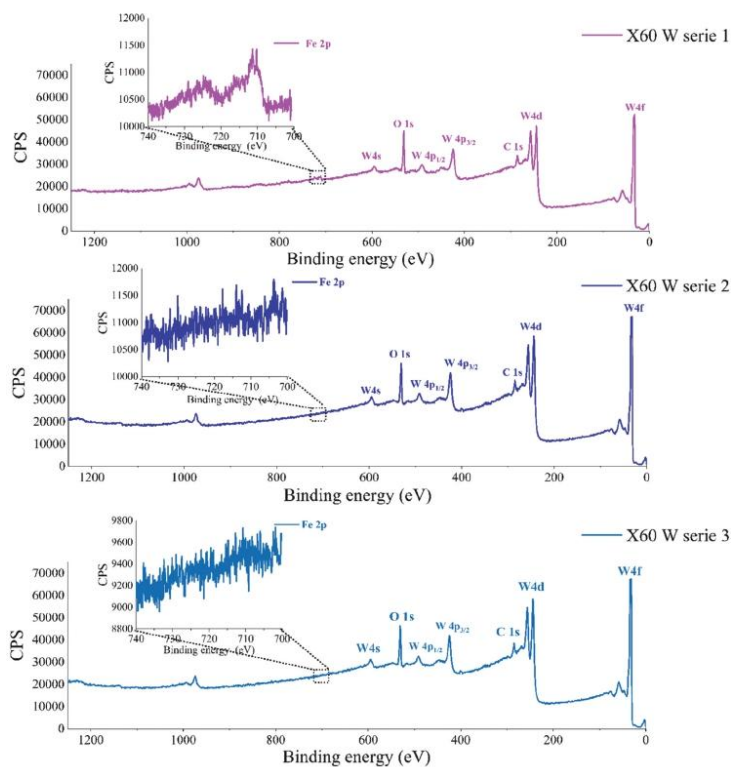


FIGURE 2 | Examples of survey spectra of W-coated X60 steel of the three series examined. The insert shows the Fe 2p region. The presence of iron was revealed for all samples of Series 1.

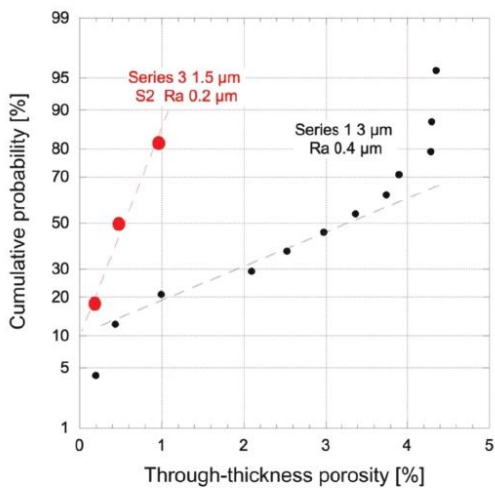


FIGURE 3 | Cumulative probability of the through-thickness porosity of W-coated X60 steel.

TABLE 3 | Calculated through-thickness porosity (%) obtained from the survey spectra of the W-coated X60 steels.

	Sample 1	Sample 2	Sample 3	Mean value (SD)
Series 1	3.0 (1.1)	3.5 (0.7)	4.0 (0.3)	3.5 (0.8)
Series 2	0	0	0	0
Series 3	0	0.5 (0.4)	0	n.d.

Abbreviation: n.d. = not determined.

The effect of the surface roughness of the substrate was tested with TiN/zirconium samples [18]. For an increasing surface roughness $R_a = 0.08$ (0.03) μm to 0.3 (0.03) μm , the appearance of the surface became worse and less smooth. Lee et al. [3] studied the corrosion behavior of 2.36 μm CrN thick films on steel substrate with roughness, R_a of 0.10, 0.20, and 0.31 μm , and observed that the coating porosity increased with increasing roughness. For a PVD CrN coating, Liu et al. [19] found a decrease in defects as surface roughness decreased with polishing, which changed from 220 grit SiC to a 6- μm diamond paste.

TABLE 4 | Maximum hydrogen permeation currents I_{ss} (μA) on W-coated X60 steel samples and permeation reduction factors (PRF) determined with hydrogen permeation tests.

	Maximum hydrogen permeation current (mA)			PRF	Through – thickness porosity (%)
	Sample 1	Sample 2	Sample 3		Mean value (SD)
Series 1	9.5	8	6.5	4–5	3.5 (0.8)
Series 2	< 1	< 1.5	< 1	> 40	0
Series 3	< 1	7	< 1	n.d.	n.d.

Note: Through-thickness porosity (%) is also given.

ISO 4527:2003 [20] recommends a roughness value of R_a lower than $0.2\mu\text{m}$ to prevent corrosion. A low porosity is even more relevant when using these alloys as HPB, as the porosity affects hydrogen diffusion. No influence on porosity was revealed for a $50\text{-}\mu\text{m}$ -thick tantalum coating on steel [21].

3.4 | Comparison With Hydrogen Permeation Tests

The hydrogen permeation tests on the X60 steel substrate were reported previously [22]. The samples were outgassed in an oven at 80°C for 15 h before the electrochemical tests.

The average maximum hydrogen permeation current I_{ss} was found to be about $40\mu\text{A}$. The results of electrochemical hydrogen permeation tests on the W-coated X60 steel samples are summarized in Table 4; full details on the electrochemical permeation test setup are given in a companion paper [22].

From the ratio of the steady-state permeation rate through the coated membrane, J_{uncoated} divided by the permeation rate through the coated membrane, J_{coated} , the permeation reduction factor (PRF) was calculated according to [4]:

$$\text{PRF} = \frac{J_{\text{uncoated}}}{J_{\text{coated}}} \quad (1)$$

The results are given in Table 4. The samples of Series 2 did not show any hydrogen detection current; the PRF was higher than 40. Samples of Series 1 instead showed a PRF of only about 4–5. Series 2 (coating $1.5\mu\text{m}$ thick) showed two samples with $\text{PRF} > 40$, and one sample (sample 2) exhibited a low PRF. The results agree with the porosity of the coatings (Table 3).

3.5 | Alternative Methods to Determine the Open Porosity in Coatings

The detection of small, sparsely populated defects can be challenging with optical or scanning electron microscopy. The small size of these defects requires high magnification, and due to the considerable average distance between neighboring defects, it is unlikely that any defect will appear within the field of view. XPS surface analysis, as utilized in this investigation, examines a relatively large area of the sample. While it does not provide details about the size and location of individual pores, it does measure the overall intensity of iron (Fe 2p) related to the oxide that forms within the pores.

The method proposed in this study is nondestructive, and it requires an XPS spectrometer to operate under high vacuum conditions. The measured spot size was $414\mu\text{m}$, and the XPS signals are averaged over this area. Due to the low escape depth of photoelectrons, defects can be revealed by the Fe 2p photoelectrons only when iron oxide is present, as the steel substrate corrodes during exposure to the atmosphere and mechanical polishing.

This is in contrast to electrochemical methods of porosity detection, where an electrolytic connection from the surface to the substrate can be formed through all thickness defects [23, 24]. As a result, the porosity indicated by electrochemical tests might be higher. A detailed comparison with electrochemical methods falls outside the scope of this paper.

4 | Conclusions

Fast and reliable methods that permit the determination of the through-thickness coating porosity are required to develop optimized coating–substrate systems that act as HPBs.

XPS surface analysis based on the survey spectra of the tungsten coatings on X60 steel has proved that analyzing the Fe 2p signal in the survey spectra can reveal the presence of pores and cracks. The through-thickness coating porosity is higher for higher surface roughness R_a of the substrate.

The W-coating on samples from series one (thickness $3\mu\text{m}$; substrate roughness, R_a , $0.4\mu\text{m}$) exhibits porosity caused by buckling. This buckling is likely due to the high surface roughness of the substrate. Since nine analyzed areas from three independent samples in each series were measured using XPS, it can be reasonably concluded that this is not merely a localized effect. The low hydrogen PRFs of the W-coatings on X60 steel can be rationalized by high porosity and vice versa.

Author Contributions

Raouaa Hannachi: investigation, writing the first draft – review and editing and visualization. **Deborah Biggio:** methodology, validation, investigation, and writing – review, editing, and supervision. **Bernhard Elsener:** conceptualization, methodology, validation, formal analysis, writing – original draft, review and editing, and supervision. **Marzia Fantauzzi:** writing – review and editing, supervision. **Nicoletta Zacchetti:** resources, writing – review and editing, supervision, funding acquisition. **Antonella Rossi:** conceptualization, methodology, validation, formal analysis, investigation,

resources, writing – original draft, review and editing, supervision and funding acquisition.

Acknowledgments

The authors would like to acknowledge the support for this work provided by RINA for the W-coated steel samples and the SEM/EDX measurements on the samples. Mr. Giovanni Emanuele Porcedda is gratefully acknowledged for maintaining and calibrating the Theta Probe spectrometer. D. Biggio, PhD, gratefully acknowledges the financial support of the European Union NextGenerationEU under the National Recovery and Resilience Plan (NRRP) of Ministero dell'Università e della Ricerca (MUR) (Project Code PE0000021, Network 4 Energy Sustainable Transition, NEST). Open access publishing facilitated by Università degli Studi di Cagliari, as part of the Wiley - CRUI-CARE agreement.

Conflicts of Interest

The authors declare no conflicts of interest.

Data Availability Statement

The data that support the findings of this study are available from the corresponding author upon reasonable request.

References

1. U. S. Meda, N. Bhat, A. Pandey, K. N. Subramanya, and M. A. Lourdu Antony Raj, "Challenges Associated With Hydrogen Storage Systems Due to the Hydrogen Embrittlement of High Strength Steels," *International Journal of Hydrogen Energy* 48, no. 47 (2023): 17894–17913, <https://doi.org/10.1016/j.ijhydene.2023.01.292>.
2. R. A. Oriani, "Hydrogen Embrittlement of Steels," *Annual Review of Materials Science* 8 (1978): 327–357, <https://doi.org/10.1146/annurev.ms.08.080178.001551>.
3. S. C. Lee, W. Y. Ho, and F. D. Lai, "Effect of Substrate Surface Roughness on the Characteristics of CrN Hard Film," *Materials Chemistry and Physics* 43, no. 3 (1996): 266–273, [https://doi.org/10.1016/0254-0584\(95\)01636-9](https://doi.org/10.1016/0254-0584(95)01636-9).
4. V. Nemanich, "Hydrogen Permeation Barriers: Basic Requirements, Materials Selection, Deposition Methods, and Quality Evaluation," *Nuclear Materials and Energy* 19 (2019): 451–457, <https://doi.org/10.1016/j.nme.2019.04.001>.
5. E. C. E. Rönnebro, R. L. Oelrich, and R. O. Gates, "Recent Advances and Prospects in Design of Hydrogen Permeation Barrier Materials for Energy Applications—A Review," *Molecules* 27, no. 19 (2022): 6528, <https://doi.org/10.3390/molecules27196528>.
6. G. A. Esteban, A. Perujo, L. A. Sedano, and K. Douglas, "Hydrogen Isotope Diffusive Transport Parameters in Pure Polycrystalline Tungsten," *Journal of Nuclear Materials* 295, no. 1 (2001): 49–56, [https://doi.org/10.1016/S0022-3115\(01\)00486-X](https://doi.org/10.1016/S0022-3115(01)00486-X).
7. V. Nemanich, J. Kovač, C. Lungu, C. Porosnicu, and B. Zajec, "Characterization of Tungsten Films and Their Hydrogen Permeability," *Journal of Vacuum Science & Technology A* 32, no. 6 (2014): 061511, <https://doi.org/10.1116/1.4898061>.
8. ISO 10308:2006(en), Metallic Coatings—Review of porosity tests, accessed May 30, 2025, <https://www.iso.org/obp/ui/en/#iso:std:iso:10308:ed-2:v1:en>.
9. S. H. Ahn, J. H. Lee, H. G. Kim, and J. G. Kim, "A Study on the Quantitative Determination of Through-Coating Porosity in PVD-Grown Coatings," *Applied Surface Science* 233, no. 1 (2004): 105–114, <https://doi.org/10.1016/j.apsusc.2004.03.213>.
10. Elsener, B. Rota, A. Böhni, H. Impedance Study on the Corrosion of PVD and CVD Titanium Nitride Coatings, *Materials Science Forum* 1989;44-45:29–38, <https://doi.org/10.4028/www.scientific.net/MSF.44-45.29>.
11. W. Taro and D. Landolt, "Electrochemical Determination of the Porosity of Single and Duplex PVD Coatings of Titanium and Titanium Nitride on Brass," *Journal of the Electrochemical Society* 145, no. 12 (1998): 4173–4181, <https://doi.org/10.1149/1.1838932>.
12. J. Vega, H. Scheerer, G. Andersohn, and M. Oechsner, "Evaluation of the Open Porosity of PVD Coatings Through Electrochemical Iron Detection," *Surface and Coating Technology* 350 (2018): 453–461, <https://doi.org/10.1016/j.surfcoat.2018.06.095>.
13. API 5L X60 Pipe Specifications (PSL1 & PSL2)—Octal Steel, accessed March 18, 2025, <https://www.octalsteel.com/resources/api-5l-gr-x60-pipe/>.
14. M. Braun, "Magnetron Sputtering Technique," in *Handbook of Manufacturing Engineering and Technology* (Springer, 2013), 1–25, https://doi.org/10.1007/978-1-4471-4976-7_28-9.
15. N. Fairley, P. Bargiela, A. Roberts, V. Fernandez, and J. Baltrusaitis, "Practical Guide to Understanding Goodness-of-Fit Metrics Used in Chemical State Modeling of x-Ray Photoelectron Spectroscopy Data by Synthetic Line Shapes Using Nylon as an Example," *Journal of Vacuum Science and Technology* 41, no. 1 (2022): 013203, <https://doi.org/10.1116/6.0002196>.
16. R. Hannachi, D. Biggio, B. Elsener, M. Fantauzzi, and A. Rossi, "X-Ray Photoelectron Spectroscopy Investigation of X60 Steel," *Surface Science Spectra* 31, no. 2 (2024): 024014, <https://doi.org/10.1116/6.0003972>.
17. J. H. Scofield, "Hartree-Slater Subshell Photoionization Cross-Sections at 1254 and 1487 eV," *Journal of Electron Spectroscopy and Related Phenomena* 8, no. 2 (1976): 129–137, [https://doi.org/10.1016/0368-2048\(76\)80015-1](https://doi.org/10.1016/0368-2048(76)80015-1).
18. W. Xiao, H. Deng, S. Zou, et al., "Effect of Roughness of Substrate and Sputtering Power on the Properties of TiN Coatings Deposited by Magnetron Sputtering for ATF," *Journal of Nuclear Materials* 509 (2018): 542–549, <https://doi.org/10.1016/j.jnucmat.2018.07.011>.
19. C. Liu, A. Leyland, S. Lyon, and A. Matthews, "An A.C. Impedance Study on PVD CrN-Coated Mild Steel With Different Surface Roughnesses," *Surface and Coatings Technology* 76 (1995): 623–631, [https://doi.org/10.1016/0257-8972\(95\)02544-8](https://doi.org/10.1016/0257-8972(95)02544-8).
20. ISO 4527:2003(en), Metallic Coatings—Autocatalytic (electroless) Nickel–Phosphorus Alloy Coatings—Specification and Test Methods, accessed May 30, 2025, <https://www.iso.org/obp/ui/en/#iso:std:iso:4527:ed-2:v1:en>.
21. S. M. Maeng, L. Axe, T. A. Tyson, L. Gladczuk, and M. Sosnowski, "Corrosion Behavior of Magnetron Sputtered α -Ta Coatings on Smooth and Rough Steel Substrates," *Surface and Coatings Technology* 200, no. 20 (2006): 5717–5724, <https://doi.org/10.1016/j.surfcoat.2005.08.128>.
22. R. Hannachi, D. Biggio, B. Elsener, M. Fantauzzi, N. Zacchetti, and A. Rossi, "A Contribution of XPS and Electrochemistry to the Understanding of Hydrogen Diffusion in X60 Steel," *Coatings* 15, no. 4 (2025): 442, <https://doi.org/10.3390/coatings15040442>.
23. B. Tjaden, D. J. L. Brett, and P. R. Shearing, "Tortuosity in Electrochemical Devices: A Review of Calculation Approaches," *International Materials Reviews* 63, no. 2 (2018): 47–67, <https://doi.org/10.1080/09506608.2016.1249995>.
24. Y. M. Chen, G. P. Yu, and J. H. Huang, "Comparison of Electrochemical Porosity Test Methods for TiN-Coated Stainless Steel," *Surface and Coatings Technology* 150, no. 2 (2002): 309–318, [https://doi.org/10.1016/S0257-8972\(01\)01528-6](https://doi.org/10.1016/S0257-8972(01)01528-6).

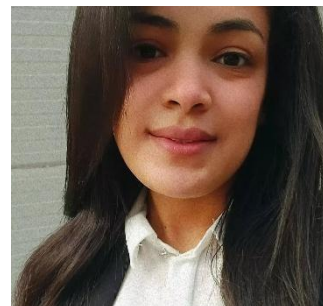
Curriculum Vitae

Raouaa Hannachi

E-mail: Raouaa.hannachi@unica.it

Phone: +39 3270499320

Date of Birth: 15/01/1996



Education Overview:

PhD in Chemical Sciences and Technology, University of Cagliari, Italy

From November 2022 - Present (Defense scheduled for May 2026)

Project: study hydrogen diffusion in uncoated and W-coated X60 steel to prevent hydrogen embrittlement of steel

Working on steel and coating materials for hydrogen storage and transportation

Techniques: X-ray photoelectron spectroscopy (XPS)

Hard X-ray photoelectron spectroscopy (HAXPS)

Master's degree in chemistry

University of Sassari, Italy

October 2018 - October 2020

Project: Synthesis of a geopolymer made from waste material and clay

Studying the mechanical properties and thermal conductivity of geopolymer synthesized using different raw materials (fly ash, rice ash, and metakaolin).

- Graduated with a score of 106 out of 110.
- Scholarship recipient (top 5% of cohort)
- Courses: Polymers, Macromolecular Chemistry, Analytical Chemistry, Organic/Inorganic Chemistry, Physical Chemistry, Catalysis, and Green Chemistry.

International master's degree in chemical sciences (Erasmus Exchange Program), University of Wroclaw, Poland, September 2019 - February 2020

- Graduated with a 4.28 out of 5.
- Recipient of a scholarship
- Courses include Electromagnetic Green Chemistry and Combinatorial Chemistry.

Bachelor's Degree in Materials Physics, University of Sousse, Tunisia,
September 2015 - July 2018

Project: Titanium dioxide properties for solar cell use.

- Techniques used: Sol-gel and hydrothermal. FTIR and XRD

Baccalaureate in Mathematics, High School of Gaafour, Tunisia, September
2011 - June 2015

- Passed National Exam
- Courses: Mathematics, Physics, Chemistry, and Experimental Science

Professional Experience Overview:

Independent Researcher, University of Cagliari, Italy

December 2025 – March 2026

- Development of oxide layers grown on steel as hydrogen permeation barriers
- Synthesis and surface treatment of metallic materials
- Characterization using X-ray Photoelectron Spectroscopy (XPS) • Hydrogen permeation testing (Electrochemical permeation test)
- Surface characterization of pure tungsten and tungsten oxides.

PhD Research: Examining hydrogen diffusion in uncoated/W-coated X60 steel to prevent embrittlement.

- Studying thermally grown oxide layers on steel as hydrogen permeation barriers.
- Working with electrochemical cell devices, including Devanathan–Stachurski and microcapillary cells.
- Performing material characterization and stress analysis using X-ray Diffraction (XRD).
- Utilizing the LECO instrument for hydrogen extraction and quantification.
- Developed and applied a combined technique using the LECO instrument and microcapillary cell for hydrogen determination in steel.

Traineeship - Rina Consulting CSM SpA, Rome, Italy

April 2024 - June 2024

- Worked on the project titled “Tungsten on Steel as Hydrogen Permeation Barrier”
- Introduction to RF Magnetron Sputtering Deposition
- Introduction to analysis with Scanning Electron Microscopy and roughness measurements.

Traineeship - Department of Chemistry, University of Sassari, Italy February 2020 - October 2020

- Frontal Geopolymerization
- Synthesis of Organic/Inorganic Materials through Frontal Geopolymerization and Polymerization
- Synthesis of Geopolymers.

Traineeship - University of Wroclaw, Poland October 2019 - February 2020

- Application of Geopolymers as adsorbents of heavy metals and organic pollutants

Traineeship - Laboratory of Nanomaterials and Renewable Energy Systems, Borj Cedria, Tunisia

June 2017 - August 2017

- Synthesis and characterization of titanium dioxide for photovoltaic applications • Used Sol-Gel and hydrothermal methods

Conferences & Seminars

Poster Presentations:

- **R. Hannachi**, B. Elsener, M. Fantauzzi, A. Rossi, "Functional properties of hydrogen permeation barriers on steel," XXX Conference of Analytical Chemistry – Italian Chemical Society, Vasto Chieti, Italy (September 17-21, 2023); poster presentation.
- **R. Hannachi**, D. Biggio, B. Elsener, M. Fantauzzi, N. Zacchetti, A. Rossi, "Tungsten coating on steel as hydrogen permeation barrier: a surface characterization," ECASIA 2024 – European Conference on Applications of Surface and Interface Analysis – Gothenburg, Sweden (June 9-14, 2024); poster presentation.
- **R. Hannachi**, D. Biggio, B. Elsener, M. Fantauzzi, N. Zacchetti, A. Rossi, "Tungsten as hydrogen permeation barrier on X60 steel," XXVIII Congresso Nazionale della Società Chimica Italiana, SCI2024 – Milan, Italy (August 26-30, 2024); poster presentation.

Participation:

- Next Generation Chemists – La Parola ai Giovani – Cagliari, Italy (November 4-5, 2022); participation.
- Seminar in “Advanced Technologies for Future Energy Carriers” – Cagliari, Italy (May 16, 2023); participation.

PhD Schools & Courses

- Winter School in Spectroscopy for Surfaces and Interfaces (CHESS2024 = “Scuola di spettroscopie convenzionali e ad alta energia per superfici e interfacce inorganiche, organiche e biomolecolari”) – Brescia, Italy (February 12-16, 2024) with a final exam (passed)
- International Summer School in ELMO-LION Battery PhD
- Educational School – Padova, Italy (July 29 - August 3, 2024) with a final exam (passed)

Courses organized by the PhD course in Chemical and Technological Sciences:

- Safety Training Course
- Training Course on Potentiostats (VersaStudio Software)
- Advanced Analytical Chemistry
- X-ray Photoelectron Spectroscopy
- Materials Technology and Applied Chemistry
- Radiation Protection
- B2 English Course
- Advanced NMR Spectroscopy
- Powder X-ray Diffraction

Collaborations & Tutoring

- Tutor in the Laboratory during Orientation Days (2023 and 2024)
- Tutor in the Laboratory for Women and Girls in Science Events (2023 and 2024)

Personal Skills Languages:

- Arabic (Mother Tongue)
- French (Second Language)
- English (B2)
- Italian (C1)

Software Proficiency:

- CasaXPS
- OriginLab Pro
- ChemDraw
- Microsoft Office Suite (Word, Excel, PowerPoint)
- Multipak
- Fityk

Problem Solving

Identifying issues and developing effective solutions

Team Working

Collaborating efficiently in diverse groups

Communication

Clear written and verbal expression of ideas

Critical Thinking

Analyzing complex information and making decisions

Adaptability

Adjusting quickly to new challenges and environments

Publication

- Hannachi, R.; Biggio, D.; Elsener, B.; Fantauzzi, M.; Rossi, A. X-Ray Photoelectron Spectroscopy Investigation of X60 Steel. *Surf. Sci. Spectra***2024**, 31, 024014,
- Hannachi, R., Biggio, D., Elsener, B., Fantauzzi, M., Zacchetti, N., & Rossi, A. (2025). A Contribution of XPS and Electrochemistry to the Understanding of Hydrogen Diffusion in X60 Steel. *Coatings*, 15(4), 442.
- Hannachi, R., Biggio, D., Elsener, B., Fantauzzi, M., Zacchetti, N., & Rossi, A. (2026). A Surface Analytical Method for Determining the Porosity of Tungsten Coatings as Hydrogen Permeation Barriers. *Surface and Interface Analysis*, 58(1), 3-8.

Acknowledgements

I would like to express my sincere gratitude to everyone who supported me throughout this journey.

First and foremost, I am deeply grateful to my supervisor, Professor Antonella Rossi, for her constant support, guidance, and encouragement. Beyond her scientific expertise and intelligence, what truly distinguishes Prof. Rossi is her genuine dedication to the growth of her students. Her ability to inspire critical thinking, her patience, and her unwavering belief in my work have been invaluable to me, both professionally and personally.

I am profoundly thankful to Professor Marzia Fantauzzi for her valuable advice and for always bringing positive energy to our group. Her intelligence and problem-solving skills contributed significantly to this research.

I am deeply grateful and thankful to Professor Bernhard Elsener for his essential contribution to this work. His deep expertise, thoughtful discussions, and ability to spark new perspectives have greatly enriched this research. I particularly appreciate his openness in sharing ideas and his constant encouragement to think more deeply and critically.

I would also like to thank Dr. Nicoletta Zacchetti for her support and guidance during my internship at Rina consulting CSM SpA in Castel Romano, Rome .

A special thanks goes to Dr. Deborah Biggio for guiding me since the very beginning of my PhD.

I would also like to thank Dr. Giovanni Emanuele Porcedda for his assistance with some XPS analyses and the calibration of the instrument, as well as Eng. Francesco Sciarrabba for his help with the deposition of the W coating.

I am very grateful to Dr. Lars P.H. Jeurgens for giving me the opportunity to join his research group at Empa Dübendorf and for the valuable scientific discussions.

I sincerely thank Dr. Claudia Cancellieri for her support, guidance, and assistance during my internship at Empa Dübendorf, as well as for our valuable scientific discussions.

I am also thankful to Dr. Jan Kollender, who introduced me to the microcapillary technique and shared many helpful ideas for my research.

I would like to warmly thank Chiara Menegus for her help, our long discussions, and the enjoyable moments we shared during my internship at Empa Dübendorf.

Finally, I am deeply grateful and thankful to my parents and my family for their unconditional support and belief in me, even when I am far from home. To my friends—my second family—thank you for being there through both the good and the challenging times. I am truly grateful to all of you.

This thesis was produced during participation in the PhD program in Chemical sciences and Technology at the University of Cagliari, XXXVIII cycle, with the support of a scholarship co-funded by Ministerial Decree No. 352 of 9.4.2022, under the PNRR - funded by the European Union - NextGenerationEU - Mission 4 “Education and Research”, Component 2 “From Research to Business”, Investment 3.3 “PNRR Scholarships for innovative PhDs addressing the innovation needs of enterprises”, and by the company Rina consulting CSM, SpA , Castel Romano, Rome.

